Lokalisatie van de epileptische aanvalszone op basis van EEG-connectiviteitsanalyse

EEG Source Connectivity for Seizure Onset Zone Localization in Epilepsy

Willeke Staljanssens

Promotoren: prof. dr. R. Van Holen, dr. ir. P. van Mierlo
Proefschrift ingediend tot het behalen van de graad van
Doctor in de ingenieurswetenschappen: biomedische ingenieurstechnieken

UNIVERSITEIT
GENT

Vakgroep Elektronica en Informatiesystemen
Voorzitter: prof. dr. ir. K. De Bosschere
Faculteit Ingenieurswetenschappen en Architectuur
Academiejaar 2017 - 2018

ISBN 978-94-6355-089-5
NUR 954
Wettelijk depot: D/2018/10.500/7

Department of Electronics and Information Systems
Faculty of Engineering and Architecture
Ghent University

UNIVERSITEIT GENT

MEDISIP
Corneel Heymanslaan 10
Entrance 36, floor 5
9000 Ghent
Belgium

Promotors
prof. dr. Roel Van Holen
dr. ir. Pieter van Mierlo

Examination board
prof. dr. ir. Patrick De Baets, Ghent University, *chairman*
prof. dr. ir. Guillaume Crevecoeur, Ghent University, *secretary*
dr. Geertjan Huiskamp, University Medical Center Utrecht
prof. dr. ir. Sabine Van Huffel, KU Leuven
prof. dr. Kristl Vonck, Ghent University
prof. dr. Serge Vulliémoz, University of Geneva
prof. dr. Roel Van Holen, Ghent University
dr. ir. Pieter van Mierlo, Ghent University

This research was funded by a PhD grant of the Agency for Innovation by Science and Technology in Flanders (IWT/131485).

Acknowledgements

Doing a PhD is a humbling experience. Every single day you get confronted with how little you know and the only thing you know for sure is that you know practically nothing. Still, after four years, all your tidbits of progress allow bundling your work into a book. Even more, you realize that doing a PhD yields more than just a book. It helps to get to know yourself better, it helps you to grow as a person and to mature. As a perfectionist, I should admit that both aspects, the book and the growing, are far from perfect nor complete. Yet, I am very proud of it - especially of the book - and I wouldn't have been able to accomplish this without the help of many people I would like to thank.

As a start, I would like to thank my promotors, prof. Roel Van Holen and dr. Pieter van Mierlo. Roel, although your expertise is in another field, you tried to advise me wherever possible and you taught me how to manage my project. If you hadn't told me to start writing my first paper, I would probably still be optimizing my first study. Also thanks for the many educational and sometimes philosophical discussions. Pieter, thank you for your thorough guidance and indispensable help in my research, for taking me along on conferences and to introduce me to so many people in your vast network. If you hadn't been there, there would be no PhD for me. I hope you can make the neuroscience part of Medisip grow.

I would like to express my gratitude to the professors of Medisip, prof. Stefaan Vandenberghe, prof. Roel Van Holen and prof. Chris Vanhove, for creating an informal atmosphere in which everybody can feel at home. You allow us to take practically whatever course we like and let us go to practically whatever conference we want in combination with a lot of flexibility to conduct our research and studies. Although this brings along great responsibility, I really enjoyed this freedom.

I am grateful to the members of the jury and all of my co-authors for reading my articles and PhD book and for providing so much useful feedback that enhanced the quality of my work. Also thanks to prof. Vonck, dr. Evelien Carrette and Stefanie Gadeyne for their help with the clinical part of my work.

A special thanks goes to my fellow office mates over the years who made the sometimes strenuous times a lot lighter. Thibault, Michael Carmichael is an even bigger hero than we first thought. I hope you have found a better stapler by now and that you can staple in peace. Thank you for being a great friend and colleague for all these years, missing the last bus was certainly much more fun when you were there. I am sure that one day, you'll have one hundred million dollars. I am curious what you will buy with it. Kim, thank you for the cute rat videos, for being my roomie in Vancouver, for your catchy laugh and your "occasional" nagging at Jelle. I wish you all the best in your buy-a-house-project. Jens, thank you for showing up randomly and, by that, brightening up the day with your many practical jokes and secret giggles. It was not soda pressing with you. Emma, for being so kind and authentic. Although you are a silent one, your presence is always more than appreciated and you can always be counted on. Milan, for being one of my best thesis students and for always being in a good mood, up for a laugh. I am convinced your PhD will be a great success. Gregor, for teaching me so many techniques I needed during my PhD. I hope Epilog will continue to grow and that one day my research can be of help. Amir, for being the nicest guy and hardest worker ever! I've never met somebody so motivated and enthusiastic and nice at the same time. I wish you all the luck in pursuing a PhD. Pieter Mollet, for being my neighbor in the office during my first months. You made me feel very welcome and made me laugh a million times. Victoria and Margo, both for your relaxed attitude and your kindness.

Furthermore thanks to the many other colleagues from Medisip. Stijn, for being so classy and for having the largest sweet tooth (decreasing my feeling of guilt when eating a second (or third) piece of cake). Mariele for being such a pleasant, open-minded, new colleague and for finding your place within Medisip so quickly. Gwenaëlle, Marek, Paulo and Prakash and of course the others, for the nice research coffee breaks and afterwork drinks. I wish you all the luck with your research! Inge, for being a true example of how you can mature without losing your cool. I really admire you. Saskia, together with Inge you are the pseudo-mothers of Medisip

and Biommeda. Without you, we would be totally lost. Many thanks for all the administrative and non-administrative support and for being the unchanging and stable factor in our environment. Carmen, Ester, Karen, Margo, Nathalie, Shandra, Victoria, and occasionally Radek, to form a super Medislip team. Bene for teaching me how to handle rats, for all your (live-saving) help during my lab animal side projects and for being so chill about 'everything' that went wrong during them.

Also thanks to the colleagues of Biommeda. Some of you have kind of very twisted minds, but that made so many lunches much more interesting and funny. Annette, Mathias and Geert, thanks for letting me throw my starter's party together with yours and for making it an unforgettable/unrememberable start.

Mijn klasgenoten uit de elektrotechniek, bedankt voor de gedeelde uren in de auditoria (altijd even wakker en even aanwezig), de goeie notities (onleesbare woorden nam ik zelf als krabbels over), de geslaagde (en ook wel minder geslaagde) projecten en het groen gezicht van Jens. Het kostte soms (letterlijk) bloed, zweet en tranen, en af en toe kropen we ervan in de kast, maar we zijn er uiteindelijk toch maar geraakt. Ook al was dat niet voor iedereen zonder kleerscheuren (... ook letterlijk).

Ik wil ook graag mijn andere burgievrienden Caro, Dorien, Willem, Jef, Max, Bob, Michiel, Yannick, Thomas, Nick en 'de aanhangsels' bedanken voor de geweldige studententijd, de skitrips en andere reizen, de vele uitjes of avonden-bij-iemand-thuis, de onvolgbare WhatsApp conversaties, de eindeloze discussies en het onbeschaamd nerd zijn. Dorien, Caro en Laurens, extra bedankt om mij uit te staan als huisgenoot de eerste drie jaar van mijn doctoraat.

Mijn vriendinnen van 'de Vijf': Fotis, Jolien, Dorien en Lien★. Bedankt voor jullie warme vriendschappen om mee op te groeien. Onze onderlinge diversiteit maakt onze band nog sterker en intenser. Jullie zijn stuk voor stuk prachtige dames met een groot hart op de juiste plaats. Bij uitbreiding ook bedankt aan jongeheer Wouter Blommaerts, Blommie, voor je nooid aflatend enthousiasme en om nog minder een blad voor de mond te nemen dan ik. Dorien en Wouter, Mattske is een fantastische dreumes en ik hoop dat er nog vele kindjes mogen bijkomen!

Mijn familie verdient ook een belangrijke plaats in dit dankwoord. Mama en papa, jullie zijn een ongelooflijk grote steun en toeverlaat en jullie liefde verwarmt mij nog steeds elke dag. Jullie doen zoveel voor ons en het is onmogelijk in woorden uit te drukken hoezeer ik dat apprecieer.

Bedankt, ik hou van jullie. Mijn zus Dorien en Nick, bedankt om dat kleine hoopje geluk genaamd Romy in mijn leven te brengen. Ze had niet schattiger kunnen zijn! Dorien, ondanks dat je mij waarschuwde en eigenlijk afraadde om een doctoraat te beginnen, was je er toch telkens wanneer dat nodig was als grote zus en ervaringsdeskundige om mij bij te staan met goede raad en daad. Bedankt.

Tenslotte wil ik nog Menno nog bedanken. Het is ongelooflijk hoe jij élke dag, hoe grijs ook, een glimlach op mijn gezicht kan toveren. Bedankt om mijn grillen te verdragen (mijn familie doet dat ook wel, maar zij hebben niet echt de keuze ...) en om mij meer in balans te brengen. Ik hoop dat we nog een lange, gezonde en vooral gelukkige toekomst tegemoet gaan en dat we, samen met Kriekie, snel in ons nieuwe huis kunnen settelen.

Willeke
22 december 2017
Gent

Summary

The purpose of this dissertation is to develop a method to noninvasively localize the seizure onset zone (SOZ) in patients with drug-resistant epilepsy based on electroencephalographic (EEG) recordings.

Epilepsy is a neurological disorder characterized by unprovoked and recurrent seizures. Seizures are caused by abnormal electrical activity in the brain, which can lead to a wide range of behaviors ranging from subtle absences to jerking of the whole body. For 60-70% of the patients, anti-epileptic drugs allow adequate seizure control. The remainder of the patients have so-called drug-resistant epilepsy. For them, the most efficient treatment option is epilepsy surgery during which the brain region responsible for the seizures is removed (resective surgery) or disconnected (disconnective surgery). Epilepsy surgery can only be performed when the region responsible for the seizures can be delineated and when there is no overlap with functional tissue in order to avoid functional deficits, such as speech or motor problems, after surgery. Unfortunately, no single modality or unique technique allows measuring or identifying this epileptogenic focus directly.

Therefore, these patients undergo a presurgical evaluation, during which a team of experts tries to form a hypothesis about this region, based on the integration of the results of different investigations. The cornerstone investigations are long-term video-EEG monitoring and Magnetic Resonance Imaging (MRI). EEG is a technique which measures the electrical activity of the brain with sensors or electrodes placed on the scalp. Since seizures (ictal) are caused by abnormal electrical activity, they result in abnormal EEG patterns. Yet, also in between seizures (interictal), short, abnormal EEG patterns can be observed. Based on these abnormal EEG patterns, epileptologists can get a rough idea about the SOZ, i.e. the region where the seizures originate from, or the irritative zone (IZ), i.e. the region where the interictal activity originates

from. MRI allows imaging the brain to reveal structural abnormalities such as lesions which could be responsible for the epilepsy. Often these investigations do not allow forming a solid hypothesis about the exact epileptogenic focus and extra investigations such as SPECT, PET, MEG and/or invasive EEG (iEEG, EEG recorded with electrodes placed inside the brain) are needed.

This whole presurgical process is time-consuming, labor-intensive, occasionally riskful for the patient (brain surgery is needed for invasive EEG) and possibly subjective since human interpretation is required. Furthermore, sometimes unambiguous delineation is still impossible. Therefore, it would be of high clinical value to have a method that is able to localize the responsible brain region in a more accurate, faster or automated, safe, and/or more objective way. In this dissertation, we aim to develop such a method for SOZ localization. The modality of choice is EEG since it is simple, safe, relatively inexpensive and the most important tool to diagnose epilepsy.

Developing such a method is not trivial because several challenges need to be addressed. The two main problems are the low spatial resolution of the EEG and the fact that epilepsy is a network disease. The low spatial resolution of EEG is due to the fact that the brain activity is propagated through the brain, skull, scalp and other tissues before it reaches the (often limited amount of) electrodes. The different conductivities of these tissues, and specifically the low conductivity of the skull, attenuate and distort the brain signals. As a consequence, the signal at a given electrode does not necessarily represent the activity of the directly underlying brain area, but is distorted and mixed with the activity of other brain areas. In this dissertation, we will tackle this problem in two ways. First, the number of electrodes can be increased with respect to standard EEG, resulting in so-called high-density EEG. Second, EEG source imaging (ESI) will be used. ESI is a technique that estimates the brain activity that generated the measured EEG. It consists of a forward model and an inverse problem. The forward model calculates how a certain source of activity in the brain will translate to an EEG measurement. In this dissertation, this forward model will be based on the MRI of the patient. The inverse solution tries to find the generating sources by minimizing a cost function based on the difference between the generated EEG by the forward model and the actually measured EEG.

By applying ESI on an EEG segment containing ictal activity, the brain regions active during the seizure can be identified. One way to estimate the SOZ is to select the most active brain region during the seizure. However, and this is the second problem, epilepsy is a network disorder rather than a focal disease. This means that during an epileptic seizure, different brain regions become active as a part of an epileptic network. There is no guarantee that the most active region during a seizure is the one causing the seizure, because a small group of neurons (associated with a less active region) could be triggering a larger group (associated with a more active region). To overcome this problem, we will analyze the epileptic network to find the driving region behind it. This can be achieved by functional brain connectivity, the study of the interactions and information flows between brain regions. In this dissertation, the connections or information flows between the active brain regions found after ESI are calculated using a time-varying multivariate autoregressive (TVAR) model in which the brain signals associated with the regions are modeled as a linear combination of their past samples plus uncorrelated white noise. This way, it can be investigated how the past samples of one signal influence the current samples of the other signals to assess the causality between these signals. The coefficients of the TVAR model are transformed to the frequency domain which results in a time-varying transfer matrix from which the spectrum weighted Adaptive Directed Transfer Function (swADTF) can be calculated. The swADTF is a measure of the information flow between two brain regions and stresses connections with high spectral power in both the receiving and the sending signal. Finally, the region with the highest outgoing information flow or swADTF values was used as an estimation for the SOZ.

In a first study, we verified this technique using simulations. We generated an epileptic network consisting of three nodes in the brain, added background activity to obtain a signal-to-noise ratio of 5 dB and used a forward model to generate high-density (204 electrodes) EEG measurements of 3 s. ESI was applied on 1000 of these simulated EEG segments and the most active brain sources were selected. Connectivity analysis as explained above was performed on the neuronal correlates of these selected brain sources and the source with the highest outgoing information flow was selected as estimation for the SOZ. The distance between the estimated SOZ and the true driver of the epileptic network, which we know from the simulation, was used to assess the quality of the estimation. To make a benchmark comparison, we compared this

distance to the distance between the most active region after ESI and the true driver. Our findings were threefold. First, we found that ESI followed by connectivity analysis (ESI + connectivity) is better than selecting the most active brain region after ESI (ESI power) to estimate the SOZ. Second, the median distance to the true driver was small, 12 mm. Third, when fewer electrodes were used (only a subset of the high-density EEG was used for ESI and connectivity analysis), the distances increased, up to a median distance of 21 mm for 32 electrodes.

In the second phase of this study, we validated the method in retrospective data of 5 patients. These patients ultimately underwent successful epilepsy surgery, so we know that the true SOZ was inside the tissue that was resected. In each of these patients, one seizure was pre-operatively recorded using high-density EEG with 204 electrodes. The first three seconds of the seizures were analyzed and connectivity analysis was done in the wide 1 to 30 Hz band, in order to be certain that the seizure frequency band was included. The estimated SOZ was compared with the resected zone. We confirmed that ESI + connectivity performs better than ESI power. ESI + connectivity was able to localize the SOZ within 10 mm of the border of the RZ in all patients, whereas ESI power could do this in only 2/5 patients. When lowering the number of electrodes used for analysis, we found again that the performance decreased. ESI + connectivity was able to localize the SOZ within 10 mm in only 1/5 patients, using 32 electrodes. We concluded that the proposed method can correctly localize the SOZ, given that the seizure is recorded with high-density EEG. Although more validation is needed, we suggested that it could become a useful tool in the presurgical evaluation of epilepsy.

Unfortunately, most clinics still lack the equipment to perform high-density EEG and it is usually not part of the default presurgical evaluation. Furthermore, long-term high-density EEG recordings are rare, since they are uncomfortable for the patient. Therefore, the chance that a patient has a seizure during a high-density EEG recording, is rather low.

For these reasons, we adapted the proposed method in a second study. Instead of strictly selecting the first 3 s of the seizure, we selected, together with an expert epileptologist, a (quasi) artifact-free epoch during the beginning of the seizure, lasting 1-5 s. Furthermore, connectivity analysis was limited to the frequency band of the rhythmic

activity in the EEG generated by the seizure. We validated this adapted approach retrospectively in 111 seizures of 27 patients (24 temporal lobe epilepsy, 3 extratemporal lobe epilepsy) who were rendered seizure-free after surgery. Again, we found that ESI + connectivity outperformed ESI power, this time statistically significant. ESI + connectivity resulted in a SOZ estimation within 10 mm of the border of the resected zone in 93.7% of the seizures. We confirmed our conclusion of the previous study that this method could serve as a useful tool in the presurgical evaluation, but now the standard long-term EEG monitoring can be used and seizures recorded with high-density EEG are not necessary. However, user-dependent input for the initial epoch and frequency selection is required. Larger studies are needed, notably with more extratemporal epilepsies and localization correlation with a range of different surgery outcomes.

In a final study, we investigated the importance of epoch and frequency band selection. In terms of epoch selection, best results were obtained when an artifact-free epoch was selected during the electrographic onset phase of the seizure, before the ictal patterns have evolved. Furthermore, we found that it is impossible to obtain a trustworthy SOZ estimation with this method during the preictal or postictal period. In terms of the frequency band, best results are obtained when the analysis is limited to the seizure frequency band corresponding to the analyzed ictal epoch. Although performance was lower when using the 1 to 30 Hz band, the difference did not reach significance and this band can possibly be used for analysis whenever the seizure frequency band is unclear.

In conclusion, we developed a method that combines ESI and functional connectivity analysis to noninvasively localize the SOZ based on ictal EEG recordings. The method is safe and proved to be accurate. Given more research, it could be made completely user-independent and automated. Yet, more validation, certainly in more heterogeneous population groups is necessary. Altogether, the method could serve as a useful and accurate tool in the presurgical evaluation of epilepsy.

Samenvatting

Het ultieme doel van dit proefschrift is het ontwikkelen van een methode voor de lokalisatie van de epileptische aanvalszone (EAZ) in patiënten met therapieresistente epilepsie op een niet-invasieve manier op basis van het elektro-encefalogram (EEG).

Epilepsie is een neurologische aandoening die gekenmerkt wordt door herhaalde aanvallen die niet uitgelokt worden. Deze aanvallen worden veroorzaakt door abnormale elektrische activiteit van de hersenen. Epileptische aanvallen kunnen gepaard gaan met stereotiepe klinische manifestaties gaande van subtiele bewustzijnsverminderingen tot ongecontroleerde spiertrekkingen over het hele lichaam. Bij 60-70% van de epilepsiepatiënten kunnen de aanvallen voldoende onderdrukt worden met behulp van anti-epileptica. De overige patiënten hebben zogenaamde therapieresistente epilepsie. Voor hen is epilepsiechirurgie de beste optie om aanvalsvrij te worden. Tijdens epilepsiechirurgie wordt de hersenregio die verantwoordelijk is voor de epilepsie verwijderd (resectieve operatie) of losgekoppeld van de rest van de hersenen (disconnectieve operatie). Epilepsiechirurgie kan enkel uitgevoerd worden wanneer voldaan is aan twee voorwaarden. Enerzijds moet de zone verantwoordelijk voor de epilepsie afgelijnd kunnen worden en anderzijds mag deze zone niet overlappen met functioneel weefsel waarvan de verwijdering zou kunnen leiden tot functionele gebreken zoals spraakproblemen. Helaas bestaat er geen manier om deze zone rechtstreeks op te meten.

Daarom worden patiënten met therapieresistente epilepsie opgenomen in de preheelkundige evaluatie waarin een team van experten een hypothese over deze zone probeert te vormen op basis van de resultaten van verscheidene onderzoeken. De belangrijkste onderzoeken zijn langdurige video-EEG registratie en *Magnetic Resonance Imaging* (MRI). EEG is een techniek die de elektrische hersenactiviteit opmeet met behulp

van sensors of elektroden die op de scalp geplaatst worden. Aangezien aanvallen gepaard gaan met afwijkende elektrische hersenactiviteit, zullen deze zichtbaar zijn als abnormale patronen in het EEG (ictale activiteit). Ook tussen aanvallen door zijn bij epilepsiepatiënten korte afwijkingen te zien in het EEG (interictale activiteit). Door het visueel inspecteren van het EEG kan een epileptoloog een ruwe schatting maken over de locatie van de epileptische aanvals- en irritatieve zone. De EAZ is de regio waar de aanvallen ontstaan en de irritatieve zone is de regio waar de interictale activiteit ontstaat. Daarnaast laat MRI toe om de hersenen te visualiseren om zo kleine afwijkingen zoals letsels te identificeren die de oorzaak van de epilepsie zouden kunnen zijn. Helaas zijn deze standaard onderzoeken vaak niet voldoende om een degelijke hypothese over de epileptische zone te maken. Daarom zijn vaak extra onderzoeken zoals SPECT, PET, MEG en/of invasief EEG (iEEG, EEG geregistreerd met elektroden die geïmplanteerd worden in de hersenen) nodig.

Deze hele preheelkundige evaluatie is een langdradig en arbeidsintensief proces. In het geval iEEG nodig is, is het ook risicovol voor de patiënt omdat een hersenoperatie nodig is. Daarnaast is het soms subjectief door de menselijke interpretatie van de resultaten. Tenslotte laat deze hele procedure niet toe om altijd een goede hypothese op te stellen en/of te bevestigen. Om deze redenen zou het van klinisch nut zijn om een methode te hebben die deze epileptische zone kan lokaliseren in een meer nauwkeurige, sneller of automatische, veilige en/of meer objectieve manier. Het doel van dit proefschrift is daarom het ontwikkelen van dergelijke methode. We kozen als basis het EEG, omdat het eenvoudig, veilig en relatief goedkoop is. Bovendien is het de belangrijkste techniek om de diagnose van epilepsie te stellen.

Het ontwikkelen van dergelijke methode is niet triviaal, omdat er enkele moeilijkheden mee gepaard gaan. De twee belangrijkste problemen zijn enerzijds de lage spatiale resolutie van het EEG en het feit dat epilepsie een netwerkziekte is, anderzijds. De lage spatiale resolutie van het EEG is te wijten aan het feit dat de elektrische hersenactiviteit eerst moet propageren door andere weefsels zoals de hersenen zelf, de schedel en de hoofdhuid alvorens zij een beperkt aantal elektroden bereikt. De verschillende elektrische geleidbaarheden van deze weefsels, en de lage geleidbaarheid van de schedel in het bijzonder, zorgen ervoor dat de hersensignalen afgezwakt en vervormd worden. Als gevolg hiervan komt het signaal gemeten aan een bepaalde elektrode niet zomaar overeen met

de hersenactiviteit van het gebied dat rechtstreeks onder de elektrode ligt, maar meet men een vervormd gemengd signaal op van verschillende hersenregio's. In dit proefschrift zullen we de lage spatiale resolutie van het EEG aanpakken op twee manieren. Eerst kunnen we het aantal elektroden sterk verhogen in vergelijking met een standaard EEG om zo tot een hoge-resolutie EEG te komen. Daarnaast zullen we EEG bronanalyse toepassen (*EEG source imaging*, ESI), een techniek die de onderliggende hersenactiviteit probeert te schatten die aanleiding geeft tot het gemeten EEG. ESI bestaat uit een voorwaarts model en een invers probleem. Het voorwaartse model beschrijft welk EEG men zal meten indien er in de hersenen een zekere, gekende bron actief is (gegenereerd EEG). In dit proefschrift wordt dit model geconstrueerd op de MRI van de patiënt. Bij het oplossen van het inverse probleem zal men een kostenfunctie, opgesteld op basis van het verschil tussen het gegenereerde en het gemeten EEG, proberen te minimaliseren. Zo kan men dan tot een schatting komen van de werkelijke hersenactiviteit.

Door ESI toe te passen op een ictaal EEG segment, krijgt men een idee welke hersenregio's actief zijn gedurende de aanval. Een manier om hieruit de EAZ af te leiden is het selecteren van de meest actieve regio. We weten echter, en dit is het tweede probleem, dat epilepsie eerder een netwerk- dan een puur focale ziekte is. Dit betekent dat gedurende de aanval verschillende hersenregio's actief worden die een deel vormen van het epileptische netwerk. Men kan niet zomaar besluiten dat de meest actieve regio tijdens de aanval de regio is die verantwoordelijk is voor de aanval, omdat een kleinere groep neuronen (geassocieerd met een minder actieve regio) een grotere groep neuronen kan aansturen (geassocieerd met een actievere regio). In dit geval willen we in staat zijn de minder actieve regio die de aanval initieerde aan te duiden als EAZ. Om dit te realiseren, zullen we het epileptische netwerk analyseren om zo de aandrijvende regio ervan te vinden. Dit kan gedaan worden met behulp van functionele connectiviteitsanalyse, de studie van de interacties en informatiestromen tussen de verschillende hersenregio's. In dit werk zullen de connecties of informatiestromen tussen de verschillende actieve hersenregio's gevonden door ESI berekend worden door gebruik te maken van een tijdsafhankelijk multivariaat autoregressief (TVAR) model dat de hersensignalen horende bij de hersenregio's modelleert als een lineaire combinatie van hun verleden plus ongecorreleerde witte ruis. Zo kan men onderzoeken hoe het verleden van het ene signaal het heden van een ander signaal beïnvloedt en een idee krijgen over de causaliteit

tussen deze signalen of regio's. De coëfficiënten van het TVAR model worden getransformeerd naar het frequentiedomein, wat resulteert in de transfermatrix. Op basis van deze matrix kan de *spectrum-weighted Adaptive Directed Transfer Function* (swADTF) berekend worden, welke een maat is voor de informatiestroom tussen twee regio's. De swADTF benadrukt connecties met een hoog spectraal vermogen in zowel het zendende als het ontvangende signaal. Tenslotte zullen we de regio met de hoogste uitgaande informatiestroom (hoogste swADTF waarden) selecteren als een schatting voor de EAZ.

In een eerste studie hebben we deze methode geverifieerd met behulp van simulaties. We simuleerden een epileptisch netwerk in de hersenen bestaande uit 3 netwerkknopen, voegden achtergrondactiviteit toe om tot een signaal-ruisverhouding van 5 dB te komen en genereerden op basis hiervan, met behulp van een voorwaarts model, hoge-resolutie EEG segmenten van 3 s met 204 elektroden. We pasten ESI toe op 1000 van deze segmenten en we selecteerden de meest actieve hersenregio's, waarna we connectiviteitsanalyse deden tussen deze regio's of bronnen. De bron met de hoogste uitgaande informatiestroom werd gebruikt als schatting voor de EAZ. De afstand tussen deze schatting en de echte aandrijver van het epileptisch netwerk (welke we kennen door de simulatie) werd gebruikt om de kwaliteit van de schatting te bepalen. Om een goede vergelijking te maken, vergeleken we deze afstand met de afstand tussen de meest actieve regio na ESI en de echte aandrijver. Onze bevindingen waren drievoudig. Ten eerste, ESI gevolgd door connectiviteitsanalyse (ESI + conn) was beter om de EAZ te schatten dan de meest actieve bron te nemen na ESI (ESI act). Ten tweede, de mediaan van de afstand tot de echte aandrijver was beperkt, 12 mm. Tenslotte vonden we dat de afstand vergrootte wanneer slechts een subset van de elektroden van het hoge-resolutie EEG gebruikt werden voor de analyse, tot 21 mm bij 32 elektroden.

In een tweede fase van deze studie, valideerden we de methode in echte retrospectieve data van 5 patiënten. Deze patiënten ondergingen uiteindelijk succesvol epilepsiechirurgie, waardoor we weten dat de echte EAZ zich in het weggenomen weefsel (*resected zone*, RZ) bevond. In elke patiënt werd 1 aanval opgenomen tijdens een preoperatieve hoge-resolutie EEG opname met 204 elektroden. De eerste 3 s van deze aanvallen werden geanalyseerd. Connectiviteitsanalyse werd gedaan in de brede 1 – 30 Hz frequentieband, zodat de aanvalsfrequentie zeker in de band zat. De geschatte EAZ werd vervolgens vergeleken met de RZ.

We bevestigden dat ESI + conn beter is dan ESI act. Met ESI + conn lokaliseerden we de EAZ in of binnen de 10 mm van de rand van de RZ in alle patiënten, terwijl ESI act dit maar in 2/5 patiënten mogelijk maakte. Wanneer we het aantal elektroden verlaagden, daalde de performantie van de methode. Wanneer slechts 32 elektroden gebruikt werden, was ESI + conn in staat om de EAZ binnen 10 mm van de RZ te schatten in 1 van de 5 patiënten. We besloten dat de voorgestelde methode, ESI + conn, de EAZ correct kan lokaliseren indien de aanval met hoge-resolutie EEG werd opgenomen. Ondanks dat meer validatie nodig is, concludeerden we dat deze methode nuttig zou kunnen zijn in de preheelkundige evaluatie van epilepsie.

Helaas hebben veel klinieken de mogelijkheid nog niet om hoge-resolutie EEG op te nemen en meestal maakt het geen deel uit van de standaard preheelkundige evaluatie. Verder zijn langdurige hoge-resolutie EEG opnames zeldzaam, omdat ze oncomfortabel zijn voor de patiënt. Dit verlaagt uiteraard de kans dat de patiënt een aanval heeft tijdens een hoge-resolutie EEG opname.

Omwille van deze redenen, hebben we onze methode aangepast in een tweede studie om deze ook te laten werken voor lage-resolutie of klinisch EEG. In plaats van strikt de eerste 3 s van de aanval te analyseren, selecteerden we samen met een expert epileptoloog een (quasi) artefactvrij stukje EEG rond het begin van de aanval, dat 1 – 5 s duurde. Daarnaast beperkten we de connectiviteitsanalyse tot de frequentieband van de aanval. We valideerden deze aangepaste methode retrospectief in 111 aanvallen van 27 patiënten (24 met temporalekwabepilepsie) die aanvalsvrij waren na operatie. Opnieuw vonden we dat ESI + conn beter presteerde dan ESI act, en door het grote aantal aanvallen, konden we dit verschil nu statistisch significant aantonen. ESI + conn resulteerde in een schatting van de EAZ binnen de 10 mm van de RZ in maar liefst 93.7% van de aanvallen. We bevestigden onze conclusie van de vorige studie dat deze methode heel nuttig zou kunnen zijn binnen de preheelkundige evaluatie van epilepsie, en dat aanvallen geregistreerd met hoge-resolutie EEG niet absoluut noodzakelijk zijn. Er is, in dit geval, wel gebruiker-afhankelijke input nodig om het stukje EEG en de frequentieband te selecteren. Grotere studies zijn nodig, met meer patiënten met extratemporalekwabepilepsie en met patiënten met verschillende operatieresultaten (bv. niet aanvalsvrij na operatie).

In een laatste studie onderzochten we het belang van de selectie van het geanalyseerd stukje EEG en de bijhorende frequentieband. Voor de selectie van het geanalyseerd stukje EEG, vonden we dat de beste resultaten bekomen werden wanneer een artefactvrij stukje EEG tijdens de elektrografische beginfase van de aanval gekozen werd, voor het EEG evolueert naar een ander patroon. Het was niet mogelijk een goede schatting van de EAZ te bekomen met deze methode op basis van EEG voor of na de aanval. Voor de frequentieband vonden we de beste resultaten wanneer de connectiviteitsanalyse beperkt wordt tot de frequentieband die geassocieerd wordt met het geanalyseerd stukje EEG. Hoewel de methode minder presteerde wanneer de brede 1 – 30 Hz band gebruikt werd, was dit verschil niet significant. Deze band zou dus gebruikt kunnen worden indien de frequentieband niet eenvoudig of eenduidig te vinden is.

In conclusie kunnen we stellen dat we een methode ontwikkeld hebben die ESI en functionele connectiviteitsanalyse combineert om zo op een niet-invasieve wijze de EAZ te lokaliseren op basis van ictale EEG opnames. De methode bleek nauwkeurig en is ook veilig. Indien er meer onderzoek gedaan wordt, zou de methode volledig gebruikers-onafhankelijk en automatisch gemaakt kunnen worden. Er is echter wel nog meer validatie nodig in een meer heterogene patiëntenpopulatie. Alles samengenomen, kan deze methode dienen als een nuttige en nauwkeurige *tool* in de preheelkundige evaluatie van epilepsie.

List of Abbreviations

AD	Alzheimer's disease
ADD	Attention-Deficit Disorder
ADHD	Attention-Deficit Hyperactivity Disorder
ADTF	Adaptive Directed Transfer Function
AED	Anti-Epileptic Drug
AIC	Akaike Information Criterion
AP	Action Potential
APDC	Adaptive Partial Directed Coherence
AR	autoregressive
ASL	Arterial Spin Labelling
BA	Brodmann Area
BCI	Brain-Computer Interface
BEM	Boundary Element Method
CAR	Common Average Reference
CLARA	Classical LORETA Recursively Applied
CNS	Central Nervous System
CSF	Cerebrospinal Fluid
CT	Computed Tomography
CTA	CT Angiography
CTP	CT Perfusion
DBS	Deep Brain Stimulation
DC	Directed Coherence
DCE	Dynamic Contrast Enhanced
DCM	Dynamic Causal Modelling
dDTF	direct Directed Transfer Function
DICS	Dynamic Imaging of Coherent Sources

DKI	Diffusion Kurtosis Imaging
DSC	Dynamic Susceptibility Contrast
DSI	Dynamic Seizure Imaging
DTF	Directed Transfer Function
DTI	Diffusion Tensor Imaging
DWI	Diffusion Weighted Imaging
ECD	Equivalent Current Dipole
ECG	Electrocardiogram
ECoG	Electrocorticography
EEG	Electroencephalogram
EOG	Electro-oculogram
EP	Evoked Potential
EPSP	Excitatory Postsynaptic Potential
ERP	Event-Related Potential
ESI	EEG Source Imaging
ETLE	Extratemporal Lobe Epilepsy
EZ	Epileptogenic Zone
FDM	Finite Difference Method
FEM	Finite Element Method
ffADTF	full-frequency Adaptive Directed Transfer Function
ffDTF	full-frequency Directed Transfer Function
FFT	Fast Fourier Transform
FLE	Frontal Lobe Epilepsy
fMRI	Functional Magnetic Resonance Imaging
FOI	Frequency band Of Interest
FSL	FMRIB Software Library
GCI	Granger Causality Index
hd	high-density
iADTF	integrated Adaptive Directed Transfer Function
ICA	Independent Component Analysis
iDTF	integrated Directed Transfer Function
IED	Interictal Epileptiform Discharge

iEEG	intracranial EEG
ILAE	International League Against Epilepsy
IPSP	Inhibitory Postsynaptic Potential
IZ	Irritative Zone
LAURA	Local Auto-Regressive Averages
LORETA	Low Resolution Electromagnetic Tomography
MEG	Magnetoencephalogram
MNE	Minimum Norm Estimates
MR	Magnetic Resonance
MRA	MR Angiography
MRI	Magnetic Resonance Imaging
MSI	MEG Source Imaging
MST	Multiple Subpial Transections
MUSIC	Multiple Signal Classification
MVAR	multivariate autoregressive
NIRS	Near-Infrared Spectroscopy
PCA	Principal Component Analysis
PDC	Partial Directed Coherence
PET	Positron Emission Tomography
R-MUSIC	Recursive MUSIC
RAP-MUSIC	Recursively Applied and Projected MUSIC
RF	radio frequency
ROI	Region-of-interest
rPDC	renormalized Partial Directed Coherence
RRE	Relative Residual Energy
RZ	Resected Zone
SBC	Schwarz Bayesian Criterion
sEEG	stereo EEG
sLORETA	Standardized Low Resolution Electromagnetic Tomography
SNR	signal-to-noise ratio
SOZ	Seizure Onset Zone
SP	Solution Point

SPECT	Single Photon Emission Computed Tomography
SPM	Statistical Parametric Mapping
SVD	Singular Value Decomposition
swADTF	spectrum-weighted Adaptive Directed Transfer Function
tDCS	Transcranial Direct Current Stimulation
TLE	Temporal Lobe Epilepsy
TMS	Transcranial Magnetic Stimulation
TVAR	Time-Varying Multivariate Autoregressive
UC	Update Coefficient
VEM	Video-EEG monitoring
VNS	Vagus Nerve Stimulation
WHO	World Health Organization
wMEM	wavelet-based Maximum Entropy on the Mean
WMNE	Weighted Minimum Norm Estimates

List of Publications

Journal Papers

[1] **Staljanssens W**, Van Holen R, van Mierlo P. EEG-based seizure onset zone localization in epilepsy: where are we now? *Neuroimage: Clinical*, submitted.

[2] Lagast S, De Steur H, Schouteten J, Gadeyne S, Hödl S, **Staljanssens W**, Vonck K, Boon P, Gellynck X, De Herdt V. Neurophysiological responses in sensory evaluation: an experiment on accepted and non-accepted solutions and drinks. *Behavioural Brain Research*, under review.

[3] van Mierlo P, Lie O, **Staljanssens W**, Coito A, Vulliémoz S. Influence of time-series normalization, number of nodes, connectivity and graph measure selection on seizure-onset zone localization from intracranial EEG. *Brain Topography*, under review.

[4] Khachatryan E, Brouwer H, **Staljanssens W**, Carrette E, Meurs A, Boon P, Van Roost D, Van Hulle M. A New Insight into Sentence Comprehension: the Impact of Word Associations in Sentence Processing as Shown by Invasive EEG Recording. *Neuropsychologia*, 108: 103–116, 2018.

[5] **Staljanssens W**, Strobbe G, Van Holen R, Keereman V, Gadeyne S, Carrette E, Meurs A, Pittau F, Momjian S, Seeck M, Boon P, Vandenberghe S, Vulliémoz S, Vonck K, van Mierlo P. EEG source connectivity to localize the seizure onset zone in patients with drug resistant epilepsy. *NeuroImage: Clinical*, 16(C): 689–698, 2017.

[6] **Staljanssens W**, Strobbe G, Van Holen R, Birot G, Gschwind M, Seeck M, Vandenberghe S, Vulliémoz S, van Mierlo P. Seizure onset zone localization from ictal high-density EEG in refractory focal epilepsy. *Brain Topography*, 30(2): 257–271, 2017.

[7] Wostyn S, **Staljanssens W**, De Taeye L, Strobbe G, Gadeyne S, Van Roost D, Raedt R, Vonck K, van Mierlo P. EEG Derived Brain Activity Reflects Treatment Response from Vagus Nerve Stimulation in Patients with Epilepsy. *International Journal of Neural Systems*, 2016.

[8] van Mierlo P, **Staljanssens W**, Carrette E, Meurs A, Van Roost D, Boon P, Vonck K. Lokalisatie van de epileptische focus op basis van netwerkanalyse van hersensignalen. *Neuron (Nederlandse ed.)*, 20(4): 8–12, 2015.

Conference Proceedings

[1] Carrette S, Klooster D, Nollet L, Duprat R, **Staljanssens W**, van Mierlo P, Van Dycke A, Carrette E, Raedt R, Meurs A, Baeken C, Vonck K, Boon P. P061 Continuous thetaburst stimulation for the treatment of refractory epilepsy - Case report. *Clinical Neurophysiology*, 128(3): e35, aug 2017.

Conference Abstracts

[1] **Staljanssens W**, Strobbe G, Van Holen R, Keereman V, Gadeyne S, Carrette E, Meurs A, Seeck M, Boon P, Vandenberghe S, Vulliémoz S, Vonck K, van Mierlo P. EEG source connectivity to localize the seizure onset zone from clinical ictal EEG in refractory epilepsy patients. *32nd International Epilepsy Congress.* Barcelona, Spain, 2017.

[2] **Staljanssens W**, Strobbe G, Van Holen R, Keereman V, Gadeyne S, Carrette E, Meurs A, Pittau F, Momjian S, Seeck M, Boon P, Vandenberghe S, Vulliémoz S, Vonck K, van Mierlo P. EEG source connectivity to localize the seizure onset zone in patients with drug resistant epilepsy. *International Conference on Basic and Clinical Multimodal Imaging.* Bern, Switzerland, 2017.

[3] Ghasemi Baroumand A, **Staljanssens W**, Hunyadi B, Strobbe G, Keereman V, Gadeyne S, Carrette E, Meurs A, Boon K Pauland Vonck, van Mierlo P. Decomposition methods help to localize the seizure onset zone from ictal EEG. *International Conference on Basic and Clinical Multimodal Imaging*. Bern, Switzerland, 2017.

[4] Lagast S, De Steur H, Schouteten J, Gadeyne S, Hödl S, **Staljanssens W**, Boon P, Gellynck X. Implicit measurement of preference and emotion in universal and personally accepted and non-accepted drinks. *12th Pangborn Sensory Science Symposium*. Providence, Rhode Island, USA, 2017.

[5] **Staljanssens W**, Strobbe G, Van Holen R, Keereman V, Gadeyne S, Carrette E, Meurs A, Pittau F, Momjian S, Seeck M, Boon P, Vandenberghe S, Vulliémoz S, Vonck K, van Mierlo P. Seizure onset zone localization from clinical ictal EEG in refractory epilepsy. *Annual Meeting of the Organization for Human Brain Mapping*. Vancouver, Canada, 2017.

[6] Klooster D, Carrette S, Besseling R, Carrette E, Raedt R, Baeken C, **Staljanssens W**, van Mierlo P, de Louw A, Aldenkamp A, Boon P, Vonck K. The effect of accelerated cTBS on functional connectivity in epilepsy patients. *Annual Meeting of the Organization for Human Brain Mapping*. Vancouver, Canada, 2017.

[7] Carrette S, Klooster D, **Staljanssens W**, Van Mierlo P, Van Dycke A, Carrette E, Raedt R, Meurs A, Baeken C, Vonck K, P B. Continuous thetaburst stimulation for the treatment of refractory epilepsy. *Congress of the European Academy of Neurology*. Amsterdam, The Netherlands, 2017.

[8] van Mierlo P, **Staljanssens W**, Strobbe G, Keereman V, Vonck K, Boon P, Seeck M, Vulliémoz S. Functional brain connectivity helps to localize seizures from EEG. *Jahrestagung der Deutschen und Österreichischen Gesellschaften für Epileptologie und der Schweizerischen Epilepsie-Liga*. Vienna, Austria, 2017.

[9] **Staljanssens W**, Strobbe G, Keereman V, Birot G, Meurs A, Carrette E, Momjian S, Van Roost D, Vonck K, Boon P, Seeck M, Vulliémoz S, van Mierlo P. Functional brain connectivity helps to

localize seizures from EEG. *Journées scientifiques Neurochirurgie HUG*. Geneva, Switzerland, 2017.

[10] Carrette S, Klooster D, **Staljanssens W**, Van Mierlo P, Van Dycke A, Carrette E, Raedt R, Meurs A, Baeken C, Vonck K, P B. Continuous thetaburst stimulation for the treatment of refractory epilepsy. *Brain plasticity in epilepsy*. Leuven, Belgium, 2017.

[11] Carrette S, Klooster D, **Staljanssens W**, Van Mierlo P, Van Dycke A, Carrette E, Raedt R, Meurs A, Baeken C, Vonck K, P B. Continuous thetaburst stimulation for the treatment of refractory epilepsy. *Update@Kempenhaege*. Heeze, The Netherlands, 2017.

[12] Carrette S, Klooster D, **Staljanssens W**, Van Mierlo P, Van Dycke A, Carrette E, Raedt R, Meurs A, Baeken C, Vonck K, P B. Continuous thetaburst stimulation for the treatment of refractory epilepsy Update and assessment of results. *SWO Midwintermeeting, Dutch League against Epilepsy*. Amsterdam, The Netherlands, 2017.

[13] Klooster D, Carrette S, Besseling R, Carrette E, Raedt R, Baeken C, **Staljanssens W**, van Mierlo P, de Louw A, Aldenkamp A, Boon P, Vonck K. The effect of accelerated cTBS on functional connectivity in epilepsy patients. *SWO Midwintermeeting, Dutch League against Epilepsy*. Amsterdam, The Netherlands, 2017.

[14] Carrette S, Klooster D, Nollet L, Duprat R, **Staljanssens W**, Van Mierlo P, Van Dycke A, Carrette E, Raedt R, Meurs A, Baeken C, Vonck K, P B. Anti-epileptic effects of continuous thetaburst stimulation in patients with refractory neocortical epilepsy Preliminary results of a pilot study. *Annual meeting of the American Epilepsy Society*, 2016.

[15] **Staljanssens W**, Strobbe G, Van Holen R, Birot G, Vulliémoz S, Seeck M, Vandenberghe S, van Mierlo P. Seizure onset zone localization from ictal high-density EEG in refractory focal epilepsy. *22nd Annual Meeting of the Organization for Human Brain Mapping*. Geneva, Switzerland, 2016.

[16] Carrette S, Klooster D, Nollet L, Duprat R, **Staljanssens W**, Van Mierlo P, Van Dycke A, Carrette E, Raedt R, Meurs A, Baeken C, Vonck K, P B. Continuous thetaburst stimulation for the treatment of refractory epilepsy - Case report. *4th Science factory summer school: TMS-EEG.* Helsinki, Finland, 2016.

[17] Carrette S, Klooster D, Nollet L, Duprat R, **Staljanssens W**, Van Mierlo P, Van Dycke A, Carrette E, Raedt R, Meurs A, Baeken C, Vonck K, P B. Continuous thetaburst stimulation for the treatment of refractory epilepsy - Case report. *Congress of the European Academy of Neurology.* Copenhagen, Denmark, 2016.

[18] Carrette S, Klooster D, Nollet L, Duprat R, **Staljanssens W**, Van Mierlo P, Van Dycke A, Carrette E, Raedt R, Meurs A, Baeken C, Vonck K, P B. Continuous thetaburst stimulation for the treatment of refractory epilepsy - Case report. *Update@Kempenhaege.* Heeze, The Netherlands, 2016.

[19] Carrette S, Klooster D, Nollet L, Duprat R, **Staljanssens W**, Van Mierlo P, Van Dycke A, Carrette E, Raedt R, Meurs A, Baeken C, Vonck K, Boon P. Continuous thetaburst stimulation for the treatment of refractory epilepsy - Case report. *SWO Midwintermeeting, Dutch League against Epilepsy.* Amsterdam, The Netherlands, 2016.

[20] **Staljanssens W**, Strobbe G, Van Holen R, Birot G, Michel C, Seeck M, Vulliémoz S, van Mierlo P. Electrical source imaging and connectivity analysis to localize the seizure-onset zone based on high-density ictal scalp EEG recordings. *International Conference on Basic and Clinical Multimodal Imaging.* Utrecht, The Netherlands, 2015.

[21] **Staljanssens W**, Strobbe G, Van Holen R, Birot G, Michel CM, Seeck M, Vandenberghe S, Vulliémoz S, van Mierlo P. Seizure onset zone localization from ictal high-density EEG in five patients. *Annual Meeting of the American Epilepsy Society.* Philadelphia, Pennsylvania, USA, 2015.

[22] **Staljanssens W**, Strobbe G, De Taeye L, Van Roost D, Vonck K, Raedt R, Van Holen R, Vandenberghe S, van Mierlo P. Source reconstruction of the P300 event-related potential as a biomarker for the efficacy of vagus nerve stimulation in epilepsy. *13th Belgian*

Day on Biomedical Engineering : joint meeting with IEEE EMBS Benelux Chapter, Abstracts. Brussels, Belgium, 2014.

[23] **Staljanssens W**, Strobbe G, De Taeye L, Van Roost D, Vonck K, Raedt R, Van Holen R, Vandenberghe S, van Mierlo P. EEG source reconstruction of the P3 event-related potential can help to understand the mechanism of action of VNS. *FEA Research Symposium 2014, Abstracts*. Ghent, Belgium, 2014.

[24] **Staljanssens W**, Strobbe G, De Taeye L, Van Roost D, Vonck K, Raedt R, Van Holen R, Vandenberghe S, van Mierlo P. Source reconstruction of the P300 event-related potential as a biomarker for the efficacy of vagus nerve stimulation in patients with epilepsy. *19th International Conference on Biomagnetism, Abstracts*. Halifax, Canada, 2014.

[25] **Staljanssens W**, Strobbe G, van Mierlo P, Van Holen R, Vandenberghe S. EEG beamforming to extract better features of motor imagery in a two-class real-time BCI. *International Conference on Basic and Clinical Multimodal Imaging, Abstracts*, volume 20, 108–109. SAGE, Geneva, Switzerland, 2013.

Contents

1 Introduction

1.1 Context

Approximately 1% of the people worldwide are diagnosed with epilepsy during their lifetime. Epilepsy is a neurological disorder characterized by recurrent and unprovoked seizures. These seizures are the result of abnormal electric activity in the brain. Depending on which brain regions are involved in the seizure, the patients can show a wide range of behaviors, called the semiology of the seizure, ranging from subtle absences to rhythmic jerking of the whole body.

The electric activity of the brain can be measured by the Electroencephalogram (EEG), in which electrodes are placed on the scalp to measure the potentials generated by the brain. Seizures give rise to aberrant patterns in the EEG. Also in between seizures, epileptic patients can have aberrant patterns in their EEG recordings, called Interictal Epileptiform Discharges (IEDs). EEG is an easy, safe and relatively inexpensive technique and therefore it serves, together with the semiology of the seizures, as the most important tool to diagnose, characterize and follow-up epilepsy.

Once a patient is diagnosed with epilepsy, treatment aimed at seizure suppression can be started. The first option is treatment with Anti-Epileptic Drugs (AEDs), which is effective in 60–70% of the patients. For the other 30–40% of the patients, who have so-called drug-resistant epilepsy, epilepsy surgery might be an option. During epilepsy surgery, the brain region that is responsible for initiating the seizures is removed (resective surgery) or disconnected (disconnective surgery). Of course,

epilepsy surgery is only possible when the brain region initiating the seizures can be identified and when this region does not overlap with functional tissue, whose removal could cause a functional deficit such as speech or motor problems. If one of these situations occur, other alternative treatment options could be offered such as neuromodulation techniques.

To determine whether a patient can benefit from epilepsy surgery, he is admitted to the presurgical evaluation. During this process, a team of experts, consisting of neurologists, radiologists, psychologists, etc., try to identify the Epileptogenic Zone (EZ) (the region that is necessary and sufficient to remove in order to render the patient seizure-free). Unfortunately, the EZ is only a conceptual region, meaning that it cannot be measured directly. The experts form a hypothesis about the EZ based on the consensus of the results of different investigations which include EEG, MRI and possibly PET, SPECT, MEG and intracranial EEG (iEEG) (EEG recorded with electrodes implanted in the brain). These investigations try to identify epileptic lesions, the Seizure Onset Zone (SOZ), i.e. the region where seizures originate, and the Irritative Zone (IZ), i.e. the region where IEDs originate. Only if a solid conclusion can be formed and there is no overlap with functional tissue, surgery will be performed.

This whole process is time-consuming, labor-intensive and possibly subject to human interpretation. Furthermore, iEEG requires brain surgery associated with possible complications. Therefore, it would be of high clinical value to have methods that are able to form a hypothesis about the EZ in a faster, more objective and safe way that can be applied in a clinical setting. The goal of this dissertation is to develop and validate such a method.

The technique of interest is EEG, since EEG is noninvasive and is the most important tool to diagnose epilepsy. It is generally accepted that epilepsy is a network disease, meaning that during a seizure several brain regions become active which influence each other in an epileptic network. During the recording of a seizure, we will identify which brain regions become active using EEG Source Imaging (ESI). ESI is a technique that estimates the brain activity that generated the measured scalp potentials. Once we know which brain regions are participating, we will map the communication between them using functional connectivity analysis to reveal the underlying seizure network.

Functional connectivity analysis can reveal the information flow between the active regions, which allows finding the *driver* of the epileptic network, the region that is responsible for initiating the seizures. This region is then an estimation of the SOZ, which can be used to form a hypothesis about the EZ.

In this dissertation, this approach will be applied on seizures recorded with scalp EEG of patients who ultimately underwent resective surgery to get an estimate of the SOZ. By comparing the estimated SOZ with the resected region, we can quantify the performance of the developed method. The performance will be compared to the performance of a benchmark method based only on ESI.

1.2 Outline

The structure of this dissertation is detailed in what follows. The rest of this book is divided into 7 chapters using a bottom-up hierarchy, in which every chapter builds on the concepts, ideas and/or results of the previous chapter. Nevertheless, every chapter can be read as a standalone entity.

Chapter 2 provides the context for this book with an introduction to the brain, EEG and epilepsy. First, the anatomy of the brain is described, both on the macroscopic scale and microscopic (level of the neuron) scale. Next, the working mechanisms of the brain are discussed, again on the macroscopic and microscopic level. After this, we describe how the structure and function of the brain can be imaged and investigated. One of these *neuroimaging* techniques is the EEG, which is explained more elaborately. We explain how it is possible to measure potentials at the scalp generated by brain activity and how these potentials are generally acquired and visualized. Typical healthy and abnormal brain rhythms and artifacts are presented next. We continue with a discussion about the temporal and spatial resolution of the EEG and we conclude this section with a list of possible applications. The most important clinical application of EEG is epilepsy. The next section defines and characterizes epilepsy as a neurological disorder before we detail how epileptic activity can be observed in the EEG. We discuss the several treatment options for epilepsy and give a detailed description of the presurgical evaluation.

As mentioned above, we will analyze the EEG of recorded seizures using ESI and functional connectivity to estimate the SOZ. Therefore, we

introduce these techniques in **Chapter 3**. ESI consists of a forward model and inverse solution, which are described separately. Next, we offer a general introduction to brain connectivity, which is divided into structural, functional and effective connectivity analysis. After, we provide more details about functional connectivity with special attention to Granger causality. Finally, we will link functional connectivity analysis to graph theory.

In **Chapter 4**, we review the literature and discuss the importance of EEG based SOZ localization. This technique is, however, not trivial and therefore the main challenges are discussed, while possible solutions are offered.

Chapter 5 details the first study and the first results obtained in this dissertation. Epochs during the beginning of seizures recorded with high-density EEG (EEG with 64 or more electrodes) of 5 patients are analyzed in a broad frequency band using the proposed approach. We provide a proof-of-concept of the technique and compare it to a benchmark method that is based only on ESI. Yet, a decrease in performance is noticed when fewer electrodes are used.

The proposed method is adapted in **Chapter 6** in order to achieve good performance in low-density or clinical setups (no more than 32 electrodes). Epoch selection is done manually to avoid artifacts and we limit the analysis to the frequency band of the seizure. We validate the approach in 111 seizures of 27 patients. We prove that the proposed method can achieve high accuracy for clinical EEG setups as well, and that it is again better than a method based only on ESI.

In **Chapter 7**, we investigate whether good performance can also be achieved when other parts of the seizure, after the initial ictal patterns have changed, or pre- and postictal data are analyzed. Furthermore, the influence of the analyzed frequency band is investigated in this chapter and we propose a technique to determine the frequency band of the seizure.

Finally, we summarize and discuss our results, future research perspectives and general conclusions in **Chapter 8**.

2
The brain, EEG and epilepsy

2.1 The brain

2.1.1 Introduction

The brain is the most important organ of the human body. It controls most of our other organs, gives us a consciousness and allows us to think, feel, sense and move. This is only possible because the brain is extremely complex and humankind is only beginning to grasp the intricacies of its functioning. The basic mechanisms are understood and in this section, we offer an elementary introduction to the anatomy, functioning and imaging of the brain in order to provide the context to follow the rest of this dissertation. We discuss the anatomy of the brain on a macro scale before we proceed to the anatomy on the level of the cell. The chapter then continues with an explanation of the major brain functions and how the brain basically works on the micro scale to accomplish these functions. Finally, we give an overview of techniques to image both the anatomy and the function of the brain in vivo. This section is mainly based on [1].

2.1.2 Anatomy

2.1.2.1 On the macro scale

The basic structural anatomy of the brain can be seen in Fig. 2.1. Together with the spinal cord, the brain forms the Central Nervous

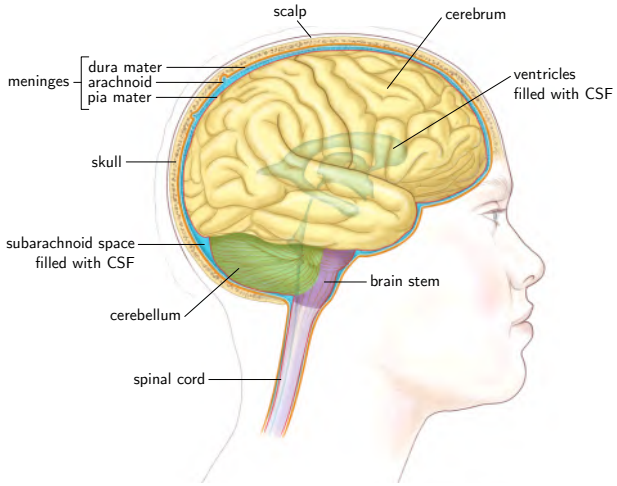

Figure 2.1: The structural anatomy of the brain. Figure adapted from [2].

System (CNS) of the human body. The CNS integrates the information it receives from all parts of the body and in turn coordinates and influences their activity. Whereas the spinal cord is primarily responsible for basic responses such as reflexes, the brain is in control of all voluntary actions.

Despite its importance, the brain is a vulnerable organ. Therefore, it is surrounded by the skull, acting as a case, to protect from injuries such as shocks, jolts and penetration. Three membranes or meninges form an extra protective layer between the brain and skull: the dura mater, attached to the inside of the skull; the blood-rich arachnoid, closely placed to the dura mater; and the pia mater, firmly adhering to the brain surface. The tough dura mater has several septa to keep the brain in place and to provide support for its own weight, like shelves in a book case.

The space between the arachnoid and the pia mater is called the subarachnoid space and is filled with Cerebrospinal Fluid (CSF), which is generated in four cavities more centrally in the brain, called ventricles. CSF acts as a physical shock absorber, but also provides immunological protection, supplies nutrients and offers a means to remove metabolic waste.

The brain itself consists of three major parts. The most inner one, the brain stem, stands up like a fist on an arm. Next, there is the cerebellum

at the lower rear of the brain. Finally, the cerebrum, dominating both physically and mentally, can be found wrapped around the brain stem. The outer part of the cerebrum consists of the cerebral cortex and deeper inside we can find some subcortical structures such as the hippocampus, thalamus, amygdala and basal ganglia.

To be able to fit the large surface (more than $0.23\,\mathrm{m}^2$ [3]) of the cerebral cortex into the relatively small skull (rouhgly $0.1\,\mathrm{m}^2$ on the outside [4]), it is folded into a characteristic pattern of bulges (gyri), and shallow and deep grooves (sulci and fissures, respectively).

The cerebrum can be subdivided into two cerebral hemispheres (left and right) by the medial longitudinal fissure. The two hemispheres are not completely separated since they are interconnected via the corpus callosum. Left and right hemisphere are largely symmetric, however, a slight torque is present, which makes the right front and the left back a little more prominent than their contralateral counterparts. The hemispheres, in turn, can be partitioned into four lobes: the frontal, temporal, parietal and occipital lobe. Within each lobe, most gyri and sulci are named based on their relative position in the brain, e.g. middle temporal gyrus, parieto-occipital sulcus, etc [5]. Others are named based on their morphology, e.g. the angular gyrus in the parietal lobe, the cuneus (Latin for 'wedge') in the occipital lobe, etc. Some are named after their relative position with respect to the latter category, e.g. the precuneus (translates to 'in front of the wedge'). Fig 2.2 shows a lateral and medial view of the brain in which the main gyri, sulci and fissures are indicated.

2.1.2.2 On the micro scale

The basic building block of the brain is the nerve cell or neuron. In a human brain, around 86 billion of these cells are present [6]. Each of these neurons connects with $5\,000$ – $200\,000$ of other neurons, forming an exceptionally complex network providing the computational backbone for our functioning from autonomous behavior up to higher-level cognitive abilities. Three types of neurons can be discriminated: motor neurons, sensory neurons and interneurons. The first two types are dedicated to conveying motor and sensory information, respectively. The interneurons are responsible to transfer information from one neuron to another neuron.

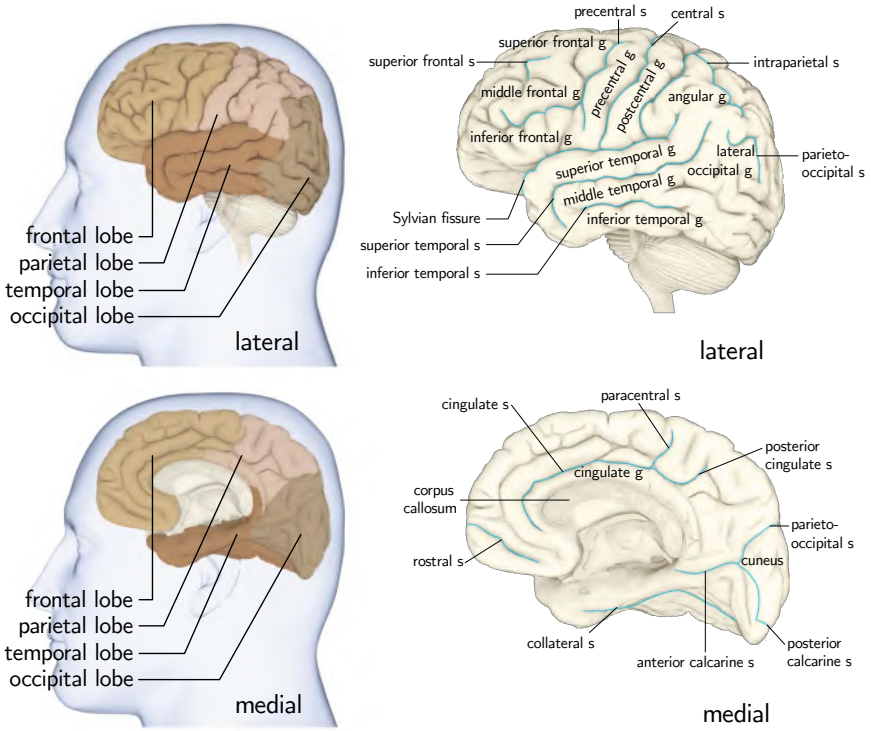

Figure 2.2: Lateral and medial views of the brain. Left: indication of the different lobes, right: indication of the main gyri (g) and sulci (s). Figure adapted from [1].

The typical anatomy of a brain neuron can be seen in Fig. 2.3. On one side of the neuron, there is a nucleus with genetic material embedded in a cell body from which many small dendrites sprout. These dendrites are very thin ($\approx 1\,\mu m$) and short (typically several $100\,\mu m$). A single dendrite can, however, branch several times so that they can reach a length of several centimeters in total. The cell body also has one large extension, the axon, which starts in the axon hillock and ends in several axon terminals. The axon is typically thicker than the dendrites ($\approx 25\,\mu m$) and can reach lengths of more than 1 m. This way, a neuron on the left side of the brain can be connected to a neuron on the right side of the brain through the corpus callosum, or even to a muscle cell in another part of the body. Yet, most axons are shorter than 1 cm. The axon is covered by a myelin sheath, which is regularly interrupted by gaps, called nodes of Ranvier. An axon terminal connects with a

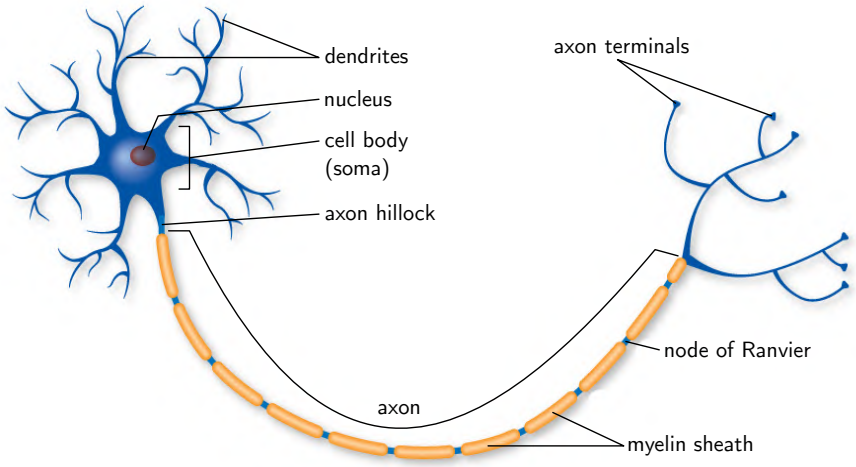

Figure 2.3: Anatomy of the brain neuron. Figure adapted from [7].

dendrite of another neuron in a synapse. A small gap, the synaptic cleft, remains between the presynaptic axon terminal and the postsynaptic dendrite.

In the cerebral cortex and the subcortical structures, mainly cell bodies reside, giving them their typical gray color. Therefore, these structures are also referred to as gray matter. On the other hand, the inner part of the brain primarily hosts axons, providing short and long range connections between neurons of different brain regions. The myelin sheath surrounding the axons has a fatty content, giving this inner part a characteristic white color, hence 'white matter'.

Not only neuronal cells are present in the brain, approximately the same amount of non-neuronal cells can be found [6]. These non-neuronal cells are primarily supporting cells or glia. First of all, cells are needed to form the myelin sheath around the axons of the neurons. These specific cells are called oligodendrocytes. On one axon, adjacent myelin segments are formed by different oligodendrocytes. One oligodendrocyte, however, can wrap around axons of several neurons [8]. Next, there are star-shaped astrocytes that maintain the chemical environment in the brain and that are part of the blood-brain barrier [9]. The oligodendrocytes and astrocytes are macroglia. Also microglia are present, which mainly form the immune defense of the brain [10].

2.1.3 Function

2.1.3.1 On the macro scale

Anatomically, three major parts in the brain can be distinguished: brain stem, cerebellum and cerebrum. Different functions can be attributed to these parts. The brain stem is highly involved in low- to mid-order mental activities. Autonomic control is regulated in this region and therefore it handles our heart rate, breathing, sleeping and eating patterns. Moreover, it serves as a gateway between the main part of the brain and the rest of the body for many motor and sensory systems. The primary role of the cerebellum is in movement-related functions. It contributes to the enhancement of coordination, accuracy and timing of movements. This way, the cerebellum assists the cerebrum to control all voluntary actions in the body. The cerebrum also plays a key role in emotions, memory, attention, perception, awareness, thought, language, higher-order cognitive functioning, etc. Thanks to the cerebrum, we have a consciousness and a personality. Particular segregated regions of the cortex and subcortical structures take care of specific functions. In Fig. 2.4, an overview of how different functions are typically dispersed over the brain can be seen.

The frontal lobe is mainly responsible for generating action plans based on the projection of future consequences resulting from current actions. It provides our conscience or 'inner speech' and makes sure that we behave socially acceptable. Damage to this area can cause a well-behaved person to become profane and impolite. Next, the primary motor cortex, the brain region regulating voluntary movement, is also located in the frontal lobe. Interesting to remark is that the left side of the brain controls the right side of our body and vice versa. Also, sensory information coming from taste and smell is processed here. Furthermore, it allows us to speak through a region that is also called Broca's area. This region was one of the first functional regions to be discovered in the late 19th century by Paul Broca. Broca examined the brain of a patient only able to say the word "Tan" and found damage to the region which became Broca's area.

Sensory information based on touch is processed in the parietal lobe. Actually, every kind of sensory information is transmitted from the sense organs to a specific site of the cortex, but all the information is integrated inside this parietal lobe to build a single multi-sensory

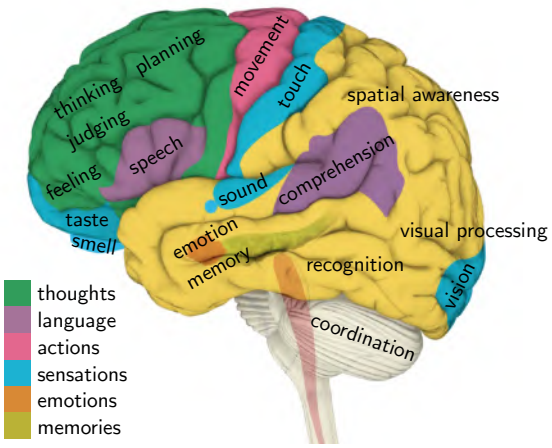

Figure 2.4: Overview of the location of different functions in the cerebrum. Figure adapted from [1].

perception. Furthermore, the parietal lobe provides us with spatial awareness, administering a spatial coordinate system to represent the world around us.

On the border of the parietal and temporal lobe, Wernicke's area can be found. This region is, together with Broca's area, important for speech [11]. Damage to this region may cause problems in recognizing and understanding language, rather than speech problems. Hearing and sound itself are also processed in the temporal lobe. The temporal lobe also has an important function in creating new memories, and in recalling previously encountered events, e.g. recognizing faces.

The occipital lobe is mainly responsible for processing visual information. It makes possible that we understand what we perceive through our eyes.

Finally, the subcortical structures play a major role in memory (together with the associated regions in the temporal lobe) and the formation and regulation of emotions.

As already mentioned, the left and right hemisphere are largely symmetric. Nonetheless, some functions are more developed in one hemisphere, e.g. speech, language and reasoning are mainly located in the left hemisphere in most people.

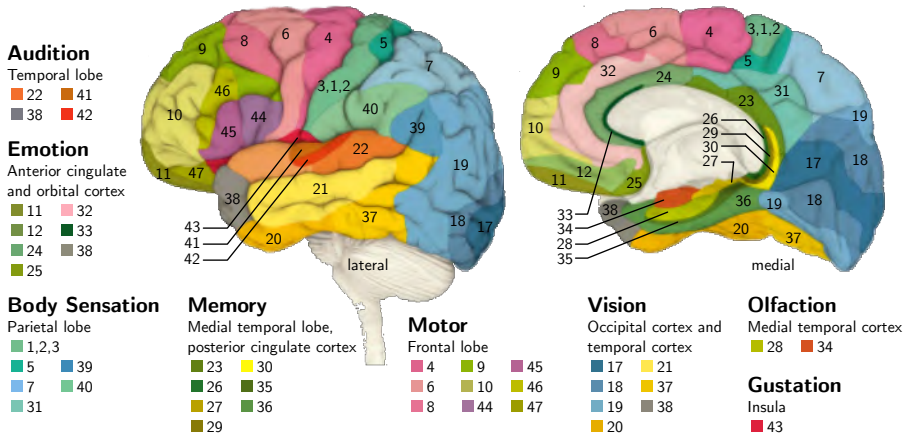

Figure 2.5: Illustration of the Brodmann areas in humans. Figure adapted from [1].

The brain cannot only be mapped by gross anatomy, i.e. the lobes, gyri and sulci, but also based on microscopic anatomy or cytoarchitecture. This way, Brodmann identified several brain areas based on the shape and type of cells and their connections. All these Brodmann Areas (BAs) can also be linked to neurological function, as can be seen in Fig 2.5. For example, BA 4 corresponds to the aforementioned primary motor cortex, BA 44 and 45 form Broca's area, and BA 39 and 40 constitute Wernicke's area.

In modern neuroscience researchers have come to the conclusion that in spite of the fact that function seems to be anatomically segregated over the brain, the cortical infrastructure supporting a simple or complex process typically spans several functionally specialized areas. These areas are structurally and/or functionally integrated, meaning that the brain works as a complex interconnected network, rather than as different focal regions working completely separately.

2.1.3.2 On the micro scale

To achieve the aforementioned functions, neurons need to communicate with both neighboring and distant neurons. The main function of a neuron is thus to process and transmit received signals across its length from dendrite to axon terminal, through the synaptic cleft to

the dendrites of other neurons or other cells such as muscle cells. In what follows, we will explain how a neuron achieves this. This section is mainly based on [12, 13].

The environment of the neuron has a certain distribution of sodium (Na^+) and potassium (K^+) ions. In rest, there is a certain imbalance in this distribution between the inside and the outside of the cell, maintained by Na^+ and K^+ pumps and voltage-dependent channels embedded in the cell membrane. More specifically, there is a higher Na^+concentration outside the cell than inside and vice versa for the K^+concentration. Due to this imbalance, a potential difference of $-70\,\text{mV}$ arises across the cell membrane. The inside of the cell is more negative than the outside. In what follows, all potentials are referenced to the outside environment of the cell.

When a neuron receives information via its dendrites, this happens in a chemical way in the synaptic cleft. The axon terminals of the sending (presynaptic) neuron release neurotransmitters such as dopamine and glutamate into the synapse. This synapse can be either excitatory or inhibitory. Due to the binding of the neurotransmitter to the receptors of the postsynaptic dendrites in an excitatory or inhibitory synapse, the Na^+ or K^+ channels will open respectively. In the excitatory case, when the Na^+ channels open, an inflow of Na^+ will occur due to the original concentration gradient at rest. As a consequence, the cell will locally become more positive and the potential difference across the cell membrane will decrease, resulting in a temporary depolarization called an Excitatory Postsynaptic Potential (EPSP). In the inhibitory case, K^+ channels open and therefore an outflow of K^+ will happen, rendering the cell on the inside even more negative than originally in rest. This temporary hyperpolarization is called Inhibitory Postsynaptic Potential (IPSP). The EPSPs and IPSPs have a relative amplitude of $\pm 10\,\text{mV}$ and last for about 10 ms [14], during which they will passively spread inside the neuron and reach the axon hillock. This is the process of conduction. Due to the influence of different EPSPs and IPSPs that can originate in the same or different dendrites and that (partially) overlap in time, the potential at the axon hillock can increase (more EPSPs than IPSPs) or decrease (vice versa). Whenever the axon hillock reaches a potential of $-55\,\text{mV}$, the signal will be transported along the axon to next neuron(s). This process is also called neuronal 'firing'. EPSPs enhances the probability that the neuron will fire, hence 'excitatory', whereas IPSPs decrease the change that the neuron will fire, hence

'inhibitory'. When the potential difference of $-55\,\mathrm{mV}$ is not attained, the neuron will gradually repolarize to resting state until the inside of the cell is again $-70\,\mathrm{mV}$ lower than the outside. In this case, the signal is stopped.

When a neuron fires, it generates an Action Potential (AP). An AP is a large and rapid depolarization up to $+30\,\mathrm{mV}$, followed by a repolarization. The AP lasts about 1 ms. After repolarization, a short period of hyperpolarization occurs, the refractory period, during which the neuron cannot fire again. The AP in relation to the EPSP and IPSP can be seen in Fig. 2.6. The AP needs to be propagated from the axon hillock to the axon terminals. Therefore, *electrotonic conduction* along the axon happens. Electrotonic conduction is helped by the myelin sheath that acts as an electrical insulator allowing rapid transmission, making this a very fast procedure. Moreover, no energy is needed to sustain this process. Yet, the signal decays rapidly over time. Despite the fact that the AP has a high amplitude, it would not be able to reach the end of the axon solely by electrotonic conduction. For this reason, the myelin sheath is intermitted with nodes of Ranvier, in which the AP is actively amplified. Although this is a slower process that requires more energy, it makes sure that signal quality is maintained throughout transmission. The alternating propagation of the AP along the myelinated segments (fast, decaying signal) and the nodes of Ranvier (slow, restoring signal), is also called *saltatory conduction* (*saltare* is Latin for 'to jump'). When the AP finally reaches the axon terminals, neurotransmitters are released into the synapses with the next neurons and the whole process of postsynaptic potentials and AP can be repeated.

2.1.4 Neuroimaging

Initial brain research was mainly based on post-mortem studies. Brains of both healthy and abnormal or diseased deceased humans or animals were taken out and carefully examined. A functional deficit could possibly be related to anatomical anomalies and this way, an anatomical area could be linked to a certain function. The areas of Broca and Wernicke, discussed above, are good examples of this. Anatomy could be studied very thoroughly this way, however it was harder to map functional regions since researchers had to rely on a limited amount of

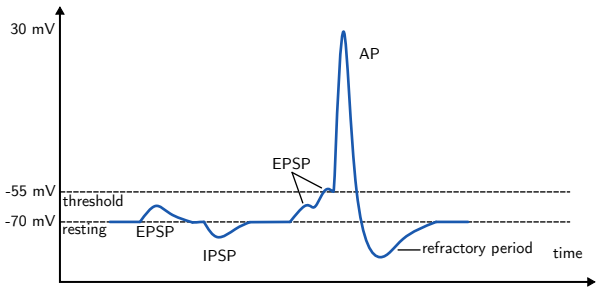

Figure 2.6: Illustration of EPSP, IPSP and AP. On the x-axis, time is represented in the order of milliseconds, the y-axis shows the amplitudes of the potentials.

case studies in which a patient with a well-defined functional disability died.

Some in vivo experiments were done as well. The lobotomies performed in the late 19th and the first half of the 20th century are one illustration. The anterior part of the frontal cortex was removed to reduce symptoms of mental illnesses such as psychosis. However, it often left people apathetic. Therefore, this technique was very controversial. The practice of drilling holes in the head has, however, been used for centuries to cure a vast array of diseases. Other examples are the use of electrical brain implants to trigger certain reactions, or the use of electrical stimulation of certain brain area's during surgery to elicit their functionality. Due to the invasive nature of these experiments and growing ethical awareness, this kind of in vivo experiments was quickly reduced to an accountable minimum. As a consequence, scientists were unable to find out much about the workings of the brain for a long time.

Fortunately, the advent of neuroimaging techniques has allowed studying the brain in vivo in a noninvasive way, giving researchers the opportunity to investigate large cohorts of healthy and diseased subjects in a safe way. In this section, we explain the terminology of the different viewing planes in the brain and we continue with giving an overview of existing modalities to image both brain anatomy and function. An overview of these modalities can be seen in Fig. 2.7.

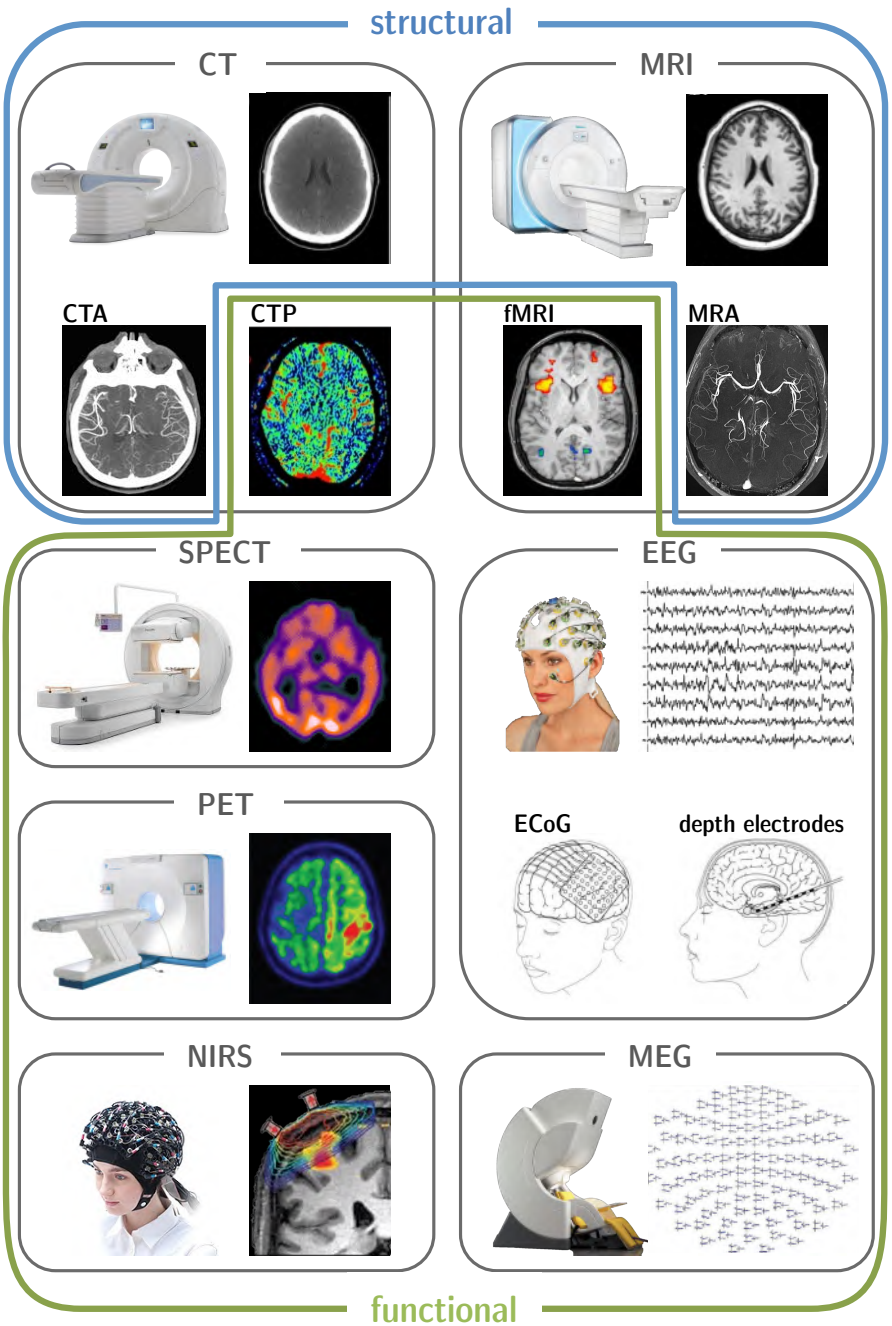

Figure 2.7: Overview of neuroimaging modalities.

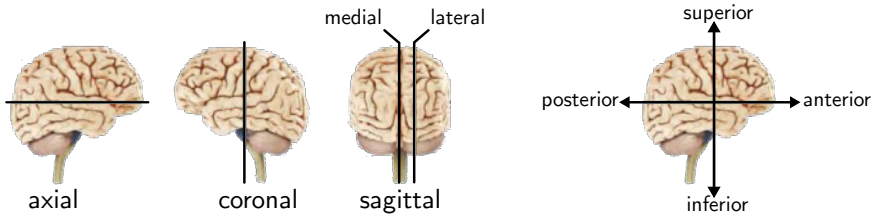

Figure 2.8: The three primary orthogonal viewing planes in neuroimaging and illustration of directional terms.

2.1.4.1 Imaging views

Researchers and doctors often look at planes or sections through the brain. These sections can be made in different ways. Three standard cuts exist, oriented perpendicular to each other. First, a transverse or axial slice can be taken, a cut which detaches the upper and lower part of the brain. The slice is perpendicular to the main length axis of the human body. Towards the bottom, parts are referred to as inferior, whether upper parts are superior. Second, a coronal view exists, based on a section that separates the front of the brain (anterior) from the back (posterior). Third, a sagittal slice divides the brain into a left and right plane. This can be done in the middle (between the two hemispheres), called medial, or more to one side, called lateral. Fig. 2.8 shows these three standard orthogonal planes to visualize the brain and the corresponding navigational terms. Of course, most modalities are not restricted to these three standard planes and every desired angle is possible. Furthermore, often it is possible to acquire or show three-dimensional images as well.

2.1.4.2 Structural imaging

Two modalities exist to capture head anatomy. **Computed Tomography (CT)** creates tomographic images by the use of X-rays. CT is actually an extension of a classical radiographic image in which X-ray photons are projected through the subject. Some X-rays are attenuated by the body, while others will pass through and will be captured by a detector. Tissues with a higher density (e.g. bone) have a higher chance of attenuating the X-rays than tissues with lower density (e.g. soft tissues, such as the brain). This way, a kind of two-dimensional

density map of the subject is made. In CT, the X-ray beam and detector rotate around the subject, making images from many angles. This way, every image incorporates different depth information and by combining these images with reconstruction algorithms, an image of the inside of the body can be obtained. CT has many clinical applications, but most important for the head and brain are the detection of tumors, calcifications, infarction, hemorrhage and bone trauma. Contrast agents can be used to study the brain's blood vessels with **CT Angiography (CTA)**.

The skull has a high density and will be well delineated on CT. The different tissues (e.g. white and gray matter) inside the brain itself, however, have all nearly the same density and therefore it is hard to image the brain with good contrast between these tissue types and to reveal subtle anomalies. Another obvious drawback of CT is the fact that the subject is exposed to ionizing radiation.

The second modality to image brain structures is **Magnetic Resonance Imaging (MRI)**. Unlike CT, MRI does not require ionizing radiation and is therefore less harmful for the patient[1]. MRI makes use of the magnetic properties of the hydrogen atoms in our body. The nuclei of these hydrogen atoms are able to absorb and emit radio frequency (RF) signals when placed in a magnetic field. By placing the subject in an external, strong, static, homogeneous magnetic field, hydrogen atoms will become aligned with this field. Next, RF sequences or pulses are applied, which excite the hydrogen atoms. As a reaction, the excited hydrogen atoms will relax and decay to their original alignment to the static field and will emit an RF signal themselves by doing so. These RF signals can then be measured. With the combination of carefully chosen magnetic gradients to encode location information and reconstruction software, it is possible to create an image of the inside of the body, highlighting different aspects of the scanned tissues. Hydrogen atoms are mainly abundant in water and fatty tissues. Hence, MRI has excellent soft tissue contrast to image the brain in a very detailed way. White and gray matter can be clearly distinguished from each other. Yet, the skull does not contain water nor fat and cannot be imaged easily with this modality. Nevertheless, a lot of research is dedicated to generating new gradient sequences in order

[1] Note that adverse health effects are possible due to the radio frequency radiation used in MRI.

to be able to image bone structures as well. Clinically, MRI is used to reveal subtle abnormalities such as cortical dysplasia and atrophy, but it is also used to diagnose tumors, demyelinating diseases, dementia, etc. Another MRI technique, called **MR Angiography (MRA)**, allows imaging blood vessels. As opposed to CTA, MRA does not require the injection of a contrast agent.

2.1.4.3 Functional imaging

CT and MRI can both be used for functional imaging as well. A contrast agent can be injected into a patient's venous system shortly before acquisition allowing to image the brain perfusion with **CT Perfusion (CTP)**. Whereas the functional imaging possibilities with CT are rather limited, MRI offers more options by the use of **Functional Magnetic Resonance Imaging (fMRI)**. With fMRI, it is possible to detect changes in the ratio of oxygenated and deoxygenated blood in the brain. These changes are an indirect measure of neuronal activity since regions that become active will need more oxygen. This technique allows measuring brain activity with high spatial resolution. The temporal resolution is however limited because changes in the oxygen levels happen slower than the neuronal activity itself. In research, fMRI is often used to unravel working mechanisms of the healthy and the diseased brain. Clinically, fMRI can be used to map regions linked to critical functions, such as speaking and moving, and can, therefore, help planning brain surgery for e.g. tumor resection. Other MRI-based functional imaging techniques are **Arterial Spin Labelling (ASL) MRI**, **Dynamic Susceptibility Contrast (DSC) MRI** and **Dynamic Contrast Enhanced (DCE) MRI** to measure brain perfusion.

Another way to measure brain perfusion is **Single Photon Emission Computed Tomography (SPECT)**. In SPECT, the patient is injected with a radiotracer. This radiotracer is a substitute biologically active molecule, antibody or other molecule, labeled with a single photon emitting isotope. The uptake time of the tracer is within 30 to 60 minutes, but the patient can be imaged several hours later. This way, the e.g. regional cerebral blood flow during time of injection can be imaged. In epilepsy patients, the tracer can be injected during the seizure and imaging can happen afterwards when the seizure has passed. Hyperperfusion may indicate the seizure focus. Other applications are

tumor and infection imaging. Since the patient is injected with a radiotracer, SPECT is called a nuclear imaging technique and the patient is subjected to ionizing radiation.

Another nuclear imaging technique is **Positron Emission Tomography (PET)**, used to image the metabolic rate in the brain. Again, the patient is injected with a radiotracer, now consisting of a molecule used for metabolism (such as glucose), labeled with a positron emitting isotope. The half life time of the isotopes used in PET are often much shorter than in SPECT, hence the time between injection and scanning is limited. The main application of PET lies in the field of oncology, where it is used to image tumors and metastases, since these structures are often growing and therefore very active from a metabolic point of view. In epilepsy, a local hypometabolic spot can point to the onset of the seizures.

The aforementioned modalities have two things in common: they create an image of the inside of the brain, and they measure neuronal activity indirectly. Yet, there are other ways of recording brain activity. In the **Electroencephalogram (EEG)**, brain activity is measured directly with a very high temporal resolution by measuring the electric fields generated by the neurons. This is done by electrodes that can be placed on the scalp, on the cortex (Electrocorticography (ECoG)) or inside the brain (intracranial or stereo EEG (sEEG)). The latter two are invasive techniques (intracranial EEG (iEEG)). The measurement or recording consists of a trace of the measured potential for every involved electrode. When the electrodes are placed on the scalp, the technique is completely noninvasive. Moreover, EEG is also mobile and relatively cheap. Though, signal quality is rather low because the electric fields are influenced (attenuated and distorted) by the skull, which is only low-conductive. Intracranial EEG with electrodes inside the brain does not suffer from this drawback, since it measures potentials locally, and offers excellent signal quality, but the procedure is invasive and associated with medical risks for the patient such as scarring, infection and functional loss. Furthermore, it is practically impossible to sample the whole brain. ECoG is somewhere in between the signal quality - medical risk trade-off. EEG has a wide application area, both clinically and in research. The EEG will be discussed more elaborately in the next section.

The **Magnetoencephalogram (MEG)** is a similar, but complementary, technique to EEG. It measures the magnetic field generated in

the brain with very sensitive magnetometers placed close to, but not touching, the head. This field is, however, several orders of magnitude smaller than the Earth's magnetic field. Therefore, recordings have to take place in special magnetic shielded rooms. Moreover, the magnetometers need to be cooled with helium to maintain proper functioning. This makes MEG immobile and it is also quite expensive. The major advantage of MEG is the fact that the signals are not distorted due to the propagation through the other tissues such as skull and CSF, since the magnetic permeabilities of these tissues are approximately the same as in empty space. Hence, the signal quality is unhampered. Therefore, it is easier to derive the underlying brain activity that generated the MEG recording (Magnetic Source Imaging (MSI)), than deriving the underlying brain activity from EEG (Electrical/EEG Source Imaging (ESI), see next chapter). EEG is sensitive to both tangential and radial components of a current source, allowing it to detect activity both in the sulci and the gyri. MEG, however, only detects the tangential components, making it more sensitive to activity originating in sulci. The main clinical application for MEG is to reveal information about the focus in epilepsy patients.

Finally, a recent non-invasive technique, called **Near-Infrared Spectroscopy (NIRS)**, uses near-infrared light to measure changes in the level of oxygenated and deoxygenated blood in the brain, like fMRI. A near-infrared light bundle is shined locally on the patient's head, the bundle will follow a banana-shaped trajectory and will exit the brain in another place on the head, where a detector is placed. Based on the spectra of the incoming and outgoing light, changes in oxygenated and deoxygenated blood levels can be detected. NIRS is very mobile and is cheaper and less intrusive than fMRI, but is also less sensitive for deeper sources and has a worse spatial resolution [15].

Structural imaging techniques image anatomy and functional techniques measure function. However, a combined map is often desired, providing an anatomical reference for a functional image. A patient undergoing a PET scan will often get a structural image as well, in order to overlay both images to get more detailed information. Yet, it can be hard to register these images since they are of a different nature and because the patient will be positioned slightly differently in the different scanning machines. Moreover, extra time is needed to plan the additional examination. Therefore, a lot of research has been and is still dedicated to creating multimodal machines, e.g. PET-CT [16], SPECT-CT [17]

and PET-MR [18]. Despite the many technical challenges associated with developing these systems, they slowly find their way to the clinic, showing promising results to help in diagnosis and treatment [19]. Also, functional combinations such as EEG-fMRI [20], EEG-MEG [21], NIRS-fMRI [15] are possible, acquiring complementary functional information simultaneously. Up to now, this is mainly used in research settings.

2.2 The electroencephalogram

2.2.1 Introduction

In the previous section, we already mentioned that in an EEG recording, brain activity is measured with electrodes placed on the scalp or inside the skull. Since EEG recorded on the scalp is the modality of interest in this dissertation, we will discuss this technique more elaborately in this section, though the concepts can be easily extended to invasive EEG. First, we explain how the activity of single neurons translates to an electrical field that can be measured at the scalp. Next, we give more details about how scalp EEG recordings are performed and how the recordings typically look like. To conclude this section, the possible application areas of EEG are discussed.

2.2.2 From neural activity to electrical potentials on the scalp

A neuron transmits an electrochemical signal across its length, causing a very small electric current in the order of femtoamperes (10^{-12} A). The corresponding electric field decays with the square of the distance (inverse-square law), and therefore the electrical activity of a single neuron cannot be measured at the scalp. To have an electric field that is measurable at the scalp, hundreds of thousands neighboring neurons need to be synchronously active and several conditions need to be fulfilled.

First of all, the electrical activity needs to overlap in space. Neighboring neurons need to be aligned in parallel so that their electric fields sum and do not cancel each other. The pyramidal cells in the cortex meet this requirement, as they are aligned perpendicularly to the cortical surface, see Fig. 2.9. Depsite the fact that the cortex is a highly folded structure,

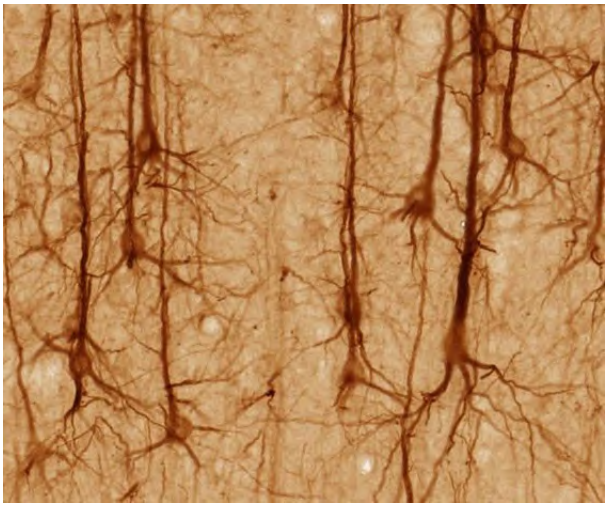

Figure 2.9: A picture of the pyramidal neurons in the cortex. They are aligned perpendicularly to the cortical surface and as a consequence, are parallel to each other.

it can be seen as locally flat on the level of the cell since there are around 10^5 neurons per $1\,\mathrm{mm}^2$ [22].

Second, the electrical activity needs to overlap in time. APs have a high amplitude, approximately 100 mV with respect to baseline, but only last for around 1 ms. It is very unlikely that neighboring neurons will fire perfectly synchronously, and as a consequence, it is not probable that APs will overlap in time so that their electrical activity gets summed. Postsynaptic potentials are typically smaller, around $\pm 10\,\mathrm{mV}$, but they last for a longer time, around 10 ms, making them more likely to overlap [14]. When they have the same polarity (EPSPs vs. IPSPs), electric fields generated by postsynaptic potentials of neighboring pyramidal neurons can thus sum in both time and space. Therefore, they are also seen as 'the generators of the EEG', since it is their superposition that can be measured at the electrodes [23]. Before the potentials reach the electrodes, however, they are smeared and attenuated because the tissues (brain, skull, scalp, etc.) they are distributed through all have a different electrical conductivity. Especially the conductivity of the skull is low, accounting for the large signal quality difference between scalp and invasive EEG. A typical normal human EEG recording has values

in the range of 10 – 100 µV, while invasive recordings have an amplitude between 1 – 20 mV.

2.2.3 Recording the EEG

To pick up the potentials at the scalp, highly conductive materials are used, such as silver/silver chloride electrodes. Electrodes can be glued to the scalp or can be embedded in a cap or a net that is tied around the subject's head. To minimize the impedance between the electrode and the skin, an electrolytic gel or solution is applied. Often, the aim is at an impedance below 5 kΩ. In clinical practice, often 19, 21, 27 or 32 electrodes are used, but configurations of 64 electrodes up to 128 or even 256 electrodes exist as well, offering a higher spatial sampling of the head. These systems are referred to as high-density (hd) or high-resolution systems. Fig. 2.10 shows a setup with 32, 128 and 256 electrodes.

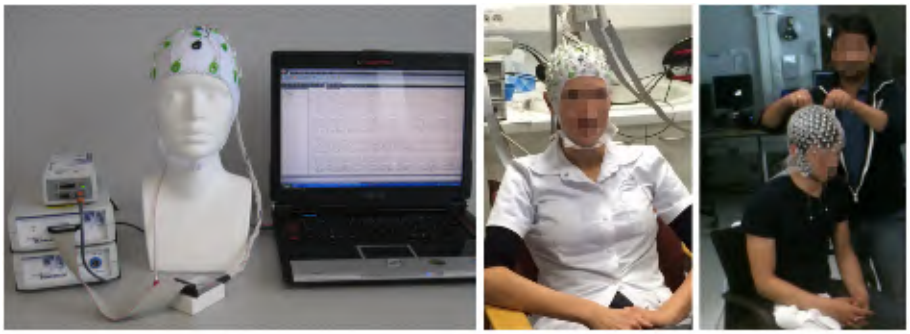

Figure 2.10: Example of the EEG setups with (a) 32 electrodes, (b) 128 electrodes, (c) 256 electrodes. Figure from [24].

The electrodes can be placed at any position on the head, but mostly an international standard is followed, depending on the number of electrodes. E.g. for 19 electrodes, the International 10-20 System can be applied [25]. In this system, the distance between neighboring electrodes is either 10% or 20% of the total left-right or front-back distance, as can be seen in Fig. 2.11. The left-right distance is measured between the left and right preauricular point and the front-back distance is measured from the nasion, i.e. the deepest point between forehead and nose, to

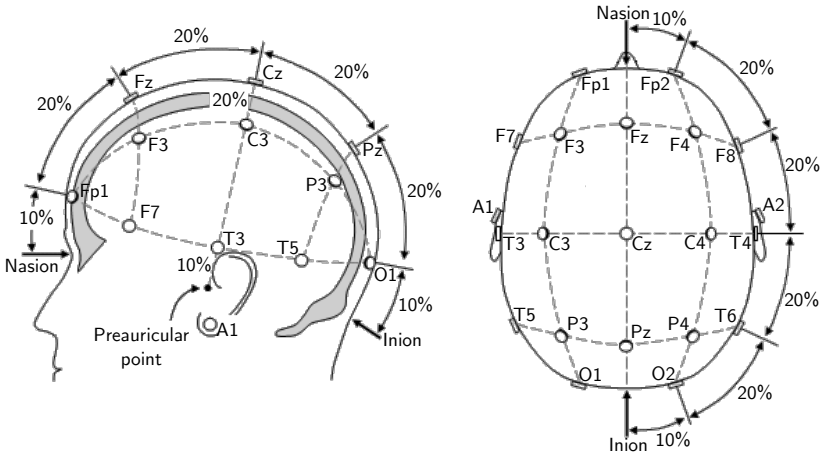

Figure 2.11: Illustration of how electrodes should be placed according to the International 10-20 system.

the inion, i.e. the lowest point of the skull from the back of the head, normally indicated by a prominent bump.

Electrodes are labeled with a letter. 'F', 'P', 'T', 'O' for electrodes covering the frontal, parietal, temporal and occipital lobe, respectively; 'C' for electrodes on the central area; 'Fp' for electrodes on the forehead (frontal polar area); and 'A' for electrodes at the ear lobes (auricular). Furthermore, the letter is accompanied by an odd number on the left side of the head and with an even number on the right side, which is the smallest next to the nasion-inion midline and increases in the direction of the ears. The electrodes on de nasion-inion midline are accompanied with the letter 'z' from zero. For systems with a higher number of electrodes, the 10-20 system has been extended to the 10-10 system and 10-5 system accordingly [26]. Combined letters can be used for the labels, e.g. 'FCz' for the electrode on the midline between the frontal and central region.

A voltage or a potential cannot be determined absolutely, but is always measured relatively between a point of interest and a reference. For EEG recordings, the points of interest are the electrodes discussed above, and the reference is often an (extra) electrode on the top of the head or an electrode placed on one or both mastoids (behind the ear). The measured potential differences are fed to an amplifier and an analog-to-digital converter before being brought to a computer for visualization

and storage. Common sampling frequencies range between 250 and 2000 Hz. For common-mode rejection in the amplifier, a separate ground electrode is added on top of the head, or anywhere on the body.

2.2.4 Visualization of the EEG

The most common way to visualize EEG signals, is to show the measured voltage traces over time. Typically, the x-axis represents time and the different channels are labeled and stacked on the y-axis. The traces can be shown in a referential way, i.e. showing the voltage difference between every electrode of interest and a reference electrode (mostly the reference electrode used for recording). An example of a referential montage is shown in Fig. 2.12(a). Mathematically, an example is given in Eq. 2.1 for electrodes T3 and T5.

$$\begin{aligned} T3(t) &= V_{T3}(t) - V_{ref}(t) \\ T5(t) &= V_{T5}(t) - V_{ref}(t) \end{aligned} \tag{2.1}$$

Another option is to make use of bipolar montages. In a bipolar montage, the difference between serial pairs of adjacent electrodes in longitudinal or transversal lines is shown. The 'double banana' montage, schematically shown in Fig. 2.13, is an example of a bipolar montage often used in clinical practice. The bipolar montage can be derived from a referential recorded EEG, using the simple formulas in Eq. 2.2. As can be seen from this equation, the bipolar montage is independent of the originally chosen reference electrode. An example of EEG visualized using a 'double banana' is depicted in Fig. 2.12(b).

$$\begin{aligned} T3 - T5(t) &= T3(t) - T5(t) \\ &= \big(V_{T3}(t) - V_{ref}(t)\big) - \big(V_{T5}(t) - V_{ref}(t)\big) \\ &= V_{T3}(t) - V_{T5}(t) \end{aligned} \tag{2.2}$$

A third option is using a Common Average Reference (CAR), in which at every time point, the mean of all channels at that time point t is subtracted from every channel at time point t, see Eq. 2.3 for N channels. Again, this reference is independent of the original recording reference.

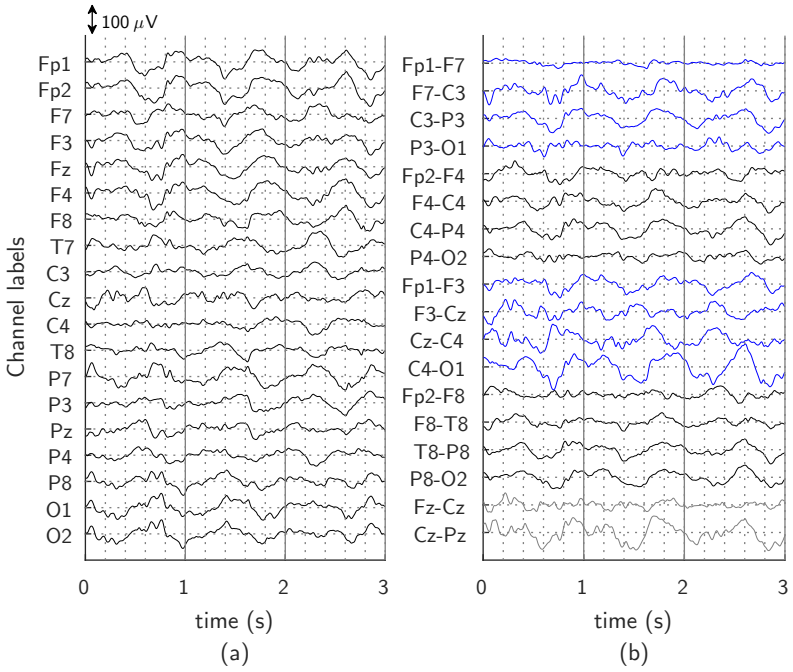

Figure 2.12: Example of an EEG recording, shown in (a) a referential montage, (b) a bipolar montage.

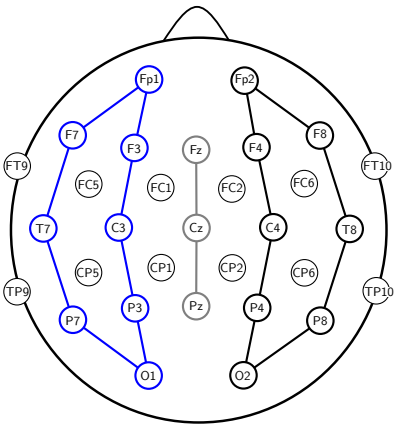

Figure 2.13: Overview of a double banana bipolar montage.

A CAR is useful to visualize small signals in noisy recordings, though artifacts in one channel may be spread over different channels.

$$\begin{aligned} T3_{avg}(t) &= T3(t) - \frac{\sum_{i=1}^{N} Ch_i(t)}{N} \\ &= \left(V_{T3}(t) - V_{ref}(t)\right) - \frac{\sum_{i=1}^{N} V_{Ch_i}(t) - V_{ref}(t)}{N} \\ &= V_{T3} - \frac{\sum_{i=1}^{N} V_{Ch_i}(t)}{N} \end{aligned} \tag{2.3}$$

Next to EEG traces, two-dimensional scalp topographies are frequently used to visualize the EEG at a certain time point. At every electrode, the potential measured at that electrode is shown using a color scale and between the electrodes, potential values are interpolated using triangular or spherical splines interpolation in order to create a colored map of activity [27, 28]. These topographies provide a clear overview of how the activity is distributed on the scalp and which areas are more or less active. An example of a topography can be seen in Fig. 2.14.

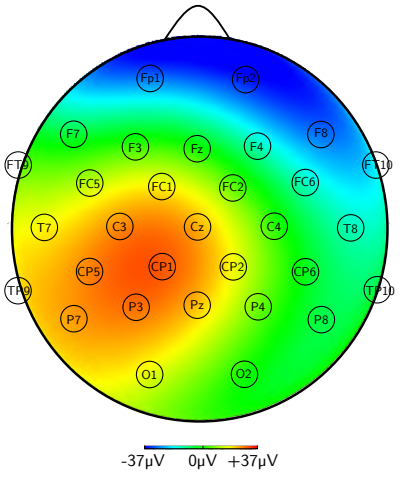

Figure 2.14: Example of a scalp topography.

2.2.5 Observed brain activity in the EEG

In EEG recordings, a distinction can be made between different types of observable activity, depending on frequency, amplitude and location. Primarily, there is rhythmical activity with an oscillatory behavior. Healthy background brain activity is typically rhythmical, but other events such as seizures (see section 2.3.4) may also display rhythmical patterns. Depending on the frequency, rhythmical brain activity can be divided into several bands (see list below), each associated with different mental states [29]. Abnormal occurrence of these rhythms may reflect a pathology.

Delta (δ): Frequencies **below 4 Hz**, high in amplitude. Associated with deep sleep and may be present in the waking state.

Theta (θ): Frequencies **between 4 and 7 Hz**. Associated with drowsiness and idle state, creative inspiration and deep mediation. Important in children, abnormal in the waking adult when present in larger groups.

Alpha (α): Frequencies **between 8 and 13 Hz**. Mainly found over the occipital region, often sinusoidally shaped. Associated with relaxed awareness, without attention or focus. Can also be observed when the eyes are closed.

Beta (β): Frequencies **between 14 and 30 Hz**, low in amplitude. Usual waking rhythm associated with active thinking, alertness, focus and concrete problem-solving. High-level beta may be associated with anxiousness and panic.

Gamma (γ): Frequencies **above 30 Hz**, low in amplitude. Associated with a state of active information processing.

Mu (μ): Frequencies **between 8 and 13 Hz**. Overlaps with alpha, but strongly related to movement. Typical rhythm that gets suppressed during an (imaginary) movement in the region associated with the body part that moves.

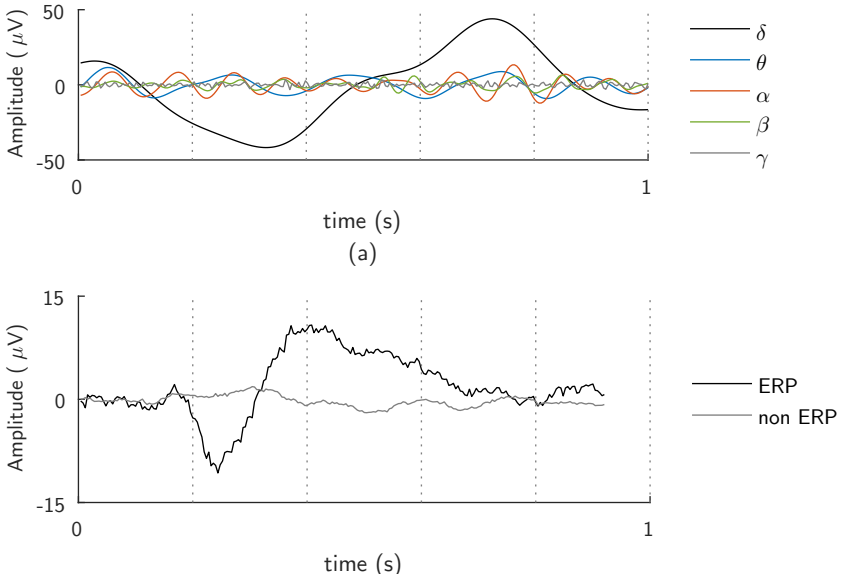

Figure 2.15: (a) Typical dominant brain rhythms: the delta, theta, alpha and beta rhythm are shown in black, blue, orange, green and gray, respectively. (b) Example of transient activity in the form of an event-related potential.

In Fig. 2.15(a), the δ, θ, α and γ rhythm are shown. As can be seen in this figure, low-frequency rhythms tend to be higher in amplitude. More specifically, the power spectrum of EEG is typically inversely proportional to the frequency ($1/f$ behavior).

Next, there are transient events that are not necessarily characterized by an oscillatory nature. Event-Related Potentials (ERPs) are one example, shown in Fig. 2.15(b), which are a response to a specific sensory, cognitive or motor event. Interictal Epileptiform Discharges (IEDs) are an example of a transient event occurring in epilepsy patients. This is elaborated in section 2.3.4. Furthermore, there can be signals with a wide frequency range, or that might be spiky, such a vertex waves which happen during sleep.

2.2.6 Artifacts

Unfortunately, not only brain activity is recorded by the electrodes, but a lot of unwanted signals are picked up as well. These undesirable components are also called 'artifacts' and can be of environmental or

biological origin. The first are obviously caused by the environment, while the latter are caused by the subject or patient himself. Examples of environmental artifacts are 50 Hz power line interference, electrical noise from electronic components, cable defects, impedance fluctuations, or a malfunctioning or detached electrode. Whereas power line noise will be visible on most channels, the artifacts due to a detached electrode will remain limited to the affected channel. Biological artifacts can arise from body movements such as chewing, biting, sneezing etc. These artifacts are also referred to as muscle artifacts and have a typical high-frequency nature (frequencies above 30 Hz). Other possible origins are eye movements and blinking. These ocular artifacts are mainly visible on the frontal polar electrodes. An eye blink artifact typically lasts around 200 ms. Furthermore, the beating of the heart (cardiac artifacts) and sweating of the subject can be visible in the EEG. Some typical artifacts are shown in Fig. 2.16.

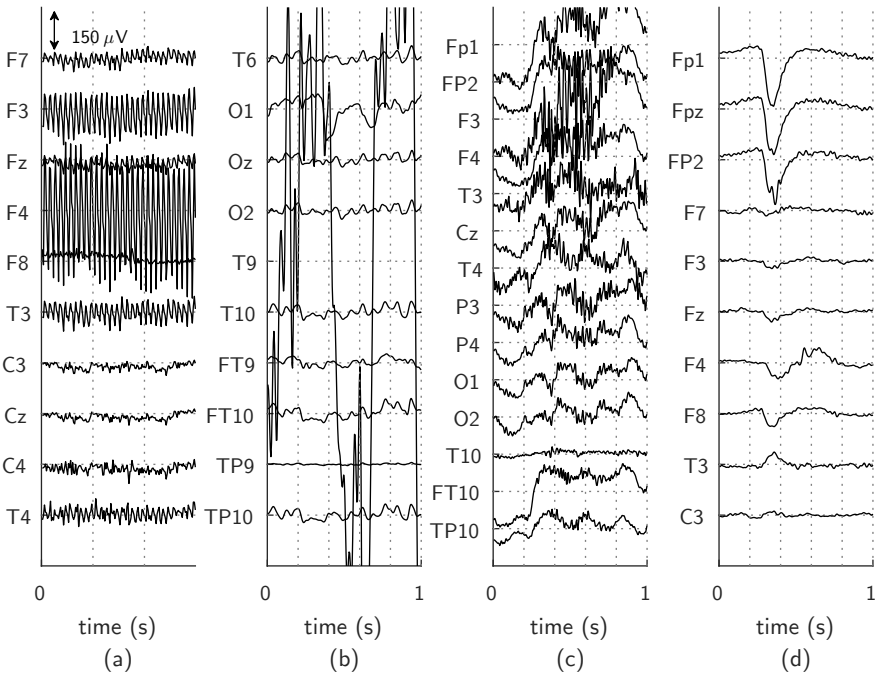

Figure 2.16: Typical artifacts in the EEG. Only a selection of channels is shown. Environmental artifacts: (a) 50 Hz power line noise and (b) a detached electrode (T9). Biological artifacts: (c) high-frequency muscle artifacts and (d) an eye blink artifact, mainly visible on the frontal polar electrodes.

To provide good data quality, artifacts should be kept to a minimum. To minimize power line artifacts during recording, the EEG system is often supplied with a DC battery. Good electrode contact and application of the conductive gel/solution can further reduce potential artifacts. The patient can be asked to sit still to avoid biological noise as much as possible. In research, subjects will be asked to repeatedly perform the same task. After the recording, several trials can be averaged, due to which the random noise will cancel out and the signal of interest is highlighted (an example can be seen in Fig. 2.15(b)). The signal-to-noise ratio (SNR) of the recorded EEG can be further enhanced by reducing or rejecting artifacts that were recorded despite the precautions during recording. Rejecting artifacts means that artifactual periods of the EEG will not be taken into account during further analysis or interpretation. To reduce remaining power line noise, a notch filter at 50 Hz can be applied. An electrode having a bad signal can be removed from the recording or can be interpolated, e.g. by the use of splines [27, 28]. Muscle artifacts can be, to a certain extent, filtered out with a low-pass filter, given that their frequency content does not overlap with that of the useful EEG signal. If an Electro-oculogram (EOG), which records the eye movements and blinking, is recorded simultaneously with the EEG, this can be used to remove the ocular artifacts [30]. This can also be done for cardiac artifacts using the Electrocardiogram (ECG). Another technique to remove artifacts is the use of decomposition techniques such as Principal Component Analysis (PCA) [31], Singular Value Decomposition (SVD) [31] or Independent Component Analysis (ICA) [32]. Decomposition methods decompose the data into several components. The component containing the artifact can be removed and the EEG data can be reconstructed without the artifactual component, resulting in a more clean EEG. To make small signal changes visible in common noise, CAR can be used, which is explained in section 2.2.4.

2.2.7 Resolution

The temporal resolution of EEG and iEEG is excellent, in the order of milliseconds. No single neuroimaging modality performs better. The spatial resolution of scalp EEG, however, is restricted to centimeters because of the volume conduction through the different tissues of the head and the limited sampling by electrodes. It can be improved

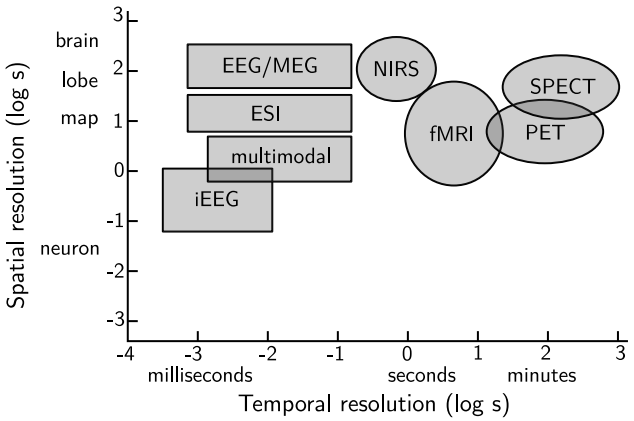

Figure 2.17: The spatial and temporal resolutions of different functional neuroimaging techniques. EEG and iEEG have superior temporal resolution. EEG has a poor spatial resolution, that of iEEG is better, but implantation of electrodes is necessary. Multimodal refers to multimodal imaging techniques combining two or more of the modalities. Figure adapted from [33].

by using higher-density setups, although the effect is limited. Other possibilities to improve the spatial resolution in a non-invasive way are the use of multimodal neuroimaging modalities (see section 2.1.4.3) and EEG Source Imaging (ESI) (see section 3.1). When recording iEEG, there is neglectable volume conduction and spatial resolution in the order of (sub)millimeters is possible. Yet, the spatial sampling is limited, since implanted electrodes cannot cover the whole brain. The spatial and temporal resolutions of EEG and iEEG with respect to other neuroimaging techniques are shown in Fig. 2.17.

2.2.8 Applications

Because EEG is a safe, inexpensive and relatively easy modality to directly measure neuronal activity, it has become an established tool in both clinical and research settings.

2.2.8.1 Clinical

In the clinical environment, the EEG is primarily used as a diagnostic and analytic tool for neurological and psychiatric disorders. In epilepsy,

EEG is an indispensable tool to diagnose and characterize the seizures. Furthermore, it can help to determine the treatment of a patient. This is further discussed in section 2.3.4. Dyslexia, autism spectrum disorders, Attention-Deficit Hyperactivity Disorder (ADHD), Attention-Deficit Disorder (ADD) and depression are examples of psychiatric disorders that may be accompanied with abnormal brain rhythms that can be measured by EEG [29]. Though in these cases, the EEG is rather a possible aid than part of a fixed standard protocol.

Furthermore, abnormal EEG patterns may indicate hemorrhage, encephalitis (swelling of the brain), tumors or head injury. The deepness of a coma can be assessed by the level of brain activity in the EEG and brain death can be confirmed.

Another application is in sleep studies. The EEG is part of the polysomnogram recorded during sleep and every sleep stage is accompanied with different typical brain activity. Abnormal sequencing or duration of the sleep stages, detected from the EEG, can point out sleep disorders such as sleep related breathing disorders, narcolepsy, parasomnias, insomnias, etc [34].

2.2.8.2 Research

All clinical applications, of course, trace back to extensive research. Even now, EEG is still used to learn more about the working mechanisms of the aforementioned disorders and research continually tries to refine or develop new analysis techniques and methods in order to increase the diagnostic and prognostic value of EEG.

Furthermore, the EEG allows studying the working mechanisms of the healthy brain as well and it is widely used in the field of cognitive neuroscience. Brain activity is monitored while the subject (or patient in the case of clinical research) repeatedly performs a certain cognitive task in response to a certain stimulus. The stimuli and their reaction to them will evoke a specific brain activity, hence they are also called Evoked Potentials (EPs). A lot of paradigms to elicit EPs exist, but one example is the auditory oddball paradigm, during which a subject gets to hear a sequence of equal tones, occasionally interrupted by a different or target tone [35]. When the subject hears a target tone, he should perform a certain task, such as pressing a button, which elicits the EPs. The EP is a direct result of a specific sensory, cognitive or

motor event (pressing the button), and is, therefore, an ERP. ERPs have a distinct transient morphology, but are, however, not larger in amplitude than regular EEG activity. As a consequence, it can be very hard to discriminate a single ERP in the EEG. Therefore, the subject should repeatedly perform the task, so the different trials can be averaged. Background EEG activity is 'random' and will, for that reason, cancel out by averaging, while the ERP has approximately the same morphology for every trial and will be kept in the average. Hence, the SNR of the ERP increases, resulting in a clear transient waveform. For the case of the auditory oddball paradigm, an averaged ERP can be seen in Fig. 2.15. ERP studies can show which brain regions are involved or functionally integrated for specific cognitive tasks, such as naming objects, visual perception, etc. It should be noted that ERPs can also be used in a clinical setting to diagnose e.g. dyslexia [36], Alzheimer's disease (AD) [37] or head injuries [38, 39]. Yet this is often still experimental.

Another field of research is in Brain-Computer Interfaces (BCIs). The purpose of a BCI is to command a device based on brain activity. Brain activity is captured, processed and translated into a command for the device. It can restore or replace certain functions for physically disabled people [40]. Examples are neuroprosthetics [41] to replace e.g. a missing limb, or thought-controlled wheelchairs [42] and mindspellers [43, 44] for people who are almost completely paralyzed or who suffer locked-in syndrome [45]. Furthermore, BCIs can provide environmental control (switching on the lights by thinking of it) for healthy subjects and patients [46] or they can enhance gaming experience (controlling a character with your thoughts in a virtual reality) [47]. In spite of the fact that a lot of research is already done in the field of BCIs and nice results have been shown, they are not widely used yet, because of the long calibration times needed that are exhausting for the user. Therefore, current research aims at reducing these calibration times [48].

An emerging field of research is in neuromarketing. Based on recorded EEGs, researchers try to find the driver behind consumer decisions and the regions that are active when buying something. This allows companies to adapt their marketing strategies accordingly [49]. Although promising, ethical considerations should be made [50].

2.3 Epilepsy

2.3.1 Introduction - definition, prevalence and incidence

Most people will associate epilepsy with a neurological disorder characterized by seizures. But what are seizures? And when exactly does a seizure become epilepsy? In 2014, the *International League Against Epilepsy (ILAE)* provided an updated practical clinical definition of epilepsy [51]:

> *"Epilepsy is a disease of the brain defined by any of the following conditions*
>
> 1. *At least two unprovoked (or reflex) seizures occurring >24 h apart*
> 2. *One unprovoked (or reflex) seizure and a probability of further seizures similar to the general recurrence risk (at least 60%) after two unprovoked seizures, occurring over the next 10 years*
> 3. *Diagnosis of an epilepsy syndrome"*

An epileptic seizure is defined as *"a transient occurrence of signs and/or symptoms due to abnormal excessive or synchronous neuronal activity in the brain"* [51]. The signs and symptoms may vary, but during a seizure, a group of neurons in the brain experience a sudden burst of uncontrolled electrical activity [52]. This abnormal activity can be measured with EEG (see section 2.3.4). During a seizure, a patient may present a wide spectrum of behaviors ranging from no abnormal behavior over subtle absences to general convulsions. That the seizures need to be unprovoked means that there should be no temporary or reversible factor that could lower the threshold for a seizure, such as concussion, fever or alcohol-withdrawal. Most of the time, epilepsy syndromes are accompanied by typical seizures, but even in absence of obvious behavioral seizures or if the risk of subsequent seizures is low, the patient is said to have epilepsy [51].

According to the World Health Organization (WHO) [53], about 10% of the population will experience a seizure during their lifetime, but not all of them will develop epilepsy. They report that roughly 50 million

people worldwide have epilepsy, which corresponds to between 0.5 and 1% of the population, making it one of the most common neurological diseases. It is estimated that approximately 50 per 100 000 people per year get epilepsy [54]. Although epilepsy may develop at every age, the incidence is highest in both young children and older adults [55]. Furthermore, the incidence is higher in lower-income countries [54].

For most epilepsy patients no identifiable cause can be found. Nonetheless, many factors could possibly cause epilepsy: loss of oxygen or trauma during birth, congenital abnormalities or genetic conditions with associated brain malformations, severe head injury, stroke, infections of the brain such as meningitis and encephalitis, tumors [53].

2.3.2 Epilepsy subtypes

Epilepsy can be classified depending on the above causes or etiology, which can be unknown, structural, genetic, infectious, metabolic or immune [56]. For some epilepsies, it is possible that two categories apply. For instance, patients suffering tuberous sclerosis, a genetic disease that causes benign tumours to grow in the brain and/or other vital organs, both have a structural and a genetic etiology.

Furthermore, there is a multilevel-classification for epilepsy based on seizure types, epilepsy types and epilepsy syndromes [56]. First, seizures can have a focal onset, i.e. starting in a specific region of the brain, a generalized onset, i.e. widespread activity that involve the entire brain, or an unknown onset. Seizures can be classified further and this is discussed in the next section. Second, based on the present seizure types, the epilepsy type can be defined as focal, generalized, combined generalized and focal, or unknown. Focal epilepsies are applicable to patients that have unifocal and multifocal seizures, or seizures that involve only one hemisphere. Obviously, generalized epilepsies apply to those patients who only suffer generalized seizures and combined generalized and focal epilepsies on those who suffer both focal and generalized seizures. Third, an epilepsy syndrome may be diagnosed. Generally, epilepsy syndromes are organized based on the co-occurrence of several features such as the (further classified) seizure types, EEG, imaging, age at onset and possible remission, seizure triggers, comorbidities (such as intellectual and psychiatric dysfunction),

and sometimes prognosis [57]. Many syndromes can be recognized, however there is no formal classification [58]. One clear example is childhood absence epilepsy, affecting young children with seizures that are usually periods (around 10 to 20 s) of staring during which the child is not aware or responsive.

2.3.3 Classification of seizures

The ILAE has very recently proposed the expanded seizure type classification shown in Fig. 2.18 in which some changes with previous classification schemes can be found [59].

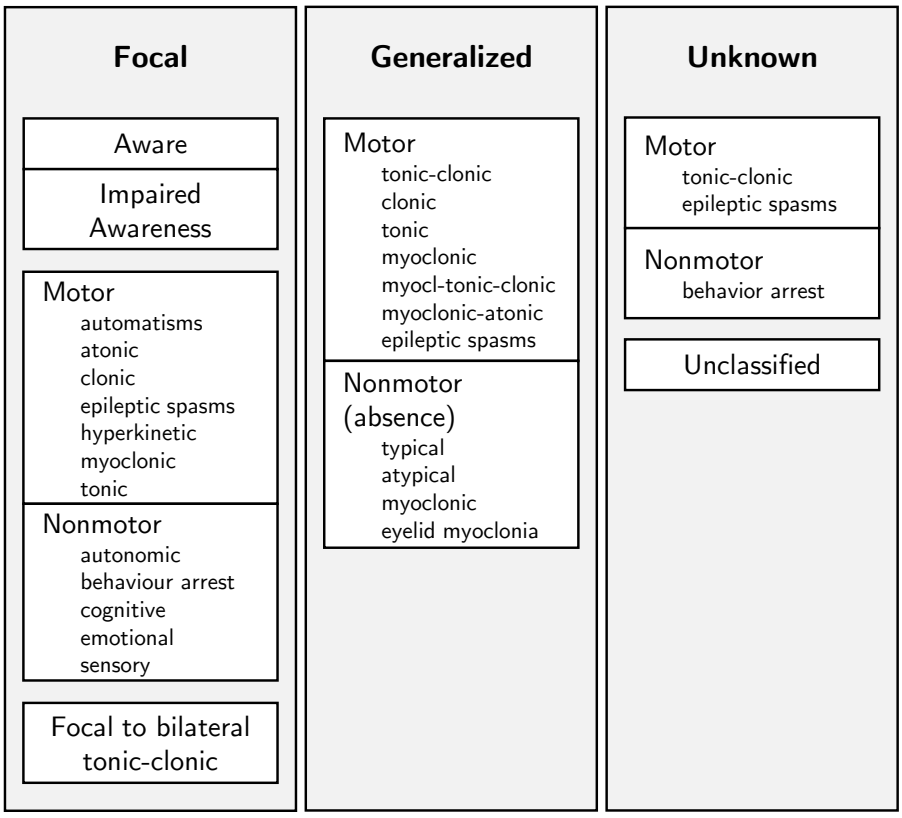

Figure 2.18: The expanded classification of seizure types as proposed by the ILAE in 2017 [59].

Focal seizures can be optionally classified according to the awareness of the patient during the seizure. When a patient is aware during a seizure, this means that he keeps being aware of himself and the environment, even if he is immobile. This kind of seizure used to be referred to as a 'simple partial seizure', but should now be called a 'focal aware seizure'. A 'focal impaired awareness' seizure used to be known as a 'complex partial seizure'. In this case, partial, simple and complex have been changed to focal, aware and impaired awareness, respectively. Furthermore, a focal seizure may be accompanied by motor or nonmotor (or overlapping) symptoms. A descriptive list of motor and nonmotor events is given below. Finally, a focal seizure may generalize, i.e. start in a focal region in the brain, but then spread until the entire brain is involved. These seizures were formerly known as 'seizures with partial onset with secondary generalization' and are now referred to as 'focal to bilateral tonic-clonic seizures'.

Seizures with generalized and unknown onset can also be further classified according to their (non)motor symptoms. Moreover, a seizure with unknown onset may be unclassified as long as their onset is unknown. The classification of an individual seizure can stop at every level, e.g. from 'focal onset' over 'focal motor seizure' up to 'focal aware tonic seizure'. We end this section with a short glossary of motor and nonmotor seizure symptoms:

Motor symptoms

automatisms repeated or automatic movements

atonic lapse in muscle tone, (a part of) the body becomes limb

clonic sustained rhythmical jerking of (a part of) the body

epileptic spasms sudden flexion and/or extension of (parts of) the body

hyperkinetic excessive motor activity, usually directed and complex

myoclonic brief shock-like jerks of a muscle or a group of muscles (mostly shorter in duration than spasms)

tonic (a part of) the body becomes stiff or tense

Nonmotor symptoms

autonomic changes in heart rate, breathing or color, etc.

behavior arrest blank stare, stop talking stop moving

cognitive confusion, slower thinking, and/or problems with talking and understanding

emotional sudden emotional experience such as anxiety or pleasure

sensory changes in hearing, vision or taste; or feelings of numbness, tingling or pain

typical absence loss of awareness, sometimes with staring or with fluttering eyelids

atypical absence patient stares, but may be able to respond a little, longer and slower onset and offset than typical absences

Epilepsy is mainly diagnosed and classified based on the semiology of the seizures, i.e. the clinical symptoms, and by EEG recordings, which will be explained in the next section. Furthermore, structural epilepsy is mostly confirmed with MR images.

2.3.4 Epilepsy in the EEG

As already mentioned above, an epileptic seizure arises due to abnormal neural activity. This abnormal neural activity can be recorded with the EEG. During a seizure, also called ictal activity, the most obvious deviations can be measured but the largest part of patients also show small abnormalities in between seizures, also called interictal activity. In focal epilepsy, the abnormal activity is often limited to the electrodes in the neighborhood of the origin of the epilepsy, whereas in generalized epilepsy it can be measured at electrodes on both sides of the head. In focal to bilateral tonic-clonic seizures, the activity is first limited to some electrodes, but later on spreads to electrodes on both sides of the head. Although the abnormal activity may be limited to a few electrodes, it can be challenging based on this to delineate where exactly in the brain the seizure originated from.

During a seizure, usually rhythmical, often sharp, waveforms can be seen. Yet, the components vary in morphology, frequency and topography depending on the seizure [60]. Some seizures show very clear ictal patterns whereas others manifest only subtle changes, an example of a recorded seizure is shown in Fig. 2.19(a). Sometimes an ictal

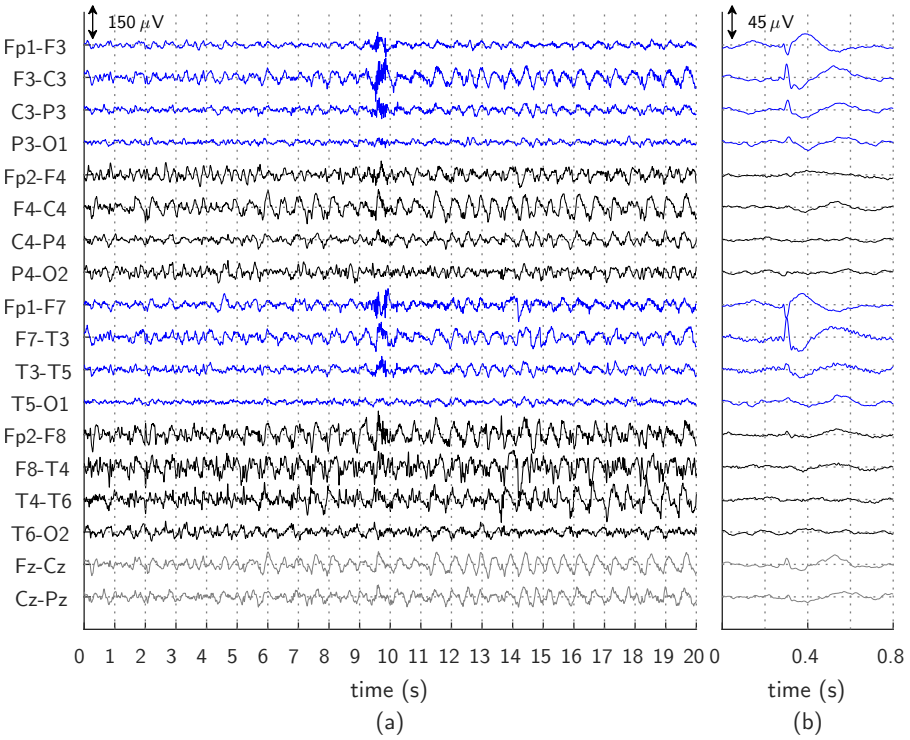

Figure 2.19: (a) 20 first seconds of a seizure originating in the right frontal lobe of a patient. Right frontotemporal (abnormal) rhythmical theta activity can be seen. (b) IED with main phase reversal over electrode F7, recorded in a different patient.

episode is preceded by a decrement which is an abrupt flattening of the background activity. It is important to remark that some seizures are visible on the EEG but pass without any clinical symptoms for the patient. These are also called subclinical seizures.

Interictal abnormalities in the EEG are also referred to as Interictal Epileptiform Discharges (IEDs) and come in different shapes [60]:

sharp wave transient activity with a pointed peak that is clearly distinguishable from the background activity, lasting 70 – 200 ms

spike same as sharp wave, however shorter in duration, lasting 20-70 ms (the distinction is, however, arbitrary)

spike-slow-wave complex spike followed by a slow wave that is typically higher in amplitude than the spike (Fig. 2.19(b))

polyspike-slow-wave complex Two or more spikes associated with one or more slow waves

In a bipolar montage, interictal spikes and slow waves show phase reversal over the electrodes of interest as the traces deflect in opposite directions.

2.3.5 Treatment

Epilepsy treatment aims at the suppression of the seizures and different options exist that will be discussed in this section. Sometimes these treatments allow resolving the epilepsy. The ILAE *"define epilepsy as being resolved for individuals who had an age-dependent epilepsy syndrome but are now past the applicable age or those who have remained seizure-free for the last 10 years, with no seizure medicines for the last 5 years"* [51].

2.3.5.1 Anti-epileptic drugs

The standard treatment for epilepsy is the administration of **Anti-Epileptic Drugs (AEDs)**, which selectively try to alter the excitability of the neurons. They try to block the abnormal synchronous neuron firing, while not disturbing normal non-epileptic activity [61]. According to the Epilepsy Society of the UK [62] and the US Epilepsy Foundation [63], more than 25 different AEDs are currently in use. The choice to treat a patient with one or a combination of these drugs depends on the epilepsy and seizure type, the sex and age of the patient, the side-effects of the drugs, the interplay with other medication, etc. In most patients, it takes some time to find the correct dose of a suitable AED. The correct dose is important to have an optimal seizure suppressing effect, while minimizing possible side-effects such as dizziness, drowsiness, mental slowing, weight gain, skin rashes, movement disorders, etc. [64]. Approximately 60-70% of epilepsy patient will be rendered seizure-free when adequately treated with AEDs [65]. 40-60% of these patients remain seizure-free after withdrawal of the AEDs after a few years. [66].

2.3.5.2 Drug-resistant epilepsy

Sufficient seizure suppression is not obtained with AEDs in 30–40% of the patients. These patients have so-called drug-resistant epilepsy. However, before diagnosing a patient as having drug-resistant epilepsy, sufficient drug treatment options should have been tried. The ILAE offers following consensus definition for drug-resistant epilepsy [67]:

> *"Drug-resistant epilepsy may be defined as failure of adequate trials of two tolerated and appropriately chosen and used AED schedules (whether as monotherapies or in combination) to achieve sustained seizure freedom"*

For these drug-resistant patients, alternative therapies such as surgery, electrical or magnetic stimulation might be the solution and these will be discussed next.

2.3.5.3 Epilepsy surgery

Epilepsy surgery is an important treatment option, since it offers high efficacy in selected patients [68, 69]. During epilepsy surgery, a surgeon tries to remove (resective surgery) or disconnect (disconnective surgery) the brain area that is responsible for the epilepsy. The area that is necessary and sufficient to remove to render a patient seizure-free is also called the Epileptogenic Zone (EZ). This is, however, only a conceptual region since it cannot be measured directly. Only in patients rendered seizure-free after surgery, we can conclude that the EZ was part of the resected tissue or Resected Zone (RZ). Therefore, drug-resistant epilepsy patients will undergo a presurgical evaluation in which doctors attempt to get an indirect estimate of the EZ and assess whether the presumed EZ does not overlap with eloquent tissue, i.e. a region of cortex that is indispensable for defined cortical functions [70]. The procedures of the presurgical evaluation will be more elaborately discussed in section 2.3.6. Only when the presurgical evaluation allows to delineate the EZ and there is not too much overlap with eloquent tissue, a surgical procedure will be performed.

Before or during the surgery, ECoG and electrical stimulation mapping can be used to exactly localize functional tissue. This tissue will be

spared as much as possible, while completely resecting or disconnecting the presumed EZ.

Resective surgery can be performed at different scales ranging from a small focal lesion (lesionectomy) that is removed, over a brain lobe (lobectomy) to even a complete hemisphere (hemispherectomy). The spatial extent of the surgery is a delicate trade-off between seizure freedom, neurological complications and quality of life [71]. Seizure-free rates between 50 and 85% [72, 73] have been reported for focal, lobar, multilobar resections, or hemispherectomy, indicating that the volume of resected tissue is not critical, as long as the entire EZ is excised [65].

Two major types of disconnective surgery exist. On the one hand, there are Multiple Subpial Transections (MST) in which small vertical incisions are made in the cortex. The goal of this procedure is to prevent that seizure activity spreads while preserving function, making it appropriate when there is (partial) overlap between the EZ and eloquent cortex [65]. With this procedure, approximately one-third of the patients are rendered seizure-free [74]. On the other hand, there is a more palliative procedure in which the corpus callosum is sectioned (callosotomy). Callosotomy prevents interhemispheric/bilateral spreading of the seizures. Patients will not be rendered seizure-free, but their quality of life may be improved [65].

For brain areas that are not easily accessible via conventional surgery, radiosurgery can be done, in which precise and accurate radiation is targeted at a volume of interest within the brain (so strictly speaking, this is not really surgery). MR images serve to identify this volume beforehand [65]. Finally, focused ultrasound is an emerging incision-less technique for ablation of tissue that is currently being researched for its possible application in epilepsy [75].

The ideal outcome of epilepsy surgery is a patient that is completely rendered seizure-free. Yet, different degrees of success are possible, and these are often categorized in different classes. One of the most used classification schemes was proposed by Engel et al. [76], and the Engel Classes are shown in Table 2.1.

Because “worthwhile improvement” is open for interpretation and patients with Engel Class I outcome could still experience seizures, the ILAE proposed a more quantitative classification scheme that overcomes these problems [77]. This classification scheme also allows discriminating

Table 2.1: Overview of the Engel Classes for epilepsy surgery outcome [77].

Engel I	free of disabling seizures
Ia	completely seizure-free since surgery
Ib	non disabling simple partial seizures only since surgery
Ic	some disabling seizures after surgery, but free of disabling seizures for at least 2 years
Id	generalized convulsions with AED discontinuation only
Engel II	rare disabling seizures ("almost seizure free")
IIa	initially free of disabling seizures, but rare seizures now
IIb	rare disabling seizures since surgery
IIc	more than rare disabling seizures since surgery, but rare seizures for the last 2 years
IId	nocturnal seizures only
Engel III	worthwhile improvement
IIIa	worthwile seizure reduction
IIIb	prolonged seizure-free intervals amounting to greater than half the follow-up period, but not <2 years
Engel IV	no worthwhile improvement
IVa	significant seizure reduction
IVb	no appreciable change
IVc	seizures worse

between patients rendered seizure-free by AEDs and patients rendered seizure-free by surgery. The scheme is shown in Table 2.2.

2.3.5.4 Other alternative therapies

For epilepsy patients that cannot be rendered seizure-free with AEDs and that are not eligible for epilepsy surgery, other alternative therapies exist. First, there are neurostimulation procedures in which the brain is electrically or magnetically stimulated to suppress the seizures. These therapies are, unlike surgery, reversible. One option is **Vagus Nerve Stimulation (VNS)**, in which an electrode is wound around the (left) vagus nerve (tenth cranial nerve) and connected to a stimulator implanted under the left clavicle. Different stimulation paradigms are possible and the stimulation settings can be adapted to the needs

Table 2.2: Overview of the ILAE Classes for epilepsy surgery outcome [77].

ILAE 1	completely seizure free; no auras
ILAE 1a	completely seizure free since surgery; no auras
ILAE 2	only auras; no other seizures
ILAE 3	1-3 seizure days per year; ± auras
ILAE 4	4 seizure days per year to 50% reduction of baseline seizure days; ± auras
ILAE 5	<50% reduction of baseline seizure days to 100% increase of baseline seizure days; ± auras
ILAE 6	>100% increase of baseline seizure days; ± auras

of the patient. Researchers are still investigating the exact working mechanism of VNS, but studies report a seizure reduction of 50% in more than one-third of the patients while the side-effects remain mild (e.g. hoarseness) [78]. Next, Deep Brain Stimulation (DBS) can be offered as a treatment. In **DBS**, one or more electrodes are placed in one or more target brain regions, e.g. the hippocampi. These electrodes stimulate the target regions, which can inhibit seizures. Again, the details of the working mechanism are still being researched. One study reported a drop in seizure frequency of 90% in approximately half of the patients [79]. Other, more recent neurostimulation techniques to treat epilepsy are emerging such as **Transcranial Direct Current Stimulation (tDCS)**, in which a low constant current is delivered to the brain (area of interest) via electrodes on the scalp [80], and **Transcranial Magnetic Stimulation (TMS)**, in which small electric currents in the brain area of interest are generated through electromagnetic induction, by applying a focal magnetic field on the brain area of interest [81, 82].

Another group of alternative therapies are dietary treatments. The **ketogenic diet**, in which 80% of the diet consists of fat, is reported to have possible seizure reduction of >90% in one-third of the patients [83]. For the **modified Atkins diet**, similar efficacy rates have been reported [65]. The main drawback of this kind of treatment is that the dietary restrictions are very strict, making them unpleasant for the patient and almost impossible to keep up.

2.3.6 Presurgical evaluation

To assess whether a patient with drug-resistant epilepsy is eligible for epilepsy surgery or should be referred to other alternative therapies, the presurgical evaluation is done. A multidisciplinary team of neurologists, neurosurgeons, psychologists, radiologists, etc will investigate via several examinations whether surgery could be beneficial for the patient. The risks of the surgery and possible post-operative neurological deficits should be balanced by how the quality of life of the patient would be benefited. Only when the team has fully considered all risks and still thinks the gain for the patient would be high enough, possible surgery is discussed with the patient.

The first goal of the presurgical evaluation is to delineate the EZ, the conceptual region that is necessary and sufficient to render the patient seizure-free. Ideally, the zone resected at surgery should be identical to the EZ, but it is often larger due to uncertainty about the localization and sometimes may exclude some areas of the EZ due to overlap with eloquent tissue. To overcome the problem that the EZ cannot be directly measured, the presurgical evaluation team will try to map different regions related to the EZ [70, 84]. The symptomatogenic zone is the area in the brain that produces the initial clinical symptoms during a seizure. The Irritative Zone (IZ) is the region where the IEDs originate, the Seizure Onset Zone (SOZ) is where the seizures originate. The epileptogenic lesion refers to a potential structural abnormality in the brain that directly causes the seizure. Finally, the functional deficit zone is the area that is functionally abnormal in the interictal period. These regions describe zones that may or may not (partially) overlap, as can be seen in Fig. 2.20. For example, a patient could be rendered seizure-free by only partial resection of the epileptogenic lesion. In this case, the complete EZ was still resected. Yet, it could also be that a patient who had a complete lesionectomy will still experience seizures. In this case, the EZ was probably larger or different than the epileptogenic lesion.

In what follows we will describe the typical protocol that is followed when a patient is diagnosed with drug-resistant epilepsy, based on [65]. First, the patient will be admitted to the epilepsy clinic for a long-term visit during which long-term Video-EEG monitoring (VEM), i.e. ictal and interictal EEG and time-locked video during several consecutive days to identify clinical symptoms, and MRI with an optimal epilepsy protocol will be done. VEM is the cornerstone investigation of any presurgical

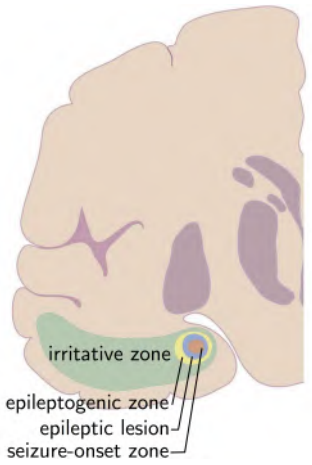

Figure 2.20: Overview of the Seizure-Onset Zone (SOZ), the epileptic lesion, the Epileptogenic Zone (EZ) and the Irritative Zone (IZ). Figure adapted from [85]

evaluation since it allows for the accurate diagnosis and subclassification of the epileptic seizures [86]. If the VEM shows that the patient suffers generalized epilepsy, curative epilepsy surgery is not an option and the patient is referred to other alternative therapies such as VNS or palliative surgery, mostly in combination with AEDs. Patients suffering from focal or unknown epilepsy are subjected to the actual presurgical evaluation protocol. In the first phase of this protocol, several investigations are done:

Phase A

- Identification of the IZ based on interictal EEG (from VEM)
- Identification of the SOZ based on ictal EEG (from VEM)
- Identification of the symptomatogenic zone based on the seizure semiology (from VEM)
- Identification of the epileptogenic lesion based on structural MRI
- Identification of a focal hypometabolism on a PET scan
- Identification of a functional deficit zone based on neuropsychological assessment

When the results of these investigations are congruent, the patients can continue to Phase B. When tests are normal or incongruent, patients continue to Phase A+ of which one or more test can be chosen:

Phase A+

- ESI[1]
- MEG Source Imaging (MSI)[1]
- ictal SPECT
- EEG-fMRI
- Magnetic Resonance Spectroscopy (MRS)

When the team is now able to formulate a hypothesis on the localization of the EZ, the patients are referred to Phase B followed by Phase C. When still no hypothesis can be formulated, patients are referred to other alternative treatment options.

In **Phase B**, possible overlap between the hypothesized EZ and eloquent tissue will be assessed. If no functional overlap with the hypothesized EZ can be illustrated, the patient can continue towards Phase C or directly to curative surgery. When there is functional overlap, the patient can be referred to Phase C to fine-tune the overlap or can directly continue towards non-surgical treatment options.

Phase C consists of invasive video-EEG monitoring with or without functional mapping. The goal of this phase in the confirmation of rejection of the hypothesis and the functional mapping of the zone that needs to be resected. If there is a focal onset without functional overlap, patients might continue towards resective surgery; when there is overlap, patients might continue towards disconnective surgery with or without a resection. When the SOZ is large or the hypothesis cannot be confirmed, the patient might continue towards an alternative treatment. IEEG is necessary in approximately 10% of the presurgical candidates.

It is obvious from the above that the presurgical evaluation is a labor-intensive, time-consuming, often challenging and sometimes subjective

[1] We already mentioned that when measuring a spike on EEG, the highest voltage deflection might be noticed at some electrodes of interest. It is, however, impossible to determine where exactly in the brain the spike originated based on this electrode information. ESI and MSI try to estimate the underlying brain activity causing the measured EEG/MEG, in order to get a more accurate estimate. This is explained in more detail in the next chapter.

process (since the procedures require careful human interpretation). In the case of molecular imaging, the patient is exposed to ionizing radiation and invasive EEG requires surgery that can have potential complications such as scarring, functional loss, infection, etc. Moreover, there is no guarantee that once the evaluation is started, the EZ will be found. Therefore, a lot of research is dedicated to improving existing or designing new methods to aid the presurgical evaluation, so that it eventually can be made less time-consuming, less labor-intensive, less subjective or less risky (better target or avoid iEEG) for the patient. This is also the goal of this dissertation, in which we use advanced signal processing techniques for EEG in order to localize the SOZ. These techniques will be explained in the next chapter.

3

EEG source imaging and brain connectivity

In the previous chapter, we introduced the brain, EEG and epilepsy to conclude that it would be useful to have a method able to localize the Seizure Onset Zone (SOZ) in epileptic patients based on EEG recordings. In this dissertation, we will achieve this by using two main signal processing techniques which are described in the current chapter. The first technique is EEG Source Imaging (ESI), which estimates the neuronal activity that generated the measured scalp EEG potentials. The result is a three-dimensional map of the brain activity. Second, brain connectivity studies how brain regions are structurally and/or functionally interconnected and how they interact with each other. Combined, these two techniques allow studying the complex networks underlying the neuronal activity that is measured by EEG. In this dissertation, this approach will be applied on epileptic seizures. During a seizure, ictal activity will, often rapidly, spread from one (unifocal) or several (multifocal) brain regions to other regions in an epileptic network [87, 88]. The combination of ESI and brain connectivity allows studying this epileptic network and finding its main driver(s) based on seizures recorded with scalp EEG.

3.1 EEG source imaging

3.1.1 Introduction

Despite the excellent temporal resolution, the spatial resolution of EEG is rather limited. Visual inspection and interpretation of EEG signals can be done on the lobar level. ESI is a technique allowing 3-dimensional imaging of the brain activity underlying the measured EEG potentials, with sublobar resolution.

ESI consists of two main parts: the forward model and the inverse solution. The forward model comprises a source model that represents the neuronal activity, a biophysical head model and the electrode positions. It calculates which potentials would be measured at the scalp electrodes based on an assumed source. This way, it allows generating EEG signals as a function of source activity. The inverse solution, on the other hand, tries to estimate the underlying sources of the measured EEG by optimizing a cost function based on the difference between the calculated or generated and measured EEG as can be seen in Fig. 3.1. The next sections will detail the different aspects in this figure.

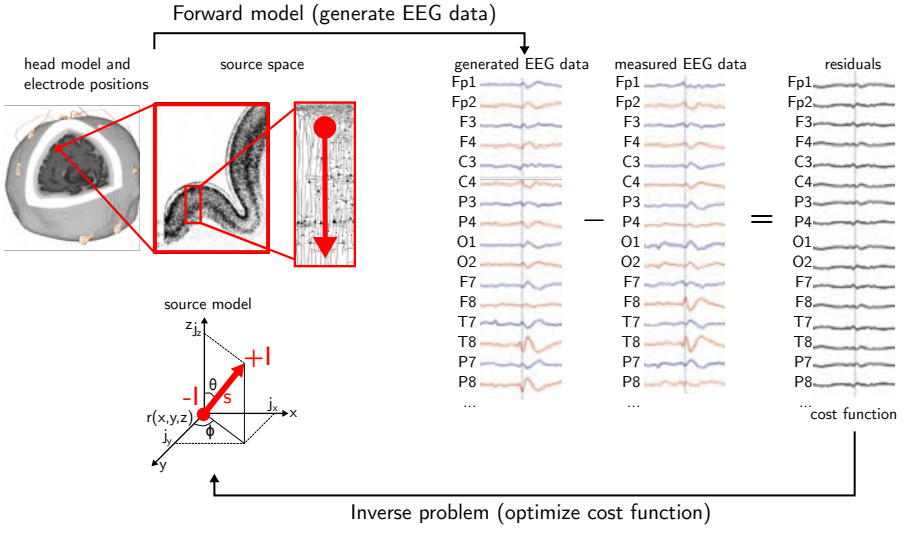

Figure 3.1: Illustration of the EEG source imaging technique consisting of the forward model and the inverse problem. Figure adapted from [24].

The main challenge of ESI is that the inverse problem is ill-posed, meaning that there is no unique solution. The activity of millions of neurons is distributed through the brain and head and is then sampled by a limited amount of electrodes, which also register noise. An infinite amount of both physiologically plausible and implausible source distributions could cause the same EEG measurement. Therefore, a priori knowledge and/or constraints should be added in order to find a unique and realistic solution.

3.1.2 Forward modeling

3.1.2.1 Source model

In order to generate EEG signals based on a known neuronal source distribution, these sources should be modeled first. In section 2.2.2 we already discussed that the pyramidal neurons in the cortex are the main generators of the EEG. The voltage gradient characterizing the propagating postsynaptic potentials is accompanied with intra- and extracellular currents. These currents can be macroscopically modeled with a current dipole parallel to the neurons, as can be seen in Fig. 3.1 in red [89–91]. The current dipole consists of a current sink ($-I$) and source ($+I$) with an inter-distance of s and is characterized by 6 parameters: 3 parameters that describe its position ($\mathbf{r} = [x\, y\, z]$), 2 parameters for the orientation ($\boldsymbol{\theta} = [\theta\ \phi]$), and 1 parameter to represent its intensity (I). The orientation and intensity can also be described by the dipole moment $\mathbf{j} = [j_x\, j_y\, j_z]$, with $||\mathbf{j}|| = sI$. The current dipole forms the basic building block of more complex source models that define the source space, which will be explained in the next section. Next to dipoles, source modeling could also be done with e.g. monopoles or quadrupoles [22], but these configurations are almost never used in practice.

3.1.2.2 Head model

To know how the neuronal electric activity, modeled by the source model, gives rise to a specific measurement at the electrodes on the scalp, a detailed characterization of the head is needed in the form of a head model that describes both the anatomical and the electrical properties

of the head. Based on the head and source model, the source space, i.e. the collection of all possible source locations, can be constructed.

Geometry

Different gradations of complexity can be used to model the geometry of the human head. Generally, it can be assumed that the more complex the model is, the more accurate. However, it should be noted that a too complex head model can lead to numerical inaccuracies or possibly increased computation times. The most simple approximation of the human head is a single sphere. Extra (concentric) spheres can be added to represent different tissue types. Examples are 3-layered spherical head models in which the inner sphere represents the brain, the middle sphere (as a layer around the inner sphere) is the skull and the outer sphere is the scalp, and 5-layered spherical models with white matter, gray matter, CSF, skull and scalp. The forward model can be calculated analytically when these spherical head models are used. It has, however, been shown that more realistic head models provide better ESI results [92–94]. Individual, realistic head models can be derived from the whole-head MR image (usually T1 or T2 weighted) of the subject from which tissue boundaries or tissue volumes are segmented. Different open source packages exist to achieve this segmentation, such as the Statistical Parametric Mapping (SPM) software [95], FreeSurfer [96], the FMRIB Software Library (FSL) [97], and Brainstorm [98]. The number of tissues that are taken into account can vary from 3 (brain, skull, scalp) to 6 (white matter, gray matter, CSF, skull, scalp, air cavities) or 7 (eyeballs extra). Especially the incorporation of CSF seems to improve ESI results [99]. Smaller structures like vessels and nerves are generally ignored while constructing the head model. Fig. 3.2 shows an individual realistic head model that incorporates 6 different tissues, based on the MRI of a patient.

In section 2.1.4.2, we already mentioned that it is hard to image the skull with MRI. So, if a CT scan of the subject is available, the skull can be modeled more accurately and it can even be further divided into compact and spongy bone [100].

When there are no structural brain images of good quality available, a template can be used, e.g. based on the ICBM152 template, which is a template based on the average of 152 normal MRI scans [101].

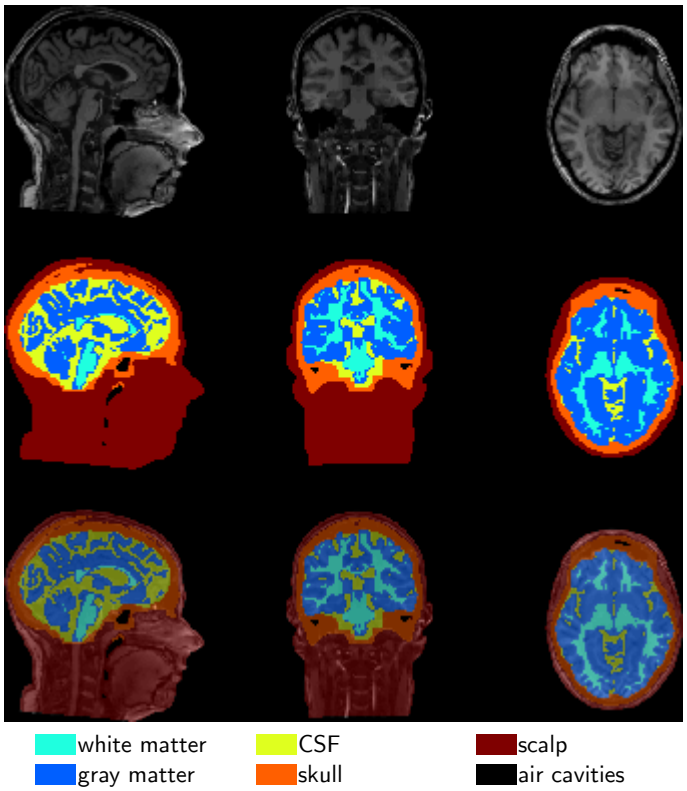

Figure 3.2: Sagittal, coronal and axial slice of the MR image of a patient (top), a head model constructed based on this MR image with incorporation of white matter, gray matter, CSF, skull, scalp and air cavities (middle), and the MR image overlaid with the head model (bottom)

Electrical conductivity

In order to model the distribution of the electric fields through the head, the electrical conductivity of the different modeled tissues should be known. It is, however, currently impossible to measure all these conductivities for every patient in vivo. Moreover, some tissues have a highly anisotropic conductivity. In the case of white matter, the conductivity along the axons is obviously higher than the transverse electrical conductivity, since they are made to conduct electrical activity along their length. Also the skull is anisotropic [100, 102]. Mostly, the electrical properties of the head are modeled by isotropic conductivity values based on literature, of which some examples are given in Table 3.1.

Table 3.1: Overview of isotropic conductivity values used for ESI reported in literature. Table from [24].

	Conductivity (S/m)			
	[103]	[104]	[100]	[105]
air	-	-	0	0
scalp	0.33	0.22	0.3279	0.43
skull	0.0041	0.015	0.0041	0.01
compact bone	-	-	0.0064	0.008
spongy bone	-	-	0.02865	0.025
CSF	-	-	1.79	1.79
gray matter	0.33	0.22	0.3333	0.33
white matter	0.33	0.22	0.1428	0.14

Source space

Based on the source model and the geometric properties of the head model, it is possible to construct a collection of all possible source or dipole locations, called source space. The pyramidal neurons are mainly located in the cortex, i.e. the gray matter and therefore, often only dipoles in the gray matter are allowed. Although the cerebellum and deep structures such as the thalamus and basal ganglia consist of gray matter, they are often excluded from the source space since they are not considered to be generators of EEG. The dipoles can be located in a mesh on the cortical surface, or also in a 3-dimensional grid inside the cortical volume. They can be spread irregularly over Regions-Of-Interest (ROIs) or they can be placed in a regular grid. The number of dipoles in the source space can vary from a few hundred up to 10 000. Sometimes, especially in the case of a cortical mesh, the orientation of the dipoles is fixed perpendicularly to the cortical surface, since this corresponds to the alignment of the neurons. A source space based on a regular grid inside the volume of gray matter with a spacing of $4\,\text{mm} \times 4\,\text{mm} \times 4\,\text{mm}$ can be seen in Fig. 3.3.

3.1.2.3 Electrode positions

Based on the geometric and electromagnetic properties of the human head, it is possible to calculate how the electric field of a modeled source (dipole or dipole distribution) will be distributed through the head. In order to be able to generate EEG, we should know where exactly we want

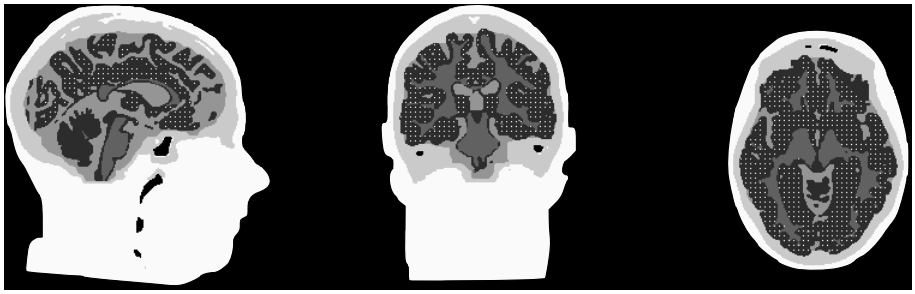

Figure 3.3: Head model with source space. The dark gray color represents the gray matter of the brain. Within this structure, the source space can be seen as a regular grid of white points, which represent the centers of the different dipoles in the source space. The spacing is 4 mm × 4 mm × 4 mm. Note: Although there is gray matter in the cerebellum, the cerebellum is not one of the main EEG generators and is therefore excluded from this source space.

to know the scalp potentials, i.e. the positions of the electrodes on the scalp. The electrode positions can be derived from a template based on several characterizing landmarks such as the nasion, the inion and both ear tragi. When the EEG was recorded with the International 10-20, 10-10 or 10-5 system, the electrodes can be correctly localized as soon as the landmarks are defined on the head model. The standard positions can be coregistered to the head model and projected on the scalp surface as can be seen in Fig. 3.4. Another possibility is to measure the actual electrode positions on the patient's scalp with dedicated positioning systems, using electromagnetic tracking (e.g. Polhemus, Colchester, USA) or special cameras (e.g. GeoScan, Electrical Geodesics, Eugene, USA). After registration of the electrode positions, they can again be coregistered to the head model and projected to the scalp surface. A final approach is to segment electrode positions from a CT or MR scan during which the subject had the electrodes attached to the scalp. Possibly, markers are attached to the electrodes in order to make them visible on these images.

3.1.2.4 Calculation of the forward model

Based on the source model, head model and electrode positions, the EEG potentials $\mathbf{V}_{gen} \in \mathbb{R}^{N_e \times 1}$ at N_e electrodes, generated by a current dipole source at location $\mathbf{r} = [x\, y\, z]$ and dipole moment $\mathbf{j} = [j_x\, j_y\, j_z]^T$,

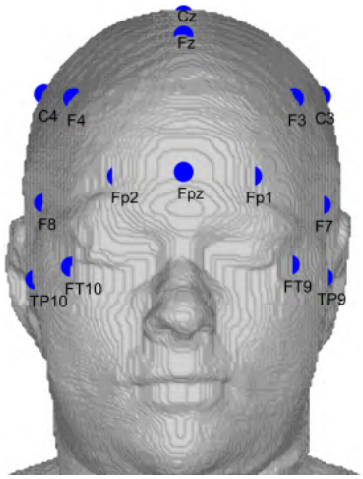

Figure 3.4: Standard electrode positions coregistered to the head model and warped onto the scalp.

can be mathematically represented as:

$$\mathbf{V}_{gen} = \mathbf{L}(\mathbf{r})\mathbf{j}(\mathbf{r}) \tag{3.1}$$

in which $\mathbf{L}(\mathbf{r}) \in \mathbb{R}^{N_e \times 3}$ is the lead field matrix that describes the field distribution from a unit current dipole at location $\mathbf{r} = [x\, y\, z]$ to the N_e scalp electrodes in the x, y and z direction. This lead field matrix is the mathematical realization of the forward model. Equation 3.1 can be extended to n active dipole sources with the superposition principle:

$$\mathbf{V}_{gen} = \sum_{i=1}^{n} \mathbf{L}(\mathbf{r}_i)\mathbf{j}(\mathbf{r}_i) \tag{3.2}$$

in which $\mathbf{L}(\mathbf{r}_i) \in \mathbb{R}^{N_e \times 3}$ is the lead field matrix for a unit current dipole at position $\mathbf{r}_i = [x_i\, y_i\, z_i]$ and $\mathbf{j}_i = [j_{x_i}\, j_{y_i}\, j_{z_i}]^T$ represents the intensity and orientation of the ith dipole.

With the chosen source model, a complete source space covering the whole brain can be constructed. The influence of all these possible current dipoles can be taken into account by extending equation 3.2 from n dipoles to all possible dipole locations N_d. In this case, the

equation can be rewritten as:

$$\mathbf{V}_{gen} = \mathbf{LJ} \tag{3.3}$$

in which $\mathbf{L} = [\mathbf{L}(\mathbf{r}_1)\,\mathbf{L}(\mathbf{r}_2)\ldots\mathbf{L}(\mathbf{r}_{N_d})] \in \mathbb{R}^{N_e \times 3N_d}$ is the lead field matrix, describing the field distribution of unit dipoles at all possible locations to the scalp electrodes. $\mathbf{J} = [\mathbf{j}_1\,\mathbf{j}_2\ldots\mathbf{j}_{N_d}]^T$ is a vector describing the dipole moment (or intensity and orientation) of all these current dipoles. In this vector $\mathbf{j}_i = [j_{x_i}\,j_{y_i}\,j_{z_i}]^T, i = 1\ldots N_d$, hence $\mathbf{J} = [j_{x_1}\,j_{y_1}\,j_{z_1}\,j_{x_2}\,j_{y_2}\,j_{z_2}\cdots j_{x_{N_d}}\,j_{y_{N_d}}\,j_{z_{N_d}}]^T \in \mathbb{R}^{3N_d \times 1}$. Once the intensities and orientations of all current dipoles $\mathbf{J}$ are known or fixed, the forward model, embodied by the lead field matrix $\mathbf{L}$, allows to calculate the potentials $\mathbf{V}_{gen} \in \mathbb{R}^{N_e \times 1}$ that would be measured at N_e scalp electrodes.

Equations 3.1–3.3 assumed sources and generated potentials at only one point in time. The extension to multiple timepoints in order to generate typical EEG traces is trivial: the lead field matrix remains constant, whereas the source activity distribution $\mathbf{J}(t)$ will vary over time, like neuronal activity will fluctuate over time, resulting in time-dependent generated scalp potentials $\mathbf{V}_{gen}(t)$.

Different techniques exist to calculate the lead field matrix based on the sources and the head model and the electrode positions. For spherical head models, the lead field matrices can be calculated analytically [91]. For realistic head models, however, numerical solving methods are required. The most widely used methods are the Boundary Element Method (BEM) [106–108], Finite Element Method (FEM) [109, 110], and Finite Difference Method (FDM) [111, 112]. We will restrict the discussion of these techniques to a short summary. A more comprehensive overview of these techniques and references to more in-depth literature can be found in [91].

When BEM is used, the head model is built from different closed surfaces. Each of these surfaces or layers encapsulates a particular tissue with its own homogeneous and isotropic conductivity, e.g. the brain-skull interface, the skull-scalp interface and the outer surface. In this way, the surfaces offer the boundaries between regions with different conductivity. Each surface is tessellated with small triangles, i.e. the boundary elements. The potentials are then only calculated at the center of every triangle, thus only on the surfaces and not in the tissue in between. The main advantage of BEM is the relatively low

computational need, the main disadvantages are the limited modeling complexity, which prevents highly accurate head models (e.g. the modeling of CSF is practically impossible since this is a highly complex structure, hard to model with a closed compartment), and the restriction to isotropic conductivities.

In FEM, the entire head model is divided into small volume elements, that do not necessarily have the same size nor shape (usually tetrahedra or regular polyhedra). Each of these volume elements is characterized by its own conductivity. The potentials are calculated at all vertices created by this tessellation. This approach allows to model very complex structures with high accuracy and flexibility and allows to incorporate anisotropic conductivities. The computational demand is, however, very high.

FDM is similar to FEM, with the main difference that the volume elements are all cubic and of the same size. This allows relatively high modeling accuracy with a lower computational demand than FEM. Furthermore, the MRI or CT images used to construct the head models, are intrinsically cubic, allowing a more direct translation from the acquired image to an FDM head model. In this dissertation, isotropic FDM head models incorporating 6 different tissues (white matter, gray matter, CSF, scalp, skull and air) will be used [112].

3.1.3 Solving the inverse problem

The forward model allows calculating the EEG $\mathbf{V}_{gen}$ that is generated when the source activity $\mathbf{J}$ is known. Solving the inverse problem, i.e. estimating the underlying sources from measured EEG $\mathbf{V}_{meas}$, comes down to finding the source activity that minimizes (a cost function of) the difference between the measured and the generated EEG. As already mentioned, this inverse problem is ill-posed, since an infinite amount of physiologically possible and impossible source distributions exist that could generate the measured EEG. Therefore, different inverse techniques have been designed that make certain assumptions and/or enforce constraints in order to obtain a unique solution. In the next sections, we will discuss the two main categories of inverse techniques: the Equivalent Current Dipoles (ECDs) and the distributed solutions.

3.1.3.1 Equivalent current dipole(s)

ECD methods assume that the measured EEG signals are generated by one (Eq. 3.1) or a small number of (Eq. 3.2) focal sources.

Single equivalent current dipole
First, assume that the measured EEG signals are generated by one source, i.e. one dipole, and that the measured scalp potentials $\mathbf{V}_{meas} \in \mathbb{R}^{N_e \times 1}$ at one time point are known. The inverse solution then tries to minimize the Relative Residual Energy (RRE):

$$\text{RRE}(\mathbf{r}, \mathbf{j}) = \frac{||\mathbf{V}_{meas} - \mathbf{V}_{gen}||}{||\mathbf{V}_{meas}||} = \frac{||\mathbf{V}_{meas} - \mathbf{L}(\mathbf{r})\mathbf{j}(\mathbf{r})||}{||\mathbf{V}_{meas}||} \tag{3.4}$$

with $||\cdot||$ the L_2-norm. This means that the location ($\mathbf{r} = [x\, y\, z]$) and intensity ($\mathbf{j} = [j_x\, j_y\, j_z]^T$) of the dipole that minimizes the RRE, i.e. the energy that cannot be explained by the model, need to be found. This is an optimization problem with 6 parameters that can be reduced to an optimization problem with 3 parameters because the optimal dipole moment at position $\mathbf{r}$ is given by [90, 113]:

$$\mathbf{j_{opt}}(\mathbf{r}) = \mathbf{L}(\mathbf{r})^{\dagger}\mathbf{V}_{meas} \tag{3.5}$$

with $\cdot^{\dagger}$ the Moore-Penrose pseudo-inverse operator. Combining equations 3.4 and 3.5 renders a minimization problem with respect to the location parameter $\mathbf{r}$:

$$\text{RRE}(\mathbf{r}) = \frac{||\mathbf{V}_{meas} - \mathbf{L}(\mathbf{r})\mathbf{L}(\mathbf{r})^{\dagger}\mathbf{V}_{meas}||}{||\mathbf{V}_{meas}||} \tag{3.6}$$

In this case, the number of unknowns (3 location parameters of the optimally oriented dipole) is smaller than the number of knowns (voltages at N_e electrodes, typically larger than 20) and the optimal dipole location can be found with dipole scanning techniques (try every location) or with optimization algorithms such as the Nelder-Mead simplex method [114]. The latter is faster but can get trapped in

local minima. The dipole moment $\mathbf{j}$ can be calculated once the optimal location $\mathbf{r}$ is found, using Eq. 3.5.

When the generating dipole of an EEG epoch of N_t time points ($\mathbf{V}_{meas} \in \mathbb{R}^{N_e \times N_t}$) needs to be found, the EEG epoch can be decomposed using Singular Value Decomposition (SVD) [115]:

$$\mathbf{V}_{meas} = \mathbf{U}\mathbf{S}\mathbf{V}^T \tag{3.7}$$

in which $\mathbf{U}$ represents scalp topographies and $\mathbf{V}$ the intensities of these topographies over time. $\mathbf{S}$ is a rectangular diagonal matrix containing the singular values in decreasing order. This way, the EEG epoch can be approximately represented with one time point or with one time series by taking the topography or time series, respectively, corresponding to the largest singular value. Approximating the EEG epoch by a single topography gives following equation for the RRE:

$$\text{RRE}(\mathbf{r}) = \frac{||\mathbf{U}(:,1)_{meas} - \mathbf{L}(\mathbf{r})\mathbf{L}(\mathbf{r})^{\dagger}\mathbf{U}(:,1)||}{||\mathbf{U}(:,1)||} \tag{3.8}$$

for which the same solution strategies can be used.

Multiple equivalent current dipoles

Now assume that the EEG is generated by a small amount n of focal sources. The RRE can be constructed similarly as for the single dipole case:

$$\text{RRE}(\mathbf{r},\mathbf{j}) = \frac{||\mathbf{V}_{meas} - \mathbf{L}(\mathbf{r_1},\mathbf{r_2},\ldots,\mathbf{r_n})\mathbf{j}(\mathbf{r_1},\mathbf{r_2},\ldots,\mathbf{r_n})||}{||\mathbf{V}_{meas}||} \tag{3.9}$$

in which $\mathbf{L}(\mathbf{r_1},\mathbf{r_2},\ldots,\mathbf{r_n})$ are the columns of the lead field matrix $\mathbf{L}$ corresponding to locations $\mathbf{r_1}$, $\mathbf{r_2}$, ..., $\mathbf{r_n}$. If we incorporate the dipole orientation $\boldsymbol{\theta}$ into the lead field matrix, Eq. 3.9 becomes:

$$\text{RRE}(\mathbf{r},\boldsymbol{\theta}) = \frac{||\mathbf{V}_{meas} - \mathbf{A}(\mathbf{r},\boldsymbol{\theta})\mathbf{I}(\mathbf{r})||}{||\mathbf{V}_{meas}||} \tag{3.10}$$

with $\mathbf{A}(\mathbf{r},\boldsymbol{\theta})$ the lead field matrix with dipole orientation information, $\mathbf{r} = [\mathbf{r_1}\,\mathbf{r_2}\,\ldots\,\mathbf{r_n}]$ the locations of the n dipoles and $\boldsymbol{\theta} = [\boldsymbol{\theta_1}\,\boldsymbol{\theta_2}\,\ldots\,\boldsymbol{\theta_n}]$ the orientations. The source vector $\mathbf{j}(\mathbf{r_1}, \mathbf{r_2}, \ldots, \mathbf{r_n})$ is then reduced to the intensity of each of the dipoles: $\mathbf{I} = [I_1\, I_2\, \ldots\, I_n]$.

The optimal intensity of the dipoles is found similar to Eq. 3.5 [116]:

$$\mathbf{I}_{opt}(\mathbf{r}) = \mathbf{A}(\mathbf{r}, \boldsymbol{\theta})^{\dagger} \mathbf{V}_{meas} \tag{3.11}$$

If this equation is used in Eq. 3.10, we get:

$$\mathrm{RRE}(\mathbf{r}, \boldsymbol{\theta}) = \frac{||\mathbf{V}_{meas} - \mathbf{A}(\mathbf{r}, \boldsymbol{\theta})\mathbf{A}(\mathbf{r}, \boldsymbol{\theta})^{\dagger} \mathbf{V}_{meas})||}{||\mathbf{V}_{meas}||} \tag{3.12}$$

Hence, the number of unknowns is 5 per dipole (3 for the location $\mathbf{r} = [x\, y\, z]$ and 2 for the orientation $\boldsymbol{\theta} = [\theta\, \phi]$), so $5n$ in total. Due to this larger number, the optimization algorithm has a higher chance of getting trapped in a local minimum. Furthermore, the number of dipoles n needs to be fixed a priori. A wrong estimation of n can lead to erroneous or meaningless results. Therefore, other algorithms to solve for multiple equivalent dipoles exist such as the Multiple Signal Classification (MUSIC) algorithm, Recursive MUSIC (R-MUSIC) [117], Recursively Applied and Projected MUSIC (RAP-MUSIC) [118], or the FINES approach [119]. These techniques are based on projections onto estimated signal subspaces. Others are based on machine learning or simulated annealing. An overview can be found in [120] and [121].

3.1.3.2 Distributed Solutions

In the previous section, we assumed that the number of sources generating the EEG was relatively limited, resulting in relatively easy to solve optimization problems to determine the number of dipoles, their locations and dipole moments. The number of unknowns remained limited. In distributed solutions, the influence of all possible source locations (ranging between 500 to over 10 000) is considered simultaneously. Although the dipole locations are now known beforehand, the estimation of their orientation and intensity is a highly underdetermined problem, since the amount of EEG channels is much lower than the number of unknowns. A unique solution can be obtained by optimizing a goodness-of-fit term and a regularization term in a carefully balanced way. When the noise in source and sensor space can be assumed to be Gaussian with zero mean, the estimation of the current distribution can be mathematically expressed as [24, 121, 122]:

$$\hat{\mathbf{J}} = \underset{\mathbf{J}}{\operatorname{argmin}} \left(||\mathbf{V}_{meas} - \mathbf{L}\mathbf{J}||_{\mathbf{R}}^2 + \alpha f(\mathbf{J}) \right) \tag{3.13}$$

in which the R-norm is used: $||\mathbf{X}||_{\mathbf{R}}^2 = \operatorname{tr}\left(\mathbf{X}^T\mathbf{R}^{-1}\mathbf{X}\right)$, with $\operatorname{tr}(\cdot)$ the trace operator and $\mathbf{R}$ the covariance matrix of the noise at the source level which is assumed to be zero mean Gaussian. The first term in Eq. 3.13 handles the data fit, whereas the second term is the regularization. $f(\mathbf{J})$ allows to incorporate (mathematical or biophysical) spatial (anatomical) or temporal priors (a priori constraints) to make the solution unique, and the regularization parameter α determines the influence of these constraints. The most simple form of regularization is the Minimum Norm Estimates (MNE) solution that tries to find the solution with minimum power. In MNE, $f(\mathbf{J}) = ||\mathbf{J}||^2 = \operatorname{tr}\left(\mathbf{J}^T\mathbf{J}\right)$. The solution of equation 3.13 then becomes:

$$\hat{\mathbf{J}}_{\text{MNE},\alpha} = \mathbf{L}^T \left(\mathbf{L}\mathbf{L}^T + \alpha \mathbf{I}_{N_e} \right)^{-1} \mathbf{V}_{meas} \tag{3.14}$$

with $\mathbf{I}_{N_e}$ the identity matrix of size N_e. The drawback of this approach is that it has the tendency to favour weak and superficial sources over deeper sources. Therefore, the Weighted Minimum Norm Estimates (WMNE) approach was introduced in which the power of the source signals are weighted with a weighting matrix $\mathbf{W} \in \mathbb{R}^{3N_d \times 3N_d}$: $f(\mathbf{J}) = ||\mathbf{W}\mathbf{J}||^2$. The solution to equation 3.13 is in this case given by:

$$\hat{\mathbf{J}}_{\text{WMNE},\alpha} = \left(\mathbf{W}^T\mathbf{W}\right)^{-1} \mathbf{L}^T \left(\mathbf{L} \left(\mathbf{W}^T\mathbf{W}\right)^{-1} \mathbf{L}^T + \alpha \mathbf{I}_{N_e} \right)^{-1} \mathbf{V}_{meas} \tag{3.15}$$

Although it can take different forms, the most straightforward weighting matrix is based on the norm of the columns of the lead field matrix: $\mathbf{W} = \mathbf{\Omega} \otimes \mathbf{I_3}$. $\mathbf{\Omega} \in \mathbb{R}^{N_d \times N_d}$ is a diagonal matrix in which the diagonal elements Ω_{ii} are calculated as follows. For every dipole $i = 1 \ldots N_d$ and every channel $j = 1 \ldots N_e$, there is a vector of length 3 in the lead field matrix ($\mathbf{L} \in \mathbb{R}^{N_e \times 3N_d}$), to describe the distribution from dipole i to electrode j in the x, y and z direction. The squared norm of this vector is taken and for every dipole i it is summed for all channels j. The diagonal element Ω_{ii} is then the square root of this sum. Due to this column normalization, all sources (deep or superficial) have the same opportunity of being reconstructed.

Low Resolution Electromagnetic Tomography (LORETA) offers another regularization approach that assumes that neighboring neurons are synchronously active [123]. If one source is active, there is a high probability that its neighboring sources are also active. Therefore, LORETA looks for the maximally smooth solution. This is done by combining column normalisation with the Laplacian operator Δ: $f(\mathbf{J}) = ||\Delta\mathbf{W}\mathbf{J}||^2$. The LORETA solution is:

$$\hat{\mathbf{J}}_{\mathrm{LOR},\alpha} = \left(\mathbf{W}^T\Delta^T\Delta\mathbf{W}\right)^{-1}\mathbf{L}^T\left(\mathbf{L}\left(\mathbf{W}^T\Delta^T\Delta\mathbf{W}\right)^{-1}\mathbf{L}^T + \alpha\mathbf{I}_{N_e}\right)^{-1}\mathbf{V}_{meas} \tag{3.16}$$

Other well-known solution strategies of this kind are Standardized Low Resolution Electromagnetic Tomography (sLORETA) [124], Local Auto-Regressive Averages (LAURA) [125] that allows to incorporate biophysical constraints, and beamformers [126] which are spatial filters that pass the signal coming from a certain source while attenuating all signals originating somewhere else. Each of these approaches has advantages and disadvantages and often the optimal inverse solution technique depends on the application it is used for. Although LORETA is criticized to possibly introduce spurious activity (and hence is not good for focal source estimation), it is the method of choice in this dissertation because of its relatively low complexity and its ability to localize multiple hotspots of activity in the brain during seizures.

It is important to mention that the estimation of the source distribution $\hat{\mathbf{J}}$ will vary when the regularization parameter α changes. Therefore, a good value for the regularization parameter is important. An L-curve approach can be used to estimate the optimal value for α [127].

3.1.4 Quality of ESI

A good forward model is a prerequisite for accurate ESI. A realistic, more complex model will result in more accurate source estimations, as long as the user does not make this model too complex due to which unwanted numerical inaccuracies can arise as well. The optimal choice of inverse solution technique is highly dependent on the application at hand. If one expects one or a few very focal sources, dipole fitting algorithms can be more appropriate. If the expected sources are more diffuse, distributed approaches might perform better. Generally, a sublobar to subcentimeter precision or accuracy can be obtained under good

conditions, with higher precision when a higher number of electrodes are used.

3.2 Functional brain connectivity

3.2.1 Introduction - a network perspective on the brain

The brain consists of billions of neurons that are highly interconnected, forming an anatomical highly complex network. The brain is not only a structural network, but its function is also network-based, meaning that several brain regions (or anatomical subnetworks) cooperate and intercommunicate to execute specific tasks. Every part of the brain has its own dedicated function, but the parts need to work together to achieve higher-order functioning. This is also called functional segregation, i.e. the segregation of functionally specialized brain regions, and functional integration, i.e. the functional interaction between these widely distributed functionally segregated brain regions [128]. The brain connectivity research domain aims at investigating the networks in the brain by examining which and how brain regions are connected and interact with each other. It can reveal how information is processed, sent to, received from or shared between these regions. Note that "regions" can be interpreted on different scales ranging from a small group of neurons, over larger structures as a gyrus, Brodmann area, or lobe to a complete hemisphere. In the next section, we will introduce the different types of brain connectivity and how they can be measured and studied. Next, we will discuss the connectivity measures of interest in this dissertation. Finally, when brain networks are mapped, they can be represented as a graph of which the network and node properties can be determined with graph theory measures. This will be discussed in the last section of this chapter.

3.2.2 Brain connectivity

Three types of brain connectivity are discriminated. The first type is **structural or anatomical connectivity** and investigates the anatomical connections between neurons or brain regions. It describes how groups of neurons are anatomically connected via axonal links. These axons are bundled into white matter fibers and tracts. Water

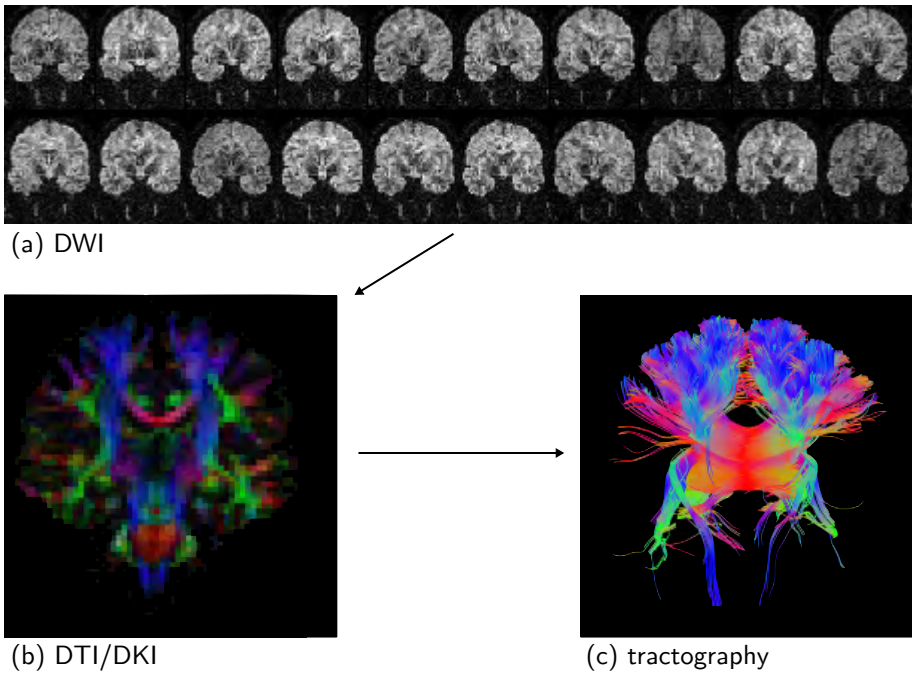

Figure 3.5: Investigation of structural brain connectivity shown in a coronal slice. (a) The diffusion of water molecules is measured with DWI in different directions (20 in this case). (b) This is combined in a diffusion tensor to DKI or DTI. The direction of the diffusion is color coded. (c) Tractography reconstructs the white matter tracts based on DTI/DKI. Here, the tracts through the corpus callosum are shown.

molecules in the brain diffuse more easily along these tracts than perpendicular to these tracts. The diffusion of water molecules in the brain can be measured with specialized gradient sequences on MRI, called Diffusion Weighted Imaging (DWI) (Fig. 3.5(a)). Applying this for 6 or 15 directions allows examining the diffusion in these directions, resulting in a diffusion tensor [129]. This is also called Diffusion Tensor Imaging (DTI) or Diffusion Kurtosis Imaging (DKI), respectively, shown in Fig. 3.5(b). Based on the diffusion tensor, parametric maps can be calculated to give a meaningful interpretation about the underlying brain structure and connections quantified in several measures [130]. Furthermore, the obtained directional diffusion can be used to reconstruct the white matter tracts in the brain in a process called tractography [131], illustrated in Fig. 3.5(c).

The second type of brain connectivity is **functional connectivity**, which is the study of the temporal correlation between spatially distinct neurophysiological activities [132]. Functional connectivity is mainly assessed using (i)EEG or fMRI time series that reflect the neuronal activity of different brain regions and considers dependencies between these time series. As such it can provide a undirected or directed (causal) measure for the information flow between two or more brain regions. This is conceptually illustrated in Fig 3.6. Functional connectivity measures can be grouped into 4 categories:

1. **Correlation and coherence**: correlation, cross-correlation, nonlinear correlation, and coherence and coherency and their derivatives

2. **Phase synchronization measures**: phase locking value (PLV) and phase lag index (PLI)

3. **Measures based on information theory**: mutual information (MI) and transfer entropy (TE)

4. **Granger causality measures**: Granger-causality index (GCI), directed coherence (DC), partial directed coherence (PDC), directed transfer function (DTF) and their derivatives

All these functional connectivity measures have their set of properties that reflect several conceptual distinctions: functional connectivity measures can be either linear or nonlinear, bivariate (i.e. between two time series) or multivariate (between more than two time series), undirected (solely detection of the connection) or directed (also the directionality of the connection is detected), related to time or frequency domain, and amplitude or phase-based. Furthermore, they can detect the direct connections (e.g. signal 1 influences signal 2 and signal 3) or the indirect connections (e.g. signal 1 influences signal 2 and via signal 2 also signal 3). In the next section, we will discuss the Granger causality measures more extensively, as they are of interest in this dissertation. For a nice overview of all categories and their properties, the reader is referred to [133].

Lastly, **effective connectivity** in the brain can be studied as the influence that one neural system exerts over another [134]. Whereas functional connectivity assesses the correlations between measured time

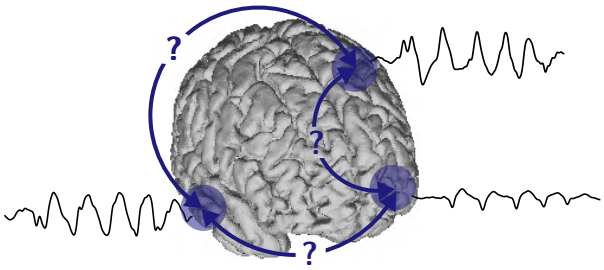

Figure 3.6: The concept of functional connectivity, which studies the interactions between spatially distinct brain regions through the analysis of temporal correlations between these regions.

series, effective connectivity is measured between hidden neuronal states that generate the measurements. Fluctuations in the hidden neuronal states cause changes in others. Effective connectivity depends on an explicit parametrized model of causal interactions [135]. Dynamic Causal Modelling (DCM) is the most widely used approach to investigate effective connectivity, and it uses hidden neuronal states to model brain activity. In practice, several generative models consisting of a neuronal (with hidden states) and observational model (what is measured) are specified and formally compared using variational Bayesian techniques [136], see Fig 3.7.

3.2.3 Functional connectivity based on Granger causality

3.2.3.1 Granger causality and autoregressive modeling

Granger causality

The concept of Granger causality was developed when Clive Granger modified the theoretical definition of causality proposed by Norbert Wiener [138] into a practical form [139]: one time series $x_1(n)(n = 1 \dots N, 0 < N < \infty)$ is said to Granger cause a second $x_2(n)$ if inclusion of the past values of x_1 improves the prediction of x_2, compared to the prediction of x_2 based solely on its own past values. Mathematically, this means that the variance of the modeling error of the second signal x_2 decreases when past values of the first signal x_1 are incorporated. Note that this definition allows directed connections, since both the Granger causality from x_1 to x_2 and from x_2 to x_1 can be investigated separately.

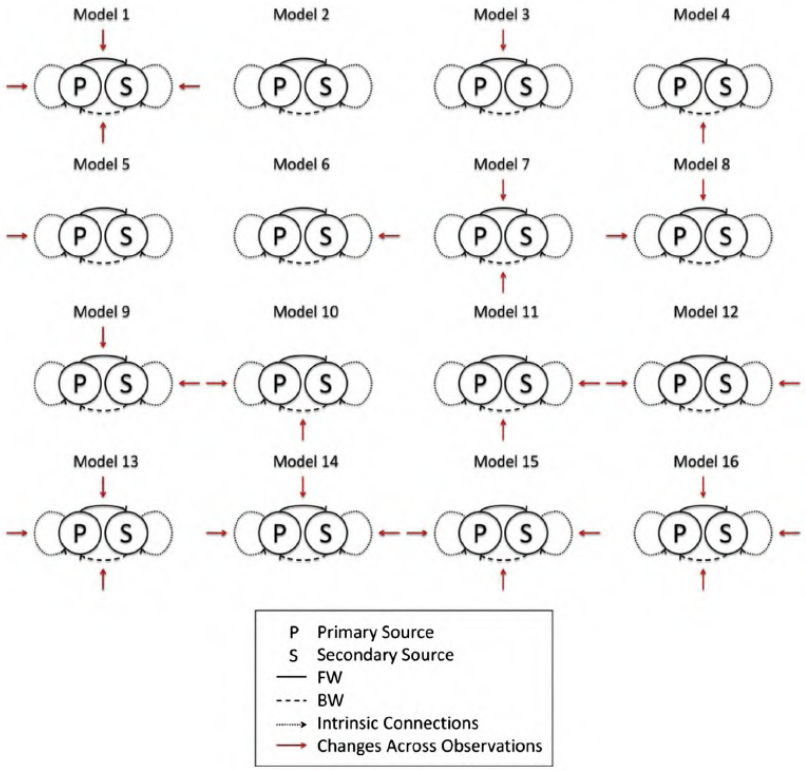

Figure 3.7: Example of dynamic causal modeling. Several models describing the neuronal activity are formally compared to each other using variational Bayesian techniques. Figure from [137].

In what follows, we will explain how to examine linear Granger causality. More information on nonlinear Granger causality can be found in [140].

Autoregressive models

Granger causality can be assessed via autoregressive (AR) models of the data that represent the signals as a linear combination of their own past plus additional uncorrelated white noise. For a time series $x(n)$ the univariate AR model is described as follows:

$$x(n) = \sum_{m=1}^{p} a(m)x(n-m) + e(n) \tag{3.17}$$

in which p is the model order, i.e. the number of past samples that are taken into account, $a(m)$ are the model coefficients and $e(n)$ are the residuals. In the bivariate case we get:

$$\begin{aligned} x_1(n) &= \sum_{m=1}^{p} a_{11}(m)x_1(n-m) + \sum_{m=1}^{p} a_{12}(m)x_2(n-m) + e_1(n) \\ x_2(n) &= \sum_{m=1}^{p} a_{21}(m)x_1(n-m) + \sum_{m=1}^{p} a_{22}(m)x_2(n-m) + e_2(n) \end{aligned} \tag{3.18}$$

or in matrix formulation:

$$\begin{bmatrix} x_1(n) \\ x_2(n) \end{bmatrix} = \sum_{m=1}^{p} \begin{bmatrix} a_{11}(m) & a_{12}(m) \\ a_{21}(m) & a_{22}(m) \end{bmatrix} \begin{bmatrix} x_1(n-m) \\ x_2(n-m) \end{bmatrix} + \begin{bmatrix} e_1(n) \\ e_2(n) \end{bmatrix} \tag{3.19}$$

where $a_{11}(m), a_{12}(m)$ and $a_{12}(m), a_{22}(m)$ are the model coefficients and $e_1(n)$ and $e_2(n)$ are the residuals (uncorrelated white noise) of signals x_1 and x_2, respectively.

The AR model can be generalized to incorporate K simultaneously recorded signals. This results in the multivariate autoregressive (MVAR) model:

$$\mathbf{X}(n) = \sum_{m=1}^{p} \mathbf{A}(m)\mathbf{X}(n-m) + \mathbf{E}(n) \tag{3.20}$$

in which $\mathbf{X}(n) = [x_1(n)x_2(n)\dots x_K(n)]^T \in \mathbb{R}^{K\times 1}$ is the signal matrix containing all signals at time point n and $\mathbf{A}(m) \in \mathbb{R}^{K\times K}$ is the coefficient matrix for delay m in which coefficient $\mathbf{A}_{ij}(m)$ estimates the influence of past sample $x_j(n-m)$ on the current sample $x_i(n)$. $\mathbf{E}(n) = [e_1(n)e_2(n)\dots e_K(n)]^T \in \mathbb{R}^{K\times 1}$ is the matrix containing the uncorrelated white noise at time point n.

Estimation of the model parameters

The estimation of the model order p is crucial, since incorporating too few past samples could prevent that existing connections are actually detected, whereas including too many samples drastically increases the necessary computational effort while possibly overfitting the model. Fortunately, there are some methods to estimate the optimal model

order, amongst others the Akaike Information Criterion (AIC) [141]:

$$\mathrm{AIC}(p) = \ln |\mathbf{\Sigma_e}(p)| + \frac{2pK^2}{N} \tag{3.21}$$

where $\mathbf{\Sigma_e}(p)$ is the covariance matrix of the residuals. The optimal value for the model order p is then chosen as that for which the AIC is minimal. Once the model order is fixed, the model coefficients can be estimated with statistical methods such as the method of least squares or the method of moments [142].

Transformation to the frequency domain

In order to investigate the spectral properties of the examined process, Eq. 3.20 can be rewritten and Fourier transformed:

$$\begin{aligned} \mathbf{X}(n) &= \sum_{m=1}^{p} \mathbf{A}(m)\mathbf{X}(n-m) + \mathbf{E}(n) \\ &\Updownarrow \\ \mathbf{E}(n) &= -\sum_{m=1}^{p} \mathbf{A}(m)\mathbf{X}(n-m) + \mathbf{X}(n) \end{aligned} \tag{3.22}$$

$$\begin{aligned} \Rightarrow \mathbf{E}(n) &= \sum_{m=0}^{p} \mathbf{A}'(m)\mathbf{X}(n-m) \\ &\text{with } \mathbf{A}'(m) = \begin{cases} -\mathbf{A}(m), & 1 \le m \le p \\ \mathbf{I}_K, & m = 0 \end{cases} \end{aligned} \tag{3.23}$$

$$\Updownarrow \text{ Fourier transformation}$$

$$\begin{aligned} \mathbf{E}(f) &= \mathbf{A}'(f)\mathbf{X}(\mathbf{f}) \\ &\text{with } \mathbf{A}'(f) = -\sum_{m=0}^{p} \mathbf{A}'(m) e^{-i2\pi \frac{f}{f_s} m} \end{aligned} \tag{3.24}$$

with f_s the sample frequency and $\mathbf{A}'(f)$ the Fourier transform of the coefficient matrix $\mathbf{A}'(m)$ in which $\mathbf{A}'(0) = -\mathbf{I}_K$ (the $K \times K$

identity matrix). $\mathbf{E}(f)$ and $\mathbf{X}(f)$ are the Fourier transformation of the uncorrelated white noise $\mathbf{E}(n)$ and signal matrix $\mathbf{X}(n)$, respectively. Eq. 3.24 can again be rewritten as:

$$\mathbf{X}(f) = \mathbf{A}^{I^{-1}}(f)\mathbf{E}(f) = \mathbf{H}(f)\mathbf{E}(f) \tag{3.25}$$

in which $\mathbf{H}(f)$ is a $K \times K$ matrix, also called the transfer matrix of the MVAR model. Element $H_{ij}(f)$ estimates the information flow from signal x_j to signal x_i at frequency f.

The spectral density matrix $\mathbf{S(f)}$ of the signals x_i, $i = 1 \dots K$ is defined as:

$$\mathbf{S}(f) = \begin{bmatrix} S_{11}(f) & S_{12}(f) & \cdots & S_{1K}(f) \\ S_{21}(f) & S_{22}(f) & \cdots & S_{2K}(f) \\ \vdots & \vdots & \ddots & \vdots \\ S_{K1}(f) & S_{K2}(f) & \dots & S_{KK}(f) \end{bmatrix} \tag{3.26}$$

in which $S_{ij}(f)$ is the cross spectral density function of the signals x_i and x_j, calculated as the Fourier transform of their cross-correlation and $S_{ii}(f)$ is the spectral density of signal x_i. The power spectral density matrix can be calculated based on the coefficients and residuals of the MVAR model as follows:

$$\begin{aligned} \mathbf{S}(f) &= |\mathbf{X}(f)|^2 = \mathbf{X}(f)\mathbf{X}^*(f) \\ &= \mathbf{H}(f)\mathbf{E}(f)\mathbf{E}^*(f)\mathbf{H}^*(f) = \mathbf{H}(f)\mathbf{S_e}(f)\mathbf{H}^*(f) \end{aligned} \tag{3.27}$$

where $\cdot^*$ denotes the complex conjugate and $\mathbf{S_e}(f)$ is the spectral density of the residuals. Since we assume that $\mathbf{E}(n)$ are uncorrelated white noise time series, $\mathbf{S_e}(f)$ will be the covariance matrix of the noise that can be approximated by a diagonal matrix with the variances of the noise:

$$\mathbf{S_e}(f) = \mathbf{\Sigma_e} = \begin{bmatrix} \sigma_{11} & \sigma_{12} & \dots & \sigma_{1K} \\ \sigma_{21} & \sigma_{22} & \dots & \sigma_{2K} \\ \vdots & \vdots & \ddots & \vdots \\ \sigma_{K1} & \sigma_{K2} & \dots & \sigma_{KK}^2 \end{bmatrix} = \begin{bmatrix} \sigma_1^2 & 0 & \dots & 0 \\ 0 & \sigma_2^2 & \dots & 0 \\ \vdots & \vdots & \ddots & \vdots \\ 0 & 0 & \dots & \sigma_K^2 \end{bmatrix} \tag{3.28}$$

This allows following estimation of the spectral density of signal x_i:

$$\hat{S}_{ii}(f) = \sum_{k=1}^{K} \mathbf{H}_{ik}(f)\sigma_k^2\mathbf{H}^* ki(f) = \sum_{k=1}^{K} \sigma_k^2 |\mathbf{H}_{ik}(f)|^2 \tag{3.29}$$

The spectral density of the signals can thus be estimated based on the transfer matrix, scaled with the variance of the residuals.

3.2.3.2 Granger causality measures

From the model coefficients and residuals, several linear Granger causality measures can be derived, both in time domain and frequency domain and both bivariate and multivariate. In what follows, the most commonly used measures are discussed.

Granger causality index
The bivariate causality from one time series $x_2(n)$ to another $x_1(n)$ can be assessed in the time domain using the Granger Causality Index (GCI):

$$\mathrm{GCI}_{12} = ln\frac{V_{x_1|x_1}}{V_{x_1|x_1x_2}} \tag{3.30}$$

where $V_{x_1|x_1}$ is the variance of the residual in the univariate case and $V_{x_1|x_1x_2}$ is the variance of the corresponding residual in the bivariate case. Assume that x_2 does not Granger cause x_1. In this case, $V_{x_1|x_1} \approx V_{x_1|x_1x_2}$ and thus $\mathrm{GCI}_{12} \approx 0$. In the opposite case, assume that x_2 does Granger cause x_1. In this case, we know from the definition of Granger causality that the variance of the residual in the bivariate case will be smaller than in the univariate case. As a consequence, the fraction in Eq. 3.30 becomes larger than 1 (a larger number divided by a smaller number) and $\mathrm{GCI}_{12} > 0$. The larger the value for GCI_{12}, the larger the influence of signal x_2 on signal x_1. The Granger causality from x_1 to x_2 can be investigated accordingly.

Partial directed coherence
The Partial Directed Coherence (PDC) calculates Granger causality in the frequency domain from signal x_j to signal x_i and is designed to show

only the direct connections [143] and not the indirect connections. The concept of direct and indirect connections is shown in Fig 3.8 and the formula for the PDC is:

$$\mathrm{PDC}_{ij}(f) = \frac{A'_{ij}(f)}{\sqrt{\sum_{k=1}^{K} |A'_{kj}(f)|^2}} \tag{3.31}$$

based on the Fourier transform of the coefficient matrix $\mathbf{A}'(f)$, so that inversion to obtain the transfer matrix $\mathbf{H}(f)$ is unnecessary. Furthermore, following normalization holds:

$$\sum_{k=1}^{K} |\mathrm{PDC}_{kj}(f)|^2 = 1 \tag{3.32}$$

meaning that the total outgoing information flow from every signal or node is 1 at every frequency.

Directed transfer function and its derivatives

In contrast to the PDC, the Directed Transfer Function (DTF) is designed to track the indirect connections to their origin, as shown in Fig. 3.8(d) [144]:

$$\mathrm{DTF}_{ij}(f) = \frac{H_{ij}(f)}{\sqrt{\sum_{k=1}^{K} |H_{ik}(f)|^2}} \tag{3.33}$$

with normalization:

$$\sum_{k=1}^{K} |\mathrm{DTF}_{ik}(f)|^2 = 1 \tag{3.34}$$

which indicates that the total incoming information flow in every signal or node is 1 at each frequency. Again, a higher value of the DTF means more information flow from x_j to x_i. Notice that DTF and PDC are independent from the noise covariance. Therefore, possible correlation of input noises among themselves, manifested in non-zero non-diagonal elements in $\mathbf{\Sigma_e}$ do not influence these measures.

The DTF has some well-known derivatives. First, it is possible to calculate the mean DTF over a predefined frequency band of interest

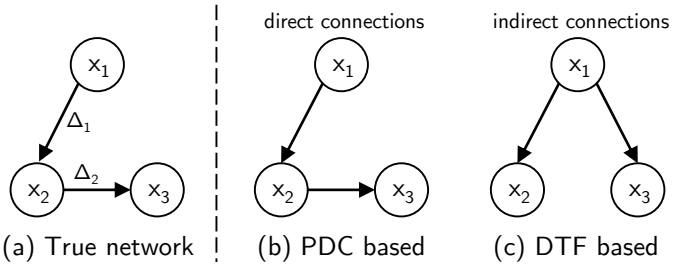

Figure 3.8: Concept of direct and indirect connections. (a) Assume a ground truth network of three signals x_1, x_2 and x_3. x_1 influences signal x_2 directly with a certain delay Δ_1. x_1 also influences x_3 indirectly via x_2 with an extra delay Δ_2. This figure shows how the connections will be detected by the (b) partial directed coherence (PDC) based measures and (c) directed transfer function (DTF) based measures.

$[f_1 f_2]$, in which every frequency contributes with the same weight [145]. This DTF derivative is called the integrated Directed Transfer Function (iDTF) and the formula is:

$$\begin{aligned} \mathrm{iDTF}_{ij}^2 &= \frac{1}{f_2 - f_1} \sum_{f=f_1}^{f_2} \left|\mathrm{DTF}_{ij}(f)\right|^2 \\ &= \frac{1}{f_2 - f_1} \sum_{f=f_1}^{f_2} \frac{\left|H_{ij}(f)\right|^2}{\sum_{k=1}^{K} \left|H_{ik}(f)\right|^2} \end{aligned} \tag{3.35}$$

As a consequence of every frequency contributing with the same weight, i.e. frequencies with low relative power contribute equally to the resulting measure as frequencies with high relative power, the DTF can be high in the parts of the spectrum where the relative power of the signal is very small (small denominator). To overcome this, we can integrate (or sum) the denominator over all frequencies in the frequency band of interest so that it does not change with frequency and hence prioritizes connections at prominent frequencies. This results in the full-frequency Directed Transfer Function (ffDTF) [146]:

$$\mathrm{ffDTF}_{ij}^2 = \sum_{f=f_1}^{f_2} \frac{\left|H_{ij}(f)\right|^2}{\sum_{f'=f_1}^{f_2} \sum_{k=1}^{K} \left|H_{ik}(f')\right|^2} = \sum_{f=f_1}^{f_2} \frac{\left|H_{ij}(f)\right|^2}{\sum_{k=1}^{K} \sum_{f'=f_1}^{f_2} \left|H_{ik}(f')\right|^2} \tag{3.36}$$

Both iDTF and ffDTF are normalized so that the total incoming information flow in every channel is 1:

$$\sum_{k=1}^{K} |\cdot \mathrm{DTF}_{ik}|^2 = 1 \tag{3.37}$$

3.2.3.3 Granger causality for non-stationary signals

In the previous section, we assumed that the time series x_i, $i = 1 \dots K$ were stationary and as a consequence, the coefficients of the AR model remained constant over time. Although baseline EEG segments can be considered quasi-stationary from segment to segment, a lot of neural transitions, e.g. the onset of an epileptic seizure, are inherently non-stationary [147]. Fortunately, it is possible to extend the above methods to accommodate for non-stationary signals by deriving the Granger causality measures from a Time-Varying Multivariate Autoregressive (TVAR) model, which is an autoregressive model that allows the model coefficients to change over time. Eq. 3.20 for a TVAR model then becomes:

$$\mathbf{X}(n) = \sum_{m=1}^{p} \mathbf{A}_m(n)\mathbf{X}(n-m) + \mathbf{E}(n) \tag{3.38}$$

in which p is the model order, $\mathbf{X}(n) = [x_1(n)x_2(n) \dots x_K(n)]^T$ is the $K \times 1$ signal matrix, $\mathbf{E}(n) = [e_1(n)e_2(n) \dots e_K(n)]^T$ is the $K \times 1$ matrix containing the residuals, which we still assume to be uncorrelated white noise, and $\mathbf{A}_m(n)$ is the time-variant $K \times K$ coefficient matrix for delay $m = 1 \dots p$ and time point n. The estimation of the time-varying coefficients is now an ill-posed problem, since there are more unknown parameters than measured data points. The Kalman filtering algorithm allows estimating the autoregressive coefficients via a state-space representation of the TVAR model [148, 149]. Two parameters influence the Kalman algorithm. On the one hand, there is the model order p, for which the optimal value can again be calculated via minimizing the AIC (Eq 3.21). On the other hand, the Update Coefficient (UC) defines how quickly the model will adapt to changes in the dataset. The lower the value, the more robust the model parameters will be, but the slower they will adapt to non-stationary transitions, and vice versa.

In the frequency domain we get for the coefficient matrix:

$$\mathbf{A}(f,n) = -\sum_{m=0}^{p} \mathbf{A}_m(n) e^{-i2\pi \frac{f}{f_s} m} \tag{3.39}$$

with f_s the sample frequency and $\mathbf{A}_0(n) = -\mathbf{I}_K$, $\forall n$. Eq. 3.25 remains valid, but a time-dependent component is added to account for the changing frequency spectrum over time:

$$\mathbf{X}(f,n) = \mathbf{A}^{-1}(f,n)\mathbf{E}(f,n) = \mathbf{H}(f,n)\mathbf{E}(f,n) \tag{3.40}$$

in which $\mathbf{X}(f,n)$ and $\mathbf{E}(f,n)$ are the Fourier transforms of $\mathbf{X}(n)$ and $\mathbf{E}(n)$ respectively. $\mathbf{H}(f,n)$ is now a time-varying matrix of which every element $H_{ij}(f,n)$ describes the information flow from signal x_j to signal x_i at time point n and for frequency f. The time-variant aspect can be taken into account into the formulas for the PDC and DTF, which results in the Adaptive Partial Directed Coherence (APDC) [150], Adaptive Directed Transfer Function (ADTF) [150, 151], integrated Adaptive Directed Transfer Function (iADTF) [150, 151] and the full-frequency Adaptive Directed Transfer Function (ffADTF)[1] [152]:

$$\mathrm{APDC}_{ij}(f,n) = \frac{A_{ij}(f,n)}{\sqrt{\sum_{k=1}^{K} |A_{kj}(f,n)|^2}} \tag{3.41}$$

$$\mathrm{ADTF}_{ij}(f,n) = \frac{|H_{ij}(f,n)|^2}{\sum_{k=1}^{K} |H_{ik}(f,n)|^2} \tag{3.42}$$

$$\mathrm{iADTF}_{ij}(n) = \frac{1}{f_2 - f_1} \sum_{f=f_1}^{f_2} \frac{|H_{ij}(f,n)|^2}{\sum_{k=1}^{K} |H_{ik}(f,n)|^2} \tag{3.43}$$

$$\mathrm{ffADTF}_{ij}(n) = \sum_{f=f_1}^{f_2} \frac{|H_{ij}(f,n)|^2}{\sum_{k=1}^{K} \sum_{f'=f_1}^{f_2} |H_{ik}(f',n)|^2} \tag{3.44}$$

[1] Note that we omit the $\cdot^2$ notation here.

The APDC is normalized so that the total outgoing information flow from each channel equals 1 at every time point and each frequency. The ·ADTF is normalized so that the total incoming information flow at each channel equals 1 at every time point and each frequency:

$$\sum_{k=1}^{K} \cdot\mathrm{ADTF}_{ik}(n) = 1 \tag{3.45}$$

Like in the DTF, the ADTF can have low values even in the presence of a connection if the incoming information flow of the other signals is high. Vice versa, it can be unreliably high when the relative power of the signal at that frequency is relatively low. This can lead to biased results for the iADTF. This is overcome in the ffADTF that prioritizes frequencies for which the power of the receiving signal x_i is high. The ffADTF does, however, not take the power of the sending signal x_j into account. Therefore, [153] proposed a more complex normalization in the spectrum-weighted Adaptive Directed Transfer Function (swADTF) that also takes the power of the sending signal x_j into account:

$$\begin{aligned}\mathrm{swADTF}_{ij}(n) &= \frac{\sum_{f=f_1}^{f_2} |H_{ij}(f,n)|^2 \hat{S}_{jj}(f,n)}{\sum_{k=1}^{K} \sum_{f'=f_1}^{f_2} |H_{ik}(f',n)|^2 \hat{S}_{kk}(f',n)} \\ &= \frac{\sum_{f=f_1}^{f_2} |H_{ij}(f,n)|^2 \sum_{l=1}^{K} |H_{jl}(f,n)|^2}{\sum_{k=1}^{K} \sum_{f'=f_1}^{f_2} |H_{ik}(f',n)|^2 \sum_{s=1}^{K} |H_{ks}(f',n)|^2}\end{aligned} \tag{3.46}$$

with $\hat{S}_{ii}(f,n)$ the time-variant extension of Eq. 3.29 for the estimation of the spectral density of signal x_i. Every element $|H_{ij}(f_0,n_0)|^2$ is weighted by the power present in the sending signal ($\hat{S}_{jj}(f_0,n_0)$). This implies that information flow can only be seen at a certain frequency if the power in the sending signal at that frequency is large enough. Again, this measure is normalized to the total incoming information flow in signal x_i at each time point:

$$\sum_{k=1}^{K} \mathrm{swADTF}_{ik}(n) = 1 \tag{3.47}$$

3.2.4 Graph analysis

Once the information flow between the different signals is known, the (brain) network can be represented in an abstract mathematical way, called a graph. We already used this representation in Fig. 3.8. A graph simply comprises a set of nodes or vertices, symbolizing different brain regions, and a set of edges connecting these nodes. Vertices that are connected via an edge are called neighbors. The edges can represent the anatomical connections or the functional or effective information flow, and can be either undirected (or bidirectional) or directed. Furthermore, the edges can be unweighted, i.e. every connection has the same strength, or weighted, i.e. every connection has a strength relative to the connectivity measure that was calculated. The graph representation allows to more easily interpret the rather complex network and the study of these graphs and their properties is called graph theory or graph analysis.

Next to the network topology, a graph can also be represented by an adjacency matrix $\mathbf{A}$ in which each element A_{ij} represents the edge from vertex j to vertex i. The value of A_{ij} is the weight of the edge, which is 0 in case there is no connection and 1 in case of connections in an unweighted graph. Undirected graphs have a symmetric adjacency matrix. An example of a weighted directed graph shown as a network topology and its corresponding adjacency matrix can be seen in Fig. 3.9 and Eq. 3.48, respectively.

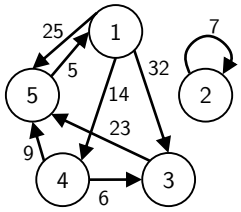

Figure 3.9: Example of a weighted directed graph, shown as a network topology. The weight of the edges is indicated with a number. Vertex 2 is unconnected with the other nodes of the graph, but is still part of the graph. Edges in two directions between the same vertices are possible (e.g. two edges between vertex 1 and 5). Loops inside a graph are possible (e.g. between vertex 1, 3 and 5). A vertex can also be connected with itself (e.g. vertex 2).

$$\mathbf{A} = \begin{bmatrix} 0 & 0 & 0 & 0 & 5 \\ 0 & 7 & 0 & 0 & 0 \\ 32 & 0 & 0 & 6 & 0 \\ 14 & 0 & 0 & 0 & 0 \\ 25 & 0 & 23 & 9 & 0 \end{bmatrix} \tag{3.48}$$

Graphs can be characterized by both node and network-related properties. The most basic parameters are the graph's order and size, which are the number of vertices and the number of edges, respectively. An important node property is the degree of a node i, which is the number of edges that connect to that node i. For directed graphs, the distinction between incoming and outgoing connections can be made, called the indegree (ID_i) and outdegree (OD_i), respectively:

$$\mathrm{ID}_i = \sum_{k=1}^{K} A_{ik} \tag{3.49}$$

$$\mathrm{OD}_i = \sum_{k=1}^{K} A_{ki} \tag{3.50}$$

with K the number of nodes in the graph. The higher the indegree of a node, the higher the incoming information flow and accordingly for the outdegree. For the example of Fig. 3.9 and Eq. 3.48, the order of the graph is 5, whereas the size is 7. For the 5 nodes, we find the in- and outdegrees shown of Table 3.2. Note that the sum of all indegrees is equal to the sum of all outdegrees, since in both cases every edge is counted once.

The degrees can be normalized. In case the PDC is used as connectivity measure, the outdegree of every node is 1. For the APDC, this holds for every time point. In case of the ·DTF, the indegree of very node is equal to 1 (for every time point).

During an epileptic seizure, different brain regions become simultaneously active in an epileptic network. To localize the Seizure Onset Zone (SOZ) of the seizure, the main driver, influencing all other regions directly or indirectly, of this network should be found. The network

Table 3.2: In- and outdegrees of the graph example.

	ID	OD
Vertex 1	5	25+14+32=71
Vertex 2	7	7
Vertex 3	32+6=38	23
Vertex 4	14	9+6=15
Vertex 5	25+9+23=57	5
Total	121	121

can also be seen as a graph, with the vertices representing the different active brain regions and the edges representing the information flow between these regions. In the graph representation, the main driver of the network corresponds to the vertex with the highest outdegree, when indirect connections are taken into account (edges determined based on ·DTF values).

Other examples of graph properties that are interesting to investigate (epileptic) brain networks are the clustering coefficient, a measure for the tendency of nodes to cluster together; the characteristic path length, the mean of the shortest path lengths[1] between every pair of nodes; and the betweenness centrality, the number of shortest paths that pass through a vertex. More information about this can be found in [154, 155].

[1] The shortest path length between two nodes is the minimal sum of the weight of the edges that need to be traversed to get from one vertex to another. For example, the possible paths from vertex 1 to vertex 5 are 1-5, 1-3-5 and 1-4-5. The path length of the first option is 25, whereas that of the second is 32 + 23 = 55 and that of the third is 14 + 9 = 23. The shortest path from vertex 1 to vertex 5 is thus via vertex 4 and the shortest path length is 23.

4

Review on seizure onset zone localization from noninvasive EEG

4.1 Introduction

In Chapter 2, we introduced epilepsy as a disorder of recurrent and unprovoked seizures that can be either focal (starting in a specific region in the brain) or generalized (the whole brain starts seizing at once). As EEG can directly measure the abnormal electrical brain activity during and in between seizures in a convenient, safe and inexpensive way, it is the most important clinical technique to diagnose and characterize epilepsy [156]. It is, however, (mostly) impossible to find the region responsible for the seizures based on visual inspection of the EEG. In this dissertation, we, therefore, develop a method to localize this region based on advanced signal processing of the EEG recordings. The importance and clinical value of this will be discussed more elaborately in section 4.2. In the next section, the main challenges encountered in this field of research are highlighted. Finally, an overview of the pioneering work, more recent studies and state-of-the-art methodologies to localize the seizure onset zone from noninvasive EEG will be discussed.

4.2 Importance

The goal of epilepsy treatment is to suppress seizures. When antiepileptic drugs (AEDs) cannot offer seizure control, surgery is an important option due to its high success-rate in selected candidates [68, 69]. During epilepsy surgery, the brain region that causes the seizures is disconnected (disconnective surgery) or removed (resective surgery). Therefore, it is of utmost importance to accurately delineate the epileptogenic zone (EZ), which is the brain area that initiates the seizures and of which surgical removal is required and sufficient to render the patient seizure-free. Unfortunately, no method can localize this EZ, since it is only a conceptual region. Epileptologists make a deliberate estimation based on the integration of the results obtained during the presurgical evaluation protocol. MRI and visual inspection of the interictal and ictal (video-)EEG with the determination of the irritative zone (IZ) and seizure onset zone (SOZ), respectively, are cornerstone investigations in this protocol [65]. However, often extra investigations such as interictal PET, interictal and ictal SPECT, etc. are needed to form a solid hypothesis about the EZ. Recently, EEG and MEG source imaging (ESI/MSI) of interictal EEG or MEG data offer an estimation of the brain activity underlying the measured data. Although not widely used yet, these techniques have started to find their way into the presurgical evaluation [157]. The results are promising, with reported sensitivity ranging between 70% and 90% for interictal PET in case of Temporal Lobe Epilepsy (TLE)[1] and between 66% and 97% for ictal SPECT [158, 159]. A study of Brodbeck et al., based on 152 (102 TLE, 50 Extra TLE (ETLE)) patients, accounted for a sensitivity of 69% and specificity of 44% for PET; a sensitivity and specificity of 58% and 47% for SPECT; and 76% and 53% for structural MRI [160]. They also reported a sensitivity and specificity of 84% and 88% for ESI of spikes marked in high-density (hd) EEG. These numbers dropped to 66% and 54%, respectively, when using 32 electrodes or less. Recently, a sensitivity and specificity of 79% and 75% were reported for ESI of automatically detected spikes in long-term low-density EEG [161]. For MSI of spikes, a sensitivity ranging between 55 and 80% is found [162, 163].

[1] The sensitivity of interictal PET is 30-60% in case of extratemporal lobe epilepsy, and up to 100% in case of lesions. The specificity, however, is considered significantly lower.

Despite these encouraging results, sometimes extra investigations, which are often time-consuming, labor-intensive and costly, are required. Next to this, these investigations are often based on interictal data, but it can be argued that localizing seizures is more informative since they directly reflect the affliction associated with epilepsy. Additionally, invasive EEG (iEEG) is still required in 10-25% of the presurgical candidates to localize the SOZ and define potential overlap with eloquent cortex [65]. The iEEG monitoring is associated with potential complications, such as scarring, infection and functional loss [164–167].

Thus, it would be of high clinical value to develop a method that is able to identify the SOZ in a noninvasive, objective and cost-effective way with high accuracy. During the last decades, increased computational power and advanced signal processing techniques have enabled novel epilepsy research dedicated to this purpose. Methods based on noninvasive scalp EEG are preferred, not only because EEG is inexpensive, portable and safe, but also because it corresponds to the most unambiguous biomarker of epileptic activity. Moreover, noninvasive EEG is routinely performed during long-term presurgical investigations. Such methods could, once perfected, allow to:

1. provide more accurate and/or objective interpretation of the EEG with respect to visual inspection,

2. better target iEEG electrode placement or obviate invasive monitoring,

3. shorten the presurgical evaluation, as long-term EEG is recorded in phase 1 of the presurgical evaluation and other investigations could possibly be bypassed.

We will address the challenges encountered in the development of EEG-based SOZ localization methods and present pioneering and state-of-the-art work reported in literature.

4.3 Main challenges and possible solutions

The main challenges encountered while developing methods for EEG-based SOZ localization are:

1. the often low quality of ictal EEG data,
2. the low spatial resolution of EEG,
3. the spread of ictal activity in the EEG,
4. the preferred validation strategy to quantify the performance of the developed method.

In what follows, we will address these four challenges in more detail and describe how these problems are generally tackled in literature.

EEG recorded during a seizure is generally of low quality, since it is often accompanied with voluntary or involuntary movements or eye blinks of the patient that cause muscle, movement and/or eye artifacts in the EEG, which significantly reduce the signal-to-noise ratio signal-to-noise ratio (SNR). It is impossible to avoid these artifacts, so researchers need to find workarounds to cope with or to enhance the low SNR. The first step in most analyses is the preprocessing of the data, which mostly involves filtering with a band-pass filter to reduce baseline drift (low frequency) and the muscle artifacts (high frequency). Additionally, decomposition techniques can be used to remove eye blink, heartbeat or other artifacts. Decomposition techniques can also be used to select the components that correspond to seizure activity and then perform the further analysis on those components. Another possibility is to select in the EEG a (quasi) artifact-free epoch that is limited in time. Some research is based on a single time-point on or in the vicinity of the seizure onset, taking care to choose a time-point at a point of high SNR. Sometimes, the analysis is limited to a frequency band of interest, in which most seizure activity is located to exclude the influence of artifacts at other frequencies. A final approach is to average ictal events such as spikes during (the beginning of) the seizure. This can be challenging because of the often non-uniform morphology of the ictal events. Moreover, the average is often restricted to a small number and as a consequence, SNR enhancement could be limited [168].

Second, although EEG has a high temporal resolution in the order of milliseconds, the spatial resolution at sensor level is low ((sub)lobar [169]), due to the fact that the recorded potentials are subject to volume conduction. Neuronal activity is distributed through different tissues (such as cerebrospinal fluid, skull and scalp) to reach the electrodes. Because of the different conductivities of these tissues, and certainly the

low conductivity of the skull, the measured activity at the electrodes is smeared and distorted. As a consequence, the potential measured at a given electrode does not necessarily represent the activity of the directly underlying brain region. One way to overcome the volume conduction problem and the resulting low spatial resolution is the use of ESI. ESI is a technique to estimate the brain activity that generated the recorded EEG and allows to improve the sublobar resolution at sensor level to centimeter resolution inside the brain (source space) [170]. It consists of a forward or generative model, which describes how specific brain activity is distributed to the electrodes, and an inverse problem/solution, in which a cost function based on the difference between the generated and measured EEG is minimized in order to provide an estimate of the brain activity. The forward model is mainly based on a model of the head, which can be simply spherical, based on a template MRI or based on the patients individual MRI. In this paper, we will not discuss the neurophysiological basis and methodological aspects of ESI, since this has already been widely covered in previous literature [91,120,121,171].

The spatial resolution of EEG can also be improved by including more electrodes in the recording setup, which also benefits the quality of ESI. Despite the fact that increasing the number of electrodes does not solve the distortion of the brain signals, previous research has shown the benefit of high-density EEG (hd-EEG) on ESI [172,173], with specificity and sensitivity increasing significantly (20-30%) with the number of electrodes used [160].

Third, ictal activity rapidly spreads in the brain and therefore it can be noticeable at many EEG electrodes simultaneously. When applying ESI to ictal epileptic data, it is intuitive to select the brain region where the reconstructed brain activity is highest in amplitude/energy/power to estimate the SOZ, as is usually done in SOZ localization studies (section 4.4.1). However, it has been generally accepted that epilepsy is a network disorder rather than a focal disease. This means that during a seizure, several brain regions become simultaneously active as part of the patient's individual epileptic network and it is often hard to distinguish the main driver(s) of this network at seizure onset from the secondary activated regions [87,88]. Furthermore, there is no direct evidence to assume that the brain activity in the SOZ is stronger than the propagated activity, because a small group of driving neurons could trigger a larger group of neurons resulting in an area of higher activity elsewhere. Because of these considerations, researchers increasingly try

to reconstruct the active regions in the brain and subsequently study the epileptic network, its interactions and the information flow between the regions associated with the epileptic network. This can be done by combining ESI with subsequent connectivity analysis (section 3.2) [174]. These studies, discussed in section 4.4.2, hypothesize that the main driver of the epileptic network should be associated with an increased information flow. The usefulness of (functional) connectivity analysis for the localization of the SOZ has already been shown for iEEG recordings [133, 153]. ESI allows extending this concept for noninavive EEG recordings.

Finally, once a method is developed, the final challenge is to find an optimal way to quantify its performance. Often, validation is based on lobar or sublobar concordance with or distance to a 'ground truth'. Yet, defining the ground truth is often not trivial since the perfect delineation of the SOZ is not known. Sometimes, it is based on the results of other investigations such as ictal SPECT or MRI. Other studies happen retrospectively and the ground truth is based on the outcome of the complete presurgical evaluation during which the presumed SOZ is delineated, or the ultimately resected area. This can be linked to the surgical outcome of the patient. Indeed, if a patient is seizure-free after surgery, the SOZ was harbored in the resected area, which was preoperatively delineated during the presurgical evaluation, and vice versa. An issue with this technique is that the area that was delineated by the presurgical protocol or that was resected can be and probably is larger than the true SOZ[1]. Therefore, it is often argued that the optimal ground truth is based on seizures recorded during iEEG, despite the fact that iEEG is avoided whenever possible since this invasive technique is potentially harmful for the patient. Also, it should be guaranteed that the invasive electrodes sample the true SOZ, since the spatial covering that can be obtained with iEEG is limited[2]. Furthermore, it is hard to apply ESI on seizures that were simultaneously recorded with iEEG and scalp EEG, because of the influence of the intracranial electrodes and the burr holes and bone flaps on the distribution of the electric field. It has

[1] As mentioned in chapter 2, the extent of the tissue to be resected is a compromise between the risk of functional loss for larger resections and the risk of not being seizure-free for smaller resections.

[2] If the electrodes would be placed close to the SOZ, but not on the SOZ, the tissue beneath the electrodes closest to the real SOZ will be incorrectly considered to harbor the SOZ.

been shown that the non-conductive part of a subdural grid attenuates scalp potential of generators located under them [175]. The solution to this is to record the EEG and iEEG separately, but in this case, it cannot be guaranteed that the seizures originated from exactly the same spot. The solution to this is to record the EEG and iEEG separately, but in this case, it cannot be guaranteed that the separately recorded seizures originated from exactly the same spot. Some studies use simulated EEG to test and quantify the performance of their methods before applying them to patient data. The advantage of simulations is that the ground truth is known exactly. Yet, it is often hard to predict how simulations translate to real data and therefore a validation step with real data is indispensable. This review paper will only cover studies (also) using real data.

4.4 EEG-based SOZ localization

In the next two sections, we offer an overview of the research on localizing the SOZ from noninvasive EEG. We included all studies up to 2016 working with real ictal EEG data reported in English to which access was provided and discuss how the authors tackled the aforementioned challenges and what their findings were. We found 30 studies and the general trend is that they all apply ESI on the scalp-recorded data. Five of the studies also used subsequent connectivity analysis. We will discuss the studies using solely ESI and those that combine it with connectivity analysis separately. Table 4.1 lists for every study the number of included patients, the amount of electrodes, the used head model and inverse method for ESI, the connectivity measures (if any), the method to estimate the SOZ based on the ESI or connectivity analysis results, and the validation approach at hand. In summary, 9/30 studies used hd-EEG recordings, while the other 21 relied on low-density EEG. One of the hd-EEG studies also used low-density subsets to study the influence of the number of electrodes. 11/30 studies used spherical head models, 15/30 used individual realistic head models and 4/30 used a template realistic head model. Finally, 18 different inverse solution techniques were used.

Fig. 4.1 shows an overview of the number of studies published over the years. The foundation of this kind of research traces back to over two decades ago and has known a first plateau around the turn of the century.

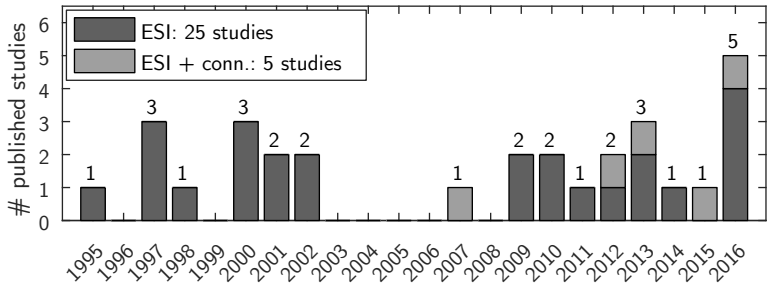

Figure 4.1: The number of studies published on EEG-based SOZ localization over the years, studies using ESI and studies using ESI with subsequent connectivity analysis are shown separately.

Yet, it is only in more recent years that it started growing faster with the emergence of and easier access to more computational power. We expect that in the coming years this relatively new research field will continue to grow faster and faster towards maturity.

In contrast, studies trying to localize the IZ based on interictal EEG data have been more frequent in the past, as can be seen in Fig. 4.2, which is the result of an exploratory search on the Web of Science (and is therefore probably an underestimation of the true amount of studies). As a consequence, EEG-based IZ localization is already a more mature research field and an established technique. This difference in growth could be explained by the observation that interictal events are less subject to artifacts and have a more frequent occurrence than seizures in the recorded EEG. ESI of interictal data is generally a more simple concept and easier to process. Often, less computational power is necessary because very complex or advanced techniques are not always required (although they could be used for it). However, the IZ may designate a (partially) different, possibly larger region than the SOZ and therefore, SOZ localization may potentially be more informative for surgery guidance [176, 177].

We should mention that other epilepsy studies exist using these signal processing techniques applied to ictal EEG data to uncover neurophysiological mechanisms of the condition [178]. These studies were not included, as they did not provide localization information. Also studies using other noninvasive modalities, such as fMRI and MEG exist. Whereas fMRI data requires a fundamentally different approach (e.g. [179]), and is therefore left out of this discussion, MEG can be

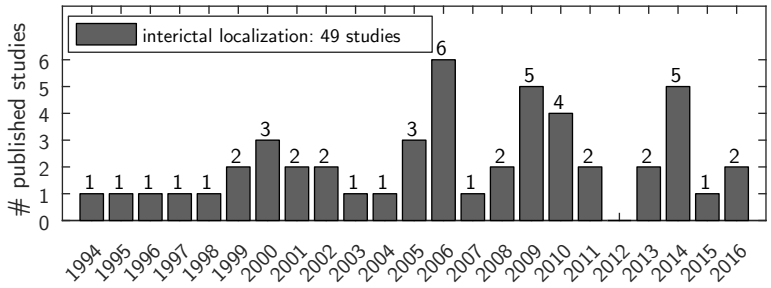

Figure 4.2: The number of studies published on EEG-based IZ localization over the years. Result of an exploratory search on the Web of Science and probably an underestimation of the true amount of studies in this research field.

processed in a similar way as EEG. Therefore, studies exist that apply source imaging and possibly connectivity analysis on MEG data to localize the SOZ [180–184]. Yet, ictal MEG data are rare (Badier et al., 2016). This is because MEG recordings need to take place in a special shielded room and long-term recordings are still impossible. Although MEG is also noninvasive, ictal MEG data are rare [184]. This is because MEG recordings need to take place in a special shielded room and long-term recordings are still impossible. As a consequence, the chance that a patient will have a spontaneous seizure during the recording is limited. Patients with a reflex epilepsy syndrome (such as musicogenic or photosensitive epilepsy) might be easier to study, as was done in [185]. Yet, they only represent a very small subpopulation of all epilepsy patients. Additionally, ictal MEG data suffers even more from seizure-related movement artifacts, since the electrodes are not fixed to the scalp of the patient. Finally, MEG is available in only a limited amount of epilepsy centers, whereas EEG is recorded in every center during the presurgical evaluation. Therefore, we focus our review on EEG studies in the field.

Table 4.1: Overview of all EEG-based SOZ localization studies up to 2016. 3-shell/layer = skull, scalp, brain; 4-tissue = skull, scalp, brain, cerebrospinal fluid (CSF); 5-tissue = skull, scalp, CSF, gray matter, white matter; BEM = Boundary Element Method; FEM = Finite Element Method; FDM = Finite Difference Method; (L)SMAC = (Locally) Spherical Model with Anatomical Constraints; ECD = Equivalent Current Dipole modeling; (s)LORETA = (standardized) Low Resolution Electromagnetic Tomography, PEFSA = Phase-Encoded Frequency Spectral Analysis; (w)MNE = (weighted) Minimum Norm Estimation; (RAP-)MUSIC = (Recursively Applied and Projected) Multiple Signal Classification; LAURA = Local Autoregressive Average; CLARA = Classical LORETA Analysis Recursively Applied; DICS = Dynamic Imaging of Coherent Sources; (A)DTF = (Adaptive) Directed Transfer Function; RPDC = Renormalized Partial Directed Coherence; DCM = Dynamic Causal Modeling, DSI = Dynamic Seizure Imaging; PARAFAC = Parallel Factor Analysis; PCA = Principal Component Analysis; RZ = Resected Zone.

Reference	**# pat.**	**# elec.**	**head model**	**inverse method**	**conn. analysis**	**SOZ localization approach**	**validation approach**
Akdeniz, 2016 [186]	15	64	ind. 3-layer BEM	LORETA	/	source map maximum at seizure onset	concordance with RZ
Assaf and Ebersole, 1997 [187]	33	23-27	3-shell spherical	19 fixed dipoles	/	most prominent source component at earliest recognizable ictal rhythm	qualitative agreement with iEEG
Beniczky et al., 2013 [188]	42	25	SMAC	LAURA	/	source map maximum at predefined time-point of averaged ictal waveform	sublobar concordance with decision epilepsy team
Beniczky et al., 2016 [189]	22	64	template FEM	ECD, CLARA, cortical-CLARA, MNE	/	dipole location or source map maximum of averaged seizure onset waveforms	sublobar concordance with RZ/clinically defined SOZ
Boon and D'Havé, 1995 [190]	15	27	3-shell spherical	ECD	/	location and orientation of the dipole of single ictal spikes	qualitative agreement with iEEG

Table 4.1: (continued)

Reference	# pat.	# elec.	head model	inverse method	conn. analysis	SOZ localization approach	validation approach
Boon et al., 1997a [191]	9	27	3-shell spherical	ECD	/	location and orientation of the dipole of single ictal spikes	qualitative agreement with iEEG
Boon et al., 1997b [168]	33	27	3-shell spherical	ECD	/	location and orientation of the dipole of single ictal spikes	qualitative agreement with iEEG
Boon et al., 2000 [192]	41	27	3-shell spherical	ECD	/	location and orientation of the dipole of single ictal spikes	qualitative agreement with iEEG
Boon et al., 2002 [193]	31	27	3-shell spherical	ECD	/	location and orientation of the dipole of single ictal spikes	influence on surgical decision process
Despotovic et al., 2013 [194]	10	17	ind. 4-tissue FDM	ECD	/	dipole location of topography after PARAFAC of ictal spikes	distance to nearest lesion border
Ding et al., 2007 [195]	5	31	ind. 3-layer BEM	FINE	DTF	identify primary driver with significant DTF value of ~3 s EEG epoch at seizure onset	concordance to MRI lesions
Elshoff et al., 2013 [196]	11	38-50	5-shell spherical	DICS	RPDC	first and second source found by DICS of 1-10s around seizure onset	sublobar concordance with RZ
Habib et al., 2016 [197]	8	21	ind. 3-layer BEM	wMNE, dSPM, sLORETA	/	source map maximum at peak of averaged ictal rhythms	lobar and hemispherical concordance with ictal SPECT foci

Table 4.1: (continued)

Reference	# pat.	# elec.	head model	inverse method	conn. analysis	SOZ localization approach	validation approach
Hallez et al., 2009 [198]	8	21	ind. 4-tissue FDM	RAP-MUSIC	/	dominant sources in moving windows of 0.25 s	distance to ictal SPECT foci
Holmes et al., 2010 [199]	10	128/256	template	LAURA	/	largest magnitude in source map at seizure onset time-point	(sub)lobar concordance with iEEG
Klamer et al., 2015 [185]	1	256	LSMAC	LORETA	DCM	2 ROIs after ESI, DCM of averaged seizure initiating spikes, from onset until peak	concordance with iEEG
Kobayashi et al., 2000 [200]	3	25	ind. 3-layer BEM	'software probe', ECD	/	largest magnitude in source map in 2.56 s epochs from the initial part of the seizure, dipole location of averaged definite ictal rhythms	qualitative agreement with iEEG
Koessler et al., 2010 [201]	10	64	ind. 3-layer BEM	ECD, rotating ECD, MUSIC, LORETA, sLORETA	/	analysis of ictal activities (few ms - 1 s), ECD: dipole with max. GOF; MUSIC: max. music metric; (s)LORETA: source with highest amplitude over space and time	sublobar concordance with iEEG
Kovac et al., 2014 [202]	8	31-46	template FEM	ECD, CLARA, LORETA	/	dipole location or source map maximum of averaged seizure cycles	concordance to lateralization of lesion on MRI
Lantz et al., 2001 [203]	15	26/29	template	wMNE	/	new data matrix based on peaks in GFP was segmented into limited amount of topographies, most important topographies inverted	correspondence with iEEG

Table 4.1: (continued)

Reference	# pat.	# elec.	head model	inverse method	conn. analysis	SOZ localization approach	validation approach
Lu et al., 2012a [204]	9	32	ind. 3-layer BEM	MNE	/	DSI	distance to border RZ, concordance with iEEG
Lu et al., 2012b [205]	10	76 (64-48-32-21)	ind. 3-layer BEM	FINE	DTF	identify primary driver with significant DTF value of 2-3 s EEG epoch at seizure onset	distance to boundary of RZ
Merlet and Gotman, 2001 [206]	9	28-40	4-shell spherical	ECD	/	localization of most active dipole (of 2) fitted to the ascending phase and the complete wave of averaged ictal waveform	distance to most active iEEG contacts
Mine et al., 1998 [207]	2	21	ind. 3-layer	ECD	/	location of the dipole at the peak of a single ictal spike	qualitative agreement with iEEG
Mine et al., 2002 [208]	9	21	ind. 3-layer	ECD	/	location of the dipole at the peak of a single ictal spike	qualitative agreement with iEEG
Pellegrino et al., 2016 [209]	15	54	ind. 3-layer BEM	wMEM	/	first component of PCA decomposition of spatiotemporal source maps of narrow time window around seizure onset	sublobar concordance with and distance to border of clinically defined SOZ
Rullmann et al., 2009 [210]	1	24	ind. anisotr. 6-tissue FEM	dipole scanning, rotating ECD, fixed ECD, MNE, sLORETA	/	dipole location or largest magnitude in source map at the peak of averaged delta bursts	qualitative agreement with lesion border and iEEG

Table 4.1: (continued)

Reference	# pat.	# elec.	head model	inverse method	conn. analysis	SOZ localization approach	validation approach
Sohrabpour et al., 2016 [211]	2	76	ind. 3-layer BEM	sLORETA	ADTF	driver by ADTF analysis of sources identified by DSI source map maximum of the estimated optimal	concordance with iEEG and RZ
Worrell et al., 2000 [212]	10	31	3-shell spherical	LORETA	/	synchronized generator that best describes the measured EEG at the seizure frequency (PEFSA [213]), at seizure onset.	lobar concordance with symptomatic lesion
Yang et al., 2011 [214]	8	76	ind. 3-layer BEM	LORETA	/	DSI (see text)	overlap with/ distance to border of RZ or ictal SPECT foci or iEEG

4.4.1 ESI to localize the SOZ

Pioneering work

One of the first studies to acknowledge the possible use of ESI of ictal scalp EEG was performed in 1995 by Boon et al., who applied dipole modeling on epochs of early single ictal discharges, filtered between 1 and 14 Hz, in 15 patients (4 underwent iEEG) with drug-resistant focal epilepsy and qualitatively described its usefulness for the presurgical evaluation [190]. They, however, concluded that confirmation and validation in a larger patient population group with iEEG was necessary and that ictal ESI is harder than interictal ESI due to the lower SNR of the data. This was done in a follow-up study in 1997, in which ictal dipole modeling was performed in 33 patients and consistent and distinct dipole patterns were found. In 9 patients of the 33, iEEG was available and the localization of the ictal dipole could be qualitatively correlated with localization based on the iEEG findings. Furthermore, 8 of the 9 patients studied intracranially underwent resective surgery and 7 of them were rendered seizure-free. The authors concluded that in the patient that was not seizure-free, the iEEG recording was misleading.

However, the ictal dipole could be correlated to the iEEG and it is not discussed how this affects the results. Nevertheless, the general results were promising. These results were also reported in [191] and with one extra iEEG patient in [192]. Up to now, these studies used the same dipole modeling strategy using a 3-shell spherical head model. They argued that the use of realistic, individual head models could improve the anatomical accuracy of the method. This is what they changed in their study in 2002, in which they prospectively investigated the clinical usefulness of ESI on ictal data [193]. In 14% of 100 patients, ictal ESI proved to be important in the presurgical decision-making process. The decision was mostly to avoid iEEG because the candidates appeared to be unsuitable for resection as the initial incongruency of visual inspection of the ictal EEG and MRI got confirmed by ictal ESI. It is, however, unknown whether these patients truly could not be helped with epilepsy surgery.

Assaf and Ebersole are other founding authors of EEG-based SOZ localization. In their study of 1997, they reconstructed ictal EEG of 40 patients with drug-resistant TLE by 19 fixed dipoles that represent specific cortical areas [187]. They correlated the most prominent source

at the first earliest recognizable ictal rhythm with the findings of iEEG, confirmed by seizure-freedom of the patients after surgery. Sensitivities between 36% and 66% and specificities between 92% and 96% for seizures with different onsets were reported. The method could reliably differentiate temporal lobe seizures of mesiobasal origin from those of lateral neocortical origin. The resolution of the algorithm was, however, limited to the 19 fixed locations of the dipoles. In a follow-up study using the same methodology in 75 patients who underwent anteromesial temporal lobectomy, they found three different ictal patterns [215]. Type 1 (16 patients) was associated with positive surgical outcome, whereas for type 2 (51 patients) and 3 (8 patients), this association could not be made. For type 2, however, the generating sources could be associated with surgical outcome and so the authors concluded that they could possibly be used as a predictor of temporal lobectomy.

In 1998, Mine et al. [207] applied dipole fitting using an individual 3-layered head model on the 10 ms around the peak of a spike close to the seizure onset in 10 or more seizures in two patients. Again, good correspondence between the localization of the dipoles and seizures recorded with iEEG was found. The patients were seizure-free after surgery targeting the SOZ found by iEEG. They confirmed this result in a follow-up study in 2002 for 9 patients [208].

Merlet and Gotman were the first to offer a more quantitative validation approach in 2001 [206]. They fitted a dipole to the ascending wave of an averaged ictal waveform and keeping this dipole fixed, but active, fitted a second one to the complete averaged ictal waveform. After this, they determined the distance between the most active dipole of these two and the most active iEEG contact. The dipole fitting was successful in 6/9 patients, and in 3/6, the distance to the most active iEEG contact was smaller than 10 mm. However, dipole fitting happened with a 4-shell spherical head model and the influence of the projection into the MRI space of the patient on the accuracy of the measured distance is unclear. Yet, the study proved that quantitative validation is possible and interesting.

These pioneering studies showed that ictal ESI is possible and that it can have a potential added value in the presurgical evaluation of epilepsy. The used methods are rather simple, the spatial resolution limited, and the validation often solely qualitative or descriptive. They only limitedly used the vast possibilities that became attainable due to increasing

computational power, which offered later studies the opportunity to use more complex methods offering higher spatial resolution and to offer more quantitative and rigorous validation. This is where we made the distinction between pioneering work and recent studies.

Recent studies

In more recent studies, authors tried to better tackle the challenges stated in the previous section. Better head models to improve ESI, better coping with artifactual data, improving the spatial resolution of EEG and ESI by including more electrodes in the recording and the analysis are examples of this. Furthermore, more attention was paid to evaluate the accuracy of ictal ESI.

More complex head models and/or inverse solutions A "software probe" for ictal activity was developed in 2000 by Kobayashi et al. [200]. This was the first study using a more complex inverse solution to characterize ictal EEG epochs of 2.56 s. The approach was based on the singular value decomposition of the data into spatiotemporal components of which a some are recombined into a new component, still orthogonal to the remaining components. This was applied on 10 seizures of 3 patients with TLE and a source corresponding to the region of seizure activity in iEEG recordings was found in every case, even when seizure activity was still not visually identifiable in the scalp EEG. When using more simple inverse models, seizure activity could not be correctly detected when it was not apparent in the scalp EEG.

In 2009, Rullmann et al. conducted the first study to show the possibility of using a complex head model for ictal ESI and to investigate the influence of more simple head models on several inverse techniques [210]. They compared dipole scanning, minimum norm estimation, a rotation dipole fit (fixed location), a moving dipole fit (fixed orientation), and Standardized Low Resolution Electromagnetic Tomography (sLORETA) by applying it on the two peak samples of the average of 9 spikes during a seizure of a patient with a brain tumor. After resection of the tumor, the patient was rendered seizure-free. A realistic, anisotropic model was used which modeled scalp, skull, CSF, white matter, gray matter and a lesion (cavity of a previously resected brain tumor and the current brain tumor, which resided in

the cavity, see Fig. 4.3). The source space was limited to gray and white matter, without the lesion. All methods were able to localize the SOZ on the border of the lesion (not incorporated in source space) and on the border of the iEEG electrodes which mainly received ictal discharges. They also made a comparison with more simple head models and found that it is most important to correctly model CSF and skull. Another study that compared different inverse solution was performed in 2010 by Koessler et al. [201]. They applied a moving dipole approach, a rotating dipole approach, Multiple Signal Classification (MUSIC), LORETA and sLORETA on ictal activities lasting from a few milliseconds up to one second depending on the kind of activity. Unlike Rullmann et al., they found differing results for the different inverse techniques, see for example Fig. 4.4. They reported concordance on the sublobar level with iEEG in 9/10 patients using the dipole fitting approaches, 7/10 using MUSIC or LORETA and 5/10 using sLORETA. For every patient, however, at least one of the methods was concordant with iEEG, stressing the differences between the inverse techniques even more. No possible explanation for this difference was offered. Also Kovac et al. used different inverse solutions, but with the purpose to investigate whether ESI could provide lateralization in 8 frontal lobe epilepsy patients of whom the ictal scalp EEG was nonlateralizing, as correct lateralization in these difficult cases could be very informative for the clinicians [202]. They were able to obtain a clear lateralization of the seizures that could not be lateralized by visual inspection of the EEG in 47% using ECD and in 29% using distributed solutions. In these cases, the lateralization was correct in 75% of the seizures with ECD and in 60-80% for the distributed solutions.

Previous studies mainly compared equivalent dipole techniques with distributed solutions using LORETA (like) techniques, Habib et al. offered a more extensive comparison between distributed solutions, using Weighted Minimum Norm Estimates (WMNE), dynamic Statistical Parametric Mapping (dSPM) and sLORETA [197]. In 8 patients, they applied these techniques to the peak of averaged ictal spikes. WMNE was concordant on the lobe level with SPECT foci (which were congruent with the clinical semiology) in 7/8 patients using WMNE and in all patients using dPSM or sLORETA.

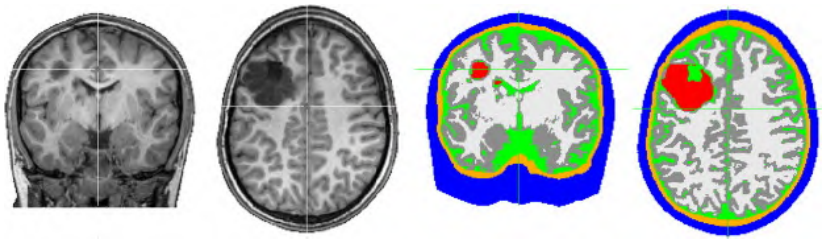

Figure 4.3: Illustration of the advanced individual head model used by Rullmann et al., in which a brain lesion is segmented separately. There are six tissue types: red indicates the lesion, dark gray the gray matter, light gray the white matter, green the CSF, orange the skull and blue indicates the skin. Figure from [210].

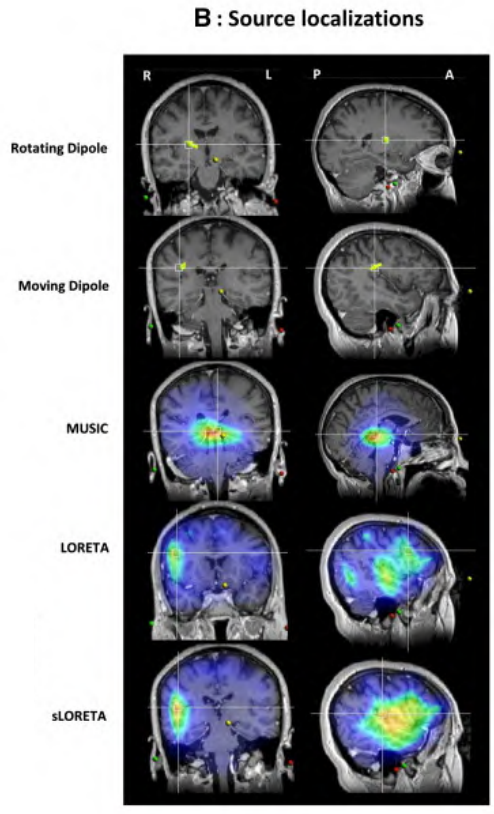

Figure 4.4: Some patients showed clearly different solutions when different inverse techniques were used in Koessler et al. [201]

Decomposition and other techniques to better represent the ictal data Worrell et al. were the first in 2000 to not apply ESI on the (averaged) temporal data directly [212]. They applied LORETA using a simple 3-shell spherical head model on a scalp map determined by phase-encoded frequency spectral analysis (PEFSA) [213]. Using PEFSA, they determined the optimal synchronized scalp map that best describes the measured scalp potentials during an epoch of 3 s at seizure onset, at the seizure frequency. This offered an opportunity to isolate the ictal generator from other activity. The LORETA source map maximum was concordant on the lobar level in 9/10 patients. Lantz et al. offered another technique which created a new data matrix based on the peaks in the global field power during the seizure [203]. This new data matrix was segmented into a limited number of topographies and the most important (most occurring) topographies were inverted using wMNE and a template head model. They found one dominant topography in 7/9 patients and the source map maximum of this topography corresponded qualitatively with the iEEG in 6 patients out of these 7.

The usefulness of decomposition techniques to clean artifactual EEG data was first investigated by Hallez et al. in 2009 [198]. Blind Source Separation based on Canonical Correlation (BSS-CCA) and Independent Component Analysis with Spatial Constraints (SCICA) were used to visually remove artifactual (both muscle and eye artifacts) components from the EEG. This improved the dipoles estimated by RAP-MUSIC (using a template 4-layered Finite Difference Method (FDM) head model) in 5 of the 8 patients, meaning that the distance to ictal SPECT activation became smaller. However, perfect correlation between the source estimations and ictal SPECT was not obtained, since the median distance was larger than 20 mm in 7/8 patients. Moreover, validation was based on ictal SPECT hyperperfusion clusters, which have low temporal resolution. Therefore, they often display not only the ictal onset zone but also regions of ictal propagation [216]. Another interesting approach for SOZ localization is to first decompose the ictal EEG data to isolate seizure components, e.g. with ICA, and then integrate ESI with a recombination approach. This is done by Yang et al. (2011), where this Dynamic Seizure Imaging (DSI) technique (see Fig. 4.5) using LORETA outperformed ESI on the raw ictal EEG data [214]. DSI identified the SOZ in good correlation with the epileptogenic zone resected during surgery (with good outcome) or defined by iEEG/SPECT imaging methods in 17 seizures of 8 patients

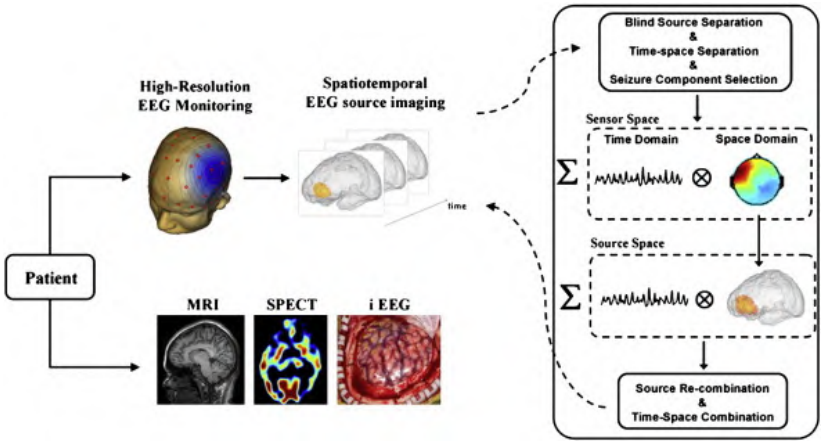

Figure 4.5: Illustration of the Dynamic Seizure Imaging Concept. The ictal data is decomposed and the components containing seizure activity are transformed individually to source space, in which they are recombined. Figure from [214].

recorded with 76 electrodes. The distance to the respective ground truth remained below 11 mm. Yet, false positives were found in two seizures. In a follow-up study, Lu et al. applied the same approach (however, using the cortical current density model and minimum norm estimation as inverse solution methods) on 32-channel EEG of 9 pediatric patients [204]. In 7 out of 9 patients, the SOZ was estimated within the resected zone (RZ) and in the other two patients, the estimation was close to the RZ. However, 3 patients had outcome Engel IV or V, and one Engel III, so the value of the RZ as ground truth is questionable. Yet, there was also good correspondence with iEEG that was recorded in 7 patients. DSI also localized multiple foci in later seizure propagation that were also concordant with propagation on iEEG.

While Lu et al. were the first to make the transition to pediatric patients, Despotovic et al. took it a step further to neonates with perinatal brain lesions [194]. One challenge in ESI in neonates is the fact that fewer EEG electrodes fit on a baby's head (17 in this study), but the main difficulty is their different head geometry and different tissue conductivity w.r.t. adults. Therefore, template head models, based on the adult brain, are not suited. Making individual head models requires the segmentation of the different tissues in the head based on MRI scans. Brain segmentation techniques, however, have been mainly developed for adults and are not

applicable to neonates. Despotovic et al. proposed a technique based on atlas-free segmentation and a brain extraction algorithm and used it to construct neonatal head models including scalp, skull (with modeling of the fontanelle), CSF and brain. ESI was applied using a single dipole fit on 45 seizures of 10 neonatal patients with clear focal onset. To increase the SNR, ictal spikes were detected during the seizure and represented by a single spatial topography using parallel factor analysis (PARAFAC) [217, 218]. In 9/10 patients, most seizures were localized within 5 mm of the closest lesion border and all seizures were localized within 15 mm. In one patient, there was no good correspondence with the lesion for all seizures.

Instead of decomposing the EEG data in sensor space, Pellegrino et al. applied Principal Component Analysis (PCA) on the spatiotemporal source maps obtained after inverting epochs starting 3 s before seizure onset until 5 s after using an inverse approach called wavelet-based Maximum Entropy on the Mean (wMEM), centered on the frequency band showing the strongest power change [209]. They selected the spatial map corresponding to the first PCA component as an estimation of the SOZ and found sublobar concordance in 9 out of 14 seizures or 6 out of 8 patients. The median distance of the source map maximum to the clinically defined SOZ based on iEEG was 11 mm in a range of 0–89 mm. Significantly better results were found for MSI. Yet, as discussed, ictal MEG data are rare.

High-density EEG Research before 2010 used between 21 and 27 electrodes for EEG recording. In 2010, the first study using high-density EEG with 256 channels for ictal ESI was reported [199]. Holmes et al. applied LAURA on the ictal onsets of 10 patients (5 Engel I after surgery, 3 Engel II, 1 Engel III, 1 non-operated patient) and found (sub)lobar concordance between the ESI result and iEEG electrodes.

The number of electrodes is not always increased to 256. Examples of studies using 64 electrodes can be found as well. In 2016, Akdeniz used 64-channel EEG to reconstruct the time-point of seizure onset using LORETA and found that the maximum of the LORETA solution was concordant with the RZ in 13/13 patients that were seizure-free after surgery [186]. For two patients with Engel III surgical outcome, the SOZ estimation pointed at a region adjacent to the RZ. The individual 3-layered BEM head models, however, were based on the post-operative

MRI of the patients and it is unknown whether this influenced the head modeling and/or the results. Also Beniczky et al. used 64-channel EEG to analyze 38 seizures of 22 patients [189]. Several inverse solutions were applied on the averaged ictal onset waveforms to investigate their agreement: dipole fitting, Classical LORETA Recursively Applied (CLARA), CLARA restricted to the cortical surface and cortex-restrained Minimum Norm Estimates (MNE). In 13/22 patients all inverse methods agreed on the localization on sublobar level, and in 6/22 there was agreement between all-but-one methods. Cortical CLARA and dipole fitting yielded the highest accuracy and were concordant at the sublobar level with the clinically defined SOZ or the RZ (in 20 operated patients) in 77% of the patients (up to 93% in case of the 14 seizure-free patients). They noted, however, that agreement between all methods did not necessarily imply accuracy of localization.

Evaluation of the diagnostic accuracy One study by Beniczky et al. in 2013 paid special attention to the validation of its diagnostic accuracy and used the STARD criteria [219] as a guideline to design their study [188]. ESI was performed in a standardized way in 42 consecutive patients fulfilling inclusion criteria. A voltage map was created for every time-point of an averaged ictal waveform of one seizure (per seizure type) for every patient. An anatomically constrained head model in combination with LAURA was used to reconstruct the latest time-point before the voltage maps changed over the course of the waveform; or in case of a constant voltage map, the peak of the waveform was used. In 33/42 patients, a reference standard, determined by the epilepsy team, could be determined and sublobar concordance between the source map maximum and this reference standard was assessed. Sensitivity and specificity were 69.7% and 75.7%, respectively. 20 patients underwent surgery and 16 patients became seizure free, resulting in a positive predictive value (PPV) of 92% and a negative predictive value (NPV) of 42.8%. They were able to prove the clinical value of ictal ESI in a blinded study designed following the STARD criteria and were thus the first to report sensitivity, specificity, PPV and NPV.

4.4.2 ESI and connectivity analysis to localize the SOZ

As already mentioned, the studies in the previous section did not explicitly take into account that epilepsy is a network disease. In what

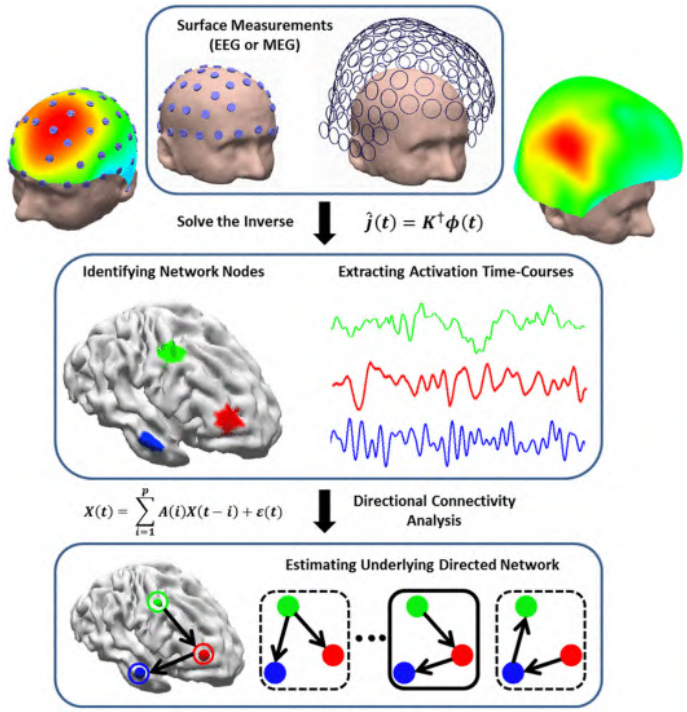

Figure 4.6: Illustration of the concept of combining ESI and connectivity analysis. ESI is used to identify network nodes inside the brain based on scalp EEG recordings. ESI also estimates the time-series associated with these network nodes. Connectivity analysis investigates the network between the found network nodes. Figure from [211].

follows, we will give an overview of the studies aimed at SOZ localization using ESI and connectivity analysis. The concept of ESI in combination with connectivity analysis is shown in Fig. 4.6 [211].

The Department of Biomedical Engineering of the University of Minnesota was the first to combine ESI and subsequent functional connectivity analysis to estimate the SOZ in two studies published in 2007 by Ding et al. [195] and 2012 by Lu et al. [205]. Quasi-stationary ictal epochs lasting 3 s directly after the onset of a seizure were selected and were reconstructed using first principle vector (FINE) spatiotemporal ESI, with individual 3-layered realistic head models. Functional connectivity between the estimated time-series of the identified sources was calculated using the Directed Transfer Function (DTF). Spatiotemporal localized sources having significant directional

DTF values to other sources were considered as the SOZ. Ding et al. used EEG recordings with 32 electrodes of 5 patients and analyzed a total of 20 seizures. They estimated the SOZ within 15 mm of the presumed EZ, based on a lesion visible on MRI scans or confirmed by SPECT images. It is, however, unreported whether patients had resective or disconnective surgery and if so, what the outcome of this procedure was. There is also no record of intracranial recordings to confirm the results. As a consequence, it remains unknown whether the MRI lesions or SPECT images referred to the true SOZ. Lu et al. studied 10 patients, 23 seizures and compared 32 and 76 electrode setups. They found better localizing results for the higher number of electrodes. In this follow-up study, patients underwent epilepsy surgery with ILAE 1 or 2 outcome. Therefore, the resected zone (RZ) as seen on the postoperative MRI was used to validate the method. The SOZ was estimated within 10 mm of the RZ in 16/23 seizures, within 20 mm in 22/23 seizures, and within 25 mm in all analyzed seizures.

In another study of this group, Sohrabpour et al. used DSI [214] in combination with Adaptive Directed Transfer Function (ADTF) analysis to study 1 patient who had 3 seizures during 76-channel EEG recording [211]. Good concordance was found between the source with the highest ADTF values and the RZ, as well as with the SOZ defined by iEEG recordings. Validation of this technique in more patients is necessary.

Elshoff et al. used ESI to localize active sources during a seizure and used subsequent connectivity analysis to describe the network evolvement during the seizure [196]. Eleven patients that had surgery with Engel class I or IIa outcome were investigated. They selected EEG epochs (38-50 electrodes) lasting maximally 10 s around seizure onset and reconstructed these epochs in source space using a beamforming technique called Dynamic Imaging of Coherent Sources (DICS). The head of the patients was modeled by a five-layered concentric-spheres model, of which the layers represented the white matter, gray matter, cerebrospinal fluid, skull and scalp. In 8/11 patients that were rendered seizure-free after surgery, the first two sources identified by DICS were concordant on the sublobar level with the RZ. For 3/11 patients, who were not seizure-free, the first two sources were not concordant with the RZ. Next, they applied functional connectivity analysis using the renormalized Partial Directed Coherence (rPDC) and found that the network at the onset of the seizure had a star-like topography, with the SOZ as the main hub, while the network in the middle of the seizure

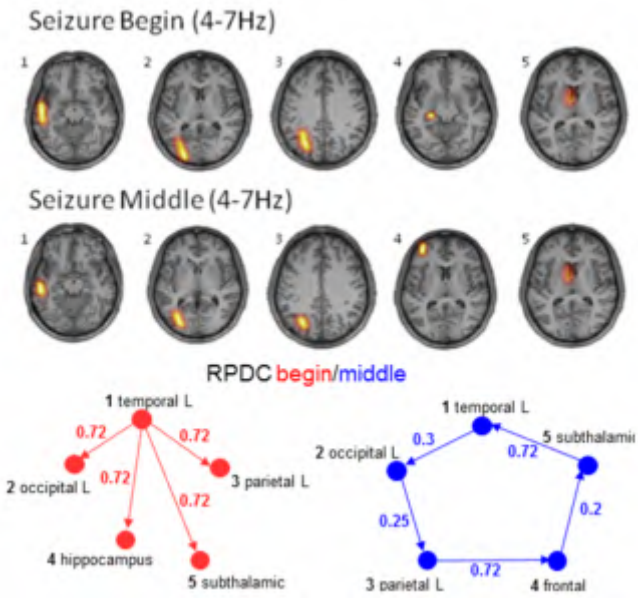

Figure 4.7: Elshoff et al. found a star-shaped network during the onset of the seizure, while a circular network was found during the middle of the seizure [196].

was rather circular. This is shown in Fig. 4.7. They provided the first proof that an epileptic network can dynamically change over the course of a seizure. Yet, only one seizure per patient was analyzed, so no information about the robustness of this finding within patients was offered.

The studies above used functional connectivity to model the information flow in the brain. Klamer et al. were the first to use effective connectivity analysis to localize the SOZ in 2015 [185]. They reported a case study about a patient with musicogenic epilepsy. 256-channel EEG was simultaneously recorded with MEG, during which seizures were triggered with rap music. The EEG was reconstructed at three time points: at the onset, the midpoint of the ascending phase and at maximum negativity of the initial spike of the seizure. ESI was done using a locally spherical head model with anatomical constraints (LSMAC, a spherical head model of which the radius is adapted to the position of every single electrode) derived from the individual MRI and LORETA.

Two ROIs, one frontal and one right mesiotemporal, were chosen as possible SOZ that corresponded with the inverse solution. The seizure initiating spikes of all recorded seizures were averaged and the segment between the onset time and the maximum negativity of the averaged spike was considered for Dynamic Causal modeling (DCM) in SPM8. The parameters of two models were estimated, each with one ROI as autonomous input over the other one, with a modulatory effect of the seizure on the connection of the two ROIs. Bayesian model comparison selected the model in which the right mesiotemporal region drives the frontal ROI, and so the right mesiotemporal region was selected as SOZ. This was confirmed by intracranial recordings, which located the SOZ in the right hippocampus.

4.5 Outlook

We have shown that current state-of-the-art methodologies can provide a more accurate and a more objective interpretation of ictal EEG over visual inspection thanks to research that started over more than 2 decades ago. Despite many promising results, the methods have not found their way to clinical practice yet (except for one prospective study of Boon et al. [193]) because of several reasons. The first is that, despite the general consensus about the need for a good head model for ESI, there is a remaining discussion about how accurate the head model should be and which inverse technique is best for the application. Also in ESI + connectivity analysis studies, it is not clear yet which combination of methods could serve the goal of SOZ localization best. Next, different studies use different techniques to deal with the low SNR of ictal EEG signals and the influence of these different techniques on the performance is not yet quantitatively compared. While some researchers claim that it is important to include the seizure onset time in the analyzed epoch, other studies state data quality is more important than capturing the start of the seizure. Although most methods are almost completely objective and some probably need minimal human intervention, some initial subjective step is often needed to start the analysis, e.g. the selection of an epoch, spikes to average or the frequency band of interest. This increases the threshold to be adopted in clinical practice. Even though there are still many uncertainties and despite the lack of a perfect

gold standard in the retrospective studies, we believe this research field is on the right track.

More research is needed to replicate, compare and extend prior findings. This should be combined with validation in larger patient groups that are preferably heterogeneous, so that possible links between patient characteristics and performance of the algorithms can be found and investigated. Preferably, more prospective studies and studies blinded to the patient's clinical data should be performed.

We can conclude that extensive validation and probably standardization of the methods are key to future research in order to reach clinical practice.

4.6 Original Contributions

This review chapter is resulted in a paper that has been submitted to the A1 journal NeuroImage: Clinical [220].

5
Seizure onset zone localization from high-density EEG

5.1 Introduction

In the previous chapter, we reviewed noninvasive EEG-based Seizure Onset Zone (SOZ) localization based on ictal EEG recordings. The main arguments for the importance of EEG-based SOZ localization were that SOZ localization is crucial in the presurgical evaluation of epilepsy and that EEG is a relatively simple, inexpensive and safe technique to directly measure the abnormal electrical activity during a seizure. Methods to localize the SOZ based on noninvasive EEG are, however, not trivial because of the low spatial resolution of EEG, the fact that epilepsy is a network disease and the often low quality of ictal EEG data. We discussed how the first challenge can be tackled by incorporating more electrodes in the EEG recording setup and/or by using EEG Source Imaging (ESI). The second challenge could be handled using connectivity analysis and we also offered some possible strategies to deal with the third challenge.

In this chapter, we investigate a combination of ESI and functional connectivity analysis to study the added value of using functional connectivity analysis compared to the more traditional method that uses power after ESI to localize the SOZ. To assess connectivity, we will use a Granger causality based measure, the spectrum-weighted Adaptive Directed Transfer Function (swADTF), which was introduced in Chapter 3. The swADTF has already been successfully applied on ictal iEEG [153]. Here, we extend the method to noninvasive ictal EEG.

First, simulated ictal high-density (hd) EEG data is used to verify the method. Next, we validate the approach in five patients. Finally, we perform the analysis on subsets of the electrodes to mimic lower-density setups to investigate the influence of the number of electrodes on the performance of the proposed algorithm.

5.2 From EEG to SOZ

An overview of the presented approach to get from the EEG data to a SOZ estimation is shown in Fig.5.1-5.3. Example data of one patient is used for illustration purposes. To summarize, we selected 3 seconds of ictal hd-EEG beginning at the marked seizure onset and reconstructed the sources generating the ictal brain activity with ESI. In the inverse solution, we selected local hotspots of higher activity. In the example, this resulted in 8 sources. As no constraints on the orientation of the sources were applied in the reconstruction, each of these 8 sources is represented by three time series, for the x, y and z direction. Therefore, we used Singular Value Decomposition (SVD) to represent each source with one time series [115]. Using these time series, functional connectivity analysis was applied with the swADTF [153]. Next, the swADTF values were summed to get the outdegree of every source as a measure for the total outgoing information flow from a source. The source with the highest outdegree, source 2 in the example (Fig. 5.3(g)), was selected as SOZ. This estimated SOZ was compared to the Resected Zone (RZ) of the patient and also to the source with highest power after ESI, i.e. source 3 (Fig. 5.3(h)). In the following sections, we present every step of this method in detail.

5.2.1 EEG preprocessing

The data was common average referenced and band-pass filtered between 1 and 30 Hz, to remove baseline drift and to reduce high frequency noise resulting from movement artifacts. An extra notch filter at 50 Hz was applied to filter out remaining power line noise. In patient 4 and 5, ICA was applied to remove remaining artifact [221].

(a) Ictal EEG epoch

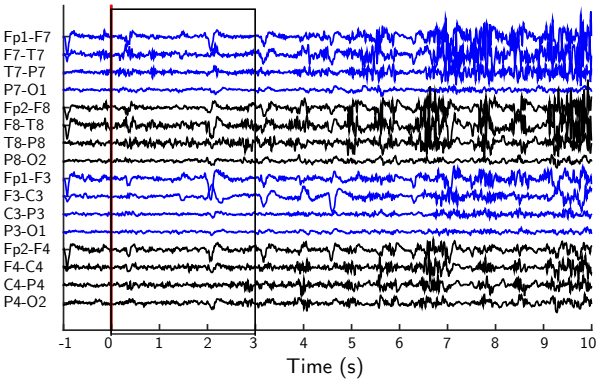

(b) ESI

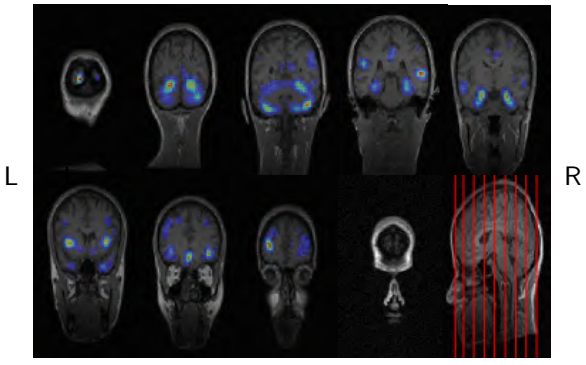

...

Figure 5.1: Overview of the analysis pipeline (part 1), in which example data of one patient is used. (a) Selection and preprocessing of an ictal hd-epoch. (b) Result of EEG source imaging overlaid on MRI.

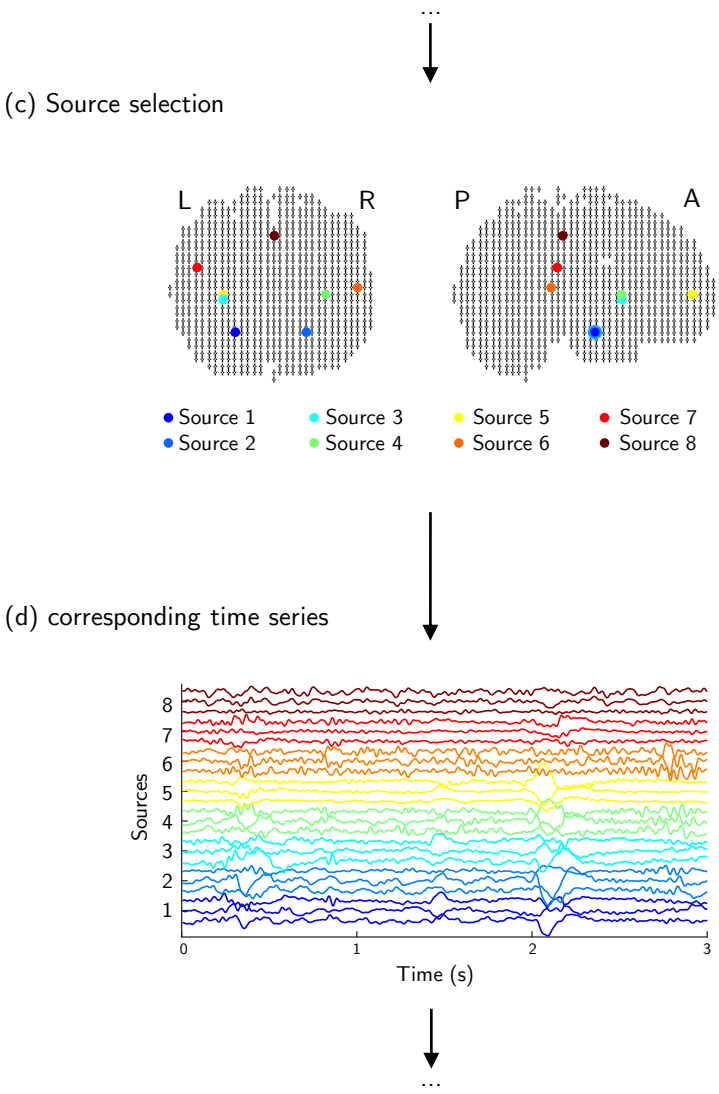

Figure 5.2: Overview of the analysis pipeline (part 2). (c) Source selection after ESI shown in solution space and (d) time series for x, y and z direction for these sources.

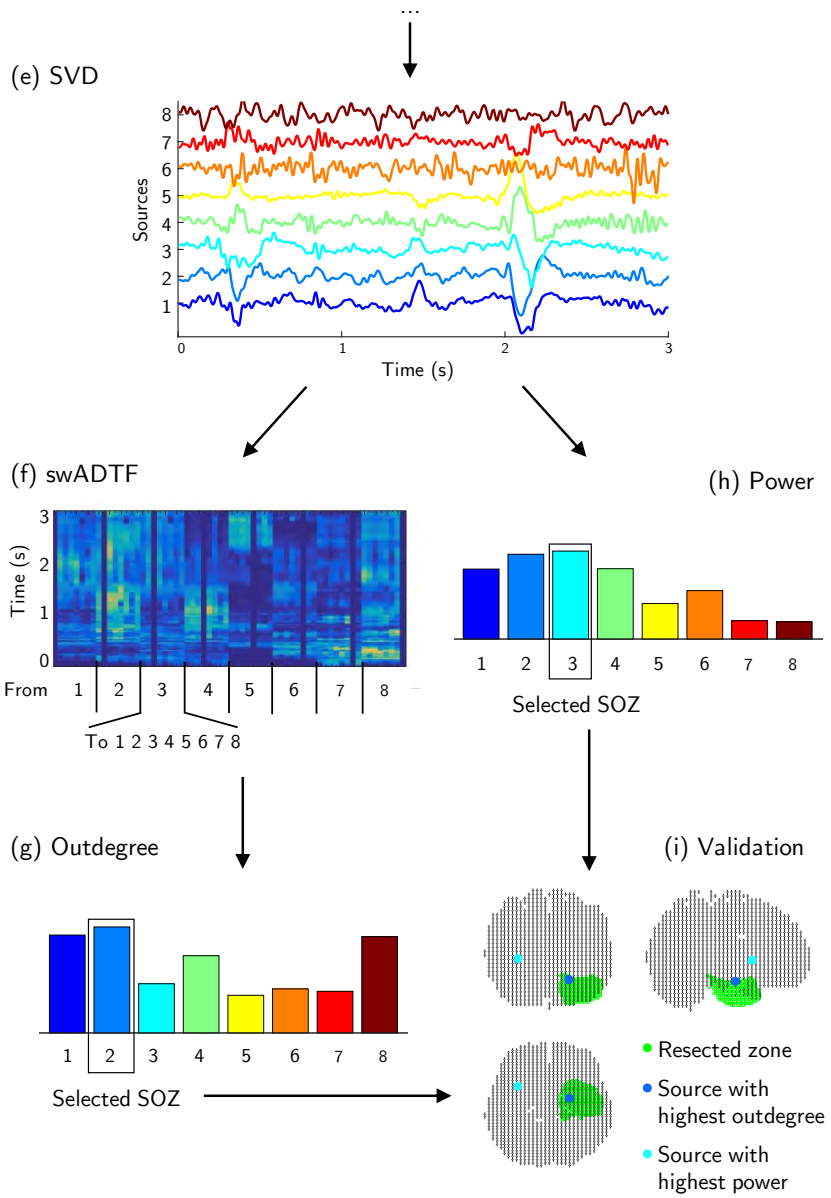

Figure 5.3: Overview of the analysis pipeline (part 3). (e) SVD to represent each selected source by one time series. (f) swADTF values over time (summed in the 3-30 Hz frequency band) for every source to every other source. (g) Summation of the swADTF values leads to the outdegree. The source with the highest outdegree is selected as estimation for the SOZ. (h) Another option is to take the source with highest power as SOZ estimation. (i) Validation by comparison to the segmented resected zone.

5.2.2 EEG source imaging

To reconstruct the sources generating the ictal epochs, ESI was done. For the forward model, patient-specific head models were constructed based on the Finite Difference Method (FDM) [222]. Air, scalp, skull, cerebrospinal fluid (CSF), gray and white matter were segmented from the individual pre-operative T1-weighted MRI of the patient (resliced to voxels of $1 \times 1 \times 1$ mm^3) using the Statistical Parametric Mapping (SPM12) toolbox (`http://www.fil.ion.ucl.ac.uk/spm`). The segmented volumes were combined into a single head model with 6 tissue classes, and following conductivity values were assigned to the different tissues: 0.33 S/m for gray matter, 0.14 S/m for white matter, 1.79 S/m for CSF [223], 0.33/25 S/m = 0.0132 S/m for the skull and 0.33 S/m for scalp [100, 105], and 0 S/m for air. The solution space was created based on the segmented gray matter. Solution Points (SPs) were uniformly distributed in the gray matter of the patient with a grid spacing of 4 mm, which resulted in approximately 8000 SP for every patient. These SPs formed the central nodes of the dipole model, so we ensured that at least 2 voxels of gray matter were left open between the SPs and the boundaries with other tissues in all directions, in order to keep the dipoles restricted to the gray matter. An in-house implementation of the Low Resolution Electromagnetic Tomography (LORETA) algorithm [123] was used to solve the inverse problem. As explained in section 3.1.3.2, this is a distributed linear method that is based on the physiological assumption that neighboring neurons are simultaneously and synchronously activated, which practically means that the solution should be as smooth as possible. Since we work with a cortical volume and not with a cortical sheet, perpendicularity to the cortical surface is rather ambiguous and therefore we did not fix the orientation of the sources beforehand, as is often done [23, 224]. Because we did not put any constraints on dipole orientation, every SP is represented by 3 time series, one for each orthogonal spatial direction (x, y, z) after solving the inverse problem.

5.2.3 Source selection and time series

In a typical LORETA solution, the brain activity is smooth throughout the volume of the brain with one or more hotspots of higher activity that vary in intensity and that may overlap partially. During an epileptic

seizure, several brain regions become active. We assume that some of the hotspots we obtain after ESI correspond with the active regions in the network. To determine these hotspots, we calculated the sphere power of every SP. We defined the sphere power of a certain SP to be the mean power of all SPs lying in a sphere centred around that certain SP. We considered the spheres with no neighbors with higher sphere power to be the center of a hotspot. The SP that had the highest power in that sphere was selected and called a source. Sources in the cerebellum were excluded. By varying the radius of the sphere, more or less sources could be found. Two extreme cases can be distinguished: when the radius is larger than the largest distance between two SPs, only one SP will be selected, i.e. the one corresponding with the maximal power, and connectivity analysis cannot be done. In the other extreme, when the radius is smaller than the resolution of the grid (here 4 mm), all sources will be selected. In this case, the subsequent connectivity analysis would still be computationally feasible with the advent of high-performance clusters. However, this situation is to be avoided because it might bias the connectivity analysis since LORETA provides a solution in which neighboring sources are correlated, and thus possibly introducing spurious connections. In this study, we want to localize the SOZ and we are not looking for whole brain functional connectivity patterns at all spatial scales (from mm to cm), but rather for those in a selected range of distances. Therefore, we limit the radius to be in a range that does not make the search area unnecessarily large, while not excluding possible network nodes (i.e. not excluding possibly relevant local maxima). We found good correspondence between the LORETA solution and the selected sources when a radius between 15 and 25 mm was chosen. We eventually used a radius of 20 mm as this provided overall best results and for which the number of selected sources varied between 4 and 13 for all patients during the analyzed ictal epoch.

Suppose that K sources were selected. As we did not impose constraints on dipole orientation, the activity in each source k of the K selected sources can be represented by a matrix $\mathbf{F}_k \in \mathbb{R}^{3\times N}$ for $k = 1 \dots K$, with N the number of time samples of the epoch. Each row of the matrix corresponds with an orthogonal spatial direction (x, y, z). We used singular value decomposition (SVD) to represent each source by a single time series $\mathbf{s}_k \in \mathbb{R}^N$, associated with the largest singular value of the SVD [115]. In SVD, there exists an intrinsic sign indeterminacy and sign flips might occur over sources. This is, however, not a problem

because the subsequent connectivity analysis (see section 5.2.4), is mathematically not dependent on the sign of the signals.

5.2.4 Functional connectivity analysis

Functional connectivity analysis was used to estimate which source is the most important, i.e. the driver behind the epileptic network. We used a Granger causality based measure to investigate the network, more specifically the spectrum-weighted adaptive directed transfer function (swADTF). The general concepts of this technique have been introduced by van Mierlo et al. in 2013 [153], and were explained in section 3.2.3.3 of this dissertation. In summary, the source signals $\mathbf{s}_k$ were modeled with a time-varying multivariate autoregressive (TVAR) model of which the coefficients were estimated using the Kalman filtering algorithm [148, 149]. The Kalman filtering algorithm is mainly influenced by the update coefficient (UC), which expresses how quickly the TVAR model coefficients will adapt to changes in the dataset. This way it provides a balance between the amount of signal and the amount of noise that is modelled. We chose a low value of 10^{-4} for the UC, as we only want to see connections that are maintained in the data and we are not interested in modelling abrupt changes. The smoothing factor was set to 100. Based on the transfer matrix $\mathbf{H}(f,t)$ of the TVAR model, the swADTF can be calculated to investigate the causal relation from source signal $\mathbf{s}_j$ to source signal $\mathbf{s}_i$ for a predefined frequency band at time t:

$$\mathrm{swADTF}_{ij}(t) = \frac{\sum_{f=f_1}^{f_2} |H_{ij}(f,t)|^2 \sum_{l=1}^{K} |H_{jl}(f,t)|^2}{\sum_{k=1}^{K} \sum_{f'=f_1}^{f_2} |H_{ik}(f',t)|^2 \sum_{s=1}^{K} |H_{ks}(f',t)|^2} \tag{5.1}$$

5.2.5 SOZ localization

The swADTF values were calculated for every source $\mathbf{s}_j$ to every other source $\mathbf{s}_i$ at every time point of the epoch in the frequency band 3-30 Hz, as this band contained the fundamental seizure frequency noticed in the EEG. For every source $\mathbf{s}_j$, we calculated the outdegree (OD) (see section 3.2.4) as the sum of the swADTF values to all other sources over

time:

$$\mathrm{OD}_j = \sum_{k=1}^{K} \sum_{t=1}^{T} \mathrm{swADTF}_{kj}(t) \tag{5.2}$$

in which we defined $\mathrm{swADTF}_{jj} = 0$. The outdegree is a measure for the total outgoing information flow from a source to all the other sources. The source with the highest outdegree was assumed to drive the epileptic network active during the seizure and was selected as SOZ.

5.3 Performance in simulated data

5.3.1 Generation of simulated data

Ictal EEG epochs of 3 s were constructed by forward projection of a simulated epileptic network in the brain. The details on the forward models used for this purpose, can be found in section 5.2.2. The epileptic network consisted of three nodes, of which the configuration can be seen in Fig. 5.4(a). The seizure originated in node 1 and propagated to node 3 via node 2. In node 1, the driver of the network, epileptic activity was mimicked by a sinusoid of decreasing frequency from 12 Hz at t = 0 s to 8 Hz at t = 3 s and its first two harmonics. Gaussian noise with 1/f spectral behaviour was added with a signal-to-noise ratio (SNR) of 5 dB to account for background brain activity. The seizure propagated to the second node with a delay of 20 ms. Extra Gaussian 1/f noise is added with an SNR of 5dB. The resulting signal is delayed with 32 ms to node 3 and again Gaussian 1/f noise is added. The three signals were constructed with a sample frequency of 250 Hz, and an example can be seen in Fig. 5.4(b).

Every node corresponded with a patch in the brain, which was constructed by growing a region in the gray matter around a randomly chosen seedpoint, until the patch enclosed 100 gridpoints of a uniform cubic grid with a spacing of 4 mm (see also section 5.2.2). This resulted in a mean volume of 8.04 cm^3 per patch. A minimal distance of 15 mm between every two patches was guaranteed. An example of three patches can be seen in Fig. 5.5(a). The activity in the patches was smoothed towards the borders in order to obtain a three-dimensional Gaussian-shaped power distribution to avoid abrupt power level changes, since

neighboring neurons tend to synchronize [225], giving rise to a smooth activity distribution. The background brain activity outside the patches was set to Gaussian 1/f noise with an SNR of 5 dB with respect to the epileptic signal in the first node. The brain activity in source space was projected to sensor space to obtain hd-EEG with 204 channels, this can be seen in Fig. 5.5(b).

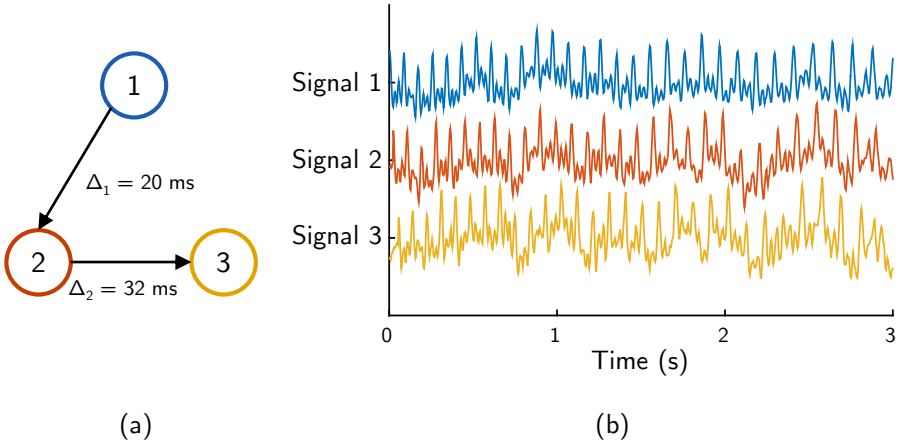

Figure 5.4: (a) Configuration of the simulated epileptic network. Source 1 is the overall driver. (b) An example of the signals that mimic epileptic activity corresponding to the three nodes of the network.

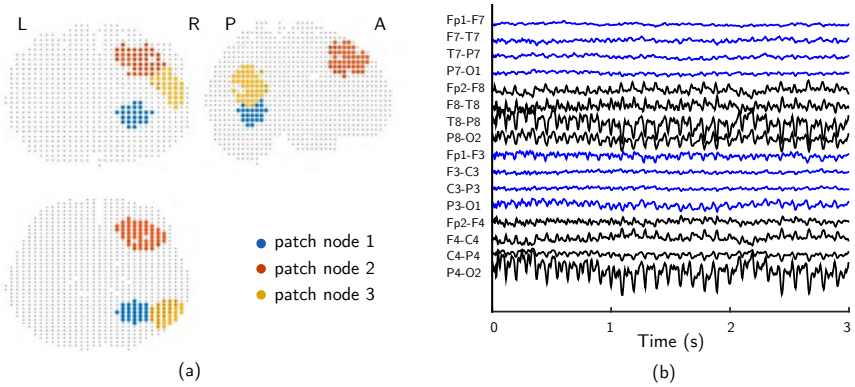

Figure 5.5: (a) Example of three randomly located epileptic patches in the brain, corresponding to the nodes of the network. (b) Montage of the resulting EEG after projection of the epileptic brain activity to sensor space.

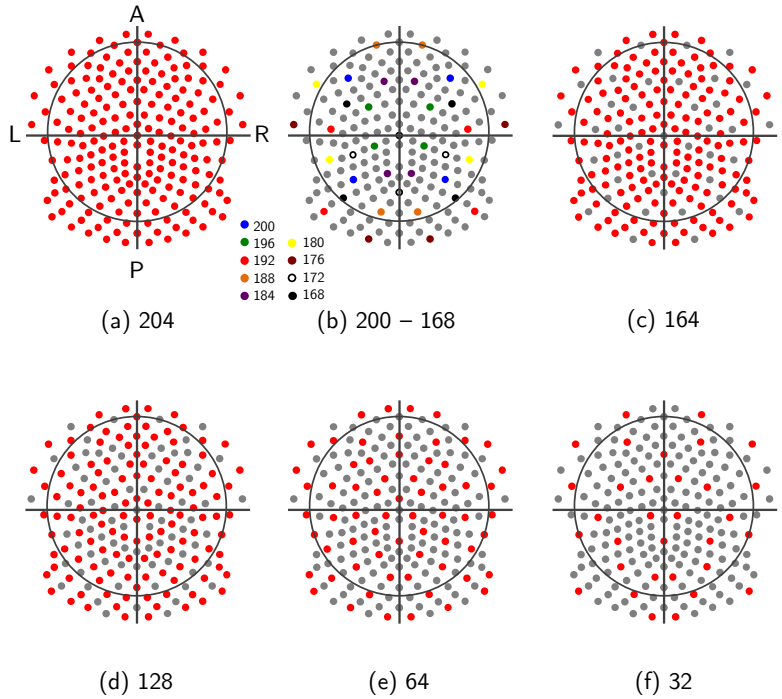

Figure 5.6: The different used electrode setups: (a) original 204 electrode setup, (b) the electrodes that were subsequently removed to obtain setups of 200-168 electrodes, (c) subset with 164 electrodes (red), (d) 128 electrodes, (e) 64 electrodes and (f) 32 electrodes. L left, R right, A anterior, P posterior.

Subsets of 200, 196, 192, 188, 184, 180, 176, 172, 168 and 164 electrodes were created by consecutive exclusion of 4 electrodes, while keeping the electrode distribution as uniform as possible. Additionally, subsets of 128, 64 and 32 electrodes were created to mimic setups that are more common in clinical practice. The resulting electrode configurations can be seen in Fig. 5.6.

5.3.2 Evaluation of the simulated data

Using the forward models of 5 patients (see section 5.4, we simulated 200 ictal hd-EEG epochs of 3 seconds, resulting in a dataset of 1000 unique epochs. For all these epochs and all electrode setups, we tried to localize the driving patch of the simulated epileptic network. We set the model order of the TVAR model fixed to 10 (= 40 ms),

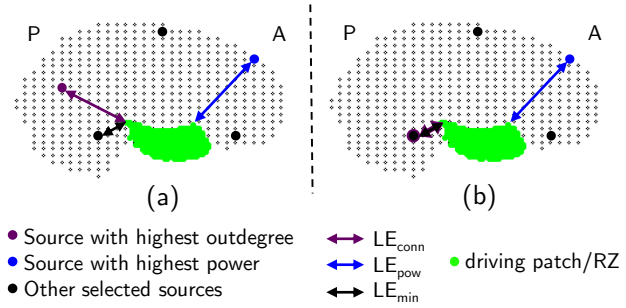

Figure 5.7: Illustration of the different localization errors. LE_{conn} = the Euclidean distance between the source with the highest outdegree and the driving patch in the simulated data or the RZ in the patient data, LE_{pow} = the Euclidean distance between the source with the highest power and the driving patch/RZ, and LE_{min} = the Euclidean distance between the source closest to the driving patch/RZ and the driving patch/RZ. (a) In this case $LE_{pow} > LE_{conn} > LE_{min}$. (b) The localization errors can be equal to each other. In this case $LE_{conn} = LE_{min}$, meaning that our method selected the best possible source to estimate the SOZ. A = anterior, P = posterior.

to minimize computational demand, following the ranges that are presented in literature [150, 152, 153, 226]. To evaluate the performance of the algorithm, the localization error (LE_{conn}) was determined as the Euclidean distance between the border of the driving patch and the estimated SOZ, i.e. the source with the highest outdegree. If the selected SOZ was in the driving patch, the LE was 0 mm. LE_{conn} was then compared to the shortest distance between the driving patch and the source with the highest power (LE_{pow}) after ESI, to see whether connectivity analysis can provide extra information compared to ESI alone.

Also the distance LE_{min} between the driving patch and the closest source of all selected sources to the driving patch was calculated to provide a measure for the quality of the combination of ESI and source selection. It offers a lower bound on the error of both the source with the highest outdegree and the source with the highest power. When $LE_{conn/pow} = LE_{min}$, the respective method achieves the best possible result, given the reconstructed sources. The different localization errors are illustrated in Fig. 5.7.

5.3.3 Results

5.3.3.1 Overall results

The results of the SOZ localization based on 1000 simulated ictal EEG epochs can be seen in Fig. 5.8. The data is represented in a boxplot, with the dot indicating the mean and the bar indicating the median of the errors. The data for 200, 192, 184, 176 and 168 electrodes are not shown, as they are very similar to their neighboring setups. From the figure, it is clear that connectivity analysis is better in localizing the epileptic driving patch than localization based on maximal power. More precisely, the localization error based on connectivity analysis was smaller than or equal to that based on power, $LE_{conn} \leq LE_{pow}$ in 85.5% of all the cases. LE_{conn} was strictly smaller than LE_{pow} in 58.5% and they were equal in 26.9% of all cases. Only in 14.5%, power outperformed connectivity analysis.

When comparing the localization errors based on connectivity and power with the minimal error that could be achieved, we found that LE_{conn} equalled LE_{min} in 66.74% of the cases. This is in contrast with LE_{pow}, which was equal to LE_{min} in only 31.64%.

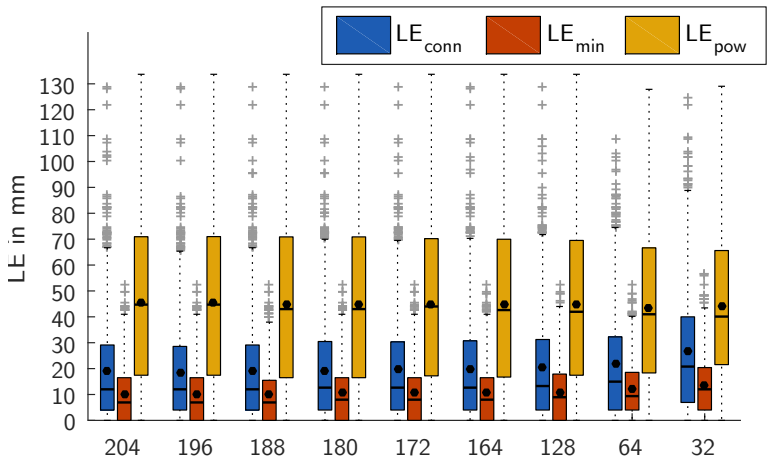

Figure 5.8: Overview of (i) the localization errors (LE) of the SOZ estimated by connectivity analysis, (ii) the LEs of the source with the highest power, and (iii) the LEs of the closest selected source for the different electrode setups for the simulated data. The distribution of the LEs is shown as a boxplot, the dot symbolizes the mean LE, while the bar indicates the median LE.

5.3.3.2 Influence of the number of electrodes

From Fig. 5.8, it can be seen that the localization errors are not distributed normally. Therefore, we consider the median to be more useful than the mean for representing the data over the different electrode setups. An overview of the different medians can be found in Table 5.1. The median of the minimal localization error LE_{min} was smaller than 10 mm for all setups except for 32 electrodes, for which it was 12 mm. The upper quartile stayed below 20 mm. For all electrode setups, it was possible to find a source very close to the origin of the simulated seizure. The median of the localization error based on connectivity analysis LE_{conn} was smaller than 15 mm in all setups, except for 32 electrodes, for which it was 20.78 mm. We notice an increase in both LE_{min} and LE_{conn} when we lowered the number of electrodes, especially in the upper quartile of LE_{conn}. Between 32 and 204 electrodes, the median of LE_{min} got 5.07 mm larger and the median of LE_{conn} 8.78 mm, which represented in both cases an increase of approximately 72%. In contrast, the median of the localization error based on power was much larger and varied between 40.10 and 44.72 mm over all electrode setups, which reflected a fluctuation of maximal 11.5%.

Table 5.1: Overview of the medians of the localization error of ESI followed by connectivity analysis, LE_{conn}, of the source with highest power after ESI, LE_{pow}, and of the minimal localization error, LE_{min}. Results are shown for the different setups (204 down to 32 electrodes) and were obtained after evaluation of 1000 simulated ictal EEG epochs.

(mm)	**median LE_{conn}**	**median LE_{min}**	**median LE_{pow}**
204	12.00	6.93	44.72
196	12.00	6.93	44.72
188	12.00	6.93	42.99
180	12.65	8.00	42.99
172	12.65	8.00	44.00
164	12.65	8.00	42.61
128	13.27	8.94	41.95
64	14.97	9.37	40.99
32	20.78	12.00	40.10

5.4 Performance in patient data

5.4.1 Collection of patient data

Patients were selected from the database of the epilepsy unit of the Geneva University Hospital with following inclusion criteria: (1) patients suffering from focal drug-resistant epilepsy; (2) they underwent hd-EEG (256 channels) monitoring and had at least one seizure during recording; (3) the patients underwent resective surgery of the supposed epileptogenic zone; (4) they had only one resection; (5) the surgical outcome of the patients was Engel Class III or higher; (6) pre- and post-operative T1-weighted MRI of the patient was available. Five patients (2 male) with mean age of 37.6 years fulfilled all criteria and were included. Table 5.2 gives an overview of the patients' age and sex, clinical and MRI findings, the result of visual analysis of the scalp EEG, the performed resective surgery, and the outcome of the surgery. The local ethical committee approved the study and all patients gave written informed consent. Long term hd-EEG was recorded for approximately 24 hours in each patient (EGI, Geodesic Sensor Net with 256 electrodes). From the 256 electrodes, the facial electrodes and the bottom line of the cap were removed due to major muscle artifacts, resulting in a setup of 204 electrodes. Electrode positions were estimated for every patient by manually fitting a template cap on the individual MRI. As in the simulation study, subsets of 200, 196, 192, 188, 184, 180, 176, 172, 168, 164, 128, 64 and 32 electrodes were created, with the configurations shown in Fig. 5.6.

The sample frequency was either 250 Hz or 1000 Hz (in 1 patient). In the latter case, the EEG was downsampled offline to 250 Hz for consistency and to reduce computation time.

For every patient, an epoch of 3 s was selected that started at the seizure onset time marked by an EEG expert.

5.4.2 Validation in patient data

For all patients, we segmented the RZ from the post-operative MRI, which we coregistered to the solution space. We used the proposed approach to try to localize the SOZ for every patient and every electrode setup.

Table 5.2: Overview of patient details. L = left, R = right, M = male, F = female, CPS = complex partial seizures, HS = hippocampal sclerosis, TPO = temporo-parieto-occipital, AH = amygdalohippocampectomy, T = temporal, O = occipital, ant = anterior.

	p1	**p2**	**p3**	**p4**	**p5**
Age (years)	36	42	36	29	45
Sex	F	F	M	F	M
Clinical findings	CPS	CPS	epigastric aura, secondary generalisation	aura of deja vu, change of taste, non-lateralized impairment of vision	CPS and generalized tonic clonic seizures
MRI findings	R HS	R HS	R HS	R cortical dysplasia in amygdala and paraventricular nucleus	L TPO gangliocytoma
Visual analysis of interictal scalp EEG	T2, F8	TP10, T8	T2, T8, P8, Tp10	T2, T8	F3, P7, CP3, P5
Surgery	R polectomy and AH	RT ant lobectomy	R AH	R polectomy and RT ant lobectomy	LO lobectomy
Engel Class	I	I	I	I	III

The optimal TVAR model order was calculated with the Akaike Information Criterion (AIC) [141]. Also for the patient data LE_{conn}, LE_{pow} and LE_{min} (Fig. 5.7) were calculated, but now with the RZ as a reference.

5.4.3 Results

We found optimal TVAR model orders between 4 and 8, see also Table 5.3. For patient 4, we found diverging results and therefore we set the model order to the maximal value found for the other patients, i.e. 8.

Table 5.3: Overview of the used model order found with the Aikake Information Criterion for every patient and every setup

	p1	**p2**	**p3**	**p4**	**p5**
204	8	4	6	8	4
200	8	4	6	8	4
196	8	4	6	8	4
192	8	4	6	8	4
188	8	4	6	8	4
184	8	4	6	8	4
180	8	4	6	8	4
176	8	4	6	8	6
172	8	4	6	8	6
168	8	4	6	8	6
164	8	4	6	8	4
128	8	4	6	8	4
64	6	6	6	8	4
32	8	6	6	8	4

5.4.3.1 Overall results

In Fig. 5.9, an overview of the localization errors (LEs) for all patients and all electrode setups can be found. A localization error of e.g. 50 mm is considered to be as unfavorable as a localization error of 80 mm, therefore we used different intervals to characterize the errors:

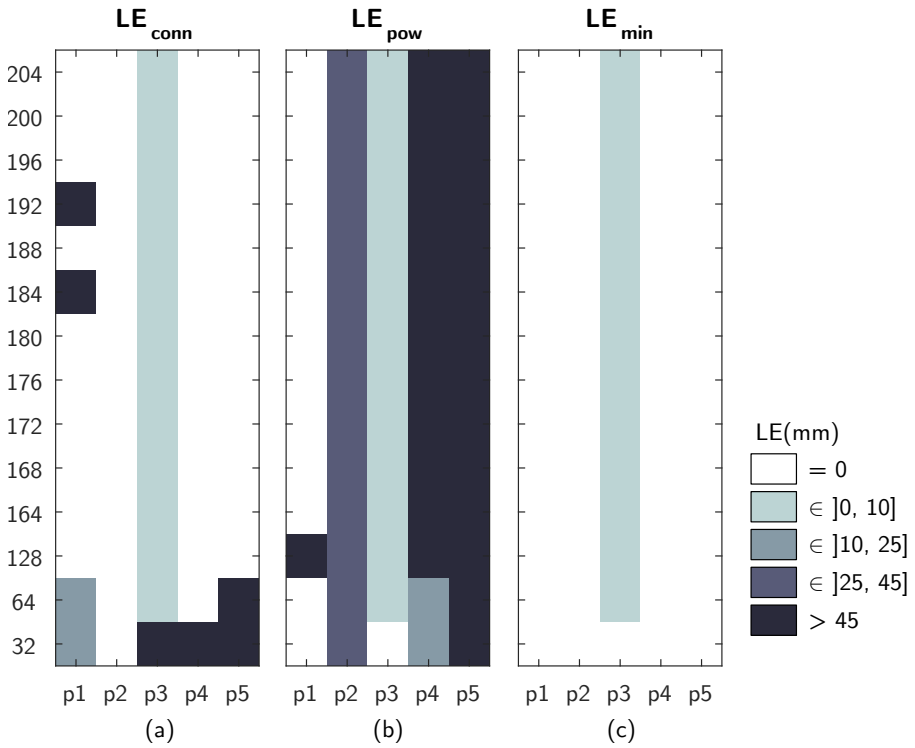

Figure 5.9: Overview of (a) the localization errors (LE) of the SOZ estimated by connectivity analysis, (b) the LEs of the source with the highest power, and (c) the LEs of the closest selected source for the different electrode setups for the 5 patients.

LE = 0 mm, LE $\in$ $]0, 10]$ mm, LE $\in$ $]10, 25]$ mm, LE $\in$ $]25, 45]$ mm, and LE > 45 mm.

From the figure, we can see that $\mathrm{LE}_{\mathrm{conn}}$ was equal to or smaller than $\mathrm{LE}_{\mathrm{pow}}$ in 91.4% of the cases, meaning that in these cases our presented method performed as well as or better than localization based on power. $\mathrm{LE}_{\mathrm{conn}}$ was strictly smaller than $\mathrm{LE}_{\mathrm{pow}}$ in 57.1 % of the cases. In 34.3 %, $\mathrm{LE}_{\mathrm{conn}} = \mathrm{LE}_{\mathrm{pow}}$ and, in 8.6 % of the cases, power outperformed connectivity analysis, $\mathrm{LE}_{\mathrm{conn}} > \mathrm{LE}_{\mathrm{pow}}$. These 8.6 % represent 6 cases that are mainly located in the low-density setups (3 for 32 electrodes and 1 for 64 electrodes, and two outliers for p1 for 184 and 192 electrodes).

For all setups, ESI and source selection were able to find a source inside the RZ for 4 patients, and within 10 mm of the border of the RZ or within

the resection for the other patient. Connectivity analysis was able to find this optimal solution in 88.6% of the cases, whereas $LE_{pow} = LE_{min}$ in 38.6% of the cases.

5.4.3.2 Influence of the number of electrodes

Fig. 5.10 shows the result of the connectivity analysis and the source with the highest power compared to the RZ for all patients for 204 electrodes. For the 204 electrodes setup, we were able to estimate the SOZ inside the RZ ($LE_{conn} = 0$ mm in p1, p2, p4, p5) or within 10 mm of the border ($LE_{conn} < 10$ mm in p3) of the RZ. In contrast, localization based on power was only able to estimate the SOZ inside the RZ in one patient and within 10 mm of the border of the RZ in one other patient. In these cases, localization based on power and connectivity found the same source. For the three other patients, the localization error LE_{pow} was larger than 25 (1/3 patients) or 45 mm (2/3 patients). The lateralization was, however, correct.

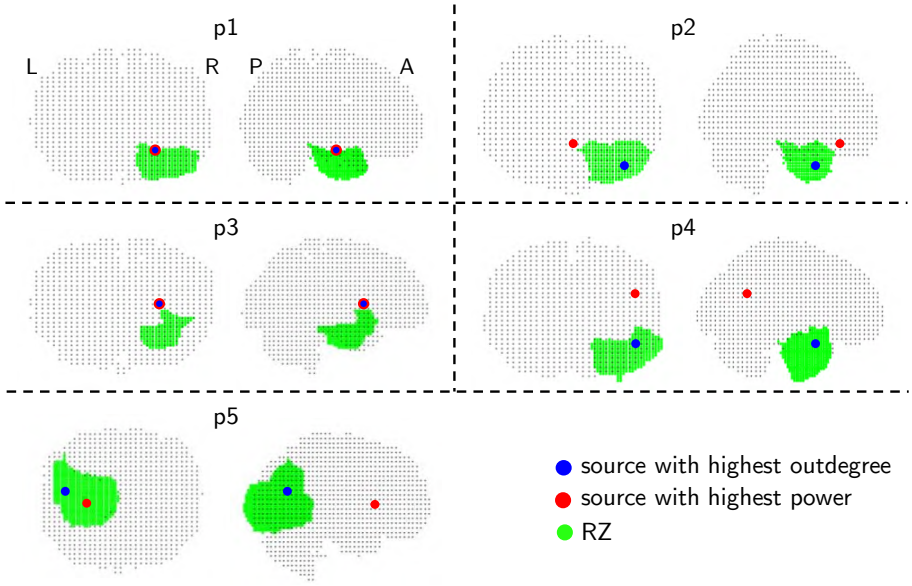

Figure 5.10: The selected SOZ based on the source with the highest outdegree (blue), the source with the highest power (red) and the resected zone (green) in the solution space for every patient, using the 204 electrode setup. L = left, R = right, A = anterior, P = posterior.

When comparing to the minimal localization error, connectivity analysis achieved the best possible result after ESI and source selection in every patient for 204 electrodes. This is also shown in Fig. 5.11, which displays in how many patients the minimal localization error was found, for every electrode setup and for both methods. On the contrary, localization based on power was only able to select the optimal source in 2 patients. The same results applied when gradually lowering the number of electrodes to 128, with the exception of three cases: for 192 and 184 electrodes, localization based on connectivity analysis does not find the optimal source in p1. For 128 electrodes, power localized the optimal source only in 1 out of 5 patients. For the high-density setups we can say that the presented approach outperformed localization based on power consistently.

For 64 electrodes, the performance of the presented approach decreased. The SOZ was estimated inside the RZ (2/5 patients) or within 10 mm of the border of the RZ (1/5 patients) in only 3 patients instead of 5. Yet, this result is better than localization based on power, for which the optimal source is only found in 2 patients. Only for one patient LE_{pow} was smaller than 10 mm. This is also reflected in Fig. 5.11 $LE_{conn} = LE_{min}$ in 3 patients and $LE_{pow} = LE_{min}$ in one patient. For the low-density setup of 32 electrodes, the SOZ was estimated inside the RZ in only one patient. The source with the highest power, was however inside the RZ in 2 out of 5 patients.

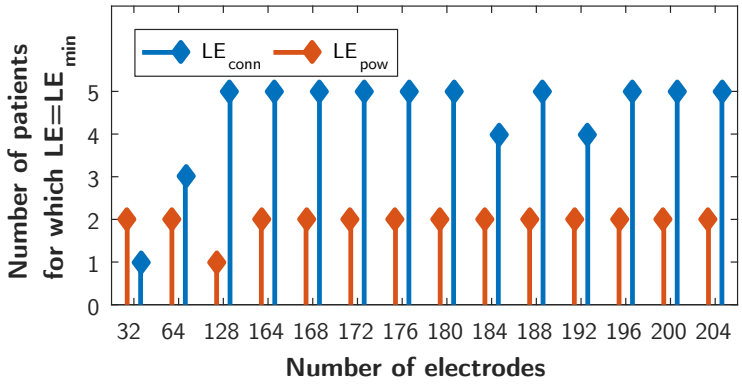

Figure 5.11: Representation of the number of patients for who the lower limit of error is achieved for each of the methods for all electrode setups, i.e. in how many patients does the source with the highest outdegree/the source with the highest power coincides with the source closest to the RZ for each setup.

5.5 Discussion

In this Chapter, we proposed an approach that combines ESI and functional connectivity analysis to localize the SOZ from noninvasive EEG in patients with drug-resistant epilepsy. We look at the connectivity instead of the power of the neuronal activity during an epileptic seizure. The presented method does not require patient-dependent parameters, which makes it suitable for use in clinical practice. We compared the localization obtained from connectivity measures with the maximal power of the electrical activity at the onset of an epileptic seizure.

We validated our method using simulated ictal EEG epochs and found that localization based on connectivity analysis had a significantly and consistently better yield than localization based on maximal power, for every electrode setup. The localizing potential of the method increased with the number of electrodes, which is in agreement with literature [173]. As a result, the performance of connectivity analysis also increased for high-density setups. The influence of the amount of electrodes was much smaller when localization was based on maximal power, but the median localization error was unacceptably high for all setups.

Next to simulations, we validated the method in five patients. For almost all high-density setups with 128 electrodes or more, we found the best possible result with the presented method: in four out of five patients the connectivity analysis selected the best possible source to localize the SOZ in every setup. For the fifth patient, the connectivity analysis was able to select the optimal source in all but two setups. The source with the highest power coincided with this optimal source in only two out of five patients. These results are better than what we found with the simulations, but this can be accounted for by the resected zones of the patients being larger than the patches of the simulated network. Next, we found equally good or better results with the connectivity method in 91.4 % of the cases compared to selecting the source with the highest power. A possible explanation for this could be that there is some remaining artifact in the selected epochs, and that connectivity analysis is more robust to artifacts and noise in the EEG than the power metric. A solution would be to limit the power analysis to a patient-specific seizure frequency range, to filter out the artifact as much as possible. This is done by Elshoff et al., where the frequency range could also change over the course of the seizure [196]. However, given

that a patient-specific seizure range could make the method subjective and less suitable to be directly used in a clinical setting, we opted not to do this and performed wide-spectrum analysis. In this study, ictal EEG segments (38-50 electrodes) of max. 10 s in the beginning and in the middle of seizures were analyzed with Dynamic Imaging of Coherent Sources (DICS) to determine the SOZ. The source with the highest power was identified as SOZ. Afterwards, functional connectivity analysis based on (renormalized) partial directed coherence ((R)PDC) was applied on the reconstructed sources, however, not to localize the SOZ, but rather to gain insight into the characteristic underlying epileptic network. In eight patients that were rendered seizure-free after surgery, the first two sources identified by DICS were concordant with the RZ. For three other patients, who were not seizure-free, the first two sources were not concordant with the RZ.

In the range of 204 down to 128 electrodes, our method generally estimated the localization of the SOZ inside (4/5 patients) or very close (< 10 mm) to the boundary of the RZ (1/5 patients). When lowering the number of electrodes down to 64, the performance of the method decreased, but it was still capable of localizing the SOZ inside (2/5 patients) or very close to the border of the RZ (1/5 patients). For the low-density setup with 32 electrodes, we experienced an extra reduction in performance. When using only 32 electrodes, there was correct localization in only one of the patients. Setups with more electrodes are thus preferred in the current approach. We assume that the performance goes down with the number of electrodes due to suboptimal estimation of the time series per source (however the goodness-of-fit did not decrease significantly) and/or SVD not being able to represent the three orthogonal time series as one time series. As a consequence, these errors propagate in the connectivity analysis and the correct source cannot be selected. Nevertheless, Ding et al. used only 31 electrodes and they were able to localize the SOZ within 15 mm of the presumed EZ by evaluating ictal epochs of 3 s by combining first principle vector (FINE) spatio-temporal ESI and directed transfer function (DTF) analysis to identify the ictal sources [195]. However, four out of the five analyzed patients in this study showed clear large lesions on MRI that were presumed to be epileptogenic and it remains to be investigated how this influenced the results, as only one patient in this study had a small lesion. Furthermore, it is not addressed whether the patients had surgery, and if so, whether surgery was successful. There

were also no intracranial EEG recordings to validate the results. Lu et al. performed a similar study with 76 electrodes, and they were able to localize the SOZ within 10 mm of the border of the RZ in 7 out of 10 patients [205]. This result is comparable with our study for the 64 electrode setup.

To improve results for lower-density setups, some suggestions can be made. A possible improvement could be to use patient-specific electrode locations in the forward model. The benefit of this has been investigated and could improve the estimation of the time series corresponding to each selected source [227–229]. We chose LORETA as inverse solution method as it is a simple, clear and easily controllable technique fit for the reconstruction of non-stationary signals that was ready at hand in our group. Nevertheless, the influence of other, more advanced inverse techniques could be investigated, such as the multiple sparse volumetric priors (MSVP) algorithm [230], the FINE algorithm [195, 231, 232], dynamic imaging of coherent sources (DICS) [233,234], or the Maximum Entropy on the Mean (MEM) approach [235, 236]. The investigation of the potential benefit of such techniques lies, however, beyond the scope of this study. In our analysis, the inverse solution is estimated for every time sample separately, but we could take into account other time samples to improve ESI.

Other functional connectivity analysis techniques, possibly in combination with graph theory measures, could be considered. Some connectivity measures related to the swADTF were tested, the integrated ADTF (iADTF) and the full-frequency ADTF (ffADTF) [152], both resulting in worse results. Another interesting approach for SOZ localization is to first decompose the ictal data to isolate seizure components, e.g. with ICA, and then integrate ESI with a recombination approach. This is done by Yang et al., where this dynamic source imaging technique identified ictal activity in good correlation with iEEG and surgical outcomes [214]. It remains to be investigated how functional connectivity analysis can possibly enhance this method.

In this study, functional connectivity analysis was performed on a limited set of network nodes, selected based on a measure of local maxima in power. It might be interesting to look at what happens on the whole-brain level during a seizure and to compare this to the brain in resting state. In the past, all-to-all functional connectivity analysis has been done by reducing the brain space to several regions-of-interest based on

a brain atlas [237, 238]. This method avoids the problem of possibly introducing spurious sources due to locally correlated sources in the ESI solution, as discussed in section 2.3.3. Recently, this has been applied on epilepsy patients by Coito et al. to investigate interictal and resting state connectivity [226, 239].

ESI resulted in all cases in a source close to the resection, reflected in an overall low LE_{min}. The selection of this optimal source was significantly better using connectivity analysis compared to selecting the source with the highest power, especially in high-density setups.

When applying functional connectivity analysis to noninvasive recordings, the volume conduction problem is a well-known phenomenon. All sources in the brain are seen by each electrode. We addressed this problem by demixing the sources, i.e. with ESI, but this technique does not mitigate the effects of volume conduction completely and spurious connections can still possibly exist [240]. There is no technique to completely alter the mixing problem, but it would be interesting to compare the current framework with other techniques, e.g. the imaginary part of the coherency [241], designed to undo the volume conduction problem in combination with functional connectivity analysis. A clear review of the volume conduction problem in functional connectivity analysis and different strategies and techniques to solve it, is given in [242].

Considering the patient data, an important remark to make is that the method was validated in a dataset limited to only 5 patients in which each patient had one seizure. Moreover, one of the patients only had Engel Class III. With this limited validation, we illustrated the potential of the method and showed its possibilities. The findings were concordant with simulation results. Extensive validation in a larger and more heterogeneous (i.e. more types of epilepsy) patient population is necessary to prove its clinical usefulness and added value in SOZ localization and to investigate the interpatient variability. This would also give a more clear view on how many electrodes are minimally needed to achieve a certain sensitivity and specificity. Besides more patients, more seizures per patient should be considered in order to validate the intrapatient robustness. Unfortunately, no other seizures were recorded in these patients. Not only more seizures per patient, but also more epochs per seizure could be the subject of future research to study whether the driver of the network changes during the seizure or not.

Also, we used a fixed ictal time-frame of 3 s starting at seizure onset, to have a time frame that is consistently the same for all patients, while also minimizing the artifacts in the EEG data. It remains to be investigated how the length of the chosen time window and its point of onset influences the results.

Validation was done by comparing the estimated SOZ with the RZ for all patients. The RZ is, however, often an overestimation of the ground truth, the real seizure onset zone. Therefore it could be useful to validate the method in simultaneous hd-EEG and intracranial EEG, to see whether the networks found with both modalities can be correlated. Even though the sampling area of iEEG is smaller, it could provide a more precise (smaller) ground truth than the RZ, provided that the SOZ is sampled.

5.6 Conclusion

We developed a method based on ESI and functional connectivity analysis to localize the seizure onset zone in a noninvasive, objective way that can potentially be used in a clinical setting. The approach consistently outperformed localization based on power, and results were more accurate for high-density EEG than for standard electrode configurations. Validation in a larger and more diverse patient group is warranted. We conclude that our presented approach and in general ESI combined with functional connectivity analysis can serve as a useful tool for SOZ localization in the presurgical evaluation of epilepsy.

5.7 Original Contributions

This study was presented at the International Conference on Basic and Clinical Multimodal Imaging (BaCi) in 2015 [243], at the Annual Meeting of the American Epilepsy Society (AES) in 2015 [244], and at the 2nd Annual Meeting of the Organization for Human Brain Mapping (OHBM) in 2016 [245]. The results of this chapter were published in the A1 journal Brain Topography [246].

6
Seizure onset zone localization from clinical EEG

6.1 Introduction

In chapter 5, we introduced a method based on ESI and functional connectivity analysis based on Granger causality that was able to successfully localize the SOZ from ictal hd-EEG data. However, the performance decreased when less electrodes were used. Unfortunately, high-density (hd)-EEG systems are often not yet available in clinical practice, certainly not for long-term monitoring. Therefore, it would be of high value to be able to localize the SOZ based on low-density or clinical recordings. In this chapter, we adapt the method of Chapter 5 to allow for successful analysis of clinical/low-density EEG. We validated the approach in the clinical scalp ictal EEG recording of 111 seizures from 27 patients (23 with temporal lobe epilepsy) who were rendered seizure-free following resective surgery.

6.2 Methods

6.2.1 Patients

27 patients, 18 from Ghent University Hospital and 9 from Geneva University Hospital, were included based on the following criteria:

1. drug-resistant epilepsy;

2. availability of EEG recordings of at least one seizure, recorded with at least 27 electrodes;
3. single resective surgery procedure of the supposed EZ;
4. surgical outcome Engel Class I with a minimal post-operative follow-up of 12 months;
5. availability of pre- and post-operative T1-weighted MRI.

Table 6.1 lists the main patient characteristics. The local ethical committees approved the study and all patients gave written informed consent.

6.2.2 EEG recording

The patients of Ghent University Hospital (PAT1 – PAT18) underwent long-term video EEG monitoring (Micromed, Treviso, Italy) lasting 3–8 days. A setup with 27 electrodes was used of which 21 were placed according to the International 10-20 system. Additionally, 3 electrodes were placed in zygomatic, preauricular, and mastoid regions on both sides of the head (F9-F10, T9-T10 and Tp9-Tp10 respectively) [168]. The sampling frequency was 256 Hz. For the 9 patients of Geneva University Hospital (PAT19 – PAT27), ictal EEG recordings, lasting at least 24h, with 29–32 electrodes placed according to the international 10-10 system were available with a sampling rate of either 250 Hz or 256 Hz.

6.2.3 EEG preprocessing and ictal epoch selection

EEG preprocessing was done in BrainVision Analyzer (BrainProducts GmbH, Germany). The patient-data was band-pass filtered between 1 and 30 Hz to remove baseline drift and to reduce high-frequency muscle artifacts. An extra notch filter at 50 Hz was applied to filter out remaining power line noise. For all recorded seizures, together with an experienced epileptologist (prof. K. Vonck, prof. S. Vulliémoz), a (quasi) artifact-free epoch close to the electrographic onset that was representative for the seizure was selected. If no clear EEG changes were observed, the clinical onset was used instead. The epochs were as long as possible, with a minimum of 1 second and a maximum of 5 seconds.

Table 6.1: Patient details. Patients 1–17 are from Ghent University Hospital and Patients 18–26 are from Geneva University Hospital. PAT = patient number, Ep. = epilepsy, surg. = surgery, FU = follow-up, dur. = duration, LE = lobe epilepsy, rhyt. = rhythmic, act. = activity, R = right, L = left, T = temporal, F = frontal, P = Parietal, O = occipital, C=central, inf = inferior, ant = anterior, HEM = hemisphere, elec. = electrodes, HIP = hippocampal, DNET = dysembryoplastic neuroepithelial tumor, IED = interictal epileptiform discharges, AH = amygdalohippocampectomy, S = selective, y = year, m=month.

PAT	Ep. type	Onset age	Surg. age	Interictal EEG	Ictal EEG	Invasive EEG	MRI	Surgery	FU dur.
1	RFLE	8y	30y	Bursts of bilateral slow sharp waves during sleep	Absence of clear ictal discharges, some bilateral and/or RF sharp act.	Low voltage fast act. on grid elec. above cortical dysplasia	RF opercular focal cortical dysplasia	RF opercular lesionectomy	48m
2	RTLE	5y	48y	RFT IED	RFT rhyt. δ act.	/	R HIP atrophy	R SAH	36m
3	RTLE	6y	33y	RFT IED	RT and HEM rhyt. θ act.	/	R HIP atrophy and secondary sclerosis of R ant T pole	R SAH	36m
4	RTLE	15y	22y	RFT IED	RFT rhyt. θ-δ act.	/	R HIP atrophy	R SAH	36m
5	RTLE	18y	55y	RFT IED	RFT and CP rhyt. θ act.	Low voltage fast act. RT neocort. grid elec. + early R HIP elec. involvement	no epileptogenic lesion	RT neocortical topectomy + SAH	33m
6	RTLE	20y	35y	RFT IED	RFT rhyt. θ-δ act. with early L HEM involvement	/	R gyrus T inf DNET	R basoT lesionectomy	18m

Table 6.1: (continued)

PAT	Ep. type	Onset age	Surg. age	Interictal EEG	Ictal EEG	Invasive EEG	MRI	Surgery	FU dur.
7	RTLE	12y	27y	RFT IED	RFT rhyt. θ act.	/	R HIP atrophy	R SAH	29m
8	LOLE	48y	49y	LF & LFT IED	LPO low voltage fast act. & L T rhyt. θ act.	Low voltage fast act. on L O grid elec.	LO cystic lesion	LO lesionectomy	25m
9	LTLE	19y	54y	LF & LT IED & infrequent RT IED	L generalized decrement followed by LT rhyt. θ act.	L HIP fast & rhyt. polyspike act.	L HIP atrophy	L SAH	21m
10	LTLE	18y	28y	LFT IED	L HEM or bilateral rhyt. θ-δ act.	L HIP rhyt. spike act.	LT cavernous hemangioma	L 2/3 ant T lobectomy	20m
11	RTLE	24y	50y	RFT IED	RFT rhyt. θ act.	/	R HIP atrophy	R SAH	12m
12	RTLE	24y	26y	RFT IED	Bilateral T rhyt. θ act.	R HIP and inf T rhyt. act.	R ant inf T gyrus abnormal structure	R 2/3 ant T lobectomy	65m
13	LTLE	31y	36y	LFT IED	LFT rhyt. act.	/	lesion L inf T gyrus	LT lesionectomy	56m
14	LTLE	40y	49y	LFT IED	LFT rhyt. θ-act.	rhyt. low voltage δ act. with spiking on basal ant T grid elec. with early spread to HIP elec.	LT, L precentral & inf P posttraumatic atrophy	L 2/3 ant T lobectomy + corticectomy of post basal T neocortex	47m
15	RTLE	35y	42y	RFT IED	RFT rhyt. δ act.	/	R HIP atrophy	R SAH	26m

Table 6.1: (continued)

PAT	Ep. type	Onset age	Surg. age	Interictal EEG	Ictal EEG	Invasive EEG	MRI	Surgery	FU dur.
16	LTLE	36y	40y	no IED	LFT rhyt. δ act.	/	L HIP atrophy	L SAH	48m
17	RTLE	4y	18y	RFT IED	R HEM θ-δ act.	/	R HIP atrophy	R SAH	48m
18	LTLE	31y	43y	LFT slow sharp waves	L HEM rhyt. δ act.	/	L HIP atrophy	L SAH	12m
19	RTLE	11y	16y	RT IED	RT delayed onset with slow sharp waves	R amygdala/HIP rhyt. β act.	R HIP atrophy	R 2/3 ant T lobectomy	60m
20	LFLE	1y	12y	LCP IED	LFC β rhythm evolving to FC rhyt. sharp waves	LF tuber rhyt. β act. evolving to LFC tuber rhyt. β act.	Tuberous sclerosis	LF and LFC lesionectomy (tuber)	60m
21	LTLE	1y	11y	bilateral FT IED & LT slow waves	L HEM rhyt. slowing propagating to R HEM, then LT rhyt. θ act.	L lateral temporal	no epileptogenic lesion	L 2/3 ant T lobectomy sparing AH	96m
22	LTLE	1 y	12y	multifocal L IED	Successive bursts of rhyt. polyspike-waves with LFC onset	RT pole rhyt. β act. propagating to basal RT	Tuberous sclerosis	L 2/3 ant T lobectomy	48m
23	RTLE	9y	32y	RT IED	LPO rhyt. θ act.	R HIP rhyt. β act. evolving to α and δ	R HIP atrophy	R 2/3 ant T lobectomy	84m
24	RTLE	25y	37y	RFT IED	RT rhyt. θ act. to RT rhyt. spiking to contralateral diffusion	/	R HIP atrophy	R 2/3 ant T lobectomy	54m

Table 6.1: (continued)

PAT	Ep. type	Onset age	Surg. age	Interictal EEG	Ictal EEG	Invasive EEG	MRI	Surgery	FU dur.
25	RTLE	20y	43y	RTP IED	RT rhyt. θ act.	/	R HIP atrophy	R 2/3 ant T lobectomy	48m
26	RTLE	20y	37y	RTP IED	rhyt. RFT δ act. with spikes to R HEM sharp waves max. FT	/	RF focal cortical dysplasia	RF lesionectomy	48m
27	RTLE	25y	30y	RT IED	R HEM rhyt. α act. with max RT	/	RT pole and amygdala dysplasia	R 2/3 ant T lobectomy with limited HIP resection	24m
mean		19y	34y						42m
med		19y	35y						47m
std		13y	13y						21m

Additional preprocessing was performed to increase signal-to-noise ratio: when poor quality channels were present, they were spatially interpolated using splines instead of removed, allowing to use the same analysis pipeline for every epoch of each patient. In case of long lasting muscle artifact, an extra band-pass filter between 1 and 10 Hz was applied. For eye blink or cardiac artifact removal, ICA [32] was used using the restricted fast ICA [247] implementation in BrainVision Analyzer on the available EEG channels. Only components showing exclusively clear artifactual activity, namely eye blinks with clear frontal topographic pattern (in 25 seizures) and cardiac artifact (in 1 seizure), were removed. The selected epochs were common average referenced and their fundamental seizure frequency band (Frequency band Of Interest (FOI)) was determined as the band with maximal global field power using the Fast Fourier Transform (FFT).

6.2.4 From ictal epoch to SOZ

As in the previous chapter, we used two methods to localize the SOZ from the selected ictal EEG epoch. The first method was based solely on ESI, and named "ESI power". The second method was based on ESI with subsequent functional connectivity analysis and named "ESI + connectivity". Both methods have been extensively described in the previous chapter. The main difference with the methodology in this chapter is the variable segment selection (described above) and the fact that we calculate the power and connectivity values in a FOI rather than in the broadband spectrum. We summarize the methods below and highlight the differences.

After the selection and preprocessing of an ictal epoch as described in section 6.2.3, ESI was applied. For this purpose, realistic finite difference method (FDM) head models consisting of six different tissues (air (0 S/m), scalp (0.33 S/m), skull (0.0132 S/m), cerebrospinal fluid (1.79 S/m), gray matter (0.33 S/m) and white matter (0.14 S/m)) were constructed based on the individual patients pre-operative T1-weighted MR image [248, 249]. The solution space was constructed as a uniform grid in the segmented gray matter, excluding the cerebellum, with a spacing of 4 mm. An in-house implementation of Low Resolution Electromagnetic Tomography (LORETA) was used as inverse solution method [123]. LORETA solutions are typically smooth throughout the brain in which some hotspots of higher activity are apparent and that

might partially overlap. We selected K hotspots as nodes or sources as possible SOZs for the subsequent analyses with the following approach. We considered the power distribution in the solution space over the complete duration of the analyzed epoch. For every solution point, we calculated the sphere power as the mean power of all solution points in a sphere centered on the considered solution point. Those solution points that had no neighbors with a higher sphere power than their own corresponded to local maxima in power and were selected as a possible sources for the SOZ. By varying the radius of the sphere, more or less sources can be selected. In one extreme case, the radius is smaller than the grid resolution (here 4 mm), and all sources will be selected. In the other extreme case, the radius is larger than the largest distance between two solution points, and only one source will be selected, corresponding to the global maximum in power. In this case, subsequent connectivity analysis is impossible, since there is only one source. In the former case, subsequent network analysis might be biased since in a LORETA solution neighboring sources are correlated and thus spurious connections might be introduced. Therefore, choosing this radius is a trade-off between not making the search area unnecessarily large and not excluding possible epileptic network nodes. For a radius of 15 mm, we found for all seizures an acceptable amount of network nodes, which ranged between $K = 4$ and $K = 24$. Increasing the radius resulted in the undesirable situation that for some seizures only one network node was found and decreasing the radius increased the upper limit of the number of sources, making the search area unnecessarily large. To continue the analysis, we considered the time series of the selected sources. No constraints were applied on the orientation of these sources; so every selected source was represented by three time series, one for each orthogonal spatial dimension. We used Singular Value Decomposition (SVD) to represent every selected source by only one time series, namely the time series associated with the largest singular value of the SVD [115]. For the ESI power method, we selected the source with maximal power in the FOI as the estimated SOZ.

For the ESI + connnectivity method, functional connectivity analysis based on Granger causality was applied on the time series of the selected sources to reveal the driver of the epileptic network. To this end, the data was modeled by a Time-Varying Multivariate Autoregressive (TVAR) model, of which the coefficients were estimated using the Kalman filtering algorithm [148, 149], with a model order of 10, an

update coefficient of 10^{-4} and a smoothing factor of 100, based on previous research [150, 152, 153, 226, 246].

From the time-varying transfer matrix $\mathbf{H}(f,t)$ of the model, the spectrum-weighted Adaptive Directed Transfer Function (swADTF) [153] was calculated at every time sample t of the selected epoch of length T and for the FOI = $[f_1 f_2]$ with a resolution of 0.1 Hz, as a measure for the information flow between every two of the Kselected sources:

$$\mathrm{swADTF}_{ij}(t) = \frac{\sum_{f=f_1}^{f_2} |H_{ij}(f,t)|^2 \sum_{l=1}^{K} |H_{jl}(f,t)|^2}{\sum_{k=1}^{K} \sum_{f'=f_1}^{f_2} |H_{ik}(f',t)|^2 \sum_{s=1}^{K} |H_{ks}(f',t)|^2} \tag{6.1}$$

Finally, the outdegree of every source j was calculated as the sum of the swADTF values to every other source:

$$\mathrm{OD}_j = \sum_{k=1}^{K} \sum_{t=1}^{T} \mathrm{swADTF}_{kj}(t) \tag{6.2}$$

in which we defined $\mathrm{swADTF}_{jj} = 0$. ESI + connectivity selected the source with the highest outdegree as presumed SOZ.

6.2.5 Validation

6.2.5.1 Localization errors

Since all patients included in this study were seizure-free for at least one year after surgery, we assume that the SOZ was located inside the resected tissue. The final result for each of the methods was one source, i.e. one point in the gray matter of the patient. Therefore, we defined the localization error of both methods, ESI power and ESI + connectivity, as the distance between the border of the Resected Zone (RZ), segmented from the post-operative MRI, and the SOZ estimated by the corresponding method. The localization errors were named $\mathrm{LE}_{\mathrm{pow}}$ and $\mathrm{LE}_{\mathrm{conn}}$, respectively. If the selected source was inside the RZ, the LE was set to zero.

6.2.5.2 Seizure level

We calculated LE_{conn} and LE_{pow} for every seizure, and determined the amount of seizures with LE = 0 mm and LE ≤ 10 mm for both methods, to account for the spatial resolution of ESI (cm-range), and the brain shift that can occur after resective surgery.

6.2.5.3 Patient level

For every patient, we calculated the percentage of seizures that were estimated inside the RZ and within 10 mm of the border of the RZ. Furthermore, the percentage of patients for who all of their seizures were localized within the given limits (0 mm and 10 mm) was determined.

6.2.5.4 Intra-patient robustness

When at least two analyzed seizures from one patient were available, the robustness of both methods against intra-patient variability could be assessed. For every seizure, a final source was selected as the estimated SOZ. In the ideal case, we would find a source inside the RZ for all the seizures of a specific patient. In reality, different sources, both within and outside (i.e. the algorithm performs wrong, or there are multiple foci) the RZ, can be found. We quantified the intra-patient spatial dispersion of patient P by calculating the geometrical centroid and standard distance SD to this centroid of the finally selected sources:

$$SD(P) = \sqrt{\frac{\sum_{i=1}^{N}(x_i - \mu_x)^2 + \sum_{i=1}^{N}(y_i - \mu_y)^2 + \sum_{i=1}^{N}(z_i - \mu_z)^2}{N}} \quad (6.3)$$

in which N is the number of seizures for patient P, (x_i, y_i, z_i) are the Cartesian coordinates of the estimated SOZ (finally selected source) for seizure i and (μ_x, μ_y, μ_z) are the Cartesian coordinates of the geometrical centroid, based on all N seizures for that patient P. When the standard distance remains low, the method is robust and the spatial dispersion could be informative for the epileptologist to find the SOZ. In contrast, a large standard distance (e.g. 8 cm) within a single patient may be a marker for a less reliable result.

6.2.5.5 Subgroup analysis based on resected volume

We calculated the resected volume in every patient using the convex hull of the segmented RZ and divided the patient population into a small RZ subgroup and a large RZ subgroup based on the resected volume. We determined whether there was a significant difference in LE_{pow} and LE_{conn} between the two subgroups. To get a more complete insight in the influence of the resected volume, we repeated this subgroup analysis based on the distance to the center of the RZ.

6.2.5.6 Statistical testing

In each of the aforementioned validation steps, the results for ESI + connectivity and ESI power were statistically compared using a Wilcoxon sign-rank test for non-normally distributed data. Statistical analysis between subgroups was done with Wilcoxon rank-sum tests for independent samples. All significant p-values ($p < 0.05$) were reported.

6.3 Results

6.3.1 Seizure level

In total, 111 seizures from 27 patients were analyzed (4.1 ± 2.9 seizures per patient). Table A.1 in Appendix A lists the selected epochs, the used frequency band of interest (FOI) and the applied preprocessing. Fig. A.1–A.3 of Appendix A show some examples of selected epochs. The localization errors for the ESI power and the ESI + connectivity approach are shown for every patient and every seizure in Table 6.2 and Table 6.3, respectively. ESI power was able to localize the SOZ inside the RZ in 30.6% (34/111) of the seizures and within 10 mm of the border of the RZ in 42.3% (47/111) of the seizures.

ESI + connectivity was inside or within 10 mm of the RZ in 72.1% (80/111) or 93.7% (104/111) of the seizures, respectively. The distribution of all the localization errors for ESI power and ESI + connectivity are shown in Fig. 6.1(a). The median localization error for ESI power was 15.7 mm in a range of 0–89.4 mm, for ESI + connectivity this was 0 mm in 0–81.1 mm. The distance to the border of the RZ

Table 6.2: Overview of the localization errors for the ESI power method of all analyzed seizures. Errors smaller than 10 mm (0 mm ≤ LE ≤ 10 mm) are coloured green, errors larger than 10 mm (LE > 10 mm) are depicted in red. The percentage of seizures per patient localized inside and within 10 mm of the RZ is indicated. Percentages ≤ 50% are shown in red, between 50% and 100% are shown in orange and percentages equal to 100% are colored green. P = Patient number, S = number of the analyzed seizure, RZ = border of resected zone.

	ESI power												% =0 mm	% ≤10 mm
P\S	**1**	**2**	**3**	**4**	**5**	**6**	**7**	**8**	**9**	**10**	**11**	**12**		
1	10	10	10	10	10	38	10	-	-	-	-	-	**0**	**86**
2	36	36	48	36	48	0	36	-	-	-	-	-	**14**	**14**
3	5	15	5	5	-	-	-	-	-	-	-	-	**0**	**75**
4	17	0	0	32	0	-	-	-	-	-	-	-	**60**	**60**
5	0	0	0	0	-	-	-	-	-	-	-	-	**100**	**100**
6	9	9	9	74	50	50	50	-	-	-	-	-	**0**	**43**
7	49	67	20	-	-	-	-	-	-	-	-	-	**0**	**0**
8	72	0	89	71	72	0	-	-	-	-	-	-	**33**	**33**
9	33	-	-	-	-	-	-	-	-	-	-	-	**0**	**0**
10	49	17	0	17	-	-	-	-	-	-	-	-	**25**	**25**
11	0	17	17	17	0	0	-	-	-	-	-	-	**50**	
12	63	0	13	0	0	0	13	13	-	-	-	-	**50**	**50**
13	78	-	-	-	-	-	-	-	-	-	-	-	**0**	**0**
14	55	13	13	13	-	-	-	-	-	-	-	-	**0**	**0**
15	20	20	31	-	-	-	-	-	-	-	-	-	**0**	**0**
16	0	0	0	0	-	-	-	-	-	-	-	-	**100**	**100**
17	78	19	73	-	-	-	-	-	-	-	-	-	**0**	**0**
18	0	0	16	-	-	-	-	-	-	-	-	-	**67**	**67**
19	23	-	-	-	-	-	-	-	-	-	-	-	**0**	**0**
20	39	39	29	0	39	0	13	29	52	39	75	39	**17**	**17**
21	0	47	-	-	-	-	-	-	-	-	-	-	**50**	**50**
22	0	6	36	36	20	53	20	20	0	-	-	-	**22**	**33**
23	0	23	0	-	-	-	-	-	-	-	-	-	**67**	**67**
24	0	-	-	-	-	-	-	-	-	-	-	-	**100**	**100**
25	40	-	-	-	-	-	-	-	-	-	-	-	**0**	**0**
26	0	-	-	-	-	-	-	-	-	-	-	-	**100**	**100**
27	0	-	-	-	-	-	-	-	-	-	-	-	**100**	**100**
% of seizures inside RZ											**30.6**			
% of seizures within 10 mm of RZ											**42.3**			
% of patients correct (100% of seiz. = 0 mm)													**18.5**	
% of patients correct (100% of seiz. ≤ 10 mm)														**18.5**

Table 6.3: Overview of the localization errors for the ESI + connectivity method of all analyzed seizures. Errors smaller than 10 mm (0 mm ≤ LE ≤ 10 mm) are coloured green, errors larger than 10 mm (LE > 10 mm) are depicted in red. The percentage of seizures per patient localized inside and within 10 mm of the RZ is indicated. Percentages ≤ 50% are shown in red, between 50% and 100% are shown in orange and percentages equal to 100% are colored green. P = Patient number, S = number of the analyzed seizure, RZ = border of resected zone.

	ESI + connectivity												% = 0 mm	% ≤ 10 mm
P\S	**1**	**2**	**3**	**4**	**5**	**6**	**7**	**8**	**9**	**10**	**11**	**12**		
1	10	10	10	10	10	10	10	-	-	-	-	-	**0**	**100**
2	0	0	0	0	0	48	0	-	-	-	-	-	**86**	**86**
3	5	5	5	5	-	-	-	-	-	-	-	-	**0**	**100**
4	0	0	0	0	0	-	-	-	-	-	-	-	**100**	**100**
5	0	0	0	0	-	-	-	-	-	-	-	-	**100**	**100**
6	9	9	9	9	9	9	9	-	-	-	-	-	**0**	**100**
7	0	0	0	-	-	-	-	-	-	-	-	-	**100**	**100**
8	0	0	81	35	0	0	-	-	-	-	-	-	**67**	**67**
9	0	-	-	-	-	-	-	-	-	-	-	-	**100**	**100**
10	0	17	0	17	-	-	-	-	-	-	-	-	**50**	**50**
11	0	0	0	0	0	0	-	-	-	-	-	-	**100**	**100**
12	0	12	13	0	0	0	0	0	-	-	-	-	**75**	**75**
13	0	-	-	-	-	-	-	-	-	-	-	-	**100**	**100**
14	0	0	0	0	-	-	-	-	-	-	-	-	**100**	**100**
15	5	0	0	-	-	-	-	-	-	-	-	-	**100**	**100**
16	0	0	0	0	-	-	-	-	-	-	-	-	**100**	**100**
17	10	0	0	-	-	-	-	-	-	-	-	-	**67**	**100**
18	0	0	0	-	-	-	-	-	-	-	-	-	**100**	**100**
19	0	-	-	-	-	-	-	-	-	-	-	-	**100**	**100**
20	0	0	0	0	0	0	0	0	0	0	0	0	**100**	**100**
21	0	0	-	-	-	-	-	-	-	-	-	-	**100**	**100**
22	0	6	6	0	6	6	0	0	6	-	-	-	**44**	**100**
23	0	0	0	-	-	-	-	-	-	-	-	-	**100**	**100**
24	0	-	-	-	-	-	-	-	-	-	-	-	**100**	**100**
25	0	-	-	-	-	-	-	-	-	-	-	-	**100**	**100**
26	0	-	-	-	-	-	-	-	-	-	-	-	**100**	**100**
27	0	-	-	-	-	-	-	-	-	-	-	-	**100**	**100**
% of seizures inside RZ											**72.1**			
% of seizures within 10 mm of RZ											**93.7**			
% of patients correct (100% of seiz. = 0 mm)													**66.7**	
% of patients correct (100% of seiz. ≤ 10 mm)														**85.2**

was significantly lower for ESI + connectivity than for ESI power ($p = 3.2 \times 10^{-11}$).

The percentage of seizures per patient that was estimated inside the RZ or within 10 mm of the border of the RZ, is shown in Table 6.2 for ESI power and in Table 6.3 for ESI + connectivity. For both limits, ESI + connectivity scored significantly better than ESI power ($p = 1.2 \times 10^{-4}$ for LE = 0 mm and $p = 3.6 \times 10^{-5}$ for LE $\leq$ 10 mm). This can also be seen in Fig. 6.1(b). ESI power was able to localize all seizures inside the RZ in only 18.5% (5/27) of the patients. This number stayed the same for seizures within 10 mm of the RZ. ESI + connectivity localized all seizures inside the RZ in 66.7% (18/27) of the patients and within 10 mm of the RZ in 85.2% (23/27) of the patients.

6.3.2 Intra-patient robustness

20 out of 27 patients had more than one seizure during recording (they had 5.2 $\pm$ 2.5 seizures on average). In Fig. 6.2, we depict the spatial dispersion obtained with both methods for three illustrative cases (2 Temporal Lobe Epilepsy (TLE), 1 Frontal Lobe Epilepsy (FLE)) by a dot on the geometrical centroid and a circle with radius equal to the standard distance, centered at the centroid. This is overlaid on the pre-operative MRI of the patient, in which we highlight the ultimately resected zone in green. Both ESI + connectivity and ESI power gave a good indication of the SOZ in PAT 17, respectively 100% and 67% of the seizures were localized correctly. The spatial dispersion of ESI+connectivity points directly to the RZ with a standard distance equal to zero. However, the spatial dispersion of ESI power also gives a good indication where to look for the true SOZ, but less precise. In PAT 12, the standard distance for ESI + connectivity larger than zero, but the spatial dispersion is still informative, remaining mainly in the temporal lobe. The spatial dispersion based on ESI power, however, crosses lobe and even hemisphere borders and could be more difficult to interpret. For PAT 8, the spatial dispersion based on ESI + connectivity contains the RZ, whereas the spatial dispersion based on ESI power does not. Although, ESI + connectivity correctly localized 67% of the seizures, the standard distance is very high due to two completely wrong localizations, rendering the spatial dispersion less informative. In the supplementary material A.2, the figures for all patients can be found.

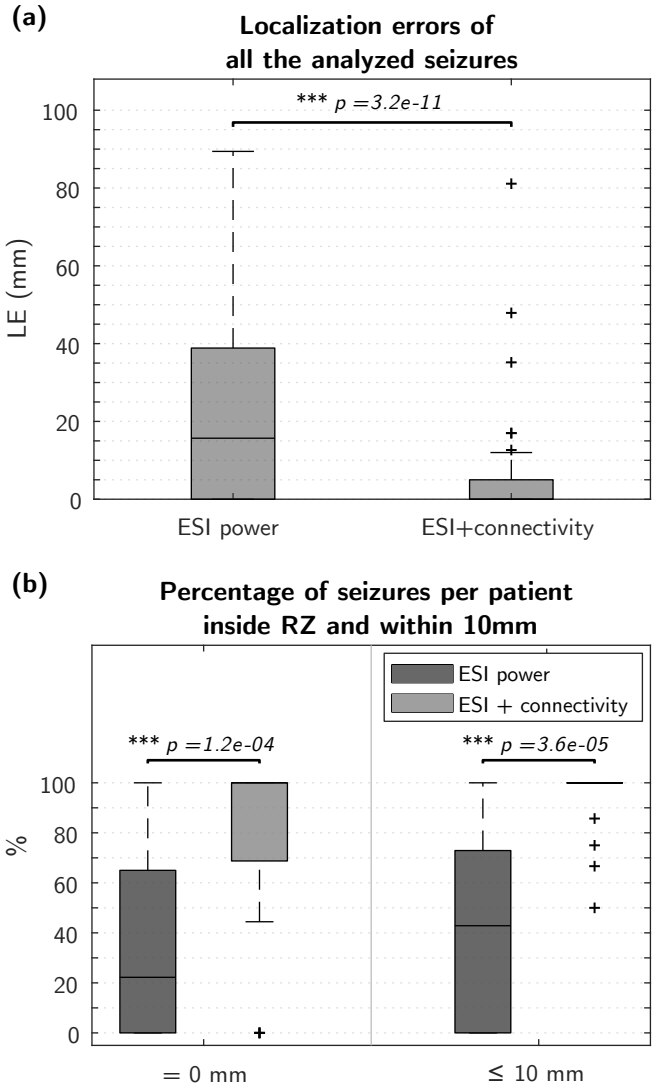

Figure 6.1: (a) Boxplot of the localization errors of all analyzed seizures, (b) percentage of correct localized seizures per patient, for both methods and both limits (LE = 0 mm and LE ≤ 10 mm).

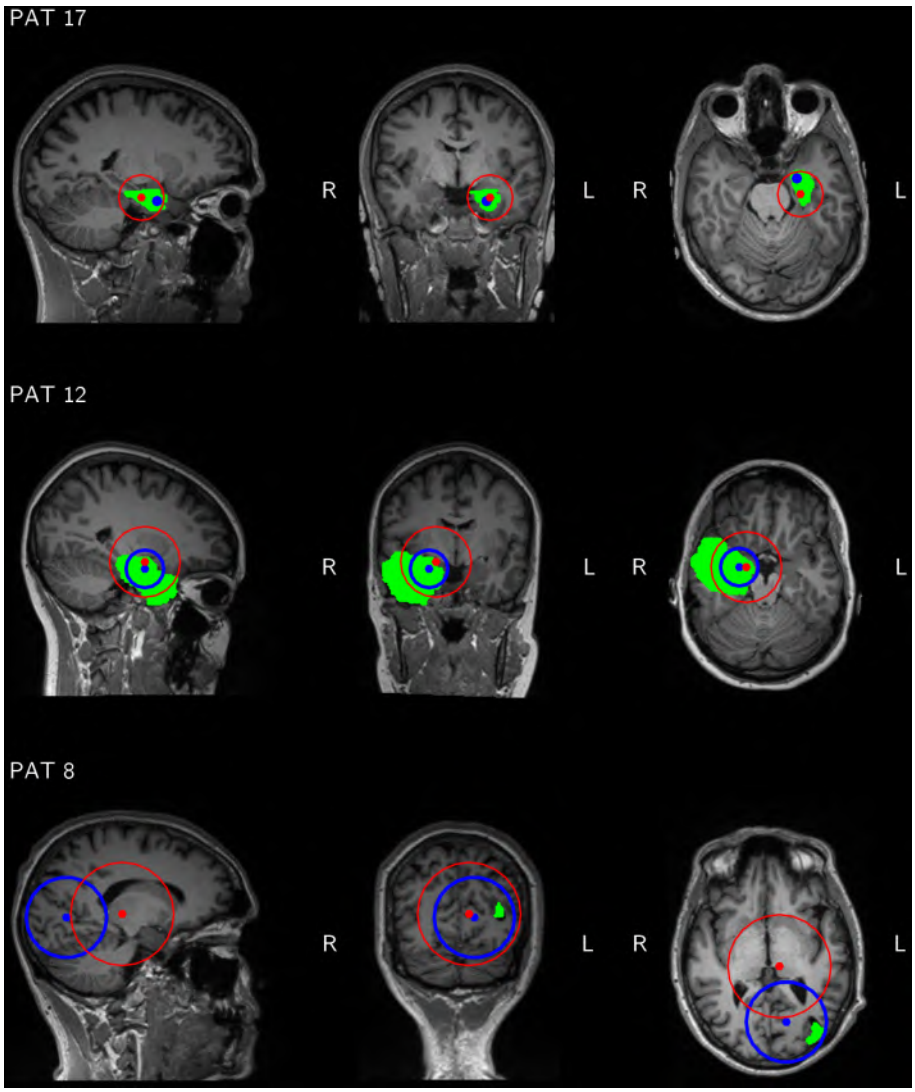

Figure 6.2: Three examples of the spatial dispersion of the estimated SOZs for ESI+connectivity (blue circle) and ESI power (red circle). The dot represents the centroid, whereas the circle represents the standard distance. The resected zone is highlighted in green.

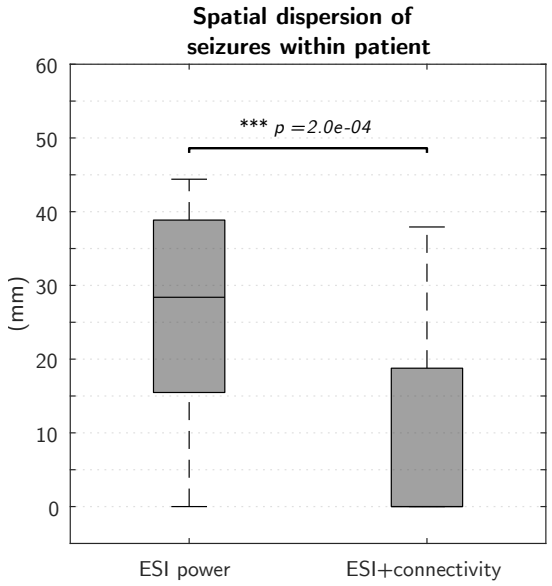

Figure 6.3: Distribution of the standard distance to the geometrical centroid within the patients who had more than one seizure during recording.

Fig. 6.3 shows a boxplot of all standard distances for both methods. ESI power had a median standard distance of 25.3 mm in a range of 0-44.4 mm, for ESI+connectivity this was 0 mm in a range of 0-37.9 mm. ESI power had a significantly higher standard distance than ESI + connectivity ($p = 2.0 \times 10^{-4}$).

6.3.3 Subgroup analysis based on resected volume

The volumes and division into a small and large RZ subgroup can be seen in Fig. 6.4. Both for small and for large resections, we found that ESI + connectivity scored significantly better than ESI power (resp. $p = 3.8 \times 10^{-6}$ and $p = 1.8 \times 10^{-6}$), shown in Fig. 6.5. ESI power for small resections had a median localization error of 12.81 mm in a range of 0–89.4 mm. For large resections, this was 17 mm in a range of 0–75.3 mm. There was no significant difference between small and large resections. For ESI + connectivity, we found a median localization error of 0 mm for both small and large resections. The range for small resections was 0–81.1 mm and for large resections 0–47.9 mm. A small significant difference was found in favour of large resections ($p = 3.3 \times 10^{-2}$). Yet,

there was no significant difference for small and large resections in the percentage of correctly localized seizures per patient. Moreover, when we repeated the analysis with the distance to the center of the RZ instead of the distance to the border of the RZ, we found significantly smaller values for small resections, for both methods, also shown in Fig. 6.6.

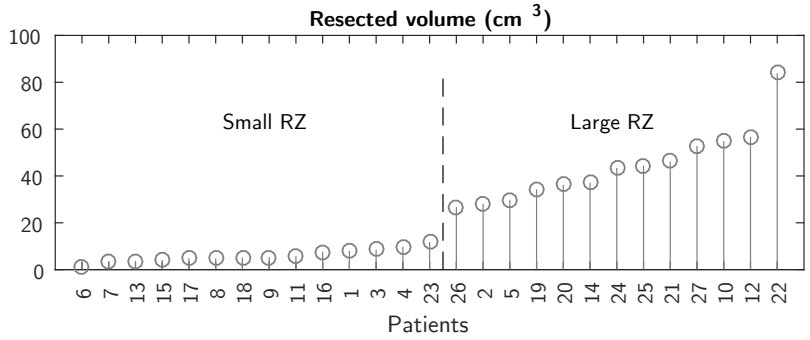

Figure 6.4: The resected volumes for every patient, sorted from small to large. The boundary for the division between small and large resections is indicated.

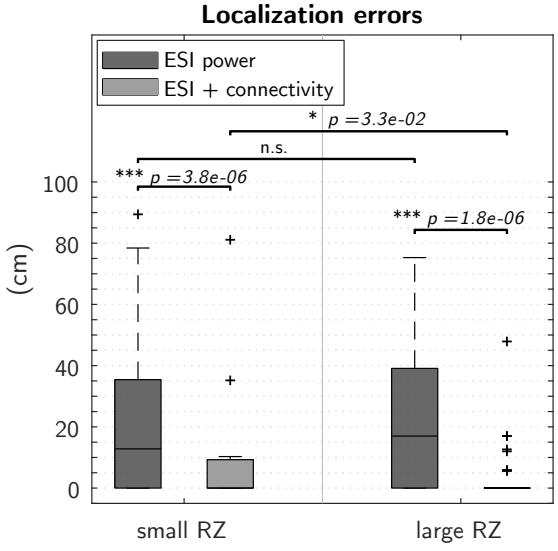

Figure 6.5: Boxplot of the localization errors corresponding to small and large resected volumes, for both methods.

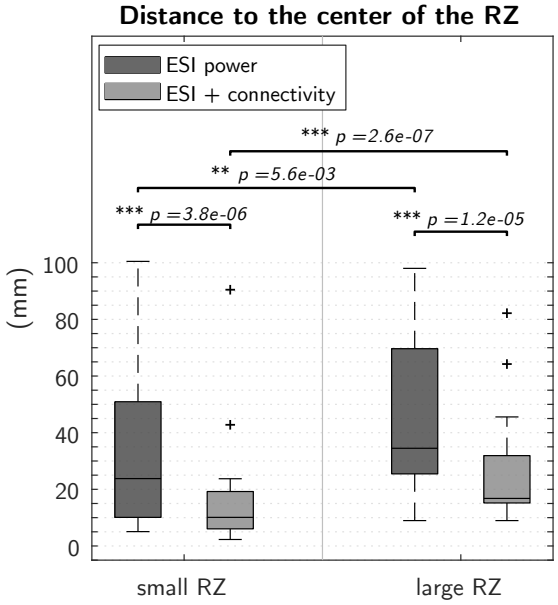

Figure 6.6: Distance to the center of the RZ for small and large resected volumes, for both methods.

6.4 Discussion

6.4.1 Performance

In this Chapter, we found that ESI with subsequent FC is superior to localize the SOZ from noninvasive ictal EEG recorded using a clinical setup ($\leq$ 32 electrodes), compared to ESI alone. We were able to indicate the SOZ inside the RZ and within 10 mm of the border of the RZ in 72.1% and 93.7% of the seizures, respectively. In 66.7% of the patients, all seizures were localized inside the RZ, and in 85.2% of the patients, all seizures were localized within 10 mm of the RZ. In contrast, ESI power was concordant in only 30.6% (0 mm error) or 42.3% (10 mm error) of the seizures. In 18.5% of the patients, all seizures were localized inside the RZ. This number stayed the same for the 10 mm tolerance. We were able to show that, in this framework, FC has a significant added value compared to ESI alone. The results of ESI power were comparable to what was found by Pellegrino et al., where for ESI a

median localization error of 11 mm in a range of 0–87 mm was found, specifically when looking at small resections [209].

The superiority of ESI + connectivity over ESI power can be explained by two reasons. First, ESI power summarizes the time series of the selected network nodes into a single value, whereas ESI + connectivity investigates the time dynamics of the source signals. As a consequence, ESI + connectivity is probably better suited to deal with remaining artifacts and noise than ESI power. Second, ESI + connectivity allows localizing a driver that is more silent (less power) than the regions it influences.

Early SOZ localization studies mainly showed the feasibility of ictal ESI [168, 187, 250, 251] and indicated the potential added value in the presurgical evaluation of epilepsy [193]. However, in these studies, validation was performed in a more qualitative way, by assessing congruency between epilepsy diagnosis/surgery and localized SOZ on the lobar or sublobar level. During the last decade, with the emergence of more powerful forward modeling and inverse solution techniques, the quality and resolution of the solutions has increased to a degree that more quantitative, rigorous validation of ictal imaging methods is possible in terms of distance, correlation, spatial dispersion etc. To our knowledge, the first study reporting quantitative measures of SOZ localization quality was done by Ding et al. and dates from 2007, reporting a localization error smaller than 15 mm in approximately 87% of the seizures undergoing 31 electrode EEG recordings [195]. We found a localization error smaller than 10 mm in more than 90% of the patients. Other SOZ imaging studies reporting quantitative results made use of setups with at least 38 electrodes [196, 205, 209, 214, 246]. Several methodological differences between these studies can be found, such as the used forward model and inverse solution for ESI, the possible application of FC and the FC measures, the frequency band of interest, etc. Although all of them show promising results, a drop in performance was reported when fewer electrodes were used [205, 246]. We were able to increase the performance when using a lower density EEG setup by manually selecting and preprocessing adequate EEG epochs and limiting the analysis to the frequency band of interest of the seizure. Although this is clinically highly recommended, most clinics unfortunately still lack the equipment to do (long-term) EEG monitoring with more than 32 electrodes. This study is, to our knowledge, the first to achieve good performance based on low-density recordings, quantitatively validated

in a more extensive patient population group than those that were used before, paving the way for a clinical use of the technique.

6.4.2 Intra-patient robustness

The standard distance to the centroid of the localized seizures was significantly smaller for ESI + connectivity than for ESI power which points out that functional connectivity analysis enhances the robustness against intra-patient variability of ictal imaging. The measure was also lower than compared to a previous study that assessed spatial dispersion, both for ESI + connectivity and ESI power [209].

Although spatial dispersion is a good measure for intra-patient robustness, the example of PAT 8 showed that the useful information obtained by the spatial dispersion could be limited due to possible outliers in the data. Using this technique prospectively, we would not be able to discriminate true outliers from seizures that could possibly have originated elsewhere. Therefore, careful interpretation of the individual seizure results is required.

6.4.3 Subgroup analysis based on resected volume

Although we found that the ESI + connectivity method scored significantly better for large than for small resections, the median distance for small resections is, like for large resections, 0 mm, indicating that the method also performs well for small resections. Both the fact that no significant difference between the percentages of correctly localized seizures per patient was found and the fact that the distance to the center of the RZ was smaller for small resections, confirms that there is no actual difference in performance for small and large resections.

6.4.4 Considerations and limitations

Since interaction with a human expert is needed to select the ictal epochs, there is some subjectivity left in the methods and it remains to be investigated how this influences the results and how robust the method is for changes in epoch/FOI selection. In most patients with clear data and clear constant ictal discharges, we found that epoch selection is not critical and results are consistent over time and selected

fragment. Yet, it is harder to compare with artifactual seizures or seizures that have a changing pattern over time. Can the SOZ also be correctly determined once the seizure evolved to another pattern? A rigorous validation is needed for this epoch selection. One possibility could be to perform an automated deterministic epoch selection, based on the temporal and spectral behaviour of the EEG during the seizure. Such an automatic selection is not trivial because often it is hard to discriminate between artifact and ictal activity, because they can have similar morphology and can have an overlapping spectral content. Nevertheless, the goal of this study was to show that it is possible to localize or indicate the SOZ based on low-density ictal scalp EEG data consistently over many seizures, rather than to build a completely automated pipeline.

A method for SOZ localization should preferably be noninvasive, objective, fast, and accurate. First, since only scalp EEG and an MR image of the patient's head (to generate the individual head model) are needed, this method is noninvasive. Second, the pipeline is not completely objective yet, since the initial epoch and FOI selection require interaction with a human expert, as discussed above. After this initial input, though, there are no subjective parameters left. Third, we did not report results on the speed of the algorithm. However, it would be possible to build a completely automated pipeline, running calculations in the background (taking approximately one hour for a new patient and less than a minute for a new seizure of this patient). This way, only a few minutes of the epileptologist's time are needed for initial epoch and FOI selection. Lastly, we have found that the accuracy of ESI + connectivity is high. All these factors point out that the method could be a useful aid in the presurgical evaluation of epilepsy.

A limitation of the study is that we compared the selected SOZ and the resected area in the brain of the patient to test whether the method worked correctly. However, using the RZ as gold standard provides a suboptimal validation. First, it is often an overestimation of the real ground truth. If a patient is seizure-free, we can assume that the SOZ was somewhere inside the RZ, but we do not know exactly where. Second, the patient being seizure-free does not prove that a specific analyzed seizure truly originated in the RZ. Finally, error estimation using Euclidean distance does not take brain anatomy into account. It could be that e.g. for a small LE larger than 0 mm, an important fissure is crossed, possibly making the estimation uninformative. Therefore,

LE, defined as the Euclidean distance to the border of the RZ, is not a perfect measure for validation. Fortunately, most of the SOZ estimations in this study (for ESI + connectivity) were inside the RZ, making this limitation less of a problem. In future research, validation results could be correlated to brain anatomy and to findings of intracranial EEG (iEEG) recordings, which can provide a more precise truth. It needs to be evaluated whether both methods point to the same brain region, provided that the (iEEG) samples the SOZ.

The SOZ localized by our method consists of one grid point. This way, we give an indication of the location of the true SOZ, but not of its spatial extent. An interesting extension of the current method would be to also provide a measure for the spatial extent of the SOZ, which might be based on the power spectrum of the neighboring sources.

In this study, we only included patients that had Engel Class I outcome at least 1 year after surgery. This allowed for assessing the percentage of SOZs that are estimated inside or close to the RZ in seizure-free patients. However, we did not estimate the SOZ and compare this to the RZ in patients that were not rendered seizure-free (Engel Class II–IV). It is important, and part of future research, to investigate whether in these patients a SOZ differing from the RZ is found or not.

Although most included patients suffered from temporal lobe epilepsy, there were 3 patients with extratemporal epilepsy (PAT1, PAT8, PAT20). Also in these patients, the presented method performed generally well (LE 10 mm in 7/7 seizures for PAT 1; LE = 0 mm in 4/6 seizures for PAT 8 and LE = 0 mm in 12/12 seizures for PAT 20). Albeit not perfect, this indicates that the application domain of the approach lies beyond temporal lobe epilepsy. Actually, we did not find any apparent relationship between performance of the ESI + connectivity algorithm and patient characteristics, ictal patterns or EEG quality. More validation in a larger, more heterogeneous population group is required to confirm this, but this finding already points out the possibly wide application area of the method.

It could be argued that the model order of the TVAR model should be determined based on e.g. the Akaike Information Criterion (AIC) or Schwarz Bayesian Criterion (SBC). For some patients, we did calculate the optimal model order with the AIC for several seizures, and generally found a value between 4 and 10. Since the computation time substantially increased to calculate the optimal model order, we opted

to fix the model order to 10 taking into account the fact that a model order that is slightly too low (connections cannot be found) is worse than a model order that is slightly too high (usually insignificant) [252].

The spatial sampling of the grid in source space was 4 mm and the inverse solution was calculated with LORETA at each of these gridpoints. However, since LORETA offers a smooth solution, the true spatial resolution is worse than 4 mm. Yet, we need sufficient spatial sampling in order to make sure that the true SOZ is sampled. Other inverse techniques, such as beamformers, could provide more focal solutions (Russell and Koles, 2007), and thus with a higher spatial resolution. It would be interesting for future research to investigate the influence of different inverse solution techniques on the performance of ESI + connectivity.

6.5 Conclusion

We showed that it is possible to estimate the SOZ from clinical or low-density scalp EEG with high accuracy using ESI and subsequent functional connectivity analysis. Moreover, the proposed method is noninvasive and requires, after initial epoch and frequency selection, minimal user-dependent input. Altogether, the method could serve as a useful tool for SOZ localization in the presurgical evaluation of epilepsy. Larger studies are warranted, notably with more extratemporal epilepsies and localization correlation with a range of different outcomes.

6.6 Original Contributions

This study was presented in 2017 at the Alpine Brain Imaging Meeting (ABIM) [253], at the *Journées scientifiques Neurochirurgie* of the Geneva University Hospital [254], at the *Jahrestagung der Deutschen und Österreichischen Gesellschaften für Epileptologie und der Schweizerischen Epilepsie-Liga* [255], at the Annual Meeting of the Organization of Human Brain Mapping (OHBM) [256], at the International Conference on Basic and Clinical Multimodal Imaging (BaCi) [257], and at the 32nd International Epilepsy Congress (IEC) [258]. This chapter resulted in a paper that is published in the A1 journal NeuroImage: Clinical [259].

7

Influence of epoch selection and analyzed frequency band on SOZ localization

7.1 Introduction

In the previous chapters, we found that analysis of the epileptic network of an EEG epoch carefully selected close to the onset of the seizure allowed correct SOZ localization with high accuracy. In this chapter, we analyze the epileptic network before and after the seizure, as well as during later phases of the seizure. We answer the question whether network analysis can also provide correct localization during these other segments. This could be useful in case the seizure onset phase is completely obscured by artifact. Of course, during these different epochs, the frequency content changes. Seizures can evolve to faster or slower patterns and during the pre- and postictal period there is no apparent rhythmic seizure activity. Therefore, we investigate the influence of the frequency band in which the network analysis is done on the performance of the method. Finally, we propose a method to more objectively determine the frequency band of interest (FOI) of the ictal onset phase and the other phases of the seizure.

7.2 Methods

7.2.1 Patients

Patient selection was done from the database of Ghent University hospital based on following inclusion criteria, corresponding to PAT 1 – PAT 18 of chapter 6 (see Table 6.1):

1. drug-resistant epilepsy;
2. availability of EEG recordings of at least one seizure, recorded with at least 27 electrodes;
3. single resective surgery procedure of the supposed EZ;
4. surgical outcome Engel Class I with a minimal post-operative follow-up of 12 months;
5. availability of pre- and post-operative T1-weighted MRI.

From these patients, 4 'clear' patients were selected that:

1. have distinct ictal EEG patterns that allow lateralization of the epilepsy based on visual inspection;
2. have seizures which after the onset phase visibly spread or changed rhythm in the recorded EEG;
3. underwent a selective amygdalohippocampectomy as surgery, to guarantee a small and clear resection volume[1].

The details of these 4 patients can be found in Table 7.1. For easy comparison with chapter 6, we will keep the patient's numbering.

7.2.2 EEG Recording

The same EEG files as in chapter 6 were used. These were recorded during a long-term video EEG monitoring (Micromed, Treviso, Italy) lasting 3 – 8 days, using 27 electrodes. The sampling frequency was 256 Hz. Only seizures during wake were considered for further analysis, so that sleeping rhythms did not hamper the interpretation of the epoch selection, explained in the next section. For PAT 11, 6 seizures were recorded, of which 3 happened during wake and were considered for further analysis. PAT 14 had 4 seizures during recording, all during

[1] These patients are considered as clear-cut cases in clinical practice

wake. For PAT 15, 3/3 recorded seizures were during the awakened state and for PAT 17, 2 seizures were during wake, while in total 3 seizures were recorded.

Table 7.1: Patient details. PAT = patient number, Ep. = epilepsy, surg. = surgery, FU = follow-up, dur. = duration, LE = lobe epilepsy, R = right, L = left, T = temporal, F = frontal, P = Parietal, rhyt. = rhythmic, act. = activity, inf = inferior, HEM = hemisphere, elec. = electrodes, HIP = hippocampal, IED = interictal epileptiform discharges, y = year, m=month.

PAT	11	14	15	17
Ep. type	RTLE	LTLE	RTLE	RTLE
Onset age(y)	24	40	35	4
Surgery age (y)	50	49	42	18
Interictal EEG	RFT IED	LFT IED	RFT IED	RFT IED
Ictal EEG	RFT rhyt. θ act.	LFT rhyt. θ act.	RFT rhyt. δ act.	R HEM θ-δ act.
Invasive EEG	/	rhyt. low voltage δ act. with spiking on basal ant T grid elec. with early spread to HIP elec.	/	/
MRI	R HIP atrophy	LT, L precentral & inf P post-traumatic atrophy	R HIP atrophy	R HIP atrophy
FU dur. (m)	12	47	26	48

7.2.3 Epoch selection and preprocessing

Together with an experienced epileptologist (prof. K. Vonck), a (quasi) artifact-free epoch lasting between 1 and 5 s was chosen during the

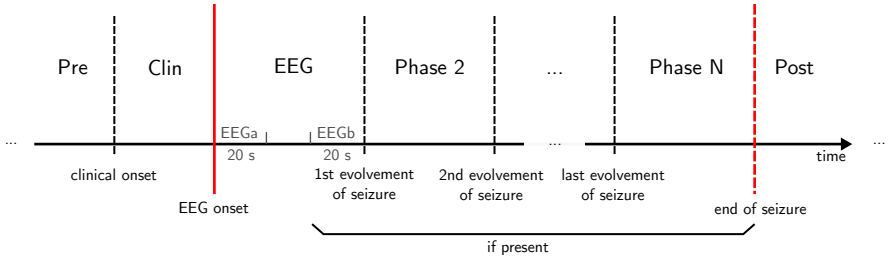

Figure 7.1: Illustration of the different phases during which an epoch was selected. Note that not every seizure necessarily evolves to other patterns or phases. The total number of phases N depends on the seizure.

beginning (within 20 s) of the following consecutive phases in or around every seizure considered for analysis:

- **Pre** preictal, i.e. right before the seizure occurs,
- **Clin** between the clinical and electrographic onset if they have a different timing,
- **EEG** after the electrographic onset, but before the ictal activity evolves,
- **Phase n** after every change in ictal EEG activity,
- **Post** postictal, i.e. right after the end of the seizure.

When the seizure onset phase (called EEG) lasted longer than 40 s, a second quasi artifact-free epoch was chosen during the last 20 s of this onset phase if the EEG quality was similar. In this case, the first epoch was called **EEGa**, while the second was called **EEGb**. The different phases are also schematically depicted in Fig. 7.1. Notice that it is possible that the phases Clin and EEG can be reversed and that not every seizure will exhibit every phase. It is e.g. possible that the clinical and EEG onset coincide, or that the initial rhythm of the seizure remains unchanged during the whole seizure.

The selected epochs were band-pass filtered between 1 and 30 Hz to remove baseline drift and to reduce high-frequency muscle artifacts[1]. An extra notch filter at 50 Hz was applied to filter out remaining power line noise. Bad quality channels were interpolated and eye blink

[1] In PAT 14, seizure 4 and PAT 20, seizure 2 an extra filter between 1 and 10 Hz was applied to remove remaining muscle artifact after initial filtering.

artifacts were removed using ICA [32], with the restricted fast ICA [247] implementation in BrainVision Analyzer on the available EEG channels. Finally, the selected epochs were common average referenced.

7.2.4 From EEG to SOZ

We estimated the SOZ from the different phases of all seizures using the "ESI + connectivity" methodology explained in the two previous chapters. To summarize, ESI was applied on the selected epoch based on an individual 6-tissue head model as forward model and LORETA was used as inverse solution. The solution space was constructed as a uniform three-dimensional grid in the gray matter of the patient with a spacing of 4 mm. From the reconstructed activity, local hotspots were selected as network nodes for the subsequent connectivity analysis. Each network node had 3 corresponding time series representing its behavior in the x, y, and z-direction. These 3 time series were combined into one using the time-series associated with the largest singular value of Singular Value Decomposition (SVD) [115]. Next, functional connectivity analysis based on Granger causality was applied on the time-series of the selected network nodes. Therefore, the data was modeled by a Time-Varying Multivariate Autoregressive (TVAR) model, of which the coefficients were estimated using the Kalman filtering algorithm [148, 149], with a model order of 10, an update coefficient of 10^{-4} and a smoothing factor of 100, as in chapter 6. From the time-varying transfer matrix $\mathbf{H}(f,t)$ of the model, the spectrum-weighted Adaptive Directed Transfer Function (swADTF) [153] was calculated in a frequency band of interest (FOI) $[f_1 \quad f_2]$ with a resolution of 0.1 Hz. The choice of the FOI will be discussed in the next section. Finally, the outdegree of every network node was calculated as the sum of the swADTF values to every other network node. The node with the highest outdegree was selected as presumed SOZ.

7.2.5 Analyzed frequency bands

In chapter 5, the connectivity analysis was done in the complete 1 – 30 Hz frequency band. Since this seemed inappropriate for SOZ localization from low-density EEG recording setups, we selected a FOI based on the fundamental seizure frequency in chapter 6.

In this chapter, we will perform the connectivity analysis in different frequency bands to investigate the influence of the frequency band on the performance of the algorithm. The chosen frequency bands are based on two properties. On the one hand, pre- and postictal EEG do not have a seizure frequency, and therefore some generic bands should be investigated. On the other hand, as the EEG evolves throughout the seizure, the frequency content will possibly change as well, and the chosen frequency band can be updated based on the new patterns. These considerations gave rise to following frequency bands which were used for connectivity analysis:

- 1 – 30 Hz
- δ, θ, α, β and γ[1] band
- FOI of the initial ictal activity, before evolvement; further called 'ictal onset FOI',
- every ictal phase (EEG, Phase 2, Phase 3, Phase 4) in the FOI for this phase; further called 'own phase FOI'.

In chapter 6, the FOI of the ictal activity was based on the fundamental seizure frequency identified by visual inspection of the spectrum of the global field power of all channels. Here, we propose a more objective method that is not influenced by the possible subjective interpretation of visual inspection. Since all of the analyzed seizures showed clear lateralization in the EEG, channels with clear ictal activity could be selected. A channel for which the ictal activity was (most) prominent was selected and the power spectral density (PSD) was estimated using Matlab's implementation of Welch's overlapped segment method between 1 and 30 Hz with a resolution of 0.05 Hz, using the default 8 segments with an overlap of 50%. The frequencies f_1 and f_2 corresponding to the lower and upper limit of the full width at half maximum of the prominence of the highest peak in this spectrum were selected to define the FOI $[f_1 f_2]$. This is shown in Fig. 7.2. If $1\,\text{Hz} \leq f_1 \leq 2\,\text{Hz}$, f_1 was rounded to 1 Hz, to account for possible spectrum underestimation due to the previous 1 – 30 Hz filtering. We did not detrend the data to eliminate the typical $1/f$ spectrum behavior, since this resulted in overestimation of the peak widths. However, in some spectra, the typical $1/f$ behavior of the EEG obscured the

[1] Note that for analysis in the γ band, the 1 – 30 Hz band pass filter was not applied.

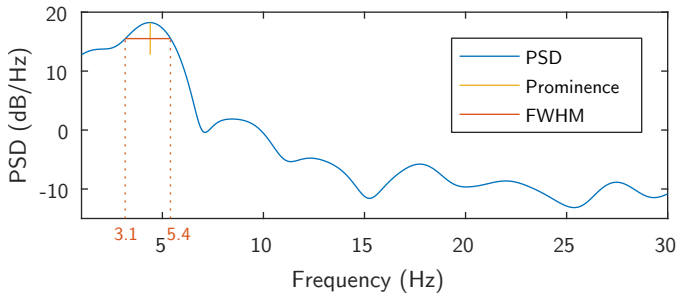

Figure 7.2: The full width at half maximum (FWHM) of the prominence of the highest peak is used to define the FOI.

peak corresponding to the seizure frequency. In those cases, the second highest peak was selected.

7.2.6 Validation

To investigate whether theoretically a correct localization can be obtained based on the ESI + connectivity analysis of a specific epoch, we determined the distance between the border of the RZ Resected Zone (RZ), segmented from the post-operative MRI and coregistered to the solution space, and the closest selected source after ESI of this epoch. Executing the subsequent connectivity analysis is only useful when at least one of the selected sources is inside or close to the border of the RZ. For the epochs for which this was the case, we carried out the subsequent connectivity analysis and estimated the SOZ using all described frequency bands. Each estimation resulted in one point or network node in solution space. To evaluate the SOZ estimation, we calculated the distance between the obtained point and the border of the RZ, called the localization error (LE). If the selected network node was inside the RZ, the LE was set to zero.

7.3 Results

7.3.1 Epoch selection

Table 7.2 lists the selected epochs in all seizures of every included patient. In all the recorded seizures, the clinical seizure onset happened before

Table 7.2: Overview of analyzed epochs. Pre = preictal; Clin = after clinical onset, but before electrographic onset; EEG = after electrographic onset, before ictal activity evolves; Phase 2 = spread in same hemisphere or faster ictal activity; Phase 3 = bilateral; Phase 4 = back to unilateral or slower bilateral activity; Post = postictal; a, b = EEGa and EEGb epoch were considered. N.A. = data not available, / = phase was not present, R = right, HEM = hemisphere.

	Pre	**Clin**	**EEG**	**Phase 2**	**Phase 3**	**Phase 4**	**Post**
11.1	x	x	x	/	x	/	x
11.2	x	x	x	/	x	/	x
11.3	x	x	x	/	x	/	x
14.1	x	x	a, b	/	x	/	x
14.2	x	x	x	/	x	/	x
14.3	N.A.	x	x	/	x	/	x
14.4	x	x	x	/	x	/	x
15.1	x	x	x	spread in R HEM	x	back to unilateral	x
15.2	x	x	x	faster	/	/	x
15.3	x	/	x	faster	/	/	x
17.1	x	x	a, b	faster	x	slower bilateral	x
17.2	x	x	x	/	x	slower bilateral	x

or simultaneous with the electrographic onset. We found a maximum of 3 seizure evolvements, leading to 4 different ictal phases. Phase 2 groups the ictal rhythms that evolved from the initial ictal activity but remained in the same hemisphere, in phase 3 there is bilateral spread and phase 4 means that the bilateral activity slowed down or became unilateral again. The seizure onset phase of the first seizure of PAT 14 and the third seizure of PAT 17 lasted longer than 40 s and the EEG quality remained similar, so a second epoch was selected, shown by 'a, b' in the table. Not all seizures expressed all phases, this is indicated with '/'. For PAT 14, seizure 3, the preictal data was not available since the data was cut just prior to the clinical onset to archive.

Fig. 7.3 shows the different phases schematically, together with the selected epochs for the first seizure of PAT 11 as an example.

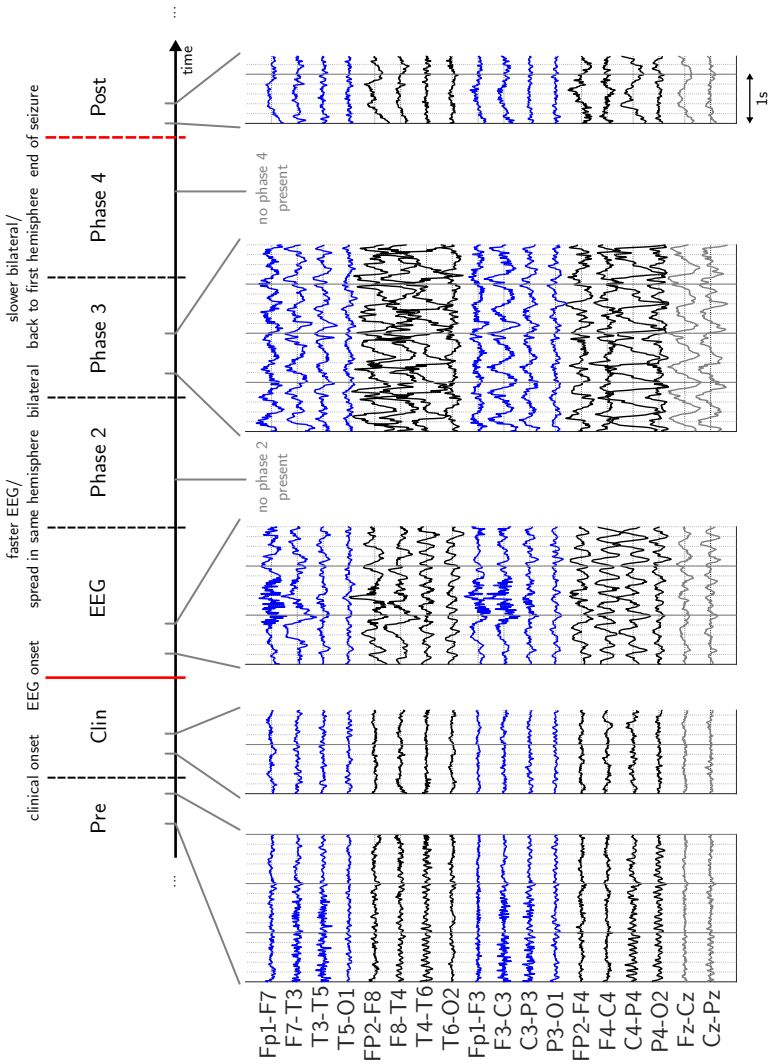

Figure 7.3: The different phases during which epochs were selected and an illustration of this epoch selection for the first seizure of PAT 11. This patient showed no Phase 2 or Phase 4 evolvements.

7.3.2 FOI selection

In Table 7.3, the FOI bands, selected like explained in section 7.2.5, associated with every phase of the ictal activity are shown for every analyzed seizure. No separate FOI was calculated for the EEGb phases of PAT 14 and PAT 17, since the ictal pattern remained constant.

Table 7.3: Overview of the FOI calculated for every phase of each analyzed seizure. '/' indicates that this seizure did not show this phase, * means that the second highest peak in the spectrum was taken instead of the first (due to $1/f$ behavior).

	EEG	**Phase 2**	**Phase 3**	**Phase 4**
11.1	2.4 – 5.7 Hz	/	7.5 – 8.3 Hz*	/
11.2	1.0 – 5.9 Hz	/	1.0 – 3.7 Hz	/
11.3	2.0 – 4.8 Hz	/	1.0 – 2.4 Hz	/
14.1	1.0 – 4.3 Hz	/	1 – 5.7 Hz	/
14.2	5.1 – 6.8 Hz	/	7.5 – 8.5 Hz*	/
14.3	5.1 – 6.4 Hz*	/	4.9 – 6.4 Hz*	/
14.4	1.0 – 4.2 Hz	/	6.6 – 7.8 Hz*	/
15.1	1.0 – 3.1 Hz	4.9 – 7.0 Hz	1.0 – 3.9 Hz	1.0 – 4.1 Hz
15.2	3.1 – 4.3 Hz	2.5 – 7.8 Hz	/	/
15.3	1.0 – 4.1 Hz	9.5 – 11.6 Hz*	/	/
17.1	1.0 – 4.6 Hz	1.0 – 5.0 Hz	3.7 – 5.9 Hz	1.0 – 4.5 Hz
17.2	1.0 – 4.0 Hz	/	1.0 – 4.4 Hz	1.0 – 3.3 Hz

7.3.3 Performance

7.3.3.1 Overall performance

For all EEG epochs considered in this study, ESI identified one or more sources inside the RZ, except for 2 epochs (14.1 PRE and 14.1 POST) for which the closest source was 13 mm away from the RZ. This indicates that subsequent connectivity analysis was meaningful for, and hence applied to, all considered epochs.

The LEs obtained for all selected epochs (EEGa in case of two selected epochs during the onset phase of the seizure) analyzed in each of the frequency bands are summarized for all patients in Fig. 7.4 and per patient in Fig. 7.5.

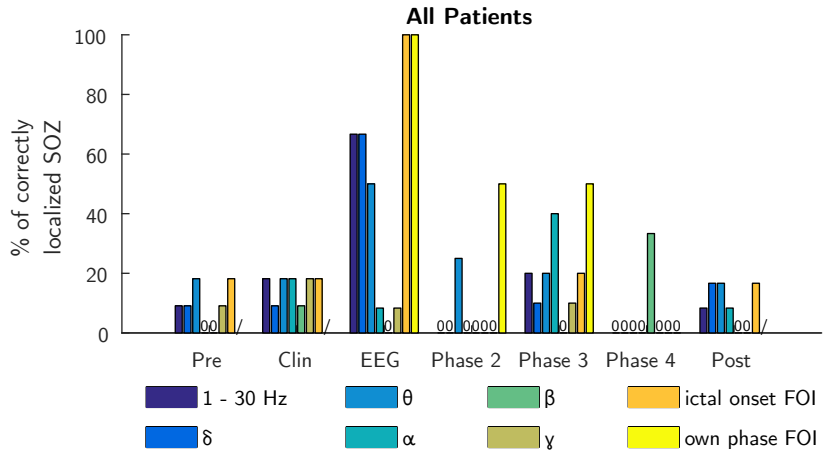

Figure 7.4: A summary of the percentage of correctly localized seizures per phase and per analyzed frequency band. A '0' indicates that none of the seizures were localized correctly, a '/' indicates that there was no data for this epoch.

Optimal performance was found when analyzing the onset phase (before visually identifiable spread of rhythm changes) of the seizure in the frequency band containing the fundamental seizure frequency. In this case, 100% of the seizures were correctly localized inside the RZ. This number dropped to 50% when phase 2 (colateral spread or faster EEG) or phase 3 (bilateral spread) were analyzed in their own frequency band of interest. For the other phases, no good localization was found in any of the frequency bands.

7.3.3.2 Performance per frequency band

The exact LEs can be found in Table B.1 to Table B.8 of Appendix B for every analyzed frequency band separately. In what follows, we will detail the results per frequency band.

Connectivity analysis in the complete $1 - 30$ Hz during the onset phase allowed correct localization of the SOZ in 67% of the analyzed seizures (between 50% and 100% on the patient level) . For the other phases, no correct localization was found, with some exceptions, mainly in PAT 14.

Connectivity analysis of the δ and θ band resulted in a correct SOZ estimation in 67% and 50% of the seizures, respectively, during the onset phase of the seizure. These bands partly overlap with the fundamental

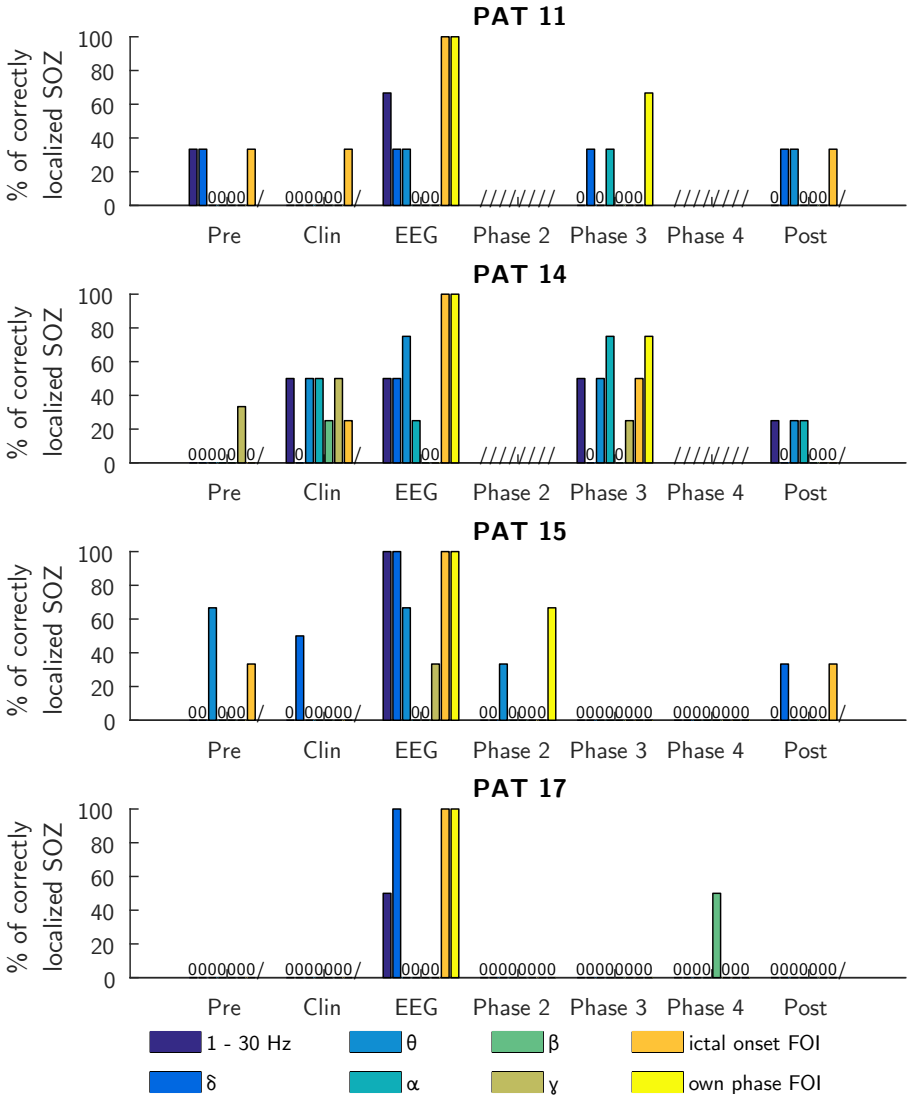

Figure 7.5: The percentage of correctly localized seizures per phase and per analyzed frequency band, shown per patient. A '0' indicates that none of the seizures were localized correctly, a '/' indicates that there was no data for this epoch.

seizure frequency of the onset of the seizure listed in Table 7.3. The same effect can be seen in the bilateral part of the seizure (Phase 3) analyzed in the α band, where an LE of zero occurred (in 40% of the seizures, mainly for PAT 14) when the FOI of this phase is inside the α band.

For the other frequency bands and selected epochs, no correct SOZ localization was found, again with some exceptions. PAT 17 showed remarkably few correct localizations in the generic EEG bands, except for the δ band during the onset phase and the β band during Phase 4.

When analyzing the epochs using the FOI for the onset phase of the seizure, the SOZ was correctly determined during this onset phase in all analyzed seizures. However this result is better than in the complete 1 – 30 Hz band, the difference is not significant (Wilcoxon signed-rank test, $p = 0.1250$). For the other phases, no more than 20% of the seizures were correctly localized using the FOI of the onset phase.

If every seizure phase is analyzed in its own FOI, we see that the percentage of correctly localized seizures increases to 50% in Phase 2 (faster EEG or spread in colateral hemisphere) and Phase 3 (bilateral EEG). It is, however, impossible to correctly estimate the SOZ during Phase 4 of slower bilateral or unilateral EEG. This is in contrast with the β band, for which a correct localization during Phase 4 was found for 1 of the 2 seizures of PAT 17.

7.3.3.3 EEGa vs. EEGb

The LEs of the seizures for which an EEGb epoch was selected (PAT 14, seizure 3 and PAT 17, seizure 1) are shown in Table 7.4 for all analyzed

Table 7.4: LEs in mm of the epochs selected during the beginning and the ending of the EEG onset phase in the third seizure of PAT 14 and the first seizure of PAT 17, for all analyzed frequency bands. The epoch during the ending of the EEG onset phase has affix b.

	1 – 30 Hz	δ	θ	α	β	γ	**ictal onset FOI**
14.3	51	13	0	46	35	51	0
14.3b	0	0	0	35	78	65	0
17.1	0	0	68	68	68	44	0
17.1b	68	0	68	68	59	57	0

frequency bands. For comparison, the LEs obtained for the epoch during the beginning of the EEG onset phase (EEG) are shown as well. Correct localization is found for both the EEG and EEGb epoch in the ictal onset band. For PAT 14, analysis of the EEGb epoch resulted in correct localization in the 1 – 30 Hz and δ band, whereas it did not for the EEG epoch in the beginning. Both epochs resulted in a correct estimation in the θ band. For PAT 17, correct localization was found in the 1 – 30 Hz for the epoch in the beginning, but not for the epoch at the end of the seizure onset phase. Analysis of the δ band resulted in correct localization in both epochs. For the other epochs, no correct localization was found.

7.3.4 Patient Example

As an example, we show Fig. 7.6 which depicts for every phase of the first seizure of PAT 11 the selected network nodes. The size of the nodes is proportional to their outdegree, calculated in the ictal onset FOI for the Pre, Clin, EEG and Post phase, and in the own phase FOI for the bilateral part. As can be seen, during the Clin, EEG onset and the bilateral phase, the node inside the resected zone is the largest and hence has the highest outdegree and is correctly selected as estimation for the SOZ. During the other phases, approximately the same nodes were selected after ESI, but the one inside the RZ does not have the highest outdegree and is therefore not selected as estimation for the SOZ. In this example, the localization error is zero for the phases Clin, EEG and Phase 3. The outdegrees increased in the EEG onset phase and increased even more during Phase 3. This observation could, however, not be made in general for other seizures of this and the other patients. Nevertheless, for each of the patients, the selected nodes were (quasi) stable over seizures and epochs.

7.4 Discussion

In this study, we investigated the influence of epoch and frequency band selection on the performance of SOZ localization using a combination of ESI and connectivity analysis. Optimal performance was found when analyzing an epoch during the electrographic onset phase. This performance declined when later phases were analyzed. No good

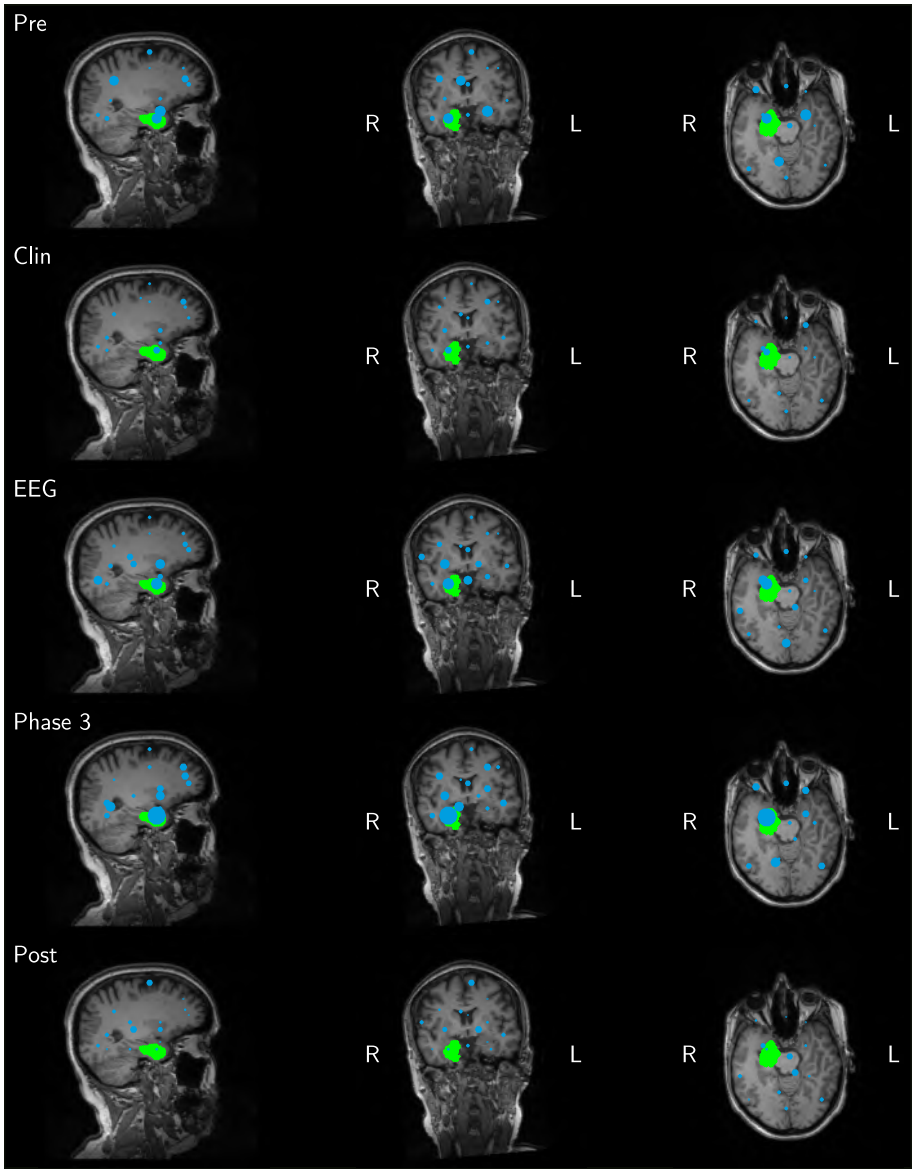

Figure 7.6: Network nodes found during the different phases of seizure 1 of PAT 11. The size of the nodes is proportional to the outdegree of that node, normalized to the maximal outdegree found over all phases of this seizure.

localization was found for the pre- and postictal phases. The fact that performance decreases in later phases of the seizure can be due to changes in the epileptic network. Although (quasi) the same nodes were found for every epoch of the same seizure, the connections, and as a consequence the outdegree, changed over time. This is suggestive (though, confirmation for a different range of regularization parameters is necessary) for a network that is (quasi) stable in its nodes, but dynamic in its connections. This is supported by Elshoff et al., who found a star-shaped network topology in the beginning of seizures, whereas a circular topology of similar sources was found in the middle of seizures [196]. Other studies, based on iEEG recordings, claimed that network dynamics change during the course of seizures as well [260–262]. Another possibility is that the initially triggering region stops behaving abnormally, but that the other regions continue to seize. This way, the originally driving region cannot be localized correctly, but one of the regions that is still seizing may be found instead. Furthermore, we found that it is impossible, with the method used in this study, to estimate the SOZ with high accuracy based on pre- or postictal EEG data.

Performing the analysis of the onset phase of the seizure in the complete 1 – 30 Hz band gave rise to generally worse results, yet the difference did not reach significance. Despite this observation, we would advise performing the analysis in the frequency band of interest, since better results are obtained. This is probably due because more spurious connections caused by noise are eliminated. Analysis in other frequency bands did not add any extra information, it was mostly successful if the band (partially) overlapped with the band of the fundamental seizure frequency. This was mainly the case in the δ and θ band.

We proposed an approach to calculate the FOI around the fundamental frequency band. Since SOZ estimation was correct in 100% of the cases during the seizure onset phase, we confirmed that this objective method is valid and could replace the visual selection used in chapter 6. It should be mentioned, however, that all patients included in this study had clear ictal rhythms and that EEG channels showing clear ictal activity could be selected easily. In cases where the ictal rhythms or the FOI are not easily identifiable, one could still opt for analysis in the complete 1 – 30 Hz band.

We were able to select a second epoch to the end of the EEG onset phase in two seizures. In both of these seizures, we found correct localization

using the ictal onset FOI. In combination with the other results, this suggests that it is crucial to select an EEG epoch during the onset phase of the seizure, but that it is less important when exactly the epoch is chosen during this phase, as long as the quality of the EEG is reasonable. This would mean that we can wait some time after seizure onset to select an epoch with fewer artifacts, given that the ictal pattern did not change. However, validation in more seizures is necessary to confirm this hypothesis. By extension, it would be interesting to study epochs in the beginning, middle and end of seizures of patients who have seizures that remain constant or do not evolve over the complete course of the seizure.

If we could confirm that the epoch can be chosen anytime during the onset phase, it still remains important to delineate this phase. Future research could not only be aimed at seizure detection, but also at seizure evolvement detection to automatically or objectively delineate these phases. This could possibly be achieved with help of functional connectivity measures since we found that the epileptic network changes throughout the seizure.

Although epoch selection during the onset phase of the seizure is important, sometimes the complete onset phase of a seizure can be artifactual. An analysis of the later parts of these seizures could still be useful for clinical practice if a hypothesis about the SOZ already exists, in order to confirm it.

7.5 Conclusion

We can conclude that SOZ localization using ESI + connectivity is optimally performed during the initial phase of the seizure. We proposed a method to select a frequency band of interest around the fundamental seizure frequency and results are best when using this band for analysis. However, whenever necessary, analysis in a broader band and/or of a later epoch could possibly provide useful information as well.

8 Conclusions and future perspectives

In this final chapter, we summarize the work performed in this dissertation and outline future perspectives. We discuss the main contributions of our work followed by the conclusions that can be drawn from them. New research questions inevitably arise when studies are done, and therefore we discuss some future research possibilities. Finally, we end this chapter and book with a final conclusion.

8.1 Summary

The goal of this dissertation was to develop a method to localize the SOZ in focal epilepsy patients in a noninvasive way, using scalp EEG recordings. Our approach consisted of two main steps. First, ESI was performed on an EEG epoch to reconstruct the active brain sources that gave rise to the measured signals. Second, we applied functional connectivity analysis on the most active brain sources, in order to find the driver behind the epileptic network. This driver was used as an estimation of the SOZ. First, this approach was tested in simulations. Next, retrospective validation was done using real patient data in which the SOZ estimation was compared to the ultimately resected zone of the patient. We were able to show that this method can localize the SOZ with high accuracy, and that functional connectivity analysis has an added value since this combined approach outperformed localization based on ESI only. It is, however, important to select an EEG epoch during the seizure onset phase, before the network has evolved.

In Chapter 5, we applied the proposed combination of ESI and functional connectivity analysis on simulated ictal EEG and on ictal high-density EEG recordings of five patients. The first 3 s of a seizure (simulated or real) were selected for analysis. Connectivity analysis was done in the frequency band of 1 – 30 Hz. In both datasets, we found that ESI followed by connectivity analysis outperformed ESI alone, in which the source with highest power was selected as SOZ estimation. Performance of ESI followed by connectivity analysis was high, but it decreased when fewer electrodes were used for analysis. It was concluded that the method can serve as a useful, objective tool in the presurgical evaluation, given that the seizures are recorded with sufficient electrodes.

Yet, a lot of hospitals still lack the equipment to perform high-density EEG recordings. Moreover, the probability of capturing a seizure during a high-density EEG recording is rather low, since these registrations are generally shorter than long-term video-EEG monitorings because of patient comfort reasons. Therefore, we adapted the method in order to obtain good performance in seizures recorded with a clinical EEG setup as well. This was done in Chapter 6. Instead of strictly selecting the first 3 s of a seizure, we chose a (quasi) artifact-free epoch lasting 1 to 5 s during the beginning of the seizure. Next, connectivity analysis was limited to the frequency band of the rhythmic activity in the EEG generated by the seizure, determined visually. We validated this adapted approach retrospectively in 111 seizures of 27 patients who were rendered seizure-free after surgery. Again, we found that ESI followed by connectivity analysis outperformed localization based on ESI alone. The large cohort of seizures allowed to make this comparison statistically significant. ESI followed by connectivity analysis resulted in a SOZ estimation within 10 mm of the border of the resected zone in 93.7% of the seizures. Furthermore, the spatial dispersion of the SOZ estimation of different seizures per patient remained low. We confirmed our conclusion of the preceding chapter that this method could serve as a useful tool in the presurgical evaluation, but now standard long-term EEG monitoring can be used and seizures recorded with high-density EEG are not necessary. However, user-dependent input for the initial epoch and frequency selection is required.

Finally, we investigated the importance of the epoch and frequency band selection in Chapter 7 to investigate whether we can also find the driver of the epileptic network just before, after or during other phases of the seizure and whether limiting the analysis to a specific frequency band is

necessary or not. In terms of epoch selection, best results were obtained when an epoch was selected during the onset phase of the seizure, before the ictal patterns have evolved. We selected epochs during the beginning and ending of this phase, and based on the results we suggested that the epoch can be chosen anytime during the onset phase, as long as the EEG quality is sufficient. Out of 12 analyzed seizures in this study, 10 evolved to a bilateral pattern. During this bilateral phase, correct SOZ localization was found in 50% of the seizures. Whenever the data during the electrographic onset phase is very artifactual and a hypothesis about the SOZ already exists, analysis of the bilateral phase could still be used to confirm the hypothesis. Yet, the results should be interpreted with extra care in this situation. Furthermore, we found that it is impossible to obtain a trustworthy SOZ estimation with this method during the preictal or postictal period. In terms of the frequency band, best results are obtained when the analysis is limited to the seizure frequency band corresponding to the analyzed ictal epoch. We offered a technique to calculated this frequency band. Although performance was lower when using the $1 - 30\,\mathrm{Hz}$ band, the difference did not reach significance and this band can possibly be used for analysis whenever the seizure frequency band is unclear.

8.2 Future research directions

The future research perspectives for this work are based on three main questions:

1. How to get this method to clinical practice?
2. How can we improve or gain more information from the method?
3. How can this research contribute to other research fields?

Although the method performed well in our retrospective studies, more validation steps are needed before it can be adopted in the standard presurgical evaluation protocol with the same importance as the other presurgical investigations. Retrospectively, a larger, more heterogeneous population group should be studied. Especially more extratemporal lobe epilepsy patients should be included. If possible, links between performance and patient or EEG characteristics should be detected and

investigated in order to identify patient groups for whom the analysis might be (un)useful. Furthermore, extra confirmation is needed for the influence of epoch/frequency band selection. In this work, validation was done in patients who benefited from epilepsy surgery and we assessed in how many patients we could correctly localize the SOZ inside the resected zone (sensitivity). Future research should also be aimed at investigating patients that had no benefit from surgery. Is, in these cases, the SOZ estimation localized outside of the resected zone (specificity)?

Not only retrospective validation should be done, but also a prospective study could be set up, to investigate the true added value of the method as a tool in the presurgical evaluation. This should answer the question as to what extent the proposed method can actually help in the decision-making process of the presurgical evaluation in terms of speed, confidence, objectivity and accuracy.

Ideally, a clinical study using the STARD (Standards for Reporting of Diagnostic Accuracy) criteria for studies on diagnostic accuracy should be performed [188, 219].

Further improvement could be the implementation of automated seizure and seizure evolvement detection, and by extension completely objective and/or automated epoch and frequency band selection which would allow complete automation of the method since no human interaction is needed anymore. Seizure detection is a wide research area, in which much progress has already been made [263, 264]. To our knowledge, the detection of seizure evolvement would be new. Since we found evidence that the epileptic network changes at the beginning and during the evolvement of the seizure, functional connectivity analysis could possibly be used for this. Automated and/or objective epoch and frequency band selection could be achieved with a method that looks both at frequency content and temporal morphology of the signals, in order to discriminate ictal activity from artifacts and background activity.

In this dissertation, the method for SOZ localization results in a point estimation. Future research could aim at adding an estimation of the extent of the SOZ as well. The three-dimensional power distribution after ESI or the correlation of the time-series of neighboring solution points or techniques such as Maximum Entropy on the Mean (MEM) [236] or Source Imaging based on Structured Sparsity (SISSY) [265] could be used for this. If it would be possible to estimate the extent of

the SOZ, it could be studied whether the method could lead to smaller resections.

The method was validated by comparison with the ultimately resected zone of the patient. However, this resected zone can be an overestimation of the true SOZ. Therefore, validation by comparison with iEEG findings could provide more precise information, both in the single point estimation and in the spatially extended estimation, although the limited spatial sampling of iEEG could be an issue.

Finally, it could be assessed how the techniques of this dissertation can be used in other (epilepsy) research fields. One option is to investigate how the network nodes and their connections relate to the type of epilepsy, the location of the SOZ or the performed surgery, in order to get more profound insights into the pathophysiology of epileptic networks. A second option is to help the diagnosis of epilepsy. Can these connectivity measures enhance (automated) diagnosis of several types of epilepsy, as was done with resting-state EEG for TLE [266]? A third option would be the use of this method as a biomarker for the efficacy of AED treatment. Clemens et al. provided first evidence that the abnormal epileptic brain networks are normalized to a certain extent when patients are successfully treated with an AED [267]. But is there a difference in the networks of patients who do and who do not respond to AEDs? Can this difference be used to predict AED outcome? A final option would be to take into account the time delays of the found connections and to integrate this with structural connectivity measures in order to obtain a delay-resolved connectome [268]. Usually, structural connections are considered instantaneous and studies are based on all possible structural connections [269–271]. Yet, the conduction speed along the axons is finite, so different delays exist between brain regions that are connected with shorter and longer and/or faster and slower neuronal fibres. Incorporating the delays as measured with functional connectivity could allow to clean or prune the connectome in order to be able to better study the collective dynamics of the (epileptic) brain at different time points.

8.3 Final conclusion

The method developed in this dissertation consists of a combination of ESI and functional connectivity analysis and is able to localize the

SOZ with high accuracy based on high- or low-density ictal scalp EEG recordings. The method is noninvasive and requires minimal user-dependent input and no special extra investigations. Therefore, it could be a useful tool to be included in clinical practice for SOZ localization in drug-resistant epilepsy patients. It is important to select an epoch during the onset phase of the seizure, and when fewer electrodes are available, the epoch and frequency band selection become more crucial. Given more research, the method could be made completely user-independent and automated. This kind of methods could eventually reduce the burden of the presurgical evaluation.

A
Results of the clinical SOZ localization study

Fig. A.1–A.3 show some examples of selected and preprocessed seizures of chapter 6. Table A.1 lists for every seizure of each patient the selected epoch with respect to the seizure onset time that was selected for further analysis. Also the frequency band of interest (FOI) and the possible additional preprocessing steps are shown.

Fig. A.4–A.10 show the spatial spread figures for all patients. In case that a patient had only one seizure, only the result for that seizure was shown, i.e. standard distance is 0 mm.

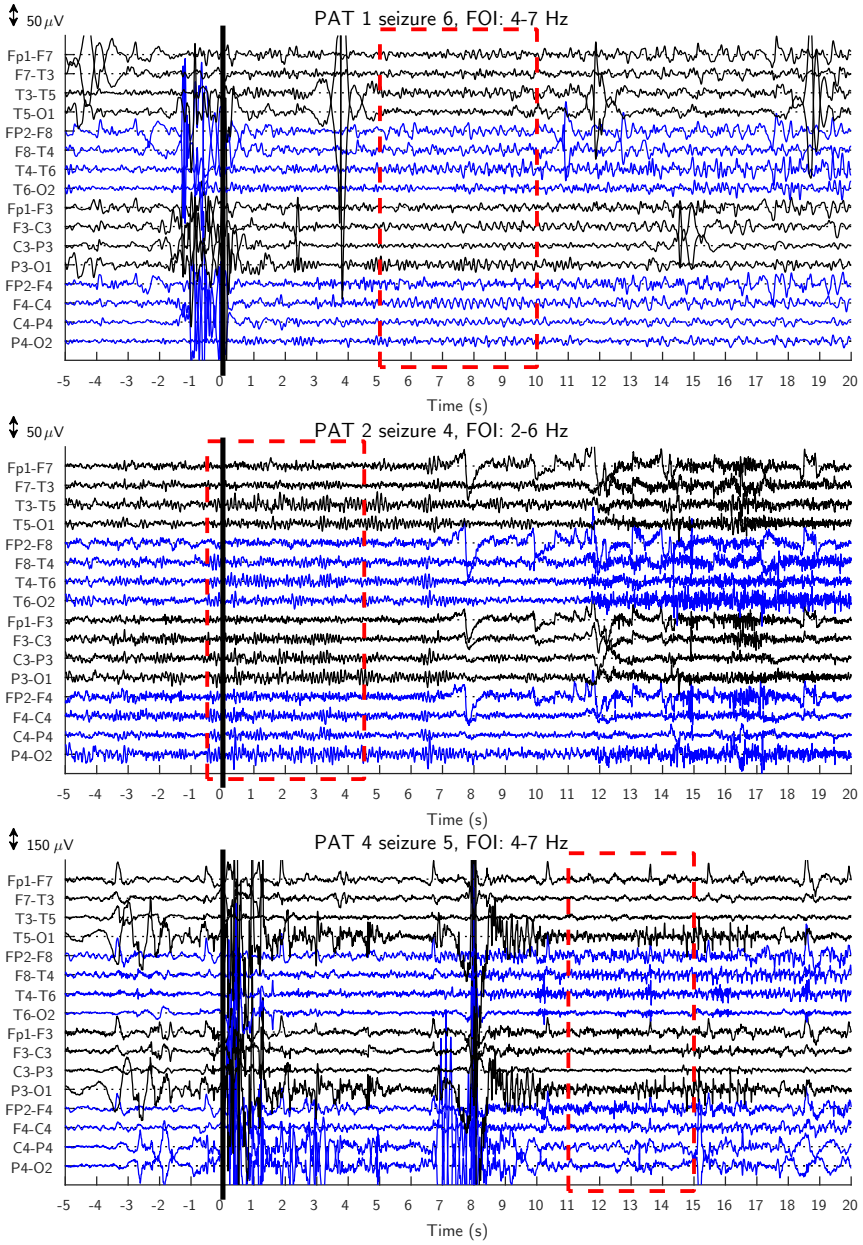

Figure A.1: Examples of epoch selection. A bipolar montage of the EEG from 5 s before until 20 s after seizure onset is shown. The red rectangle indicates the chosen time frame. The used frequency band of interest for analysis is shown in the title. Note that the actual segment selection also happened based on channels that are not shown in this montage (e.g. the midline electrodes).

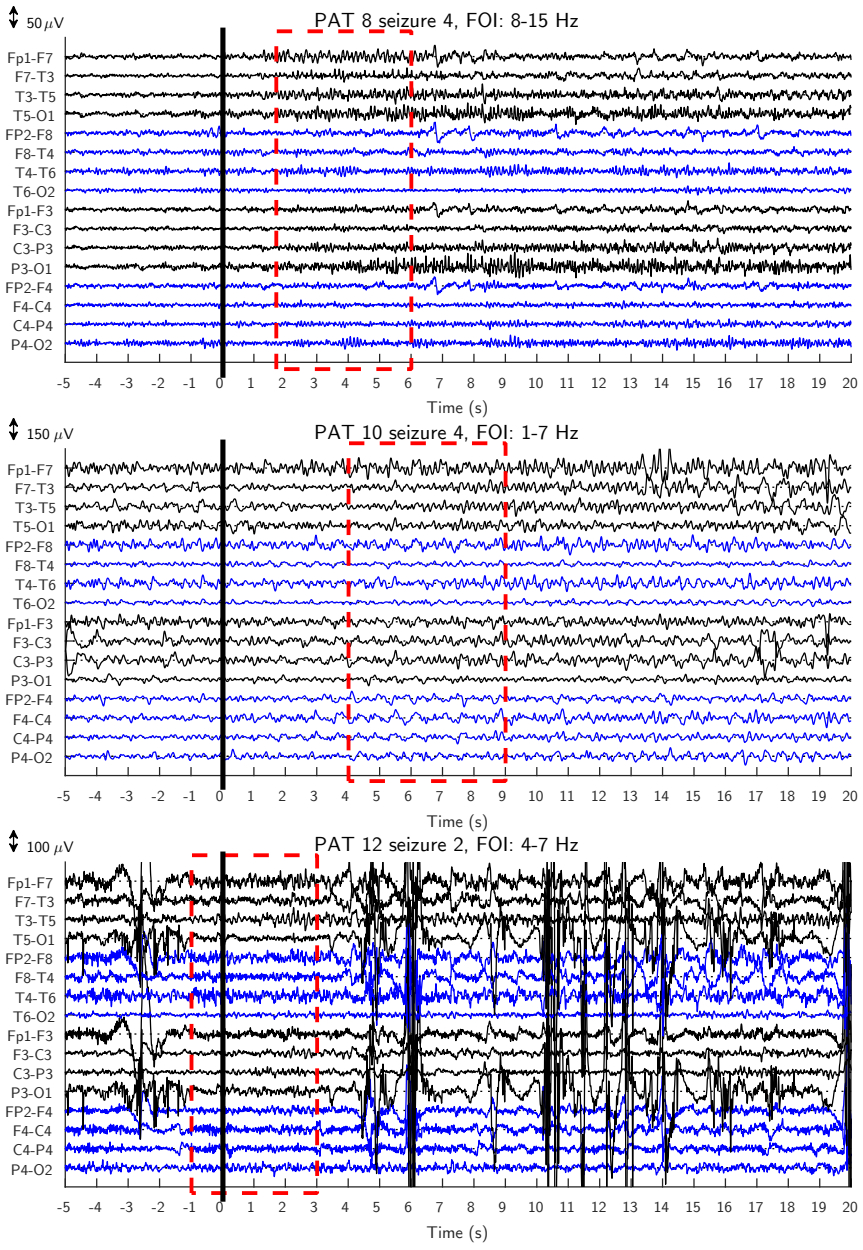

Figure A.2: Examples of epoch selection. A bipolar montage of the EEG from 5 s before until 20 s after seizure onset is shown. The red rectangle indicates the chosen time frame. The used frequency band of interest for analysis is shown in the title. Note that the actual segment selection also happened based on channels that are not shown in this montage (e.g. the midline electrodes).

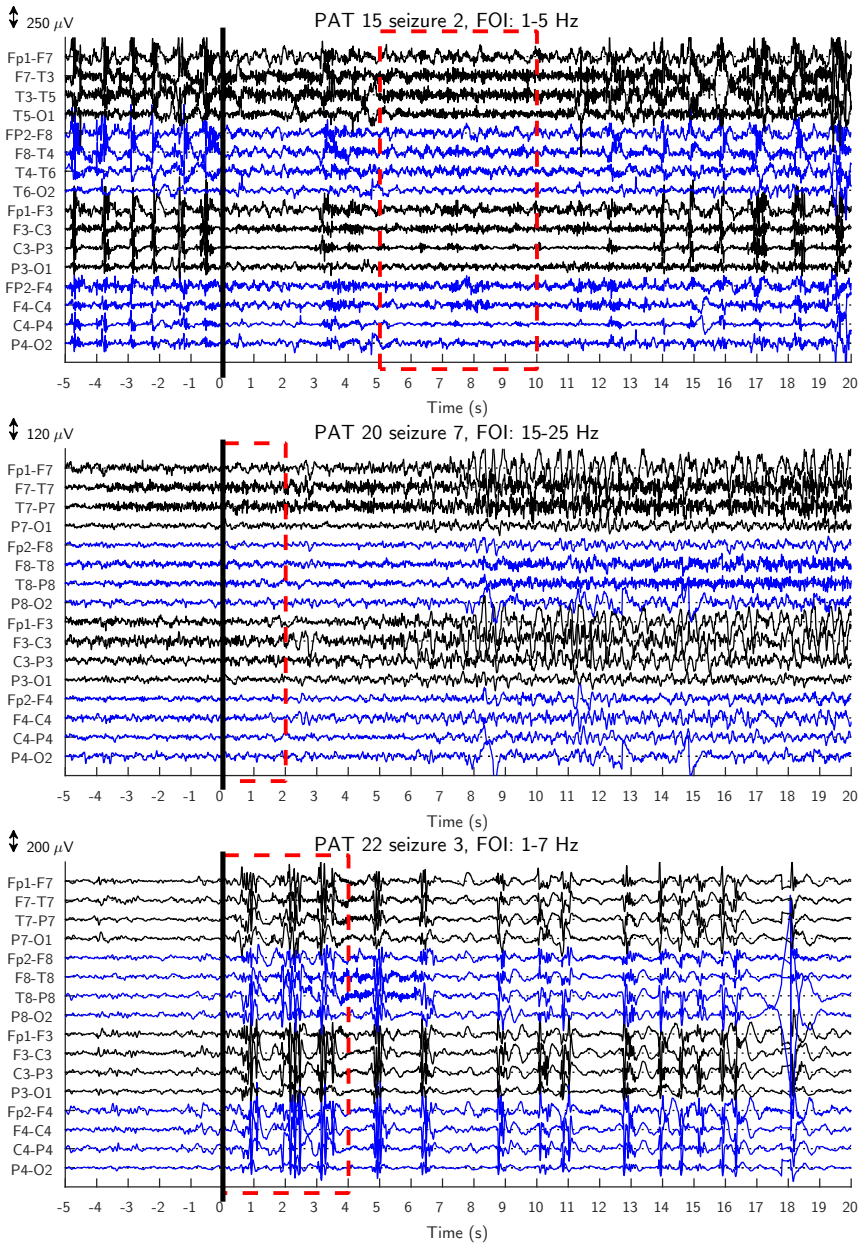

Figure A.3: Examples of epoch selection. A bipolar montage of the EEG from 5 s before until 20 s after seizure onset is shown. The red rectangle indicates the chosen time frame. The used frequency band of interest for analysis is shown in the title. Note that the actual segment selection also happened based on channels that are not shown in this montage (e.g. the midline electrodes).

Table A.1: Overview of the analyzed seizures for every patient. The selected epoch w.r.t. to the marked seizure onset (time of interest, TOI), the seizure frequency and possible extra preprocessing steps are mentioned. ICA was applied on clear eyeblink artifacts, unless mentioned otherwise. Interp = Interpolation, HB = heartbeat.

PAT		Seizure											
		1	**2**	**3**	**4**	**5**	**6**	**7**	**8**	**9**	**10**	**11**	**12**
1	**TOI (s)**	[1 5]	[-1 3]	[8.8 10]	[3 8]	[1.5 4]	[5 10]	[0 4]					
	FOI (Hz)	[4 7]	[4 7]	[4 7]	[1 7]	[4 12]	[4 7]	[4 12]					
	extra preproc.	-	-	filter 1-10 Hz	Interp T9	Interp T9, FT10	filter 1-10 Hz	Interp Fpz					
2	**TOI (s)**	[-2 1.5]	[0 3]	[1 6]	[-0.5 4.5]	[0 3.5]	[0 2]	[0 5]					
	FOI (Hz)	[12 15]	[1 8]	[1 8]	[2 6]	[2 8]	[2 6]	[1 8]					
	extra preproc.	Interp T5	-	ICA	-	-	-	-					
3	**TOI (s)**	[-2 3]	[-2 1]]	[3.5 8]	[0 5]								
	FOI (Hz)	[4 10]	[4 7]	[4 7]	[4 7]								
	extra preproc.	filter 1-10 Hz	ICA	Interp FT10, C3	-								
4	**TOI (s)**	[0 4]	[3 6]	[8 10]	[6 11]	[11 15]							
	FOI (Hz)	[4 7]	[4 7]	[4 7]	[4 7]	[4 7]							
	extra preproc.	-	Interp C3	Interp C5, O1, Oz	Interp T5, O1; ICA	-							
5	**TOI (s)**	[2.8 4.8]	[2 7]	[5 10]	[1 6]								
	FOI (Hz)	[4 8]	[4 8]	[4 8]	[4 9]								
	extra preproc.	Interp P4, T3	Interp T6	-	-								
6	**TOI (s)**	[-5 0]	[-5 0]	[-4 -2]	[-1.8 0.5]	[6 10]	[0 5]	[1 3.5]					
	FOI (Hz)	[8 15]	[8 15]	[8 15]	[8 15]	[4 7]	[3 10]	[3 10]					
	extra preproc.	ICA	-	ICA	Interp FT10	filter 1-10 Hz	filter 1-10 Hz	filter 1-10 Hz					

Table A.1: (continued)

PAT		Seizure											
		1	2	3	4	5	6	7	8	9	10	11	12
7	**TOI (s)**	[-1 1]	[11.1 12.8]	[18 20]									
	FOI (Hz)	[1 4]	[1 4]	[2 7]									
	extra preproc.	filter 1-10 Hz	filter 1-10 Hz	-									
8	**TOI (s)**	[0 3]	[-3 2]	[-3 2]	[1.7 6]	[0 3]	[0 4]						
	FOI (Hz)	[8 15]	[8 15]	[8 15]	[8 15]	[8 10]	[8 10]						
	extra preproc.	ICA	-	-	-	filter 1-10 Hz	filter 1-10 Hz						
9	**TOI (s)**	[-1 1.9]											
	FOI (Hz)	[1 3]											
	extra preproc.	Interp Oz, ICA											
10	**TOI (s)**	[-5 0]	[15 20]	[0 5]	[4 9]								
	FOI (Hz)	[1 7]	[1 7]	[10 15]	[1 7]								
	extra preproc.	-	-	-	filter 1-10 Hz								
11	**TOI (s)**	[5 10]	[2.5 7.5]	[2.2 7.2]	[4 6]	[4 7]	[2 5]						
	FOI (Hz)	[4 7]	[4 7]	[1 7]	[4 7]	[1 7]	[1 5]						
	extra preproc.	Interp T10, ICA and filter 1-10 Hz	Interp T10, FT10; ICA; filter 1-10 Hz	Interp T10, ICA and filter 1-10 Hz	ICA	ICA	ICA						
12	**TOI (s)**	[0 3]	[-1 3]	[0 3]	[0 2.5]	[0 2.5]	[-1.5 0]	[0 5]	[-1 1]				
	FOI (Hz)	[4 7]	[4 7]	[3 6]	[3 6]	[4 7]	[3 6]	[4 7]	[3 6]				
	extra preproc.	Interp T10; ICA	ICA	-	-	-	-	ICA	Interp O1				

Table A.1: (continued)

PAT		Seizure											
		1	**2**	**3**	**4**	**5**	**6**	**7**	**8**	**9**	**10**	**11**	**12**
13	**TOI (s)**	[0 2]											
	FOI (Hz)	[10 15]											
	extra preproc.	-											
14	**TOI (s)**	[1 2.5]	[4 7]	[9.5 14.5]	[0.2 3.8]								
	FOI (Hz)	[1 4]	[3 7]	[3 7]	[3 7]								
	extra preproc.	ICA	Interp O1, T9	Interp O1	Interp O1, filter 1-10 Hz								
15	**TOI (s)**	[0 5]	[5 10]	[0.5 2.5]									
	FOI (Hz)	[1 5]	[1 5]	[1 5]									
	extra preproc.	ICA	ICA	ICA									
16	**TOI (s)**	[0 3.5]	[-1.5 3.5]	[0 5]	[0 5]								
	FOI (Hz)	[4 7]	[4 7]	[4 7]	[4 7]								
	extra preproc.	-	ICA	-	Interp Oz								
17	**TOI (s)**	[17.5 20]	[0 3]	[4 7]									
	FOI (Hz)	[1 4]	[1 4]	[1 4]									
	extra preproc.	filter 1-10 Hz	ICA	filter 1-10 Hz									
18	**TOI (s)**	[3 7]	[0 5]	[0 5]									
	FOI (Hz)	[1 4]	[1 4]	[1 4]									
	extra preproc.	-	-	-									

Table A.1: (continued)

PAT		Seizure											
		1	**2**	**3**	**4**	**5**	**6**	**7**	**8**	**9**	**10**	**11**	**12**
19	**TOI (s)**	[2 6]											
	FOI (Hz)	[1 5]											
	extra preproc.	filter 1-10 Hz											
20	**TOI (s)**	[-3 0]	[-5 0]	[4 7.5]	[0 5]	[0 4]	[0 4]	[0 2]	[3.5 8.5]	[0 5]	[-1 4]	[0 5]	[0 5]
	FOI (Hz)	[1 5]	[25 30]	[20 30]	[20 30]	[7 15]	[15 25]	[15 25]	[20 25]	[7 15]	[7 10]	[15 25]	[7 15]
	extra preproc.	-	-	-	-	-	ICA	ICA	-	Interp Fp2, Tp10	-	Interp Fp1	-
21	**TOI (s)**	[5 9.5]	[4 9]										
	FOI (Hz)	[1 5]	[1 5]										
	extra preproc.	filter 1-10 Hz	filter 1-10 Hz										
22	**TOI (s)**	[4.5 9.5]	[0 5]	[0 4]	[-1 1.5]	[0 5]	[-0.5 4.5]	[3.8 8.7]	[1.8 6]	[0 5]			
	FOI (Hz)	[1 7]	[1 7]	[1 7]	[7 12]	[1 12]	[1 12]	[1 15]	[1 12]	[1 7]			
	extra preproc.	-	-	-	-	-	-	-	-	-			
23	**TOI (s)**	[0 5]	[0 2]	[0 5]									
	FOI (Hz)	[1 10]	[4 7]	[3 8]									
	extra preproc.	-	filter 1-10 Hz	ICA									
24	**TOI (s)**	[0 3.5]											
	FOI (Hz)	[4 7]											
	extra preproc.	ICA											
25	**TOI (s)**	[0 5]											
	FOI (Hz)	[4 12]											
	extra preproc.	-											

Table A.1: (continued)

PAT		Seizure											
		1	**2**	**3**	**4**	**5**	**6**	**7**	**8**	**9**	**10**	**11**	**12**
26	**TOI (s)**	[0 5]											
	FOI (Hz)	[1 7]											
	extra preproc.	-											
27	**TOI (s)**	[1 5]											
	FOI (Hz)	[24 26]											
	extra preproc.	ICA (HB)											

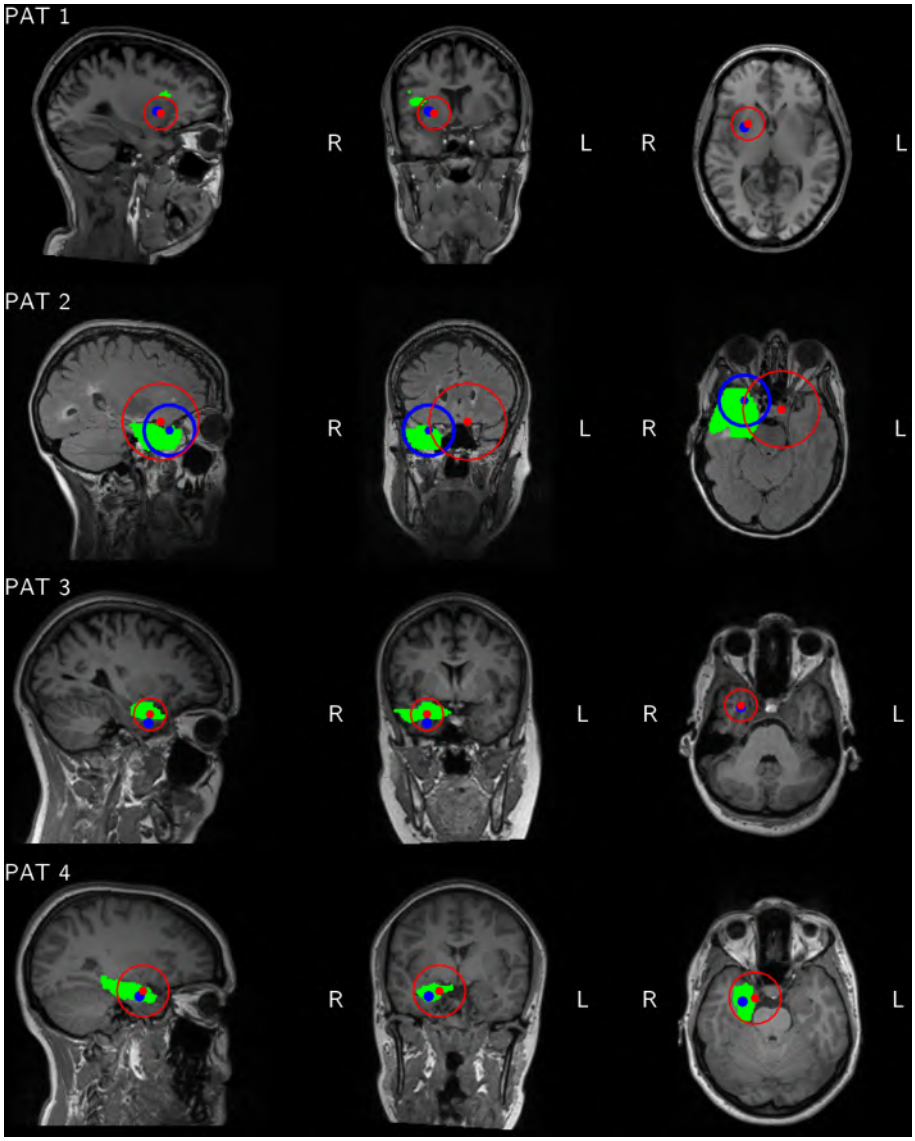

Figure A.4: Spatial spread of all patients. The standard distance of patients that had only one analyzed seizure is shown as zero (no circle). Remark that the slices shown in the visualization are optimized for the ESI + connectivity results. As a consequence, some ESI power results may seem to lie outside source space, but this is not the case. When no blue dot is clearly visible, the red and blue dot are overlapping.

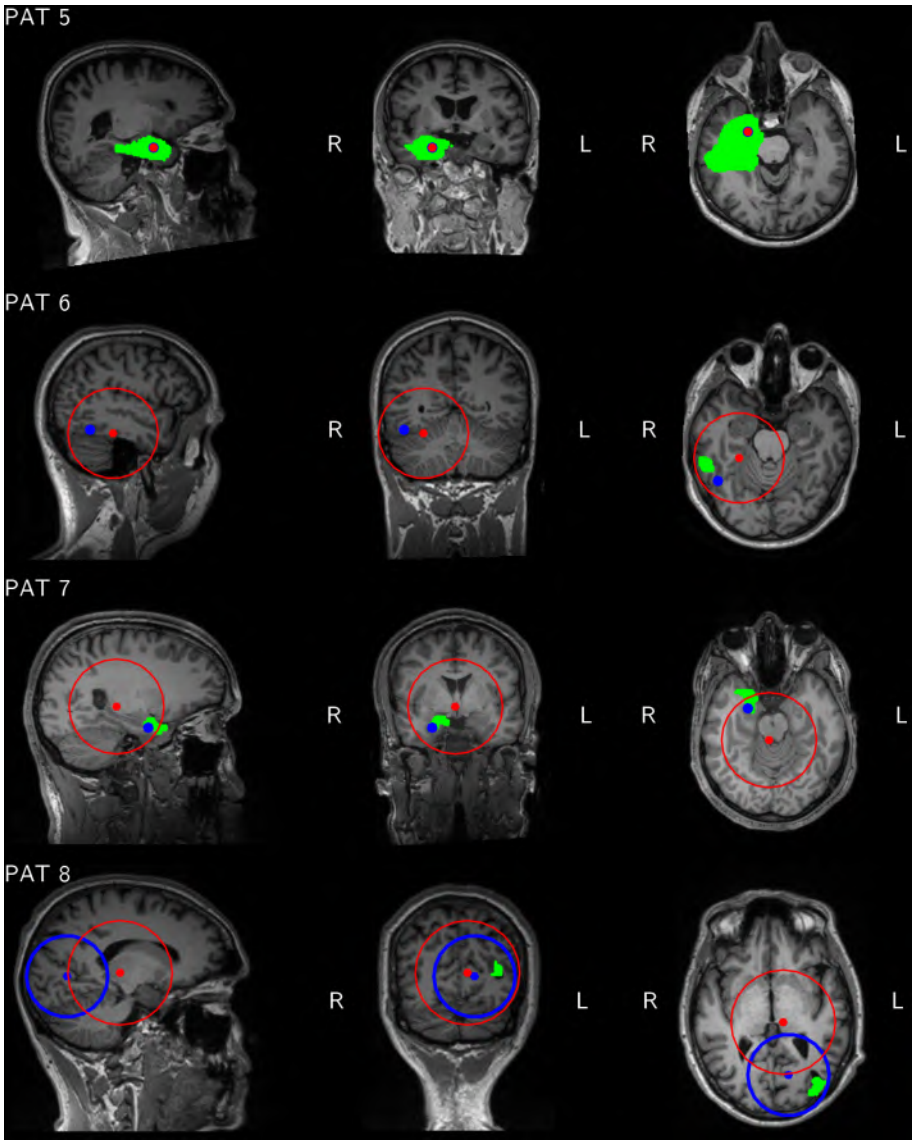

Figure A.5: Spatial spread of all patients. The standard distance of patients that had only one analyzed seizure is shown as zero (no circle). Remark that the slices shown in the visualization are optimized for the ESI + connectivity results. As a consequence, some ESI power results may seem to lie outside source space, but this is not the case. When no blue dot is clearly visible, the red and blue dot are overlapping.

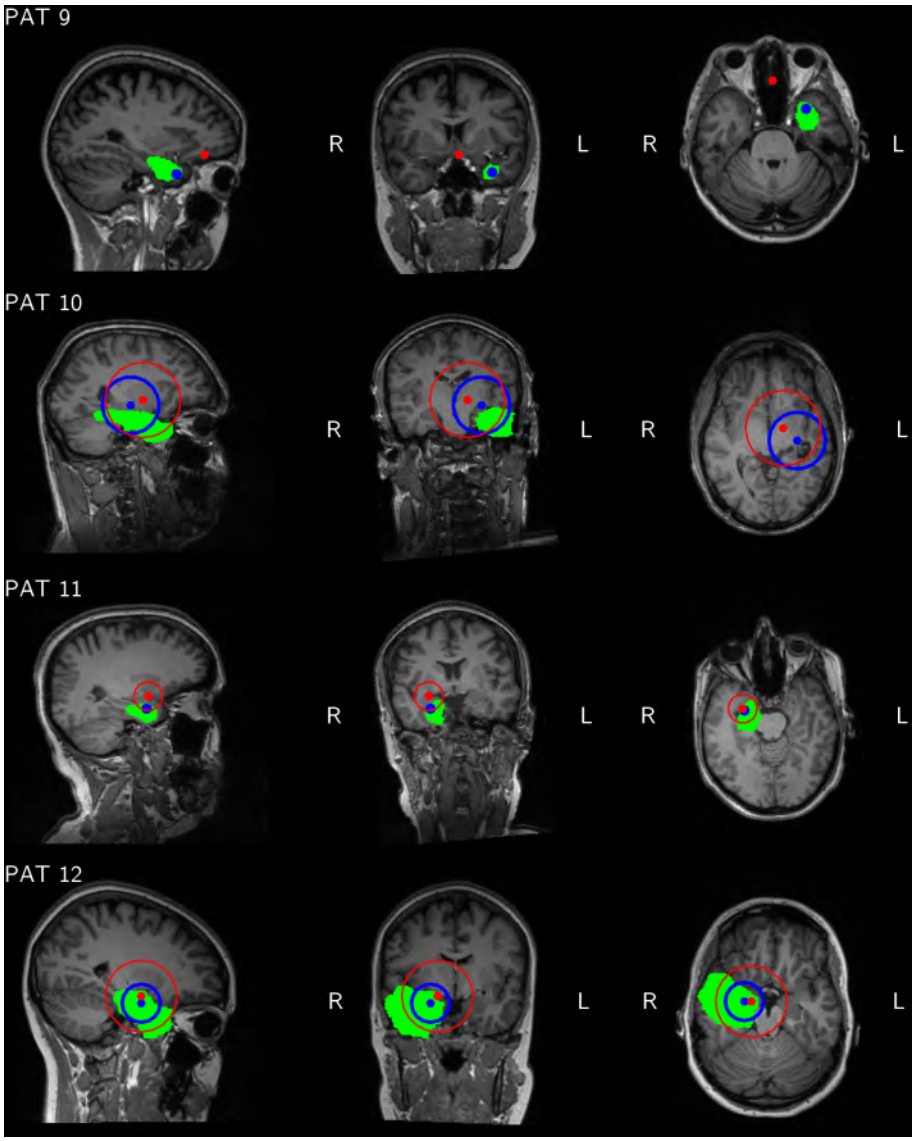

Figure A.6: Spatial spread of all patients. The standard distance of patients that had only one analyzed seizure is shown as zero (no circle). Remark that the slices shown in the visualization are optimized for the ESI + connectivity results. As a consequence, some ESI power results may seem to lie outside source space, but this is not the case. When no blue dot is clearly visible, the red and blue dot are overlapping.

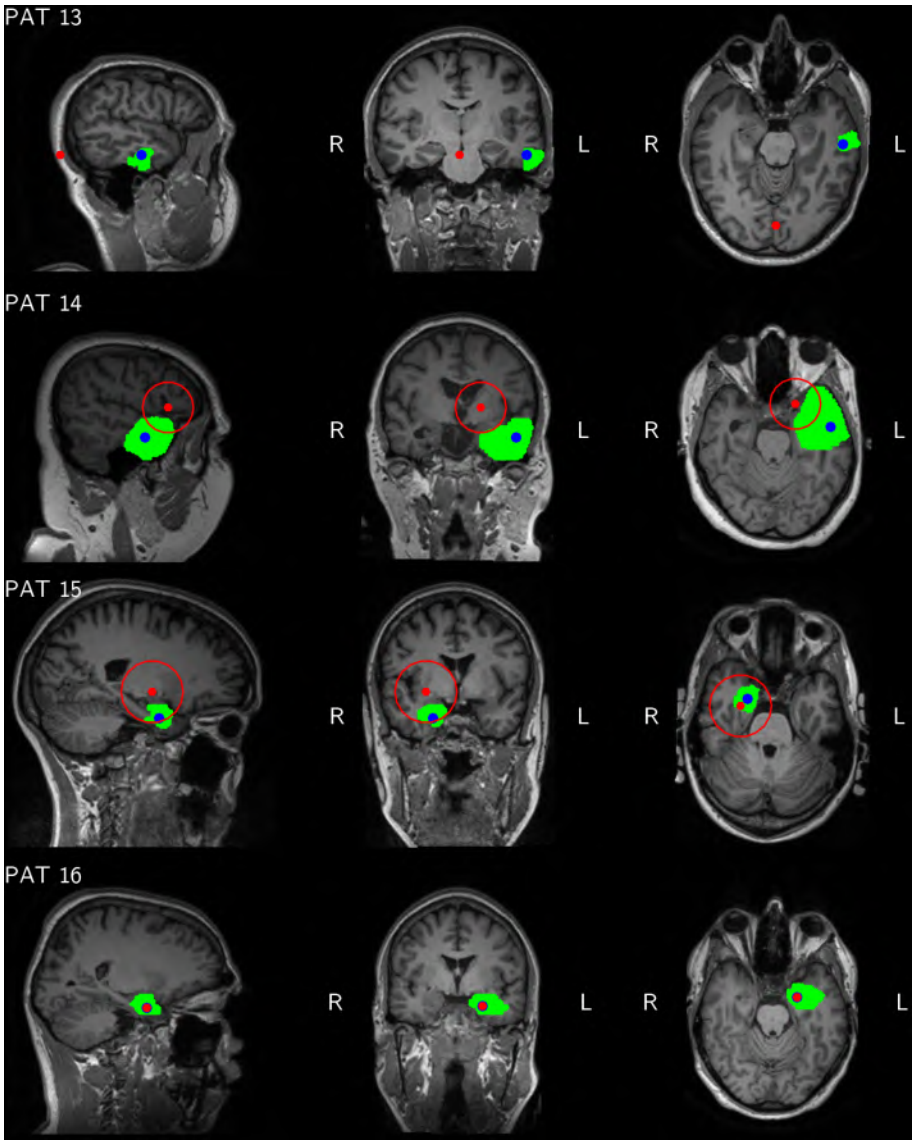

Figure A.7: Spatial spread of all patients. The standard distance of patients that had only one analyzed seizure is shown as zero (no circle). Remark that the slices shown in the visualization are optimized for the ESI + connectivity results. As a consequence, some ESI power results may seem to lie outside source space, but this is not the case. When no blue dot is clearly visible, the red and blue dot are overlapping.

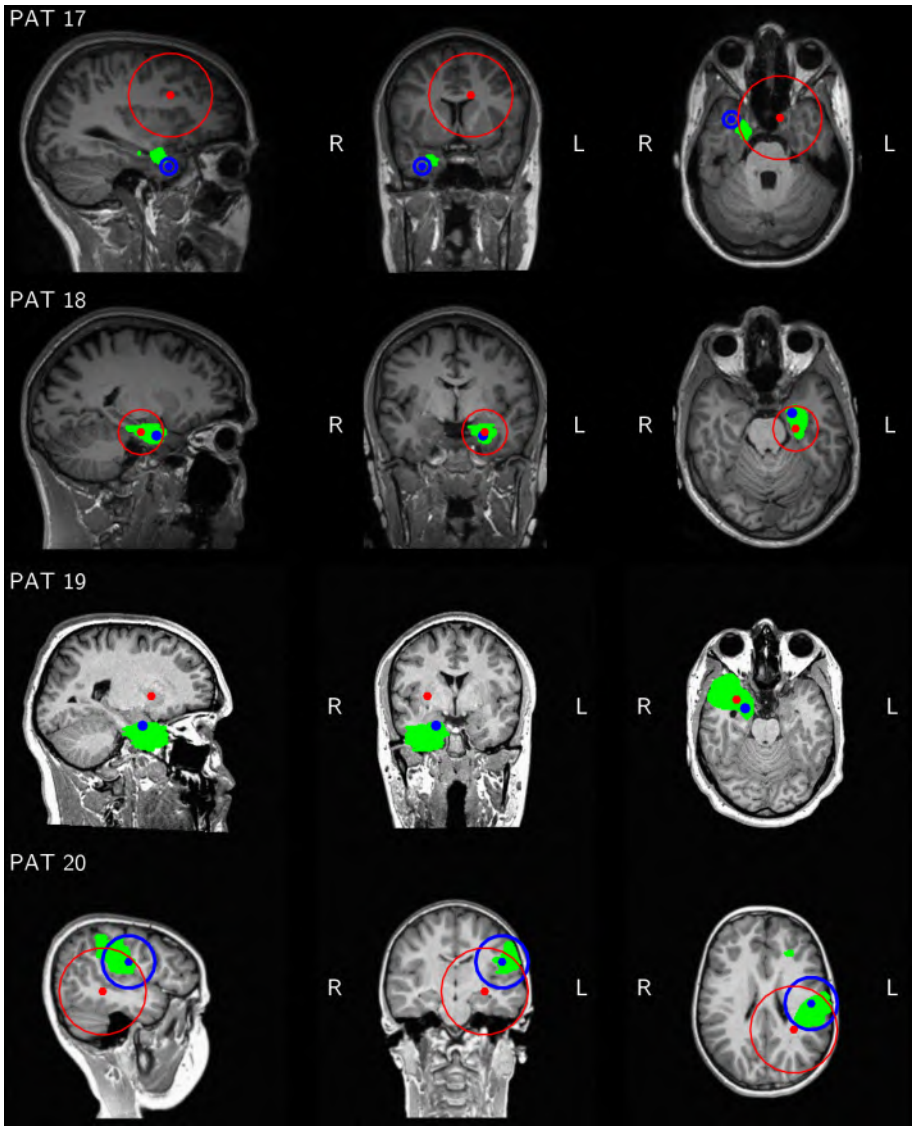

Figure A.8: Spatial spread of all patients. The standard distance of patients that had only one analyzed seizure is shown as zero (no circle). Remark that the slices shown in the visualization are optimized for the ESI + connectivity results. As a consequence, some ESI power results may seem to lie outside source space, but this is not the case. When no blue dot is clearly visible, the red and blue dot are overlapping.

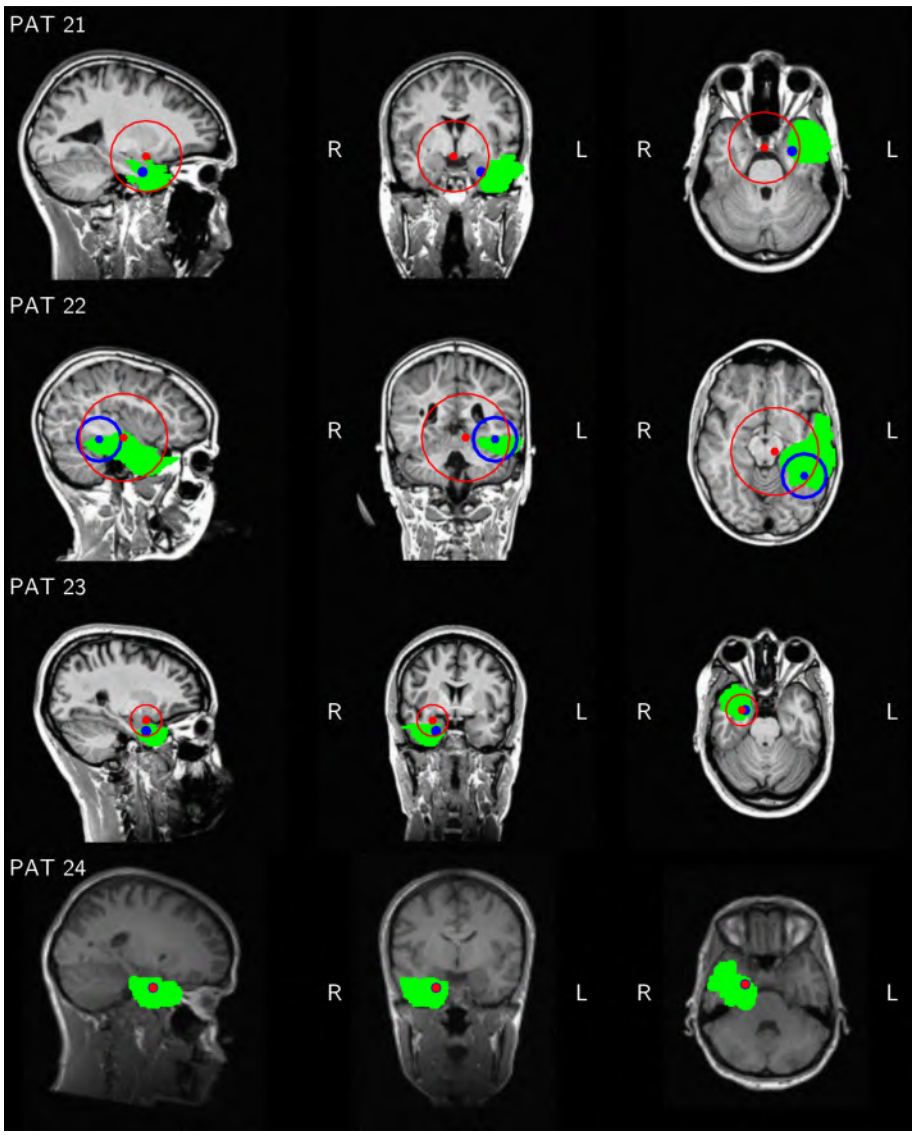

Figure A.9: Spatial spread of all patients. The standard distance of patients that had only one analyzed seizure is shown as zero (no circle). Remark that the slices shown in the visualization are optimized for the ESI + connectivity results. As a consequence, some ESI power results may seem to lie outside source space, but this is not the case. When no blue dot is clearly visible, the red and blue dot are overlapping.

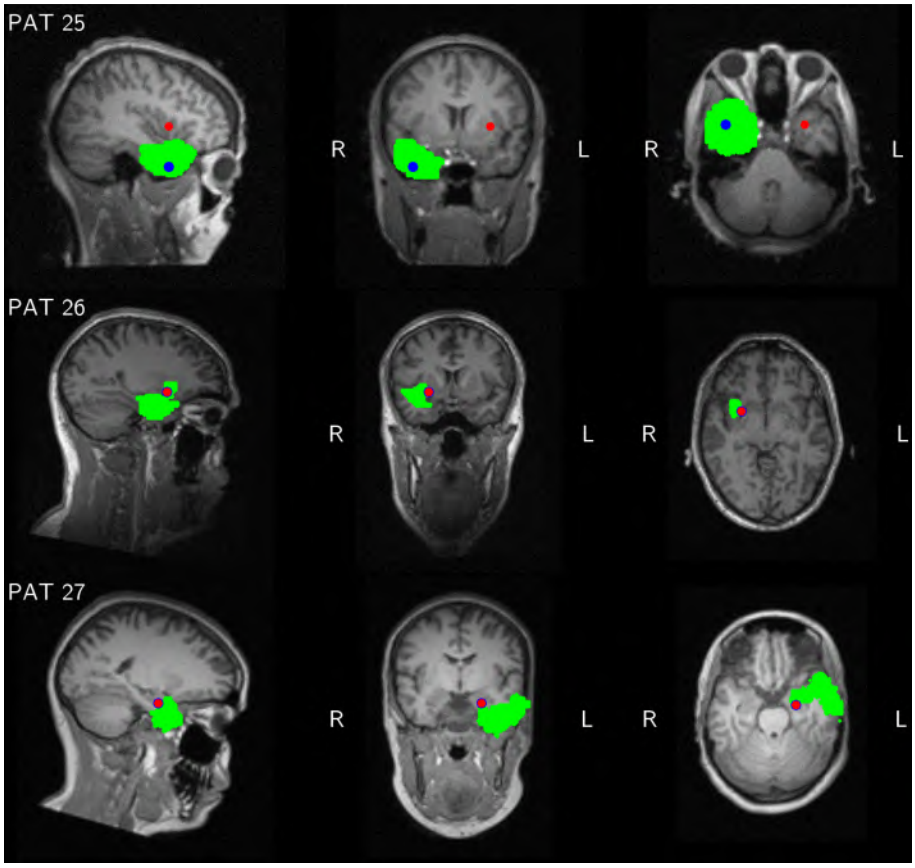

Figure A.10: Spatial spread of all patients. The standard distance of patients that had only one analyzed seizure is shown as zero (no circle). Remark that the slices shown in the visualization are optimized for the ESI + connectivity results. As a consequence, some ESI power results may seem to lie outside source space, but this is not the case. When no blue dot is clearly visible, the red and blue dot are overlapping.

B

Results of the epoch and frequency band selection

In the following sections, the localization errors obtained in chapter 7 for every analyzed epoch are listed. Table B.1 lists the localization errors found when the analysis was done in the 1 – 30 Hz band, Table B.2 to Table B.6 list them for the δ, θ, α, β and γ band, respectively. In Table B.7 the frequency band of the ictal onset phase was used, and in Table B.8 the different seizure phases are analyzed in their own frequency band.

Table B.1: LEs in mm of all selected epochs analyzed in the complete **1 – 30 Hz**. Errors equal to zero are colored green, the others are depicted in red. For each phase, the percentage of correctly localized seizures is indicated.

	Pre	Clin	EEG	Phase 2	Phase 3	Phase 4	Post
11.1	43	56	36	/	43	/	75
11.2	0	56	0	/	75	/	37
11.3	17	54	0	/	75	/	54
14.1	46	73	35	/	46	/	49
14.2	55	0	0	/	0	/	64
14.3	N.A.	35	51	/	0	/	29
14.4	35	0	0	/	51	/	0
15.1	31	58	0	59	20	81	36
15.2	58	68	0	36	/	/	70
15.3	20	/	0	59	/	/	59
17.1	48	78	0	83	83	68	46
17.2	19	65	83	/	73	83	59
0 mm	**9%**	**18%**	**67%**	**0%**	**20%**	**0%**	**8%**

Table B.2: LEs in mm of all selected epochs analyzed in the ***δ* band**. Errors equal to zero are colored green, the others are depicted in red. For each phase, the percentage of correctly localized seizures is indicated.

	Pre	Clin	EEG	Phase 2	Phase 3	Phase 4	Post
11.1	36	17	36	/	36	/	17
11.2	0	56	0	/	51	/	37
11.3	17	54	54	/	51	/	0
14.1	52	13	0	/	46	/	49
14.2	55	13	31	/	73	/	64
14.3	N.A.	78	13	/	85	/	52
14.4	46	52	0	/	51	/	49
15.1	79	0	0	70	20	81	36
15.2	79	68	0	36	/	/	70
15.3	20	/	0	68	/	/	0
17.1	44	48	0	46	78	68	46
17.2	19	65	0	/	73	83	59
0 mm	**9%**	**9%**	**67%**	**0%**	**0%**	**0%**	**17%**

Table B.3: LEs in mm of all selected epochs analyzed in the ***θ* band**. Errors equal to zero are colored green, the others are depicted in red. For each phase, the percentage of correctly localized seizures is indicated.

	Pre	**Clin**	**EEG**	**Phase 2**	**Phase 3**	**Phase 4**	**Post**
11.1	54	56	17	/	17	/	45
11.2	77	54	0	/	53	/	37
11.3	36	54	53	/	75	/	0
14.1	52	52	46	/	73	/	49
14.2	29	0	0	/	0	/	13
14.3	N.A.	35	0	/	0	/	54
14.4	35	0	0	/	51	/	0
15.1	79	59	0	59	31	79	59
15.2	0	68	0	0	/	/	70
15.3	0	/	59	59	/	/	59
17.1	48	78	68	83	83	68	39
17.2	78	51	49	/	49	46	51
0 mm	**18%**	**18%**	**50%**	**25%**	**20%**	**0%**	**17%**

Table B.4: LEs in mm of all selected epochs analyzed in the ***α* band**. Errors equal to zero are colored green, the others are depicted in red. For each phase, the percentage of correctly localized seizures is indicated.

	Pre	**Clin**	**EEG**	**Phase 2**	**Phase 3**	**Phase 4**	**Post**
11.1	43	56	43	/	0	/	45
11.2	56	54	43	/	43	/	56
11.3	37	56	53	/	75	/	56
14.1	46	52	46	/	35	/	71
14.2	54	54	0	/	0	/	13
14.3	N.A.	0	46	/	0	/	65
14.4	35	0	35	/	0	/	0
15.1	31	59	59	59	20	20	81
15.2	59	81	59	55	/	/	70
15.3	59	/	59	59	/	/	59
17.1	68	68	68	83	83	41	78
17.2	46	39	83	/	58	46	46
0 mm	**0%**	**18%**	**8%**	**0%**	**40%**	**0%**	**8%**

Table B.5: LEs in mm of all selected epochs analyzed in the β **band**. Errors equal to zero are colored green, the others are depicted in red. For each phase, the percentage of correctly localized seizures is indicated.

	Pre	Clin	EEG	Phase 2	Phase 3	Phase 4	Post
11.1	73	56	73	/	75	/	43
11.2	73	43	42	/	75	/	46
11.3	46	45	45	/	43	/	75
14.1	46	73	29	/	78	/	46
14.2	35	85	78	/	78	/	85
14.3	N.A.	29	35	/	64	/	65
14.4	46	0	46	/	35	/	34
15.1	70	31	59	58	71	36	55
15.2	78	71	58	58	/	/	59
15.3	31	/	59	78	/	/	58
17.1	80	28	68	48	39	0	44
17.2	60	60	19	/	48	46	51
0 mm	**0%**	**9%**	**0%**	**0%**	**0%**	**33%**	**0%**

Table B.6: LEs in mm of all selected epochs analyzed in the γ **band**. Errors equal to zero are colored green, the others are depicted in red. For each phase, the percentage of correctly localized seizures is indicated.

	Pre	Clin	EEG	Phase 2	Phase 3	Phase 4	Post
11.1	51	51	46	/	73	/	73
11.2	75	36	75	/	75	/	77
11.3	69	36	45	/	73	/	75
14.1	13	0	29	/	78	/	31
14.2	0	0	51	/	0	/	78
14.3	N.A.	65	51	/	65	/	65
14.4	52	65	65	/	73	/	46
15.1	59	31	58	59	59	79	79
15.2	79	58	0	79	/	/	55
15.3	79	/	58	58	/	/	58
17.1	39	58	44	84	80	39	73
17.2	68	48	68	/	68	68	68
0 mm	**9%**	**18%**	**8%**	**0%**	**10%**	**0%**	**0%**

Table B.7: LEs in mm of all selected epochs analyzed in the **ictal onset band**. Errors equal to zero are colored green, the others are depicted in red. The percentage of correctly localized seizures is indicated.

	Pre	Clin	EEG	Phase 2	Phase 3	Phase 4	Post
11.1	36	0	0	/	17	/	37
11.2	0	56	0	/	75	/	37
11.3	17	54	0	/	51	/	0
14.1	52	13	0	/	46	/	49
14.2	29	0	0	/	0	/	13
14.3	N.A.	35	0	/	0	/	54
14.4	46	52	0	/	51	/	49
15.1	79	70	0	70	20	81	36
15.2	0	68	0	79	/	/	70
15.3	20	/	0	68	/	/	0
17.1	44	48	0	83	68	68	46
17.2	19	65	0	/	73	83	59
0 mm	**18%**	**18%**	**100%**	**0%**	**20%**	**0%**	**17%**

Table B.8: LEs in mm of the epochs selected during the seizure, analyzed in the corresponding FOI. Errors equal to zero are colored green, the others are depicted in red. The percentage of correctly localized seizures is indicated.

	EEG	Phase 2	Phase 3	Phase 4
11.1	0	/	0	/
11.2	0	/	0	/
11.3	0	/	51	/
14.1	0	/	46	/
14.2	0	/	0	/
14.3	0	/	0	/
14.4	0	/	0	/
15.1	0	59	20	81
15.2	0	0	/	/
15.3	0	0	/	/
17.1	0	83	83	68
17.2	0	/	73	83
0 mm	**100%**	**50%**	**50%**	**0%**

References

[1] Carter R, Aldridge S, Page M, Parker S. *The brain book: An illustrated guide to its structure, function and disorders*. Dorling Kindersley Limited, London, 2009.

[2] Genetics Science Learning Centre of the University of Utah. Neurons Transmit Messages In The Brain. `http://learn.genetics.utah.edu/content/neuroscience/neurons/`. Accessed: 2017-07-31.

[3] Toro R, Perron M, Pike B, Richer L, Veillette S, Pausova Z, Paus T. Brain size and folding of the human cerebral cortex. *Cerebral Cortex*, 18(10): 2352, 2008.

[4] Sholts SB, Wärmländer SK, Flores LM, Miller KW, Walker PL. Variation in the measurement of cranial volume and surface area using 3D laser scanning technology. *Journal of Forensic Sciences*, 55(4): 871–876, 2010.

[5] Gousias IS, Rueckert D, Heckemann RA, Dyet LE, Boardman JP, Edwards AD, Hammers A. Automatic segmentation of brain MRIs of 2-year-olds into 83 regions of interest. *NeuroImage*, 40(2): 672–684, 2008.

[6] Azevedo FA, Carvalho LR, Grinberg LT, Farfel JM, Ferretti RE, Leite RE, Lent R, Herculano-Houzel S, et al. Equal numbers of neuronal and nonneuronal cells make the human brain an isometrically scaled-up primate brain. *Journal of Comparative Neurology*, 513(5): 532–541, 2009.

[7] National Cancer Institute of the USA. Brain Cancer. `https://www.cancer.gov/types/brain/patient/adult-brain-treatment-pdq`. Accessed: 2017-07-31.

[8] Baumann N, Pham-Dinh D. Biology of oligodendrocyte and myelin in the mammalian central nervous system. *Physiological Reviews*, 81(2): 871–927, 2001.

[9] Blackburn D, Sargsyan S, Monk PN, Shaw PJ. Astrocyte function and role in motor neuron disease: a future therapeutic target? *Glia*, 57(12): 1251–1264, 2009.

[10] Filiano AJ, Gadani SP, Kipnis J. Interactions of innate and adaptive immunity in brain development and function. *Brain Research*, 1617: 18–27, 2015.

[11] Hickok G, Poeppel D. The cortical organization of speech processing. *Nature Reviews Neuroscience*, 8(5): 393–402, 2007.

[12] Malmivuo J, Plonsey R. *Bioelectromagnetism*. Oxford University Press, New York, Oxford, 1995.

[13] Niedermeyer E, da Silva FL. *Electroencephalography: basic principles, clinical applications, and related fields*. Lippincott Williams & Wilkins, 2005.

[14] Hämäläinen M, Hari R, Ilmoniemi RJ, Knuutila J, Lounasmaa OV. Magnetoencephalographytheory, instrumentation, and applications to noninvasive studies of the working human brain. *Reviews of Modern Physics*, 65(2): 413, 1993.

[15] Mehagnoul-Schipper DJ, van der Kallen BF, Colier WN, van der Sluijs MC, van Erning LJ, Thijssen HO, Oeseburg B, Hoefnagels WH, Jansen RW. Simultaneous measurements of cerebral oxygenation changes during brain activation by near-infrared spectroscopy and functional magnetic resonance imaging in healthy young and elderly subjects. *Human Brain Mapping*, 16(1): 14–23, 2002.

[16] Townsend DW. Combined positron emission tomography–computed tomography: the historical perspective. *Seminars in Ultrasound, CT and MRI*, 29(4): 232–235, 2008.

[17] Schillaci O. Hybrid SPECT/CT: a new era for SPECT imaging? *European Journal of Nuclear Medicine and Molecular Imaging*, 32(5): 521–524, 2005.

[18] Herzog H, Van Den Hoff J. Combined PET/MR systems: an overview and comparison of currently available options. *The Quarterly Journal of Nuclear Medicine and Molecular Imaging*, 56(3): 247–267, 2012.

[19] Martí-Bonmatí L, Sopena R, Bartumeus P, Sopena P. Multimodality imaging techniques. *Contrast Media & Molecular Imaging*, 5(4): 180–189, 2010.

[20] Ritter P, Villringer A. Simultaneous EEG–fMRI. *Neuroscience & Biobehavioral Reviews*, 30(6): 823–838, 2006.

[21] Aydin Ü, Vorwerk J, Dümpelmann M, Küpper P, Kugel H, Heers M, Wellmer J, Kellinghaus C, Haueisen J, Rampp S, Stefan H, Wolters CH. Combined EEG/MEG can outperform single modality EEG or MEG source reconstruction in presurgical epilepsy diagnosis. *PLoS ONE*, 10(3): e0118753, 2015.

[22] Nunez PL, Srinivasan R. *Electric fields of the brain: the neurophysics of EEG*. Oxford University Press, USA, 2006.

[23] Baillet S, Mosher JC, Leahy RM. Electromagnetic brain mapping. *IEEE Signal Processing Magazine*, 18(6): 14–30, 2001.

[24] Strobbe G. *Advanced forward models for EEG source imaging*. Ph.D. thesis, Ghent University, 2015.

[25] Klem GH, Lüders HO, Jasper H, Elger C. The ten-twenty electrode system of the International Federation. *Electroencephalography and Clinical Neurophysiology*, 52(3): 3–6, 1999.

[26] Oostenveld R, Praamstra P. The five percent electrode system for high-resolution EEG and ERP measurements. *Clinical Neurophysiology*, 112(4): 713–719, 2001.

[27] Perrin F, Pernier J, Bertrand O, Echallier J. Spherical splines for scalp potential and current density mapping. *Electroencephalography and Clinical Neurophysiology*, 72(2): 184–187, 1989.

[28] Perrin F, Pernier J, Bertrand O, Echallier J. Corrigenda: EEG 02274. *Electroencephalography and Clinical Neurophysiology*, 76: 565, 1990.

[29] Sanei S, Chambers JA. *EEG signal processing*. John Wiley & Sons, Chichester, England, 2007.

[30] Croft RJ, Barry RJ. Removal of ocular artifact from the EEG: a review. *Clinical Neurophysiology*, 30(1): 5–19, 2000.

[31] Lagerlund TD, Sharbrough FW, Busacker NE. Spatial filtering of multichannel electroencephalographic recordings through principal component analysis by singular value decomposition. *Journal of Clinical Neurophysiology*, 14(1): 73–82, 1997.

[32] Makeig S, Bell AJ, Jung TP, Sejnowski TJ, et al. Independent Component Analysis of electroencephalographic data. *Advances in Neural Information Processing Systems*, 145–151, 1996.

[33] He B, Liu Z. Multimodal functional neuroimaging: integrating functional MRI and EEG/MEG. *IEEE Reviews in Biomedical Engineering*, 1: 23–40, 2008.

[34] Kushida CA, Littner MR, Morgenthaler T, Alessi CA, Bailey D, Coleman J, Friedman L, Hirshkowitz M, Kapen S, Kramer M, et al. Practice parameters for the indications for polysomnography and related procedures: an update for 2005. *Sleep*, 28(4): 499–523, 2005.

[35] Duncan CC, Barry RJ, Connolly JF, Fischer C, Michie PT, Näätänen R, Polich J, Reinvang I, Van Petten C. Event-related potentials in clinical research: guidelines for eliciting, recording, and quantifying mismatch negativity, P300, and N400. *Clinical Neurophysiology*, 120(11): 1883–1908, 2009.

[36] Fawcett A, Chattopadhyay A, Kandler R, Jarratt J, Nicolson R, Proctor M. Event-related Potentials and Dyslexia. *Annals of the New York Academy of Sciences*, 682(1): 342–345, 1993.

[37] Polich J, Ladish C, Bloom FE. P300 assessment of early Alzheimer's disease. *Electroencephalography and Clinical Neurophysiology/Evoked Potentials Section*, 77(3): 179–189, 1990.

[38] Rugg M, Pickles C, Potter D, Doyle M, Pentland B, Roberts R. Cognitive brain potentials in a three-stimulus auditory oddball task after closed head injury. *Neuropsychologia*, 31(4): 373–393, 1993.

[39] Potter DD, Bassett MR, Jory SH, Barrett K. Changes in event-related potentials in a three-stimulus auditory oddball task after mild head injury. *Neuropsychologia*, 39(13): 1464–1472, 2001.

[40] Moore MM. Real-world applications for brain-computer interface technology. *IEEE Transactions on Neural Systems and Rehabilitation Engineering*, 11(2): 162–165, 2003.

[41] Horch KW, Dhillon GS. *Neuroprosthetics: theory and practice*, volume 2. World Scientific, 2004.

[42] Kaufmann T, Herweg A, Kübler A. Toward brain-computer interface based wheelchair control utilizing tactually-evoked event-related potentials. *Journal of Neuroengineering and Rehabilitation*, 11(1): 7, 2014.

[43] Verhoeven T, Buteneers P, Wiersema J, Dambre J, Kindermans P. Towards a symbiotic brain–computer interface: exploring the application–decoder interaction. *Journal of Neural Engineering*, 12(6): 066027, 2015.

[44] Donchin E, Spencer KM, Wijesinghe R. The mental prosthesis: assessing the speed of a P300-based brain-computer interface. *IEEE Transactions on Rehabilitation Engineering*, 8(2): 174–179, 2000.

[45] Laureys S, Pellas F, Van Eeckhout P, Ghorbel S, Schnakers C, Perrin F, Berre J, Faymonville ME, Pantke KH, Damas F, et al. The locked-in syndrome: what is it like to be conscious but paralyzed and voiceless? *Progress in Brain Research*, 150: 495–611, 2005.

[46] Edlinger G, Holzner C, Guger C. A hybrid brain-computer interface for smart home control. *Human-Computer Interaction. Interaction Techniques and Environments*, 417–426, 2011.

[47] Nijholt A, Tan D, Allison B, del R Milan J, Graimann B. Brain-computer interfaces for HCI and games. *CHI'08 extended abstracts on Human factors in computing systems*, 3925–3928. ACM, 2008.

[48] Verhoeven T, Hübner D, Tangermann M, Müller KR, Dambre J, Kindermans PJ. Improving zero-training brain-computer interfaces by mixing model estimators. *Journal of Neural Engineering*, 14(3): 036021, 2017.

[49] Morin C. Neuromarketing: the new science of consumer behavior. *Society*, 48(2): 131–135, 2011.

[50] Murphy ER, Illes J, Reiner PB. Neuroethics of neuromarketing. *Journal of Consumer Behaviour*, 7(4-5): 293–302, 2008.

[51] Fisher RS, Acevedo C, Arzimanoglou A, Bogacz A, Cross JH, Elger CE, Engel J, Forsgren L, French JA, Glynn M, et al. ILAE official report: a practical clinical definition of epilepsy. *Epilepsia*, 55(4): 475–482, 2014.

[52] Sörnmo L, Laguna P. *Bioelectrical signal processing in cardiac and neurological applications*, volume 8. Academic Press, 2005.

[53] WHO. Epilepsy Fact Sheet. `http://www.who.int/mediacentre/factsheets/fs999/en/`. Accessed: 2017-05-23.

[54] Ngugi AK, Kariuki S, Bottomley C, Kleinschmidt I, Sander J, Newton C. Incidence of epilepsy A systematic review and meta-analysis. *Neurology*, 77(10): 1005–1012, 2011.

[55] Strawbridge LM, Schultz AM, Liverman CT, England MJ, et al. *Epilepsy Across the Spectrum: Promoting Health and Understanding*. National Academies Press, 2012.

[56] Scheffer IE, Berkovic S, Capovilla G, Connolly MB, French J, Guilhoto L, Hirsch E, Jain S, Mathern GW, Moshé SL, et al. ILAE classification of the epilepsies: Position paper of the ILAE Commission for Classification and Terminology. *Epilepsia*, 58(4): 512–521, 2017.

[57] on Classification C, of the International League Against Epilepsy T. Proposal for Revised Classification of Epilepsies and Epileptic Syndromes. *Epilepsia*, 30(4): 389–399, 1989.

[58] Berg AT, Berkovic SF, Brodie MJ, Buchhalter J, Cross JH, van Emde Boas W, Engel J, French J, Glauser TA, Mathern GW, et al. Revised terminology and concepts for organization of seizures and epilepsies: report of the ILAE Commission on Classification and Terminology, 2005–2009. *Epilepsia*, 51(4): 676–685, 2010.

[59] Fisher RS, Cross JH, French JA, Higurashi N, Hirsch E, Jansen FE, Lagae L, Mosh SL, Peltola J, Roulet Perez E, Scheffer IE, Zuberi

SM. Operational classification of seizure types by the International League Against Epilepsy: Position Paper of the ILAE Commission for Classification and Terminology. *Epilepsia*, 58(4): 522–530, 2017.

[60] Noachtar S, Binnie C, Ebersole J, Mauguiere F, Sakamoto A, Westmoreland B. A glossary of terms most commonly used by clinical electroencephalographers and proposal for the report form for the EEG findings. The International Federation of Clinical Neurophysiology. *Electroencephalography and Clinical Neurophysiology. Supplement*, 52: 21, 1999.

[61] Rogawski MA, Löscher W. The neurobiology of antiepileptic drugs. *Nature Reviews Neuroscience*, 5(7): 553–564, 2004.

[62] Epilepsy Society. List of anti-epileptic drugs. `https://www.epilepsysociety.org.uk/list-anti-epileptic-drugs`. Accessed: 2017-05-25.

[63] Epilepsy Foundation. Seizure medication list. `http://www.epilepsy.com/learn/treating-seizures-and-epilepsy/seizure-and-epilepsy-medicines/seizure-medication-list`. Accessed: 2017-05-25.

[64] Walia KS, Khan EA, Ko DH, Raza SS, Khan YN. Side Effects of Antiepileptics A Review. *Pain Practice*, 4(3): 194–203, 2004.

[65] Carrette E, Vonck K, Boon P. The Management of Pharmacologically Refractory Epilepsy. *International Journal of Clinical Reviews*, 1(2), 2011.

[66] Bessant P, Chadwick D, Eaton B, Taylor J, Holland A, Joannou J, Johnson A, Oldfield L, Reader N, Gumpert E, et al. Randomised study of antiepileptic drug withdrawal in patients in remission. *The Lancet*, 337(8751): 1175–1180, 1991.

[67] Kwan P, Arzimanoglou A, Berg AT, Brodie MJ, Allen Hauser W, Mathern G, Moshé SL, Perucca E, Wiebe S, French J. Definition of drug resistant epilepsy: consensus proposal by the ad hoc Task Force of the ILAE Commission on Therapeutic Strategies. *Epilepsia*, 51(6): 1069–1077, 2010.

[68] Téllez-Zenteno JF, Dhar R, Wiebe S. Long-term seizure outcomes following epilepsy surgery: a systematic review and meta-analysis. *Brain*, 128(5): 1188–1198, 2005.

[69] de Tisi J, Bell GS, Peacock JL, McEvoy AW, Harkness WF, Sander JW, Duncan JS. The long-term outcome of adult epilepsy surgery, patterns of seizure remission, and relapse: a cohort study. *The Lancet*, 378(9800): 1388–1395, 2011.

[70] Rosenow F, Lüders H. Presurgical evaluation of epilepsy. *Brain*, 124(9): 1683–1700, 2001.

[71] Okonma SV, Blount JP, Gross RE. Planning extent of resection in epilepsy: limited versus large resections. *Epilepsy & Behavior*, 20(2): 233–240, 2011.

[72] Spencer S, Huh L. Outcomes of epilepsy surgery in adults and children. *The Lancet Neurology*, 7(6): 525–537, 2008.

[73] Terra-Bustamante VC, Inuzuka LM, Fernandes RMF, Escorsi-Rosset S, Wichert-Ana L, Alexandre V, Bianchin MM, Araújo D, Santos AC, dos Santos RO, et al. Outcome of hemispheric surgeries for refractory epilepsy in pediatric patients. *Child's Nervous System*, 23(3): 321–326, 2007.

[74] Devinsky O, Romanelli P, Orbach D, Pacia S, Doyle W. Surgical treatment of multifocal epilepsy involving eloquent cortex. *Epilepsia*, 44(5): 718–723, 2003.

[75] Piper RJ, Hughes MA, Moran CM, Kandasamy J. Focused ultrasound as a non-invasive intervention for neurological disease: a review. *British Journal of Neurosurgery*, 30(3): 286–293, 2016.

[76] Engel J, Van Ness P, Rasmussen T, Ojemann L. *Surgical treatment of the epilepsies*. Raven Press, New York, 1993.

[77] Wieser H, Blume W, Fish D, Goldensohn E, Hufnagel A, King D, Sperling M, Lüders H, Pedley TA. Proposal for a new classification of outcome with respect to epileptic seizures following epilepsy surgery. *Epilepsia*, 42(2): 282–286, 2001.

[78] Vonck K, De Herdt V, Boon P. Vagal nerve stimulation–a 15-year survey of an established treatment modality in epilepsy surgery. *Advances and technical standards in neurosurgery*, 111–146. Springer, 2009.

[79] Vonck K, Sprengers M, Carrette E, Dauwe I, Miatton M, Meurs A, Goossens L, De Herdt V, Achten R, Thiery E, et al. A decade of experience with deep brain stimulation for patients with refractory medial temporal lobe epilepsy. *International Journal of Neural Systems*, 23(01): 1250034, 2013.

[80] San-juan D, Morales-Quezada L, Garduño AJO, Alonso-Vanegas M, González-Aragón MF, López DAE, Gregorio RV, Anschel DJ, Fregni F. Transcranial direct current stimulation in epilepsy. *Brain Stimulation*, 8(3): 455–464, 2015.

[81] Theodore WH. Transcranial Magnetic Stimulation in Epilepsy. *Epilepsy Currents*, 3(6): 191–197, 2003.

[82] Pereira LS, Müller VT, da Mota Gomes M, Rotenberg A, Fregni F. Safety of repetitive transcranial magnetic stimulation in patients with epilepsy: a systematic review. *Epilepsy & Behavior*, 57: 167–176, 2016.

[83] Freeman J, Veggiotti P, Lanzi G, Tagliabue A, Perucca E, et al. The ketogenic diet: from molecular mechanisms to clinical effects. *Epilepsy Research*, 68(2): 145–80, 2006.

[84] Engel JJ. Surgery for Seizures. *New England Journal of Medicine*, 334(10): 647–653, 1996.

[85] Cleveland Clinic. Epilepsy. `http://www.clevelandclinicmeded.com/medicalpubs/diseasemanagement/neurology/epileptic-syndrome/`. Accessed: 2017-08-07.

[86] Boon P, De Reuck J, Drieghe C, Debruycker K, Aers I, Pengel J. Long-term video-EEG monitoring revisited. The value of interictal and ictal video-EEG recording, a follow-up study. *European Neurology*, 33-39 Suppl. 1, 1994.

[87] Richardson MP. Large scale brain models of epilepsy: dynamics meets connectomics. *Journal of Neurology, Neurosurgery & Psychiatry*, 83(12): 1238–1248, 2012.

[88] Spencer SS. Neural networks in human epilepsy: evidence of and implications for treatment. *Epilepsia*, 43(3): 219–227, 2002.

[89] De Munck JC, Van Dijk BW, Spekreijse H. Mathematical dipoles are adequate to describe realistic generators of human brain activity. *IEEE Transactions on Biomedical Engineering*, 35(11): 960–966, 1988.

[90] Scherg M. Fundamentals of dipole source potential analysis. *Auditory Evoked Magnetic Fields and Electric Potentials*, 6: 40–69, 1990.

[91] Hallez H, Vanrumste B, Grech R, Muscat J, De Clercq W, Vergult A, D'Asseler Y, Camilleri KP, Fabri SG, Van Huffel S, et al. Review on solving the forward problem in EEG source analysis. *Journal of Neuroengineering and Rehabilitation*, 4(1): 46, 2007.

[92] Buchner H, Waberski TD, Fuchs M, Wischmann HA, Wagner M, Drenckhahn R. Comparison of realistically shaped boundary-element and spherical head models in source localization of early somatosensory evoked potentials. *Brain Topography*, 8(2): 137–143, 1995.

[93] Vanrumste B, Van Hoey G, Van de Walle R, Michel RD, Lemahieu IA, Boon PA. Comparison of performance of spherical and realistic head models in dipole localization from noisy EEG. *Medical Engineering & Physics*, 24(6): 403–418, 2002.

[94] Vatta F, Meneghini F, Esposito F, Mininel S, Salle FD. Realistic and spherical head modeling for EEG forward problem solution: a comparative cortex-based analysis. *Computational Intelligence and Neuroscience*, 2010: 13, 2010.

[95] Wellcome Trust Centre for Neuroimaging. Statistical Parametric Mapping. `http://www.fil.ion.ucl.ac.uk/spm/`.

[96] Fischl B. FreeSurfer. *NeuroImage*, 62(2): 774–781, 2012.

[97] Jenkinson M, Beckmann CF, Behrens TE, Woolrich MW, Smith SM. FSL. *NeuroImage*, 62(2): 782–790, 2012.

[98] Tadel F, Baillet S, Mosher JC, Pantazis D, Leahy RM. Brainstorm: a user-friendly application for MEG/EEG analysis. *Computational Intelligence and Neuroscience*, 2011: 8, 2011.

[99] Strobbe G, van Mierlo P, De Vos M, Mijović B, Hallez H, Van Huffel S, López JD, Vandenberghe S. Bayesian model selection of template forward models for EEG source reconstruction. *NeuroImage*, 93: 11–22, 2014.

[100] Montes-Restrepo V, van Mierlo P, Strobbe G, Staelens S, Vandenberghe S, Hallez H. Influence of skull modeling approaches on EEG source localization. *Brain Topography*, 27(1): 95–111, 2014.

[101] Fonov VS, Evans AC, McKinstry RC, Almli C, Collins D. Unbiased nonlinear average age-appropriate brain templates from birth to adulthood. *NeuroImage*, 47: S102, 2009.

[102] Marin G, Guerin C, Baillet S, Garnero L, Meunier G. Influence of skull anisotropy for the forward and inverse problem in EEG: simulation studies using FEM on realistic head models. *Human Brain Mapping*, 6(4): 250–269, 1998.

[103] Oostenveld R, Fries P, Maris E, Schoffelen JM. FieldTrip: open source software for advanced analysis of MEG, EEG, and invasive electrophysiological data. *Computational Intelligence and Neuroscience*, 2011: 1, 2011.

[104] Oostendorp TF, Delbeke J, Stegeman DF. The conductivity of the human skull: results of in vivo and in vitro measurements. *IEEE Transactions on Biomedical Engineering*, 47(11): 1487–1492, 2000.

[105] Vorwerk J, Cho JH, Rampp S, Hamer H, Knösche TR, Wolters CH. A guideline for head volume conductor modeling in EEG and MEG. *NeuroImage*, 100: 590–607, 2014.

[106] Hall WS. Boundary element method. *The Boundary Element Method*, 61–83, 1994.

[107] Meijs JW, Weier OW, Peters MJ, Van Oosterom A. On the numerical accuracy of the boundary element method (EEG application). *IEEE Transactions on Biomedical Engineering*, 36(10): 1038–1049, 1989.

[108] Fuchs M, Wagner M, Kastner J. Boundary element method volume conductor models for EEG source reconstruction. *Clinical Neurophysiology*, 112(8): 1400–1407, 2001.

[109] Dhatt G, Touzot G, et al. *Finite element method*. John Wiley & Sons, 2012.

[110] Awada KA, Jackson DR, Williams JT, Wilton DR, Baumann SB, Papanicolaou AC. Computational aspects of finite element modeling in EEG source localization. *IEEE Transactions on Biomedical Engineering*, 44(8): 736–752, 1997.

[111] Mitchell AR, Griffiths DF. *The finite difference method in partial differential equations*. John Wiley, 1980.

[112] Hallez H, Vanrumste B, Van Hese P, D'Asseler Y, Lemahieu I, Van de Walle R. A finite difference method with reciprocity used to incorporate anisotropy in electroencephalogram dipole source localization. *Physics in Medicine & Biology*, 50(16): 3787, 2005.

[113] Mosher JC, Lewis PS, Leahy RM. Multiple dipole modeling and localization from spatio-temporal MEG data. *IEEE Transactions on Biomedical Engineering*, 39(6): 541–557, 1992.

[114] Nelder JA, Mead R. A simplex method for function minimization. *The Computer Journal*, 7(4): 308–313, 1965.

[115] Golub GH, Reinsch C. Singular value decomposition and least squares solutions. *Numerische Mathematik*, 14(5): 403–420, 1970.

[116] Golub GH, Pereyra V. The differentiation of pseudo-inverses and nonlinear least squares problems whose variables separate. *SIAM Journal on Numerical Analysis*, 10(2): 413–432, 1973.

[117] Mosher JC, Leahy RM. Recursive MUSIC: a framework for EEG and MEG source localization. *IEEE Transactions on Biomedical Engineering*, 45(11): 1342–1354, 1998.

[118] Mosher JC, Leahy RM. Source localization using recursively applied and projected (RAP) MUSIC. *IEEE Transactions on Signal Processing*, 47(2): 332–340, 1999.

[119] Xu XL, Xu B, He B. An alternative subspace approach to EEG dipole source localization. *Physics in Medicine & Biology*, 49(2): 327, 2004.

[120] Michel CM, Murray MM, Lantz G, Gonzalez S, Spinelli L, de Peralta RG. EEG source imaging. *Clinical Neurophysiology*, 115(10): 2195–2222, 2004.

[121] Grech R, Cassar T, Muscat J, Camilleri KP, Fabri SG, Zervakis M, Xanthopoulos P, Sakkalis V, Vanrumste B. Review on solving the inverse problem in EEG source analysis. *Journal of Neuroengineering and Rehabilitation*, 5(1): 25, 2008.

[122] Pascual-Marqui RD. Review of methods for solving the EEG inverse problem. *International Journal of Bioelectromagnetism*, 1(1): 75–86, 1999.

[123] Pascual-Marqui RD, Michel CM, Lehmann D. Low resolution electromagnetic tomography: a new method for localizing electrical activity in the brain. *International Journal of Psychophysiology*, 18(1): 49–65, 1994.

[124] Pascual-Marqui RD, et al. Standardized low-resolution brain electromagnetic tomography (sLORETA): technical details. *Methods and Findings in Experimental and Clinical Pharmacology*, 24(Suppl D): 5–12, 2002.

[125] de Peralta Menendez RG, Murray MM, Michel CM, Martuzzi R, Andino SLG. Electrical neuroimaging based on biophysical constraints. *NeuroImage*, 21(2): 527–539, 2004.

[126] Van Veen BD, Van Drongelen W, Yuchtman M, Suzuki A. Localization of brain electrical activity via linearly constrained minimum variance spatial filtering. *IEEE Transactions on Biomedical Engineering*, 44(9): 867–880, 1997.

[127] Hansen PC. Analysis of discrete ill-posed problems by means of the L-curve. *SIAM review*, 34(4): 561–580, 1992.

[128] Zeki S, Shipp S. The functional logic of cortical connections. *Nature*, 335(6188): 311–317, 1988.

[129] Tournier JD, Mori S, Leemans A. Diffusion tensor imaging and beyond. *Magnetic Resonance in Medicine*, 65(6): 1532–1556, 2011.

[130] Jones DK, Knösche TR, Turner R. White matter integrity, fiber count, and other fallacies: the do's and don'ts of diffusion MRI. *NeuroImage*, 73: 239–254, 2013.

[131] DellAcqua F, Catani M. Structural human brain networks: hot topics in diffusion tractography. *Current Opinion in Neurology*, 25(4): 375–383, 2012.

[132] Friston K, Frith C, Liddle P, Frackowiak R. Functional connectivity: the principal-component analysis of large (PET) data sets. *Journal of Cerebral Blood Flow & Metabolism*, 13(1): 5–14, 1993.

[133] van Mierlo P, Papadopoulou M, Carrette E, Boon P, Vandenberghe S, Vonck K, Marinazzo D. Functional brain connectivity from EEG in epilepsy: Seizure prediction and epileptogenic focus localization. *Progress in Neurobiology*, 121: 19–35, 2014.

[134] Friston KJ. Functional and effective connectivity in neuroimaging: a synthesis. *Human Brain Mapping*, 2(1-2): 56–78, 1994.

[135] Friston K, Moran R, Seth AK. Analysing connectivity with Granger causality and dynamic causal modelling. *Current Opinion in Neurobiology*, 23(2): 172–178, 2013.

[136] Friston KJ, Harrison L, Penny W. Dynamic causal modelling. *NeuroImage*, 19(4): 1273–1302, 2003.

[137] Papadopoulou M, Leite M, van Mierlo P, Vonck K, Lemieux L, Friston K, Marinazzo D. Tracking slow modulations in synaptic gain using dynamic causal modelling: validation in epilepsy. *NeuroImage*, 107: 117–126, 2015.

[138] Wiener N. The theory of prediction. *Modern Mathematics for Engineers*, 1: 125–139, 1956.

[139] Granger CW. Investigating causal relations by econometric models and cross-spectral methods. *Econometrica: Journal of the Econometric Society*, 424–438, 1969.

[140] Marinazzo D, Liao W, Chen H, Stramaglia S. Nonlinear connectivity by Granger causality. *NeuroImage*, 58(2): 330–338, 2011.

[141] Akaike H. A new look at the statistical model identification. *IEEE Transactions on Automatic Control*, 19(6): 716–723, 1974.

[142] Pardey J, Roberts S, Tarassenko L. A review of parametric modelling techniques for EEG analysis. *Medical Engineering & Physics*, 18(1): 2–11, 1996.

[143] Sameshima K, Baccalá LA. Using partial directed coherence to describe neuronal ensemble interactions. *Journal of Neuroscience Methods*, 94(1): 93–103, 1999.

[144] Kaminski M, Blinowska KJ. A new method of the description of the information flow in the brain structures. *Biological Cybernetics*, 65(3): 203–210, 1991.

[145] Franaszczuk PJ, Bergey GK. Application of the directed transfer function method to mesial and lateral onset temporal lobe seizures. *Brain Topography*, 11(1): 13–21, 1998.

[146] Korzeniewska A, Mańczak M, Kamiński M, Blinowska KJ, Kasicki S. Determination of information flow direction among brain structures by a modified directed transfer function (dDTF) method. *Journal of Neuroscience Methods*, 125(1): 195–207, 2003.

[147] Sakkalis V. Review of advanced techniques for the estimation of brain connectivity measured with EEG/MEG. *Computers in Biology and Medicine*, 41(12): 1110–1117, 2011.

[148] Arnold M, Milner X, Witte H, Bauer R, Braun C. Adaptive AR modeling of nonstationary time series by means of Kalman filtering. *IEEE Transactions on Biomedical Engineering*, 45(5): 553–562, 1998.

[149] Schlögl A, Roberts S, Pfurtscheller G. A criterion for adaptive autoregressive models. *Engineering in Medicine and Biology Society, 2000. Proceedings of the 22nd Annual International Conference of the IEEE*, volume 2, 1581–1582. IEEE, 2000.

[150] Astolfi L, Cincotti F, Mattia D, Fallani FDV, Tocci A, Colosimo A, Salinari S, Marciani MG, Hesse W, Witte H, et al. Tracking the time-varying cortical connectivity patterns by adaptive multivariate estimators. *IEEE Transactions on Biomedical Engineering*, 55(3): 902–913, 2008.

[151] Wilke C, Ding L, He B, et al. Estimation of time-varying connectivity patterns through the use of an adaptive directed

transfer function. *IEEE Transactions on Biomedical Engineering*, 55(11): 2557–2564, 2008.

[152] Van Mierlo P, Carrette E, Hallez H, Vonck K, Van Roost D, Boon P, Staelens S. Accurate epileptogenic focus localization through time-variant functional connectivity analysis of intracranial electroencephalographic signals. *NeuroImage*, 56(3): 1122–1133, 2011.

[153] van Mierlo P, Carrette E, Hallez H, Raedt R, Meurs A, Vandenberghe S, Van Roost D, Boon P, Staelens S, Vonck K. Ictal-onset localization through connectivity analysis of intracranial EEG signals in patients with refractory epilepsy. *Epilepsia*, 2013.

[154] Stam CJ, Reijneveld JC. Graph theoretical analysis of complex networks in the brain. *Nonlinear Biomedical Physics*, 1(1): 3, 2007.

[155] Sporns O, Honey CJ, Kötter R. Identification and classification of hubs in brain networks. *PLoS one*, 2(10): e1049, 2007.

[156] Smith S. EEG in the diagnosis, classification, and management of patients with epilepsy. *Journal of Neurology, Neurosurgery & Psychiatry*, 76(suppl 2): ii2–ii7, 2005.

[157] Mouthaan BE, Rados M, Barsi P, Boon P, Carmichael DW, Carrette E, Craiu D, Cross JH, Diehl B, Dimova P, et al. Current use of imaging and electromagnetic source localization procedures in epilepsy surgery centers across Europe. *Epilepsia*, 57(5): 770–776, 2016.

[158] Knowlton RC. The role of FDG-PET, ictal SPECT, and MEG in the epilepsy surgery evaluation. *Epilepsy & Behavior*, 8(1): 91–101, 2006.

[159] La Fougère C, Rominger A, Förster S, Geisler J, Bartenstein P. PET and SPECT in epilepsy: a critical review. *Epilepsy & Behavior*, 15(1): 50–55, 2009.

[160] Brodbeck V, Spinelli L, Lascano AM, Wissmeier M, Vargas MI, Vulliémoz S, Pollo C, Schaller K, Michel CM, Seeck M. Electroencephalographic source imaging: a prospective study of 152 operated epileptic patients. *Brain*, 134(10): 2887–2897, 2011.

[161] van Mierlo P, Strobbe G, Keereman V, Birot G, Gadeyne S, Gschwind M, Carrette E, Meurs A, Van Roost D, Vonck K, et al. Automated long-term EEG analysis to localize the epileptogenic zone. *Epilepsia Open*, 2017.

[162] Kirchberger K, Hummel C, Stefan H. Postoperative multichannel magnetoencephalography in patients with recurrent seizures after epilepsy surgery. *Acta Neurologica Scandinavica*, 98(1): 1–7, 1998.

[163] Knowlton RC, Elgavish RA, Bartolucci A, Ojha B, Limdi N, Blount J, Burneo JG, Ver Hoef L, Paige L, Faught E, et al. Functional imaging: II. Prediction of epilepsy surgery outcome. *Annals of Neurology*, 64(1): 35–41, 2008.

[164] Lee Ws, Lee JK, Lee SA, Kang JK, Ko Ts. Complications and results of subdural grid electrode implantation in epilepsy surgery. *Surgical Neurology*, 54(5): 346–351, 2000.

[165] Hamer H, Morris H, Mascha E, Karafa M, Bingaman W, Bej M, Burgess R, Dinner D, Foldvary N, Hahn J, et al. Complications of invasive video-EEG monitoring with subdural grid electrodes. *Neurology*, 58(1): 97–103, 2002.

[166] Van Loo P, Carrette E, Meurs A, Goossens L, Van Roost D, Vonck K, Boon P. Surgical successes and failures of invasive video-EEG monitoring in the presurgical evaluation of epilepsy. *Panminerva Medica*, 53(4): 227–40, dec 2011.

[167] Sprengers M, Vonck K, Carrette E, Marson AG, Boon P. Deep brain and cortical stimulation for epilepsy. *The Cochrane Database of Systematic Reviews*, 6, 2014.

[168] Boon P, D'Havé M, Adam C, Vonck K, Baulac M, Vandekerckhove T, De Reuck J. Dipole modeling in epilepsy surgery candidates. *Epilepsia*, 38(2): 208–218, 1997.

[169] Burle B, Spieser L, Roger C, Casini L, Hasbroucq T, Vidal F. Spatial and temporal resolutions of EEG: Is it really black and white? A scalp current density view. *International Journal of Psychophysiology*, 97(3): 210–220, 2015.

[170] Mégevand P, Spinelli L, Genetti M, Brodbeck V, Momjian S, Schaller K, Michel CM, Vulliemoz S, Seeck M. Electric source

imaging of interictal activity accurately localises the seizure onset zone. *Journal of Neurology, Neurosurgery, and Psychiatry*, 85(1): 38–43, 2014.

[171] Kaiboriboon K, Lüders HO, Hamaneh M, Turnbull J, Lhatoo SD. EEG source imaging in epilepsy practicalities and pitfalls. *Nature Reviews Neurology*, 8(9): 498–507, 2012.

[172] Lantz G, de Peralta RG, Spinelli L, Seeck M, Michel CM. Epileptic source localization with high density EEG: how many electrodes are needed? *Clinical Neurophysiology*, 114(1): 63–69, 2003.

[173] Michel CM, Murray MM. Towards the utilization of EEG as a brain imaging tool. *NeuroImage*, 61(2): 371–385, 2012.

[174] Van de Steen F, Faes L, Karahan E, Songsiri J, Valdes-Sosa PA, Marinazzo D. Critical comments on EEG sensor space dynamical connectivity analysis. *Brain Topography*, 1–12, 2016.

[175] von Ellenrieder N, Beltrachini L, Muravchik CH, Gotman J. Extent of cortical generators visible on the scalp: effect of a subdural grid. *NeuroImage*, 101: 787–795, 2014.

[176] Jayakar P, Duchowny M, Resnick TJ, Alvarez LA. Localization of seizure foci: pitfalls and caveats. *Journal of Clinical Neurophysiology*, 8(4): 414–431, 1991.

[177] Rémi J, Vollmar C, de Marinis A, Heinlin J, Peraud A, Noachtar S. Congruence and discrepancy of interictal and ictal EEG with MRI lesions in focal epilepsies. *Neurology*, 77(14): 1383–1390, 2011.

[178] Piros P, Puskas S, Emri M, Opposits G, Spisak T, Fekete I, Clemens B. Uppermost synchronized generators of spike–wave activity are localized in limbic cortical areas in late-onset absence status epilepticus. *Seizure*, 23(3): 213–221, 2014.

[179] Hunyadi B, Tousseyn S, Dupont P, Van Huffel S, De Vos M, Van Paesschen W. A prospective fMRI-based technique for localising the epileptogenic zone in presurgical evaluation of epilepsy. *NeuroImage*, 113: 329–339, 2015.

[180] Yagyu K, Takeuchi F, Shiraishi H, Nakane S, Sueda K, Asahina N, Kohsaka S, Umeoka S, Usui N, Baba K, Saitoh S. The applications

of time-frequency analyses to ictal magnetoencephalography in neocortical epilepsy. *Epilepsy Research*, 90(3): 199–206, 2010.

[181] Medvedovsky M, Taulu S, Gaily E, Metsähonkala EL, Mäkelä JP, Ekstein D, Kipervasser S, Neufeld MY, Kramer U, Blomstedt G, Fried I, Karppinen A, Veshchev I, Roivainen R, Ben-Zeev B, Goldberg-Stern H, Wilenius J, Paetau R. Sensitivity and specificity of seizure-onset zone estimation by ictal magnetoencephalography. *Epilepsia*, 53(9): 1649–1657, 2012.

[182] Miao A, Xiang J, Tang L, Ge H, Liu H, Wu T, Chen Q, Hu Z, Lu X, Wang X. Using ictal high-frequency oscillations (80500Hz) to localize seizure onset zones in childhood absence epilepsy: A MEG study. *Neuroscience Letters*, 566: 21–26, 2014.

[183] Miao A, Tang L, Xiang J, Guan Q, Ge H, Liu H, Wu T, Chen Q, Yang L, Lu X, Hu Z, Wang X. Dynamic magnetic source imaging of absence seizure initialization and propagation: A magnetoencephalography study. *Epilepsy Research*, 108(3): 468–480, 2014.

[184] Badier JM, Bénar CG, Woodman M, Cruto C, Chauvel P, Bartolomei F, Gavaret M. Ictal Magnetic Source Imaging in Presurgical Assessment. *Brain Topography*, 29(1): 182–192, 2016.

[185] Klamer S, Rona S, Elshahabi A, Lerche H, Braun C, Honegger J, Erb M, Focke NK. Multimodal effective connectivity analysis reveals seizure focus and propagation in musicogenic epilepsy. *NeuroImage*, 113: 70–77, 2015.

[186] Akdeniz G. Electrical source localization by LORETA in patients with epilepsy: Confirmation by postoperative MRI. *Annals of Indian Academy of Neurology*, 19(1): 37–43, 2016.

[187] Assaf BA, Ebersole JS. Continuous source imaging of scalp ictal rhythms in temporal lobe epilepsy. *Epilepsia*, 38(10): 1114–1123, 1997.

[188] Beniczky S, Lantz G, Rosenzweig I, Åkeson P, Pedersen B, Pinborg LH, Ziebell M, Jespersen B, Fuglsang-Frederiksen A. Source localization of rhythmic ictal EEG activity: a study of diagnostic accuracy following STARD criteria. *Epilepsia*, 54(10): 1743–1752, 2013.

[189] Beniczky S, Rosenzweig I, Scherg M, Jordanov T, Lanfer B, Lantz G, Larsson PG. Ictal EEG source imaging in presurgical evaluation: High agreement between analysis methods. *Seizure*, 43: 1–5, 2016.

[190] Boon P, D'Havé M. Interictal and ictal dipole modelling in patients with refractory partial epilepsy. *Acta Neurologica Scandinavica*, 92(1): 7–18, 1995.

[191] Boon P, D'havé M, Vandekerckhove T, Achten E, Adam C, Clemenceau S, Baulac M, Goossens L, Calliauw L, De Reuck J. Dipole modelling and intracranial EEG recording: correlation between dipole and ictal onset zone. *Acta Neurochirurgica*, 139(7): 643–652, 1997.

[192] Boon P, D'Have M, Van Hoey G, Vanrumste B, Vonck K, Adam C, Vandekerckhove T. Interictal and ictal source localization in neocortical versus medial temporal lobe epilepsy. *Advances in Neurology*, 84: 365–375, 2000.

[193] Boon P, D'Havé M, Vanrumste B, Van Hoey G, Vonck K, Van Walleghem P, Caemaert J, Achten E, De Reuck J. Ictal source localization in presurgical patients with refractory epilepsy. *Journal of Clinical Neurophysiology*, 19(5): 461–468, 2002.

[194] Despotovic I, Cherian PJ, De Vos M, Hallez H, Deburchgraeve W, Govaert P, Lequin M, Visser GH, Swarte RM, Vansteenkiste E, Van Huffel S, Philips W. Relationship of EEG sources of neonatal seizures to acute perinatal brain lesions seen on MRI: A pilot study. *Human Brain Mapping*, 34(10): 2402–2417, 2013.

[195] Ding L, Worrell GA, Lagerlund TD, He B. Ictal source analysis: localization and imaging of causal interactions in humans. *NeuroImage*, 34(2): 575–586, 2007.

[196] Elshoff L, Muthuraman M, Anwar AR, Deuschl G, Stephani U, Raethjen J, Siniatchkin M. Dynamic imaging of coherent sources reveals different network connectivity underlying the generation and perpetuation of epileptic seizures. *PLoS one*, 8(10): e78422, 2013.

[197] Habib MA, Ibrahim F, Mohktar MS, Kamaruzzaman SB, Rahmat K, Lim KS. Ictal EEG Source Imaging for Presurgical Evaluation of Refractory Focal Epilepsy. *World Neurosurgery*, 2015.

[198] Hallez H, De Vos M, Vanrumste B, Van Hese P, Assecondi S, Van Laere K, Dupont P, Van Paesschen W, Van Huffel S, Lemahieu I. Removing muscle and eye artifacts using blind source separation techniques in ictal EEG source imaging. *Clinical Neurophysiology*, 120(7): 1262–1272, 2009.

[199] Holmes MD, Tucker DM, Quiring JM, Hakimian S, Miller JW, Ojemann JG. Comparing Noninvasive Dense Array and Intracranial Electroencephalography for Localization of Seizures. *Neurosurgery*, 66(2): 354–362, 2010.

[200] Kobayashi K, James C, Yoshinaga H, Ohtsuka Y, Gotman J. The electroencephalogram through a software microscope: non-invasive localization and visualization of epileptic seizure activity from inside the brain. *Clinical Neurophysiology*, 111(1): 134–149, 2000.

[201] Koessler L, Benar C, Maillard L, Badier JM, Vignal JP, Bartolomei F, Chauvel P, Gavaret M. Source localization of ictal epileptic activity investigated by high resolution EEG and validated by SEEG. *NeuroImage*, 51(2): 642–653, 2010.

[202] Kovac S, Chaudhary UJ, Rodionov R, Mantoan L, Scott CA, Lemieux L, Wehner T, Scherg M, Diehl B. Ictal EEG Source Imaging in Frontal Lobe Epilepsy Leads to Improved Lateralization Compared With Visual Analysis. *Journal of Clinical Neurophysiology*, 31(1): 10–20, 2014.

[203] Lantz G, Michel C, Seeck M, Blanke O, Spinelli L, Thut G, Landis T, Rosen I. Space-oriented segmentation and 3-dimensional source reconstruction of ictal EEG patterns. *Clinical Neurophysiology*, 112(4): 688–697, 2001.

[204] Lu Y, Yang L, Worrell GA, Brinkmann B, Nelson C, He B. Dynamic imaging of seizure activity in pediatric epilepsy patients. *Clinical Neurophysiology*, 123(11): 2122–2129, 2012.

[205] Lu Y, Yang L, Worrell G, He B. Seizure source imaging by means of FINE spatio-temporal dipole localization and directed transfer function in partial epilepsy patients. *Clinical Neurophysiology*, 2012.

[206] Merlet I, Gotman J. Dipole modeling of scalp electroencephalogram epileptic discharges: correlation with intracerebral fields. *Clinical Neurophysiology*, 112(3): 414–430, 2001.

[207] Mine S, Yamaura A, Iwasa H, Nakajima Y, Shibata T, Itoh T. Dipole source localization of ictal epileptiform activity. *Neuroreport*, 9(18): 4007–4013, 1998.

[208] Mine S, Oka N, Yamaura A, Iwasa H, Nakajima Y. Dipole source localization of ictal epileptiform activity in estimation of epileptogenic zone. *International Congress Series*, volume 1232, 453–459. Elsevier, 2002.

[209] Pellegrino G, Hedrich T, Chowdhury R, Hall JA, Lina JM, Dubeau F, Kobayashi E, Grova C. Source localization of the seizure onset zone from ictal EEG/MEG data. *Human Brain Mapping*, 37(7): 2528–2546, 2016.

[210] Rullmann M, Anwander A, Dannhauer M, Warfield SK, Duffy FH, Wolters CH. EEG source analysis of epileptiform activity using a 1 mm anisotropic hexahedra finite element head model. *NeuroImage*, 44(2): 399–410, 2009.

[211] Sohrabpour A, Ye S, Worrell GA, Zhang W, He B. Noninvasive Electromagnetic Source Imaging and Granger Causality Analysis: An Electrophysiological Connectome (eConnectome) Approach. *IEEE Transactions on Biomedical Engineering*, 63(12): 2474–2487, 2016.

[212] Worrell GA, Lagerlund TD, Sharbrough FW, Brinkmann BH, Busacker NE, Cicora KM, O 'brien TJ. Localization of the Epileptic Focus by Low-Resolution Electromagnetic Tomography in Patients with a Lesion Demonstrated by MRI. *Brain Topography*, 12(4), 2000.

[213] Lehmann D, Michel C. Intracerebral dipole source localization for FFT power maps. *Electroencephalography and Clinical Neurophysiology*, 76(3): 271–276, 1990.

[214] Yang L, Wilke C, Brinkmann B, Worrell GA, He B. Dynamic imaging of ictal oscillations using non-invasive high-resolution EEG. *NeuroImage*, 56(4): 1908–1917, 2011.

[215] Assaf BA, Ebersole JS. Visual and quantitative ictal EEG predictors of outcome after temporal lobectomy. *Epilepsia*, 40(1): 52–61, 1999.

[216] Van Paesschen W, Dupont P, Sunaert S, Goffin K, Van Laere K. The use of SPECT and PET in routine clinical practice in epilepsy. *Current Opinion in Neurology*, 20(2): 194–202, 2007.

[217] De Vos M, Vergult A, De Lathauwer L, De Clercq W, Van Huffel S, Dupont P, Palmini A, Van Paesschen W. Canonical decomposition of ictal scalp EEG reliably detects the seizure onset zone. *NeuroImage*, 37(3): 844–854, 2007.

[218] Deburchgraeve W, Cherian PJ, De Vos M, Swarte RM, Blok JH, Visser GH, Govaert P, Van Huffel S. Neonatal seizure localization using PARAFAC decomposition. *Clinical Neurophysiology*, 120(10): 1787–1796, 2009.

[219] Bossuyt PM, Reitsma JB, Bruns DE, Gatsonis CA, Glasziou PP, Irwig L, Lijmer JG, Moher D, Rennie D, De Vet HC, et al. STARD 2015: an updated list of essential items for reporting diagnostic accuracy studies. *Radiology*, 277(3): 826–832, 2015.

[220] Staljanssens W, Van Holen R, van Mierlo P. EEG-based seizure onset zone localization in epilepsy: where are we now? *NeuroImage: Clinical*, submitted.

[221] Makeig S, Bell AJ, Jung TP, Sejnowski TJ, et al. Independent component analysis of electroencephalographic data. *Advances in Neural Information Processing Systems*, 145–151, 1996.

[222] Hallez H, Vanrumste B, Van Hese P, D'Asseler Y, Lemahieu I, Van de Walle R. A finite difference method with reciprocity used to incorporate anisotropy in electroencephalogram dipole source localization. *Physics in Medicine & Biology*, 50(16): 3787, 2005.

[223] Baumann SB, Wozny DR, Kelly SK, Meno FM. The electrical conductivity of human cerebrospinal fluid at body temperature. *IEEE Transactions on Biomedical Engineering*, 44(3): 220–223, 1997.

[224] Lopez J, Litvak V, Espinosa J, Friston K, Barnes GR. Algorithmic procedures for Bayesian MEG/EEG source reconstruction in SPM. *NeuroImage*, 84: 476–487, 2014.

[225] Haalman I, Vaadia E. Dynamics of neuronal interactions: relation to behavior, firing rates, and distance between neurons. *Human Brain Mapping*, 5(4): 249–253, 1997.

[226] Coito A, Plomp G, Genetti M, Abela E, Wiest R, Seeck M, Michel CM, Vulliémoz S. Dynamic directed interictal connectivity in left and right temporal lobe epilepsy. *Epilepsia*, 56(2): 207–217, 2015.

[227] Van Hoey G, Vanrumste B, D'Havé M, Van de Walle R, Lemahieu I, Boon P. Influence of measurement noise and electrode mislocalisation on EEG dipole-source localisation. *Medical & Biological Engineering & Computing*, 38(3): 287–296, 2000.

[228] Wang Y, Gotman J. The influence of electrode location errors on EEG dipole source localization with a realistic head model. *Clinical Neurophysiology*, 112(9): 1777–1780, 2001.

[229] Dalal SS, Rampp S, Willomitzer F, Ettl S. Consequences of EEG electrode position error on ultimate beamformer source reconstruction performance. *Frontiers in Neuroscience*, 8, 2014.

[230] Strobbe G, van Mierlo P, De Vos M, Mijović B, Hallez H, Van Huffel S, López JD, Vandenberghe S. Multiple sparse volumetric priors for distributed EEG source reconstruction. *NeuroImage*, 100: 715–724, 2014.

[231] Xu XL, Xu B, He B. An alternative subspace approach to EEG dipole source localization. *Physics in Medicine & Biology*, 49(2): 327, 2004.

[232] Ding L, He B. Spatio-temporal EEG source localization using a three-dimensional subspace FINE approach in a realistic geometry inhomogeneous head model. *IEEE Transactions on Biomedical Engineering*, 53(9): 1732–1739, 2006.

[233] Groß J, Kujala J, Hämäläinen M, Timmermann L, Schnitzler A, Salmelin R. Dynamic imaging of coherent sources: studying neural interactions in the human brain. *Proceedings of the National Academy Science*, 98(2): 694–699, 2001.

[234] Groß J, Timmermann L, Kujala J, Dirks M, Schmitz F, Salmelin R, Schnitzler A. The neural basis of intermittent motor control in humans. *Proceedings of the National Academy Science*, 99(4): 2299–2302, 2002.

[235] Clarke C, Janday B. The solution of the biomagnetic inverse problem by maximum statistical entropy. *Inverse Problems*, 5(4): 483, 1989.

[236] Grova C, Daunizeau J, Lina JM, Bénar CG, Benali H, Gotman J. Evaluation of EEG localization methods using realistic simulations of interictal spikes. *NeuroImage*, 29(3): 734–753, 2006.

[237] Hillebrand A, Barnes GR, Bosboom JL, Berendse HW, Stam CJ. Frequency-dependent functional connectivity within resting-state networks: an atlas-based MEG beamformer solution. *NeuroImage*, 59(4): 3909–3921, 2012.

[238] Brovelli A, Chicharro D, Badier JM, Wang H, Jirsa V. Characterization of cortical networks and corticocortical functional connectivity mediating arbitrary visuomotor mapping. *The Journal of Neuroscience*, 35(37): 12643–12658, 2015.

[239] Coito A, Genetti M, Pittau F, Iannotti GR, Thomschewski A, Höller Y, Trinka E, Wiest R, Seeck M, Michel CM, et al. Altered directed functional connectivity in temporal lobe epilepsy in the absence of interictal spikes: A high density EEG study. *Epilepsia*, 57(3): 402–411, 2016.

[240] Schoffelen JM, Gross J. Source connectivity analysis with MEG and EEG. *Human Brain Mapping*, 30(6): 1857–1865, 2009.

[241] Nolte G, Bai O, Wheaton L, Mari Z, Vorbach S, Hallett M. Identifying true brain interaction from EEG data using the imaginary part of coherency. *Clinical Neurophysiology*, 115(10): 2292–2307, 2004.

[242] Bastos AM, Schoffelen JM. A tutorial review of functional connectivity analysis methods and their interpretational pitfalls. *Frontiers in Systems Neuroscience*, 9, 2015.

[243] Staljanssens W, Strobbe G, Van Holen R, Birot G, Michel C, Seeck M, Vulliémoz S, van Mierlo P. Electrical source imaging and connectivity analysis to localize the seizure-onset zone based on high-density ictal scalp EEG recordings. *International Conference on Basic and Clinical Multimodal Imaging*. Utrecht, The Netherlands, 2015.

[244] Staljanssens W, Strobbe G, Van Holen R, Birot G, Michel CM, Seeck M, Vandenberghe S, Vulliémoz S, van Mierlo P. Seizure onset zone localization from ictal high-density EEG in five patients.

Annual Meeting of the American Epilepsy Society. Philadelphia, Pennsylvania, USA, 2015.

[245] Staljanssens W, Strobbe G, Van Holen R, Birot G, Vulliémoz S, Seeck M, Vandenberghe S, van Mierlo P. Seizure onset zone localization from ictal high-density EEG in refractory focal epilepsy. *22nd Annual Meeting of the Organization for Human Brain Mapping*. Geneva, Switzerland, 2016.

[246] Staljanssens W, Strobbe G, Van Holen R, Birot G, Gschwind M, Seeck M, Vandenberghe S, Vulliémoz S, van Mierlo P. Seizure onset zone localization from ictal high-density EEG in refractory focal epilepsy. *Brain Topography*, 30(2): 257–271, 2017.

[247] Hyvarinen A, Karhunen J, Oja E. *Independent Component Analysis*. J. Wiley, 2001.

[248] Montes-Restrepo V, Carrette E, Strobbe G, Gadeyne S, Vandenberghe S, Boon P, Vonck K, van Mierlo P. The Role of Skull Modeling in EEG Source Imaging for Patients with Refractory Temporal Lobe Epilepsy. *Brain Topography*, 29(4): 572–589, 2016.

[249] Strobbe G, Carrette E, López JD, Restrepo VM, Van Roost D, Meurs A, Vonck K, Boon P, Vandenberghe S, van Mierlo P. Electrical source imaging of interictal spikes using multiple sparse volumetric priors for presurgical epileptogenic focus localization. *NeuroImage: Clinical*, 11: 252–263, 2016.

[250] Lantz G, Michel CM, Seeck M, Blanke O, Landis T, Rosén I. Frequency domain EEG source localization of ictal epileptiform activity in patients with partial complex epilepsy of temporal lobe origin. *Clinical Neurophysiology*, 110(1): 176–184, 1999.

[251] Jung KY, Kang JK, Kim JH, Im CH, Kim KH, Jung HK. Spatiotemporospectral characteristics of scalp ictal EEG in mesial temporal lobe epilepsy with hippocampal sclerosis. *Brain Research*, 1287: 206–219, 2009.

[252] Schlindwein FS, Evans DH. Selection of the order of autoregressive models for spectral analysis of doppler ultrasound signals. *Ultrasound in Medicine & Biology*, 16(1): 81–91, 1990.

[253] van Mierlo P. Functional brain connectivity helps to localize seizures from EEG. *Alpine Brain Imaging Meeting*. Champéry, Switzerland, 2017.

[254] Staljanssens W, Strobbe G, Keereman V, Birot G, Meurs A, Carrette E, Momjian S, Van Roost D, Vonck K, Boon P, Seeck M, Vulliémoz S, van Mierlo P. Functional brain connectivity helps to localize seizures from EEG. *Journées scientifiques Neurochirurgie HUG*. Geneva, Switzerland, 2017.

[255] van Mierlo P, Staljanssens W, Strobbe G, Keereman V, Vonck K, Boon P, Seeck M, Vulliémoz S. Functional brain connectivity helps to localize seizures from EEG. *Jahrestagung der Deutschen und Österreichischen Gesellschaften für Epileptologie und der Schweizerischen Epilepsie-Liga*. Vienna, Austria, 2017.

[256] Staljanssens W, Strobbe G, Van Holen R, Keereman V, Gadeyne S, Carrette E, Meurs A, Pittau F, Momjian S, Seeck M, Boon P, Vandenberghe S, Vulliémoz S, Vonck K, van Mierlo P. Seizure onset zone localization from clinical ictal EEG in refractory epilepsy. *Annual Meeting of the Organization for Human Brain Mapping*. Vancouver, Canada, 2017.

[257] Staljanssens W, Strobbe G, Van Holen R, Keereman V, Gadeyne S, Carrette E, Meurs A, Pittau F, Momjian S, Seeck M, Boon P, Vandenberghe S, Vulliémoz S, Vonck K, van Mierlo P. EEG source connectivity to localize the seizure onset zone in patients with drug resistant epilepsy. *International Conference on Basic and Clinical Multimodal Imaging*. Bern, Switzerland, 2017.

[258] Staljanssens W, Strobbe G, Van Holen R, Keereman V, Gadeyne S, Carrette E, Meurs A, Seeck M, Boon P, Vandenberghe S, Vulliémoz S, Vonck K, van Mierlo P. EEG source connectivity to localize the seizure onset zone from clinical ictal EEG in refractory epilepsy patients. *32nd International Epilepsy Congress*. Barcelona, Spain, 2017.

[259] Staljanssens W, Strobbe G, Van Holen R, Keereman V, Gadeyne S, Carrette E, Meurs A, Pittau F, Momjian S, Seeck M, Boon P, Vandenberghe S, Vulliémoz S, Vonck K, van Mierlo P. EEG source connectivity to localize the seizure onset zone in patients with drug resistant epilepsy. *NeuroImage: Clinical*, 16(C): 689–698, 2017.

[260] Ponten S, Bartolomei F, Stam C. Small-world networks and epilepsy: graph theoretical analysis of intracerebrally recorded mesial temporal lobe seizures. *Clinical Neurophysiology*, 118(4): 918–927, 2007.

[261] Schindler KA, Bialonski S, Horstmann MT, Elger CE, Lehnertz K. Evolving functional network properties and synchronizability during human epileptic seizures. *Chaos: An Interdisciplinary Journal of Nonlinear Science*, 18(3): 033119, 2008.

[262] Wilke C, Worrell G, He B. Graph analysis of epileptogenic networks in human partial epilepsy. *Epilepsia*, 52(1): 84–93, 2011.

[263] Tzallas AT, Tsipouras MG, Tsalikakis DG, Karvounis EC, Astrakas L, Konitsiotis S, Tzaphlidou M. Automated epileptic seizure detection methods: a review study. *Epilepsy-histological, electroencephalographic and psychological aspects*. InTech, 2012.

[264] Fürbass F, Kampusch S, Kaniusas E, Koren J, Pirker S, Hopfengärtner R, Stefan H, Kluge T, Baumgartner C. Automatic multimodal detection for long-term seizure documentation in epilepsy. *Clinical Neurophysiology*, 2017.

[265] Becker H, Albera L, Comon P, Nunes JC, Gribonval R, Fleureau J, Guillotel P, Merlet I. SISSY: An efficient and automatic algorithm for the analysis of EEG sources based on structured sparsity. *NeuroImage*, 157: 157–172, 2017.

[266] Verhoeven T, Coito A, Plomp G, Thomschewski A, Pittau F, Trinka E, Wiest R, Schaller K, Michel C, Seeck M, Dambre J, Vulliémoz S, van Mierlo P. Automated diagnosis of temporal lobe epilepsy in the absence of interictal spikes. *NeuroImage: Clinical*, 17: 10–15, 2018.

[267] Clemens B, Puskás S, Besenyei M, Kovács N, Spisák T, Kis S, Emri M, Hollódy K, Fogarasi A, Kondákor I, Fekete I. Valproate treatment normalizes EEG functional connectivity in successfully treated idiopathic generalized epilepsy patients. *Epilepsy Research*, 108(10): 1896–1903, 2014.

[268] Sanz-Leon P. *Development of a computational and neuroinformatics framework for large-scale brain modelling*. Ph.D. thesis, Aix-Marseille, 2014.

[269] DeSalvo MN, Douw L, Tanaka N, Reinsberger C, Stufflebeam SM. Altered structural connectome in temporal lobe epilepsy. *Radiology*, 270(3): 842–848, 2013.

[270] Ji GJ, Zhang Z, Xu Q, Wei W, Wang J, Wang Z, Yang F, Sun K, Jiao Q, Liao W, et al. Connectome reorganization associated with surgical outcome in temporal lobe epilepsy. *Medicine*, 94(40), 2015.

[271] Liao W, Ji GJ, Xu Q, Wei W, Wang J, Wang Z, Yang F, Sun K, Jiao Q, Richardson MP, et al. Functional connectome before and following temporal lobectomy in mesial temporal lobe epilepsy. *Scientific Reports*, 6: 23153, 2016.